

Electron Beam Freeform Fabrication of Aluminum: Investigating Properties and Cracking in Alloys 2219 and 7075

A Thesis

Presented to

the faculty of the School of Engineering and Applied Science

University of Virginia

in partial fulfillment
of the requirements for the degree

Master of Science

by

Mary Cecilia Mulvaney

December 2019

APPROVAL SHEET

This Thesis
is submitted in partial fulfillment of the requirements
for the degree of
Master of Science

Author Signature: Mary Cecilia Mulvaney

This Thesis has been read and approved by the examining committee:

Advisor: James Fitz-Gerald

Committee Member: Sean Agnew

Committee Member: Ji Ma

Committee Member: Marcia Domack

Committee Member: Karen Tamingler

Committee Member: _____

Accepted for the School of Engineering and Applied Science:



Craig H. Benson, School of Engineering and Applied Science

December 2019

Abstract

Aluminum alloys are of great interest to the aeronautics community due to their high strength-to-weight ratio and relatively low cost (compared to other aerospace alloys such as titanium). Specifically, 7xxx-series alloys are desirable due to their high tensile strength, moderate toughness, and low corrosion susceptibility in certain temperatures. High deposition rate additive manufacturing (AM) methods represent a current technology that may play a role in future aircraft structures and would benefit from the high strength of 7xxx-series alloys. However, the ability to weld and additively manufacture structures from 7xxx-series alloys is limited by their susceptibility to hot cracking during fusion welding. This work investigates the AM compatibility and resulting properties of two common aerospace aluminum alloys, 2219 and 7075, deposited with the electron beam freeform fabrication (EBF³) process.

2219 is a weldable, Al-6.3Cu aerospace alloy used in rocket structures due to its moderate strength, excellent toughness, and good corrosion resistance. Linear walls and a brick-shaped deposit were fabricated, and the builds showed no evidence of cracking and minimal porosity, indicative of excellent AM compatibility. The microstructure and tensile properties of the deposits were studied in both the as-deposited (AD) and the artificially aged (T6) heat-treated (HT) conditions. The microstructure of 2219 in the AD condition included grains slightly elongated in the vertical direction, with an area-averaged grain diameter of 130 μm . The AD tensile properties were anisotropic, with yield strength (YS) and ultimate tensile strength (UTS) values ranging from 16.8 and 38.8 ksi in the longitudinal orientation to 21.5 and 40.7 ksi in the transverse orientation. All AD properties fell between typical values for 2219 wrought plate in the annealed (O) and naturally aged (T4) conditions. The HT tensile properties were isotropic, with an average YS of 43.4 ksi and a UTS of 63.0 ksi, and were consistent with typical 2219-T62 wrought product values (YS of 42.1 ksi and UTS of 60.2 ksi).

In comparison, 7075 is an Al-5.7Zn-2.4Mg-1.5Cu alloy with limited weldability and is used in aircraft structures due to its high strength. Linear wall deposits were fabricated with the EBF³ process to study the effects of beam parameters and base-plate conditions on the extent of hot cracking. In these deposits, both solidification and liquation cracks were observed, indicating that similar hot cracking mechanisms are in operation for both conventional welding and EBF³ of 7075. However, there were differences in the cracking behavior between the two processes due to the distinct geometry and thermal history of layer-by-layer AM. In the welding literature, solidification cracks typically occur parallel to the weld direction in the fusion zone, while

liquation cracks occur in the partially melted zone of the base metal. In the 7075 EBF³ deposits, periodic solidification cracks appeared as large macrocracks transverse to the weld direction that propagated through the deposit layers. Between these solidification macrocracks, microstructural-scale liquation cracks developed below the topmost layer of the deposits.

As a first order effect, both the thickness and the initial temperature of the baseplate altered hot cracking density, with baseplate thickness affecting the periodicity and length of solidification cracks and temperature affecting the number and average length of liquation cracks. In addition, the composition of the fusion zone and its solidification characteristics contributed to cracking. During processing, Zn and Mg were vaporized from the molten pool due to their high vapor pressures, with losses ranging from 10% to 65% across the deposits. Solidification diagrams calculated from the Scheil solidification model were used to gain insight into both the hot cracking susceptibility (HCS) of the deposit compositions and the propensity for liquation cracking at the deposit-baseplate intersection.

A substantial reduction in cracking was observed when printing with a focused beam (keyhole) condition. The resulting deposit was free from solidification cracks in the steady state region and showed a 4x reduction in liquation crack density. The keyhole regions of the microstructure showed equiaxed grains on the order of 40 μm in diameter that disrupted solidification crack formation and lowered the liquation crack density. These improvements illustrate the impact of grain refinement in a material predicted to have a high HCS.

Analysis was also completed to explore future directions of alloy design for AM that would reduce the HCS of Al-Zn-Mg-Cu alloys. Results indicate that increasing the Cu content reduces cracking susceptibility by changing the solidification pathway, while maintaining a high concentration of Zn and Mg in the alloy retains strength. The HCS index of such Cu-rich 7xxx-series alloys was 1.5x higher than that of 2219 due to the Zn and Mg additions but 1.9x lower than that of 7075.

The results of this work indicate that achieving wrought 7075 properties with AM of 7xxx-series alloys is challenging due to Zn and Mg vaporization losses. These losses increase the susceptibility of 7075 to solidification and liquation cracking, inhibiting the use of 7xxx-series alloys in AM products. In addition, solute vaporization contributes to a loss of strength compared to wrought product, limiting the final application of the AM material. Future work involving alloy design in combination with in-situ grain refinement is pivotal to the successful deposition of high-strength aluminum alloys with EBF³.

Acknowledgements

I would like to begin by thanking my UVA advisor, Professor James Fitz-Gerald, as well as my two advisors from NASA Langley Research Center, Marcia Domack and Karen Taminger. Each has inspired me to become a better researcher, and I have been so fortunate to learn from these top-notch scientists and wonderful mentors.

Thanks also to NASA Langley for providing the additive manufacturing, non-destructive evaluation, and characterization facilities to enable this research, and to the NASA Advanced Air Transportation Technology (AATT) project for funding the work. I am so fortunate to have the opportunity to conduct my graduate research at NASA. Thanks also to the National Institute of Aerospace for coordinating my remote degree and making me feel included in the NIA family.

I would also like to thank my officemates at NASA - Libby and Bryan - for their friendship, collaboration, and patience over the past few years, as well as Jonathan, Rebecca, John, and Will at UVA for their support and encouragement from afar.

Thank you also to the other researchers at NASA who have supported my work, including Chris D., Chris L., and Patty, as well as to the Advanced Materials and Processing Branch for a wonderful environment for my growth as a researcher. Special thanks goes to Clay, Jim, Stewart, and Dave for their tireless support of my lab work and for keeping me lighthearted, as well as to Richard in actualizing my EBF³ deposits and to Will for conducting the XCT scans.

I want to also thank my family for encouraging my love of science and the aerospace field, and especially my kind, patient, and supportive husband, John, for understanding my recent late nights and walking with me during this journey.

Most importantly, I thank God for leading this thesis work and all things. May all my pursuits be *ad majorem Dei gloriam!*

Contents

Abstract	iii
Acknowledgements	v
List of Figures	ix
List of Tables	xiii
1 Introduction	1
1.1 Motivation	1
1.2 Materials and Property Targets	2
1.3 Knowledge Gaps	3
1.4 Thesis Objectives and Outline	3
2 Review of Electron Beam Freeform Fabrication	5
2.1 Fusion Welding Fundamentals	5
2.2 Review of Common Welding Processes	8
2.2.1 Gas-Tungsten Arc Welding	8
2.2.2 Gas-Metal Arc Welding	10
2.2.3 Laser Beam Welding	10
2.2.4 Electron Beam Welding	12
2.3 Review of Common Additive Manufacturing Methods	13
2.3.1 Wire-Arc Additive Manufacturing	14
2.3.2 Laser Beam Melting	16
2.3.3 Electron Beam Freeform Fabrication	17
2.4 Defects in Welding and Additive Manufacturing	19
2.4.1 Alloying Element Volatility	19
2.4.2 Porosity	21
2.4.3 Solidification Cracking	21
2.4.4 Liquation Cracking	25

3	Behavior and Properties of EBF³ Deposited 2219	27
3.1	Abstract	27
3.2	Background	28
3.2.1	Wrought 2219	28
3.2.2	Welding of 2219	31
3.2.3	Additive Manufacturing of 2219	32
3.3	Experimental Procedures	35
3.3.1	Starting Materials	35
3.3.2	Machine Setup and Deposition Procedures	36
3.3.3	Deposit Evaluation Procedures and Specimen Preparation	41
3.3.4	Specimen Characterization and Mechanical Testing Procedures	43
3.4	Results	44
3.4.1	Non-Destructive Evaluation of Deposits	44
3.4.2	As-Deposited and Heat Treated Microstructures	46
3.4.3	X-ray Diffraction	53
3.4.4	Hardness	54
3.4.5	Tensile Properties and Fracture Surfaces	55
3.5	Discussion	60
3.5.1	As-Deposited Microstructure and Properties	61
3.5.2	Heat Treated Microstructure and Properties	63
3.5.3	EBF ³ Compatibility and Meeting the 7050 Property Target	65
3.6	Summary	67
4	Behavior and Properties of 7075	69
4.1	Abstract	69
4.2	Background	70
4.2.1	Wrought 7075	70
4.2.2	Welding of 7xxx-Series Aluminum	72
4.2.3	Additive Manufacturing of 7xxx-Series Aluminum	73
4.3	Experimental Procedures	76
4.3.1	Starting Materials	77
4.3.2	Deposition Setup	78
4.3.3	Specimen Analysis Procedures	79
4.3.4	Nondestructive Testing	80
4.3.5	Cracking Analysis Methods	80
4.4	Results	82

4.4.1	7075 Deposition Series Overview	82
4.4.2	Deposit Composition	94
4.4.3	As-Deposited Microstructures	96
4.4.4	Non-Destructive Evaluation	104
4.4.5	Fractography	111
4.4.6	Hardness	117
4.5	Discussion	118
4.5.1	Variations in Microstructure and Composition with Processing Parameters	118
4.5.2	Solidification Cracking	120
4.5.3	Liquation and Liquation Cracking	128
4.5.4	Effect of Composition on Cracking and Hardness	136
4.5.5	Directions for Crack Mitigation and Elimination	141
4.6	Summary	145
5	Conclusions and Future Work	147
5.1	Conclusions	147
5.2	Future Work	149
A	AA2219 Deposit Cut Plans	151
B	Sub-size Tensile Specimen Drawing	154
C	7075 Deposit Cut Plans	155
D	Solidification Rate and Liquation Depth Analysis	159
D.1	Thermal Model Setup	159
D.2	Results	161
D.2.1	Solidification Rate Predictions	161
D.2.2	Liquation Depth Analysis	162

List of Figures

2.1	Regions of a Weld Joint	6
2.2	Weld Zone Microstructures	7
2.3	HAZ Width	7
2.4	Metallurgical Joining Processes	9
2.5	GTAW Process Diagram	10
2.6	GMAW Process Diagram	11
2.7	LBW Process Diagram	11
2.8	EBW Process Diagram	12
2.9	Effect of Pressure on Electron Beam Shape and Weld Penetration . .	14
2.10	Breakdown of AM Processes	15
2.11	WAAM Machine and Resulting Deposit	15
2.12	SLM Diagram	16
2.13	EBF ³ Diagram	17
2.14	Elemental Vapor Pressures	20
2.15	Dendritic Solidification Crack Surface	22
2.16	Liquid Channel Feeding	23
2.17	Influence of Back-Diffusion on Crack Susceptibility	24
2.18	Liquated and Cracked Microstructures	25
3.1	Al-Cu Phase Diagram	29
3.2	2219 As-Cast Microstructure	30
3.3	Comparison of 2219 Weld Microstructures for GTAW and EBW . . .	31
3.4	Microstructures from GTA-Additive Deposits	33
3.5	2319 Wire Microstructure	36
3.6	Machine Setup and Completed Walls	37
3.7	Wall and Brick Deposit Dimensions	37
3.8	Multibead vs. Single Bead Wall Deposits	38
3.9	Brick Deposition Sequence	39

3.10	Completed Wall and Brick Deposits	40
3.11	XCT Setup	42
3.12	Tensile Testing Setup	44
3.13	Typical XCT Scan for a 2219 Wall Deposit	45
3.14	Defect Resulting from Beam Arc-Out Event	45
3.15	2219 Etched AD Microstructure	46
3.16	2219 SEM AD Microstructure	47
3.17	2219 As-Deposited Precipitates Composition	48
3.18	2219 Etched Heat Treated Microstructure	49
3.19	2219 Heat Treated Precipitates Linescan	50
3.20	Brick Deposit Microstructure	51
3.21	Brick Deposit Anomaly	52
3.22	2219 Wall Deposit EBSD	53
3.23	2219 XRD Results	54
3.24	2219 As-Deposited Hardness	54
3.25	2219 Heat Treated Hardness	55
3.26	Hardness Indents	56
3.27	2219 As-Deposited Tensile Properties	57
3.28	As-Deposited Tensile Fracture Surfaces	58
3.29	2219 HT Tensile Properties	58
3.30	Heat Treated Tensile Fracture Surfaces	59
3.31	Low-Elongation LT-13 Specimen Fracture Surface	60
4.1	Cast and Wrought 7075 Microstructures	71
4.2	Circular Patch Test for Solidification and Liquation Cracking	73
4.3	SLM-printed 7075 Defects	74
4.4	Successful SLM-Printed 7075 + Zr	75
4.5	Successful SLM-Printed 7075 + Zr	77
4.6	7075 Wire Microstructure	78
4.7	7075 Wall Dimensions	79
4.8	Macrocrack Opening Procedure	81
4.9	XCT Voxel and Microcrack Size Comparison	82
4.10	Plate 19 Deposit	83
4.11	Plate 49 Deposit	88
4.12	Plate 60 Deposit Radiographs	90
4.13	Plates 68-71 Build Plans	92

4.14	Series 3 Macrocrack Initiation and Progression with Build Height . . .	93
4.15	Comparison of Single-Layer Builds on 1 in. and 0.25 in. Baseplate . . .	94
4.16	Liquated Basemetal Microstructure	97
4.17	Plate 49 Microcracks	98
4.18	FZ Border Shrinkage	98
4.19	Intercepted Plate 49 Macrocrack	99
4.20	Plate 49 Microcracks	100
4.21	Plate 46 Microcracks	100
4.22	Plate 60-C8 Etched Microstructure	101
4.23	Plate 49 EBSD	103
4.24	Plate 50 EBSD	103
4.25	Plate 60-C8 EBSD	104
4.26	XCT Scans Highlighting Macrocracks in Plates 46, 49, and 50	106
4.27	Plates 69 and 71 XCT	107
4.28	70 μm XCT Scan Microcracks	107
4.29	Comparison of Deposit Microcracking	109
4.30	Liquation Cracking at Baseplate Intersection	110
4.31	Plate 46 Crack 1 Dendritic Features	112
4.32	Plate 49 Crack 2 Dendritic Features	113
4.33	Plate 50 Crack 1 Dendritic Features	114
4.34	Plate 46 Liquation Features	115
4.35	Near-Baseplate Macrocrack Surface	116
4.36	Near-Baseplate Macrocrack Features	117
4.37	Comparison of 68-1L, 68-2L, and 69-3L Builds	120
4.38	Plate 68-2L Solidification Cracks	122
4.39	Macrocrack Formation in Layer 3	123
4.40	Plate 50 Solidification Cracks	124
4.41	Comparison of Plates 46 and 50 Macrocracks	126
4.42	69-40L and 71-40L XCT Scans	127
4.43	Plate 46 Liquated Microstructures	129
4.44	Plate 49 Liquation Cracks	131
4.45	Plate 60-C8 Liquation Cracks	131
4.46	Plates 49 and 50 Liquation Cracks	132
4.47	Liquated Region at a Macrocrack Tip	134
4.48	Liquation Cracking in the Baseplate	135
4.49	Liquation Cracks Below the Plate 60-C8 Deposit	136

4.50	Liquation Crack Formation	136
4.51	$T-f_s^{1/2}$ Plots for 7075 Wire and Deposits	137
4.52	Comparison of Plates 49 and 50 Crack Densities	139
4.53	Scheil Plots for 2219, 7075, and Recently-Patented Alloy X	144
A.1	AA2219 Wall 1 Cut Plan	151
A.2	AA2219 Wall 2 Cut Plan	152
A.3	AA2219 Wall 3 Cut Plan	152
A.4	AA2219 Brick Cut Plan	153
B.1	Subsize Tensile Specimen Drawing	154
C.1	7075 Plate 46 Cut Plan	156
C.2	7075 Plate 49 Cut Plan	157
C.3	7075 Plate 50 Cut Plan	157
C.4	7075 Plate 60-C8 Cut Plan	158
D.1	Double Conical Heat Source	160
D.2	Reference Point Locations	161
D.3	Liquated Depth Predictions and Observations	162
D.4	Time Molten of Critical Thickness Γ	163

List of Tables

3.1	ASTM B209-14 Composition Limits for 2219	29
3.2	2319 Wire Composition	35
3.3	2219 EBF ³ Parameters	40
3.4	Standard 2219-T6 Heat Treatment Practice	42
3.5	2219 Deposit Grain Size Results	52
4.1	ASTM B209-14 Composition Limits for 7075	71
4.2	7075 Mechanical Properties	72
4.3	7075-T6 Wire and 7475-T7351 Baseplate Compositions	77
4.4	EBF ³ Parameters for 7075 Series 1 and 2 Deposits	84
4.5	EBF ³ Parameters for the 7075 Series 3 Deposits	85
4.6	7075 Series 1 Deposit Comparisons	89
4.7	7075 Wire and Deposit Compositions	95
4.8	7075 Deposit Grain Sizes	102
4.9	7075 Series 1 Macrocracking Summary	105
4.10	Deposit Microcracking Comparison	108
4.11	Microhardness of 7075 Deposits	118
4.12	Few-Layer Deposits' Crack Statistics	121
4.13	69-40L and 71-40L Cracking Comparison	127
4.14	Maximum Steepness Criterion for Solidification Cracking	138
4.15	Plates 49 and 50 Macrocrack Densities	139
4.16	Crack Susceptibility Comparison of 2219, 7075, and Alloy X	144
D.1	Thermal Analysis Model Parameters	161
D.2	Solidification Rate Results	162

Chapter 1

Introduction

1.1 Motivation

The thrust of this work stems from the commercial need for the advancement of Al alloy additive manufacturing for applications in aircraft structures. There are significant economic benefits that accompany manufacturing processes that reduce the time-to-flight, number of parts, structural weight, and cost of aircraft. Furthermore, increasing the structural efficiency and automated assembly of aircraft structures will also lower costs and lead times.

Additive manufacturing (AM) is a family of processes that is projected to play a significant role in future aircraft structures. Certain wire-based, high deposition rate AM processes such as wire-arc additive manufacturing (WAAM) and electron beam freeform fabrication (EBF³) have competitive deposition rates of 1 to 10 kg/h that could feasibly be incorporated into the production line for certain aircraft structures [1]. It has been found that redesigning stiffened panels for AM can readily enable concepts such as curvilinear stiffeners, which help optimize loading conditions and may reduce structural weight [2]. Other designs such as functionally-graded stiffeners or joints [3] are also made feasible with AM and could further improve the efficiency of the aircraft structures.

NASA Langley Research Center (LaRC) is exploring high deposition rate additive processes for building up circumferential ribs on integrally stiffened cylinders for aircraft fuselages. LaRC has a Sciaky electron beam (EB) welding machine that has been modified in recent years for EBF³. Recent work has examined the AM compatibility and resulting mechanical properties of three EBF³-deposited Al alloys (AAs)

- 2219, 7075, and a recently-patented 7xxx-series alloy [4].

1.2 Materials and Property Targets

This study focuses on the Al material system because of its economic advantages. Compared with other aerospace materials such as Ti, AAs are preferred for aircraft structures due to their good strength-to-weight ratio balanced by their low cost and ease of fabrication.

NASA and leading aerospace companies are interested in an AM-compatible, drop-in replacement for 7050-T7, which is commonly used in spars, ribs, and internal fuselage structures in aircraft [5]. This 7xxx-series alloy has a nominal composition of Al-6.2Zn-2.3Cu-2.2Mg-0.12Zr and was developed to have high strength, high stress corrosion cracking resistance, and good fracture toughness [6]. Typical yield and ultimate strengths of 7050-T7451 are 68 and 76 ksi, respectively [7].

This desire for an AM-compatible, drop-in replacement for 7050-T7 proves challenging, since a number of setbacks occur with fusion-based welding and AM of 7xxx-series AAs. With their high Zn and Mg content (and occasional additions of Cu), these alloys tend to exhibit poor weldability due to alloying element volatility, porosity, solidification cracking, and liquation cracking. Due to the fusion welding heritage of EBF³, 7xxx-series alloys are expected to exhibit some or all of the above defects with AM, making them a difficult first alloy to study with the EBF³ process.

To pursue an AM compatibility for 7xxx-series alloys, this work first investigates alloy 2219 [8]. This alloy has established EBF³ compatibility from prior work performed at NASA LaRC [9, 10, 11] but inherently cannot achieve 7xxx-series properties since it is essentially a binary Al-6.3Cu alloy. However, 2219 is a favorable alloy candidate for developing deposition procedures and parameters in preparation for depositing a 7xxx-series alloy.

The second alloy investigated in this work is 7075 [12], an alloy similar to 7050 and widely referenced in welding and recent AM literature. 7075 has well-documented issues with fusion welding [13, 14, 15, 16] and recently with AM [17, 18, 19], so it was expected that similar defects would arise with EBF³ processing.

Depositing both alloys with EBF³ will highlight the range of properties and AM compatibility of very different AAs to shed light on future research directions for developing AM of 7xxx-series alloys for commercial aircraft applications.

1.3 Knowledge Gaps

With EBF³ and other AM processes only a few decades old, there are still a number of knowledge gaps surrounding the AM of AAs 2219 and 7075. The list below highlights underemphasized areas in the literature that must be addressed to advance EBF³ deposition of AAs, particularly the 7xxx series.

1. Despite a number of studies in the welding literature assessing the compatibility and defects associated with welding of 7xxx-series AAs, there is limited published work on the AM of such alloys. In particular, high deposition rate processes such as WAAM and EBF³ are not addressed, leaving a gap in knowledge regarding the compatibility of 7xxx-series AAs with such processes.
2. Welding defects of 7xxx-series alloys are well known to include solidification and liquation cracks, alloying element losses, and porosity. While the defects and properties of 7xxx-series AAs has been investigated in literature for the selective laser melting (SLM) process [19, 20], it is not known whether the same defects and the same mechanisms are operating across welding, SLM, and high deposition rate AM processing of 7xxx-series AAs.
3. Recent literature has demonstrated successful AM of 7xxx-series AAs with the SLM process through extensive grain refinement [17, 21]. Furthermore, welding literature also supports the design of new filler and base metal combinations to circumvent crack-susceptible compositions [22]. Both avenues are hopeful directions for the future of AM of 7xxx-series alloys, but neither has been explored in the literature with WAAM or EBF³.
4. While there is some published work on high deposition rate AM of 2219 [9, 10, 11, 23], further research is needed to fully characterize as-deposited and heat treated 2219 microstructures and properties. Additionally, no WAAM or EBF³ literature investigates more complex, multi-bead geometries for 2219 and the resulting transverse properties across multiple beads.

1.4 Thesis Objectives and Outline

To address the knowledge gaps surrounding high deposition rate AM of 7xxx-series alloys, this work had the primary objective of characterizing the types and extent of cracking and other defects in EBF³-deposited 7075. This enabled comparisons with

defects in the welding literature to analyze the mechanisms driving similar defects in AM.

A secondary objective of this work was to utilize knowledge of the mechanisms behind cracking of the 7075 deposits to pursue directions for crack mitigation and elimination. This involved study of hot cracking susceptibility with composition for 7xxx-series alloys and the effects of grain refinement on crack elimination.

To pursue these objectives for 7xxx-series alloys, it was first necessary to deposit an alloy with proven EBF³ compatibility for developing processing strategies and to study the resulting microstructure and properties. For this reason, 2219 was selected for deposition prior to that of 7075. A tertiary objective for this research was in-depth characterization of the 2219 microstructure in addition to transverse properties of multi-bead deposits, which has not been addressed in the literature.

To achieve these objectives, the following outline presents EBF³, AM process of interest, and the deposition results of two AAs that demonstrate a range of EBF³ compatibility and resulting mechanical properties.

Chapter 2 presents the EBF³ process within the context of other welding and AM methods, highlighting its unique capabilities over traditional welding processes and its rapid deposition abilities compared to more common additive techniques such as SLM. This chapter also introduces defects common in both welding and AM that play a significant role in the weldability of AAs.

Chapter 3 deals with 2219, a nearly binary Al-Cu alloy that exhibits excellent AM compatibility. Wall- and brick-shaped deposits of 2219 were fabricated with EBF³, tensile and metallurgical specimens were prepared and tested, and results were compared to those from other 2219 AM studies and the 7050-T7 property targets.

Chapter 4 presents 7075, which trails 2219 in welding and AM compatibility and surpasses it in strength. While 7075 wrought product possesses comparable properties to 7050, its high alloy content of Zn, Mg, and Cu affects the solidification kinetics and contributes to ubiquitous solidification cracking during welding and SLM. The chapter focuses on characterizing the cracking mechanisms and extent for various 7075 deposits fabricated with EBF³ in an effort to identify future avenues of research for improving 7075 AM compatibility.

The final chapter presents conclusions garnered from this work with regard to both alloys' properties and AM compatibility, as well as comparisons to the 7050 property targets. The chapter also outlines future research directions for increasing the strength of EBF³-deposited 2219 and achieving AM compatibility for 7075 with EBF³ processing.

Chapter 2

Review of Electron Beam Freeform Fabrication

This chapter presents EBF³ by first studying its welding heritage and comparing it to other fusion-based welding and additive processes. Additional detail is then given about the EBF³ process at NASA LaRC, focusing on machine parameters and compatible materials systems. Defects common in both welding and AM are also highlighted. Of these, particular attention is paid to hot cracking during welding, which is a frequent problem for high-strength aluminum alloys and was ubiquitous in the 7075 work in this study.

2.1 Fusion Welding Fundamentals

Fusion welding involves the melting of metal - either base metal or a combination of base metal and filler wire. The significant heating involved in melting metal produces a microstructural gradient in the weld joint, which is sketched in Fig. 2.1. The horizontal lines represent base metal grains, while the columnar grains in the center reflect the solidified weld. This microstructural gradient may be classified into zones with differing microstructures and mechanical properties.

The primary regions of a weld are the fusion zone (FZ), the heat-affected zone (HAZ), and the partially-melted zone (PMZ). The FZ is the region of the weld that has undergone complete melting. It possesses an as-solidified microstructure that can be columnar or equiaxed, depending on the solidification rate and other factors. The FZ may have a different composition from the base metal if a filler metal was

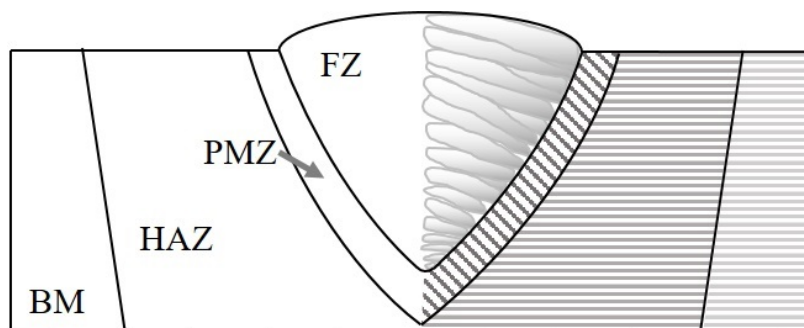


Figure 2.1: Schematic of the regions of a weld joint, including the fusion zone (FZ), the partially-melted zone (PMZ), the heat-affected zone (HAZ), and the unaffected base metal (BM).

used, or if significant vaporization of alloying elements occurred. Often, filler metals are utilized to strengthen the weld joint or to circumvent compositions susceptible to cracking during solidification of the FZ [24].

Figure 2.2 shows columnar and equiaxed grain structures that can develop in the FZ of a weld. These depend on a number of factors, including the amount of undercooling and the amount and type of heterogeneous nucleation sites [13]. The more typical weld microstructure is the columnar one shown in Fig. 2.2(a), where grains nucleate on the edges of the weld pool and grow along the thermal gradient. This grain structure is not ideal for mechanical properties of the weld, since the elongated grains usually corresponds with lower ductility and cracking in sensitive alloys [13]. Since an equiaxed microstructure improves weld ductility and is also much less susceptible to solidification cracking, a columnar-to-equiaxed transition in welding is often sought. Such grain refinement, shown in Fig. 2.2(b) is usually accomplished through use of filler wire inoculants or molten pool agitation with ultrasonic waves, arc or beam oscillations, or power pulsation [1, 13, 25, 26].

The PMZ of a weld is the region of the base metal that directly borders the FZ and undergoes partial melting due to the high temperatures of the neighboring FZ [13]. The PMZ consists of base metal grains - usually elongated in the rolling direction of the workpiece - that have undergone some melting around the edges. The PMZ can thus be susceptible to cracking or, at minimum, solute segregation defects based upon the strain field surrounding it or the amount of time it spends partially molten [28, 29, 30].

The HAZ is a larger region containing the PMZ that extends from the FZ to some distance away from the weld and in which properties and microstructure are affected by the heat of welding. Factors that influence the microstructure in the HAZ

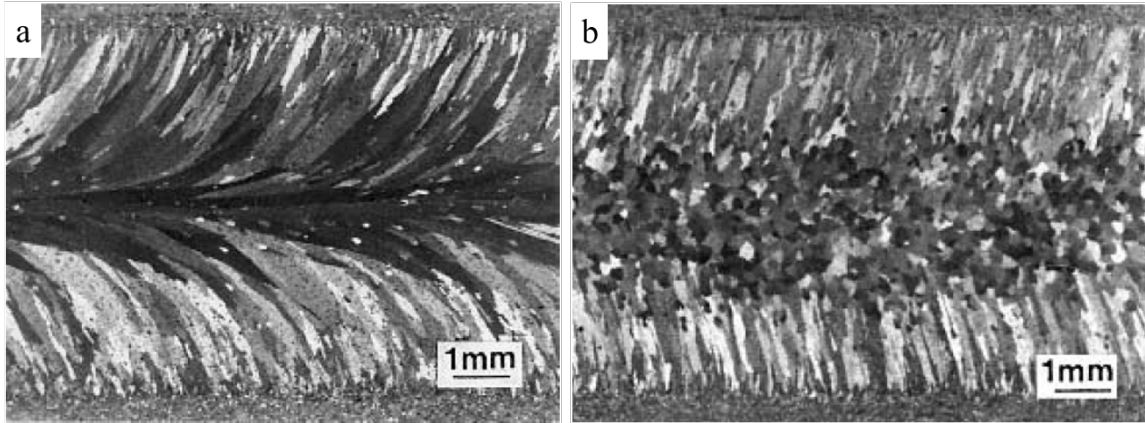


Figure 2.2: Top view of weld beads exhibiting (a) columnar grain growth in the direction of solidification and (b) equiaxed grains in the FZ [27].

include the peak temperature experienced and the subsequent cooling rate. Often, the HAZ experiences a loss of strength from that of the base metal due to coarsening of strengthening precipitates [13]. Welding processes that have higher energy densities - such as electron beam welding - usually result in narrower heat-affected zones and may have less of an impact on mechanical properties [1]. Figure 2.3 shows the relationship of HAZ width with heat source intensity [1].

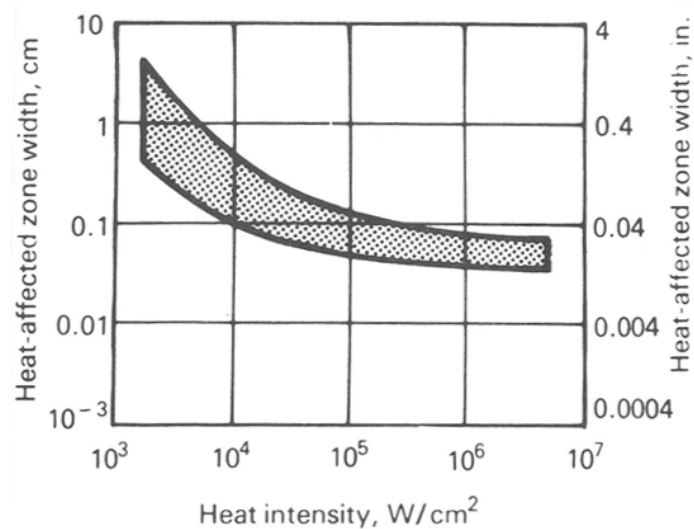


Figure 2.3: Relationship of the HAZ width with power density of the welding heat source [1].

2.2 Review of Common Welding Processes

There are a plethora of welding processes that use a variety of energy sources and mechanisms for joining material. Figure 2.4 displays this broad spectrum of processes, with the major delineations involving fusion and nonfusion welds, as well as homogeneous and heterogeneous processes. The family of processes that includes electron beam welding (the precursor to EBF³) is found within the fusion-based, homogeneous segment of the chart. Many of these processes have the flexibility to be welded autogenously or with a filler wire, depending on the geometry of the weld joint and the desired mechanical properties. Processes that involve filler wire are precursors to some AM processes, since they involve the deposition and solidification of additional material.

However, AM processes are complicated by the layer-by-layer construction of deposits. This results in a complex thermal history for a particular layer, initially with partial remelting from subsequent layers, followed by solid-state reheating and aging as further layers are added. Other factors to consider in understanding AM processing are slower cooling rates with increasing build height and the paradigm shift that in AM, layer N is the new “base metal” for layer N+1.

Of the fusion-based welding processes, four that supply significant heritage to current AM processes of interest are gas-tungsten arc welding (GTAW), gas-metal arc welding (GMAW), laser beam welding (LBW), and electron beam welding (EBW). These processes all share the traits that they can accommodate filler material (the basis for AM), they use a relatively high-power and controllable heat source, and they are capable of medium-to-high deposition rates. A brief introduction is given for each of these welding processes, and their transformation to additive processes is demonstrated subsequently.

2.2.1 Gas-Tungsten Arc Welding

GTAW, also known as tungsten inert gas (TIG) welding, involves establishing an arc between a nonconsumable tungsten electrode and the workpiece to melt metal for the weld joint [13]. The arc is typically shielded by an inert gas - such as Ar or He - which serves as a medium for the arc current and protects the electrode and weld pool from contamination from the environment [1]. GTAW is applicable to most metals, though special care is needed for reactive metals such as Ti, Zr, Mg, and Al (due to its oxide). GTAW may be performed manually or robotically, with optional use of filler wire. Figure 2.5 shows a schematic of this process.

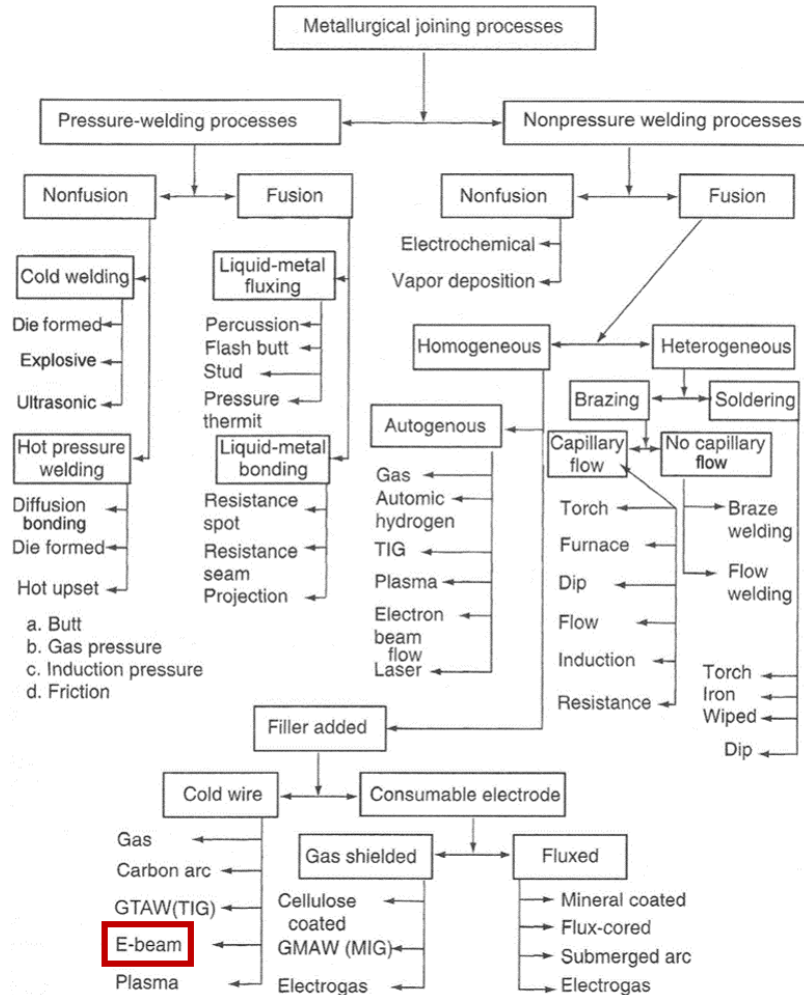


Figure 2.4: Breakdown of metallurgical joining process, with delineations of pressure state, fusion/nonfusion status, and addition of filler materials [1]. Modified to highlight EBW, the parent process for EBF³.

Some advantages of GTAW are high weld quality due to the inert gas flow, weldability of thin materials such as sheet or plate, low spatter, and different arc polarity configurations that allow control of welding heat experienced by the workpiece [1, 13].

Disadvantages of GTAW include possible brittle inclusions of tungsten if the electrode inadvertently melts, lower deposition rates than consumable electrode processes such as GMAW, and problems in certain humid or drafty environments due to shielding gas interference [1].

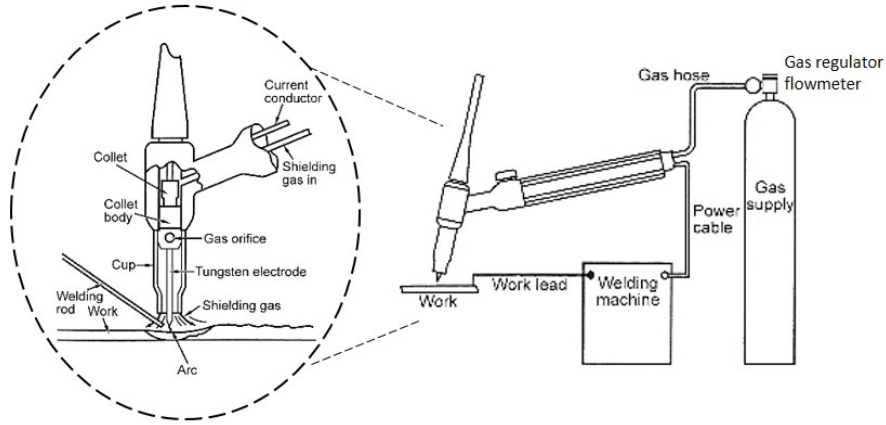


Figure 2.5: Diagram of the GTAW assembly, complete with shielding gas, arc power source, and optional off-axis filler wire feeder. Modified from [1].

2.2.2 Gas-Metal Arc Welding

GMAW, also known as metal inert gas (MIG) welding, is a fusion welding process that establishes an arc between a continuously-fed wire electrode and the base metal [1]. Typical energy densities for the GMAW and GTAW processes are on the order of 5×10^6 to 5×10^8 W/m² [1]. The process takes place at atmospheric pressure with a continuous flow of inert gas around the arc to mitigate reactions between the environment and the molten metal and to reduce weld contamination. Figure 2.6 shows a schematic of this process [1].

GMAW is often used to weld thin and thick plates alike, with faster welding speeds and less spatter than in GTAW. The weld quality is similar to that of GTAW due to the beneficial shielding gas, and the GMAW process may also be completed semi-automatically or robotically [1, 13].

Some detriments of GMAW include the bulkiness of the equipment due to the extra wire-feeding tools, as well as potential welding hazards for the operator [1, 13].

2.2.3 Laser Beam Welding

LBW is a high-energy density fusion welding process that uses a laser to heat and melt base metal, with energy densities of 10^9 to 10^{11} W/m² [1]. LBW may be executed in the atmospheric environment with a shielding gas, or in an inert environment to protect the molten pool [13]. Various continuous-wave lasers may be used for high-power welds, including CO₂ lasers and neodymium-doped yttrium-aluminum-garnet (Nd:YAG) lasers [13]. Besides their applications in welding, lasers may also be used

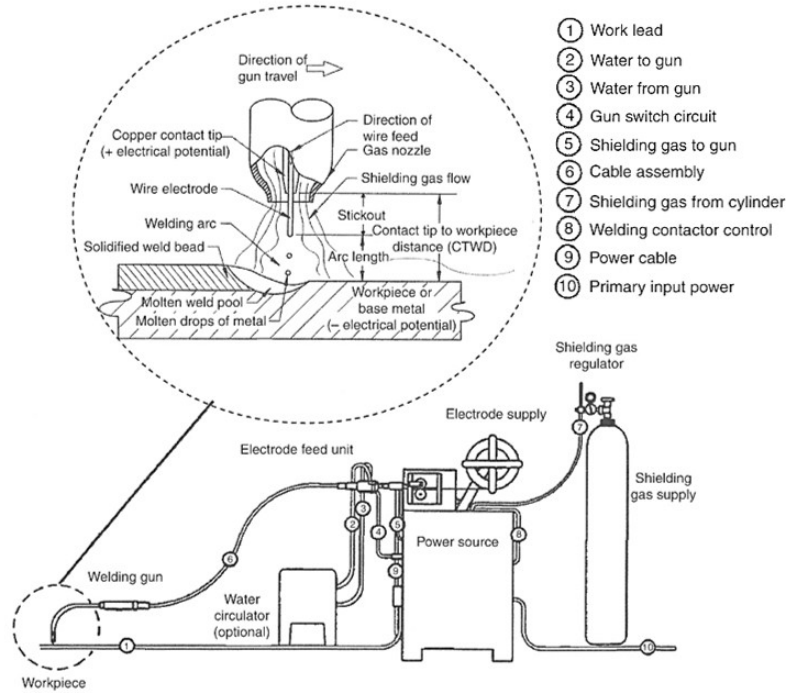


Figure 2.6: Diagram of the GMAW process, which includes the consumable filler wire electrode, the arc source, and the shielding gas [1].

for various hardening and cutting processes [1]. A schematic of the LBW process is shown in Fig. 2.7 [31].

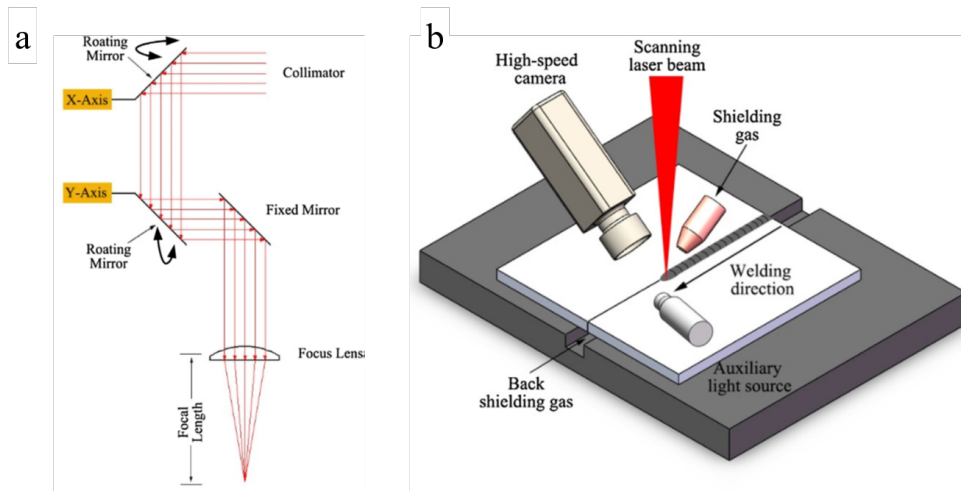


Figure 2.7: Diagram of the LBW process, which includes the laser source, resulting plasma, keyholing mode, and shielding gas to remove the plasma and spatter [31].

Some advantages of LBW include rapid stopping and starting due to its use of light for the beam, focused spots as small as 0.1 to 1.0 mm for high-energy density welds,

no consumable electrode or filler materials required, a very narrow HAZ, flexible standoff distances (since photons are barely scattered by atmosphere), and potential for time-sharing of the laser beam [13, 1].

A number of limitations of LBW also are present, including the high cost of the machinery, requirements for precise part positioning due to the small spot size, high reflectivity of the laser from the metal surface, and a lower penetration depths than that in EBW [13].

2.2.4 Electron Beam Welding

EBW is another high-energy density welding process that involves generating electrons from a filament and accelerating them to form a beam. This electron beam (EB) impinges on the workpiece, where the instantaneous conversion of the electrons' kinetic energy to thermal energy causes melting of the material [1]. Figure 2.8 shows a schematic of the electron beam gun - its filament, cathode, anode, focusing coil(s), and deflection coil(s) - as well as a keyholed EBW [1].

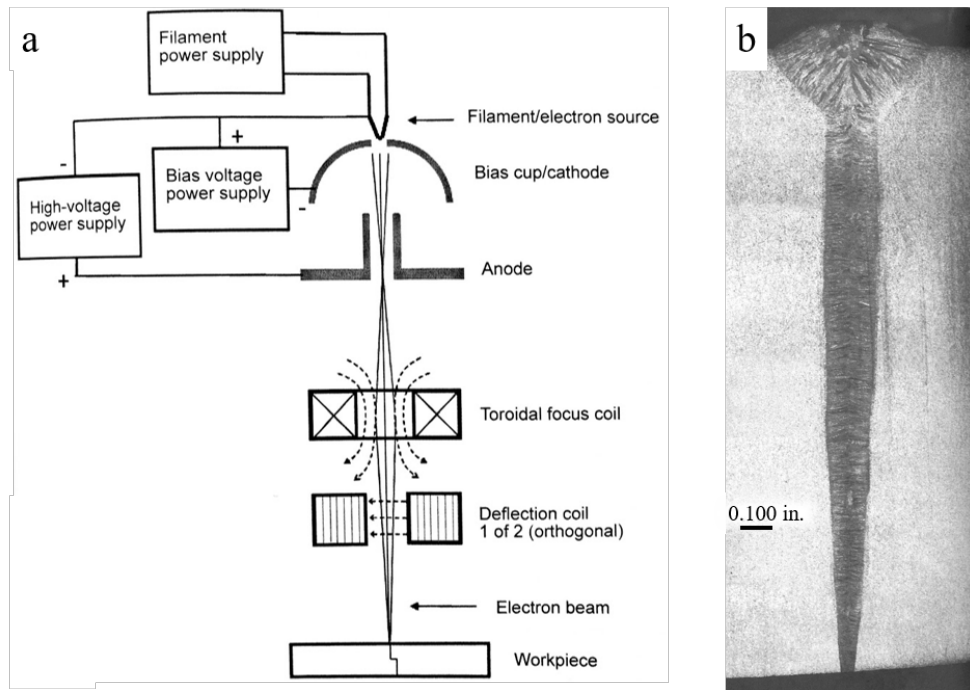


Figure 2.8: (a) Schematic of the EB gun column assembly and the impingement of the focused beam on the workpiece surface, and (b) a resulting keyhole weld in Inconel 718 [1].

EBW provides the primary benefit that welding takes place in a high-vacuum

environment, often around 10^{-6} Torr, to eliminate weld metal contamination from or reaction with the atmosphere. Another key benefit of EBW is the ability to create keyhole welds which have a narrow FZ and HAZ and very deep penetration. The geometry of a keyhole weld is shown in Fig. 2.8(b). Furthermore, the high energy density of up to 10^{12} W/m² allows for efficient welding, since typically only a single pass is required to join thick sections [1]. EBW is also safer for the welding operator, since welding occurs inside of a vacuum-sealed chamber, so the threats of electrical shock, fume inhalation, and injury from spatter as in arc welding are eliminated. However, x-rays are produced during EBW, so the vacuum chamber must include the necessary shielding to protect the operator and surrounding environment.

The largest setback to EBW is the equipment cost due to the high-vacuum capabilities and chamber size. The impact of chamber size can be significant, since chamber evacuation time can limit the production time. Some EBW may take place at lower chamber pressures to increase production rates but is accompanied by scattering of the electron beam and lost depth of penetration in the base metal, as shown in Fig. 2.9. Like LBW, EBW also requires precise fit-up of workpieces, since typical spot sizes are on the order of 0.3 to 0.8 mm [13].

2.3 Review of Common Additive Manufacturing Methods

AM derives its origin from welding, with the first modifications of welding processes to additive ones occurring in the early 1990's [32]. One of the greatest divisions in AM lies in the trade-off of deposition rate with feature size. Typically, this is accompanied by the type of feedstock used, with a transition from fine powder to wire with increasing deposition rate. Figure 2.10 depicts such distinctions between common additive processes.

Much like in the welding chart in Fig. 2.4, additive processes are also divided along fusion and nonfusion lines. Solid-state processes do not require melting and include processes such as additive friction stir (AFS) manufacturing and ultrasonic additive manufacturing (UAM). Fusion-based processes, such as WAAM, laser beam melting (LBM), and electron beam melting (EBM), require the melting of material for fusing deposit layers. The sections below highlight prominent AM processes that parallel the welding process presented in Section 2.2 and are of note for comparison with EBF³. Additional details are given regarding the EBF³ capabilities at LaRC.

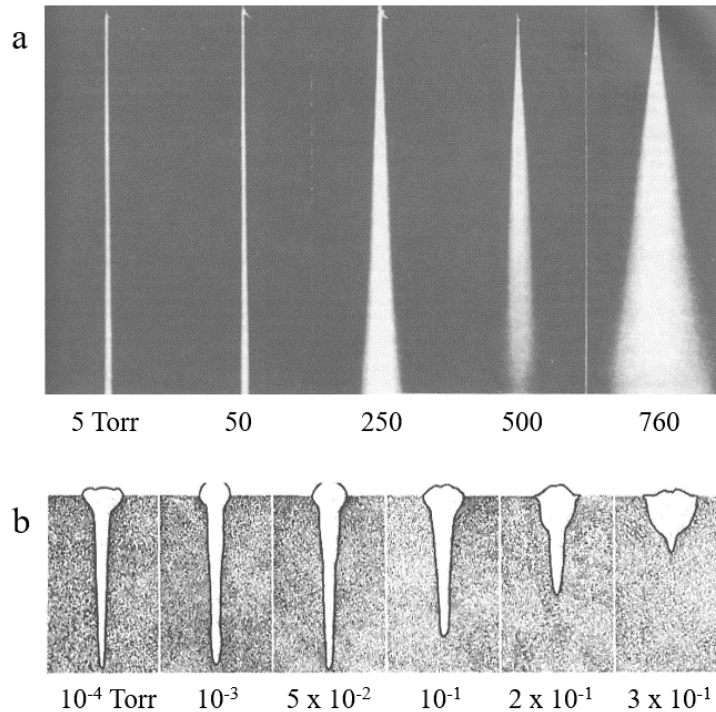


Figure 2.9: (a) Image sequence showing the effect of chamber pressure on the EB shape, and (b) diagrams depicting the effect of chamber pressure on weld penetration depth and bead cross-section [1].

2.3.1 Wire-Arc Additive Manufacturing

WAAM has emerged as a common AM process due to its low cost, flexible environmental requirements, and broad alloy compatibility [34, 35]. Originating from the GMAW and GTAW processes, the WAAM process establishes an arc between the wire feedstock and the substrate to additively deposit metal in layers to build up three-dimensional parts. The GMAW configuration is ideal for WAAM since the wire feedstock is introduced coaxially with the arc, allowing for easier programming than if the wire were fed from a separate, off-axis nozzle as for GTAW. The off-axis feeding in additive GTAW would cause different presentations of the wire in the melt pool with changing toolpaths, which can result in higher defect levels. Thus, extra code is required to maintain the same wire presentation with changing build path direction if the GTAW configuration is used [35]. Figure 2.11 shows a robotic WAAM machine and a demonstration article built up by WAAM [35].

The greatest benefit of WAAM technology is its low equipment cost since the process - like its welding predecessors - is executed at ambient conditions for most

AM PROCESS CATEGORY ¹	AM PROCESS TYPE	MATERIAL			BINDER OR FUSION MECHANISM						FEEDSTOCK FORM			
		METALS	POLYMERS	CERAMICS	LASER BEAM	ELECTRON BEAM	PLASMA ARC	ULTRAVIOLET	LIQUID BINDING AGENT	ULTRASONIC	OTHER HEAT / POST-PROCESSING	POWDER	FILAMENT	RESIN
Binder Jetting	---	●	●	●					●	●	●		●	
Directed Energy Deposition	Blown Powder	●	●	●	●						●	●		
	Ion Fusion Formation	●					●				●		●	
	Electron Beam Direct Manufacturing	●				●					●		●	
Material Extrusion	Fused Deposition Modeling		●								●		●	
	Multiphase Jet Solidification	●	●	●							●	●	●	
Material Jetting	---		●					●						●
Powder Bed Fusion	Laser Sintering		●	●	●						●	●		●
	Laser Melting	●			●						●	●		
	Electron Beam Melting	●				●					●	●		
Sheet Lamination	Laminated Object Manufacturing	●	●	●							●	●		●
	Ultrasonic Consolidation	●								●	●			●
Vat Photo-polymerization	---		●	●					●	●	●		●	

Figure 2.10: Breakdown of common AM processes, separated by type of feedstock, power source, deposition rate, and build environment [33].

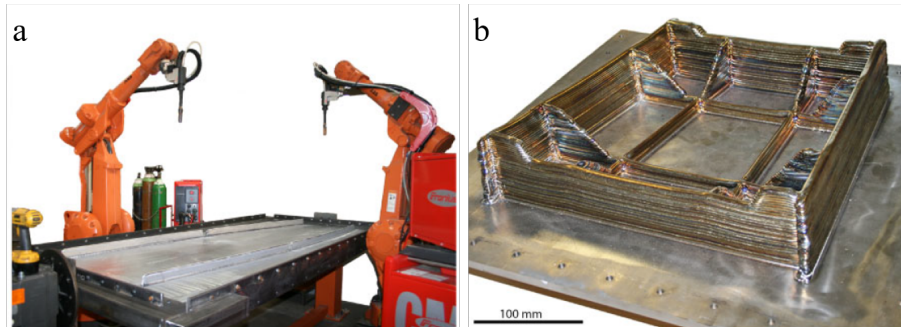


Figure 2.11: (a) WAAM robot, and (b) resulting WAAM deposit [35].

materials [35]. However, more reactive metals such as titanium require an inert atmosphere, which constrains the build environment in an enclosure and limits the mobility of the WAAM robot for printing large parts. Another key benefit to the WAAM process is the ability to add in mid-process machining and deformation passes to improve the microstructure and to relieve residual stresses [35, 23, 36].

Sizable deposition rates of 1 kg/h are cited for AAs, with the potential to deposit at higher rates but at the expense of increased surface roughness [35]. Furthermore, the capital cost of a basic WAAM machine for AM of Al or stainless steel is on the

order of \$100,000 - much less than laser-based systems or electron beam systems, which have stricter atmospheric requirements and require higher power sources.

The greatest limitations for the WAAM process are the build-up of residual stresses and resulting deformation due to the high heat input. Strategies exist for reducing residual stresses, such as building symmetrically on opposite sides of a build plate or adding interpass rolling into the build procedure [35]. Porosity can also be an issue for Al WAAM deposits due to low quality weld wire or poorly defined deposition parameters.

2.3.2 Laser Beam Melting

LBM is typically used with either powder-bed (SLM) or blown powder systems rather than wire-fed systems. Much like in welding, the LBM process offers a higher energy density than arc processes and is typically performed in an inert environment. Powder-bed systems usually involve layers of 20 to 100 μm [37], thus limiting the deposition rate of material to 0.1 to 0.2 kg/h [38]. However, the low deposition rate due to fine powder size is compensated by the high dimensional accuracy and the capability of depositing fine, geometrically-complex parts. Figure 2.12 shows a schematic of the LBM process [39].

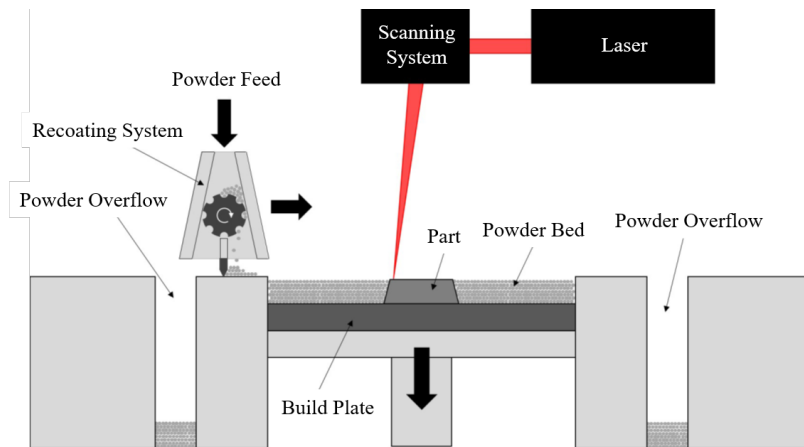


Figure 2.12: Diagram of the SLM powder-bed process, where a laser melts certain regions of the powder bed to make a deposit layer. After the layer is complete, the stage moves down and a recoater blade applies a new layer of powder from an adjacent hopper [39].

Blown powder processes offer deposition rates up to 2 kg/h [38]. This allows printing of larger-scale components while still utilizing powder feedstock, which can

offer more flexibility in tailoring composition, producing functional gradients based on composition, and fabricating finer features than wire-based systems.

A drawback of LBM processes is that the inert environment requires a special chamber for operation, so the size of the parts are limited to the usable volume of the chamber. Additionally, powder-bed systems are constrained by the size of the bed and the amount of powder required to fill it, which may or may not be recyclable.

2.3.3 Electron Beam Freeform Fabrication

Also known as electron beam additive manufacturing (EBAM), EBF³ is a prominent high-deposition rate metal additive process that has widening use in industry [40, 41, 42]. A modification of the EBW process, EBF³ utilizes an EB to melt and deposit wire feedstock on a substrate in a high-vacuum (i.e. 10^{-5} Torr) environment. The EBF³ machine at NASA LaRC is a modified Sciaky AccuBeam VX.4 Welder with dual-wire feed capabilities, a heated or cooled platen, and a tilt/rotate positioner, with the developing capability of closed-loop control. The machine's build volume measures roughly 72 in. long x 24 in. wide x 24 in. high, with six controllable axes consisting of X , Y , and Z axis movements, gun tilt B , build table rotation R , and table tilt T . Figure 2.13 provides a picture of the EBF³ machine with the relevant coordinate system.

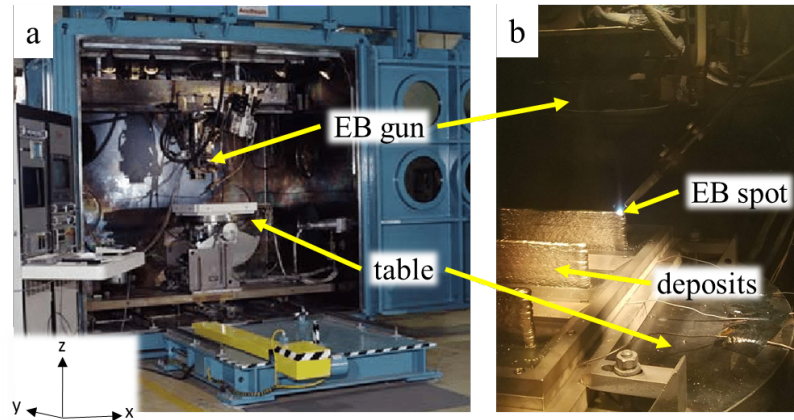


Figure 2.13: Schematic of the EBF³ machine at NASA Langley Research Center, complete with the gun column, positioning table, and the X , Y , and Z axes labeled. Modified from [43].

The key benefits of EBF³ are high quality, high energy efficiency builds; cheaper feedstock compared to powder-fed systems; high deposition rates on the order of 3 to 11 kg/h [38]; and the potential for a greater standoff distance - on the order of

10 in. - than in arc welding. This process is also believed to be ideal for use in the near-vacuum of space as both a cutting and joining process, as well as for additive deposits or repairs by the crew [44].

The primary drawbacks of EBF³ mirror those for EBW and include non-negligible chamber evacuation time and high capital cost.

EBF³ Controllable Parameters

The controllable machine parameters in EBF³ are EB accelerating voltage (AV), beam current (BC), beam focus (BF), wire feed rate (WF), travel speed (TS), raster X and Y scaling factors (X/YSF), raster frequency (RF), beam pulsation frequency (PF), and others [45].

Besides these machine parameters, other parameters that contribute to the geometry and solidification kinetics of the build are wire feedstock diameter and composition, working temperature (controlled either directly by a heated/cooled platen or indirectly by pauses between layers), baseplate thickness, thermal conductivity and rigidity of the clamping fixtures, layer step height (Δz), and others.

EBF³ Materials

EBF³ is compatible with many aerospace and commercial alloys. The most commonly used feedstock materials at LaRC are weldable AAs, stainless steels, and Ti alloys, although other material systems such as Inconel have been successfully deposited. Some work has been completed with metal matrix composites in the form of powder-cored wire feedstock, where metal powder containing ceramic reinforcement particles or reactive elements is encased in a metal sheath and deposited similarly to solid-cored wires [46].

Wire feedstock ranging in diameter from 0.030 in. to 0.125 in. can be accommodated in the Sciaky welder without additional modifications to the machine. Outside of this range, the wire is too compliant or too stiff to be handled with the existing wire feed mechanism and rollers.

For proper adhesion of the deposit to the baseplate and the necessary electrical contact for EB processing, metallic baseplate is required. Often, the baseplate is selected to complement or duplicate the feedstock material. Differing baseplate and wire feedstock chemistries could lead to a compositional gradient at the deposit-baseplate interface and result in the formation of brittle intermetallic phases. Additionally, materials with very different coefficients of thermal expansion could result in large

residual stresses or cracking.

2.4 Defects in Welding and Additive Manufacturing

Many challenges appear for the welding, and likewise AM, of AAs, particularly the 7xxx series. Of these, the most prominent are changes in alloy composition due to the volatile nature of certain alloying elements in the molten pool, cracks stemming from solidification phenomena in the FZ and liquation in the PMZ, and other FZ defects such as porosity, incomplete fusion, and inclusions. The following sections describe defects relevant to this work, particularly in reference to EBF³ of 7075.

2.4.1 Alloying Element Volatility

Of all the families of AAs, the 7xxx series proves to be one of the most susceptible to composition changes in fusion-based welding processes given the volatility of Zn and Mg at the melting temperature of Al. Figure 2.14 shows the vapor pressure and temperature relationships for various elements in 7xxx-series alloys [47], which illustrates the high vapor pressures of Zn and Mg relative to Al and Cu. At the melting temperature of 7075 - approximately 640°C (913 K) [48] - the vapor pressures of Zn and Mg are over 10⁹ times that of Al, suggesting preferential losses of those elements [47].

Depending on the welding or additive process of interest, the volatility of susceptible constituents in the molten pool can be accentuated. He et al. [49] describe two contributions to the total vaporization flux - (1) the concentration gradient of element i at the weld pool surface and in the surrounding atmosphere, and (2) the pressure gradient between the vapor pressure of element i over the molten pool and the ambient pressure. The sum of these yields the total vaporization flux J_i of element i , which is given by

$$J_i = \frac{\lambda P_i}{\sqrt{2\pi M_i R T}}, \quad (2.4.1)$$

where P_i is the vapor pressure of i over the alloy, M_i is the molecular weight of species i , R is the gas constant, T is the temperature, and λ is a positive constant that accounts for condensation of a portion of the vaporized atoms at atmospheric

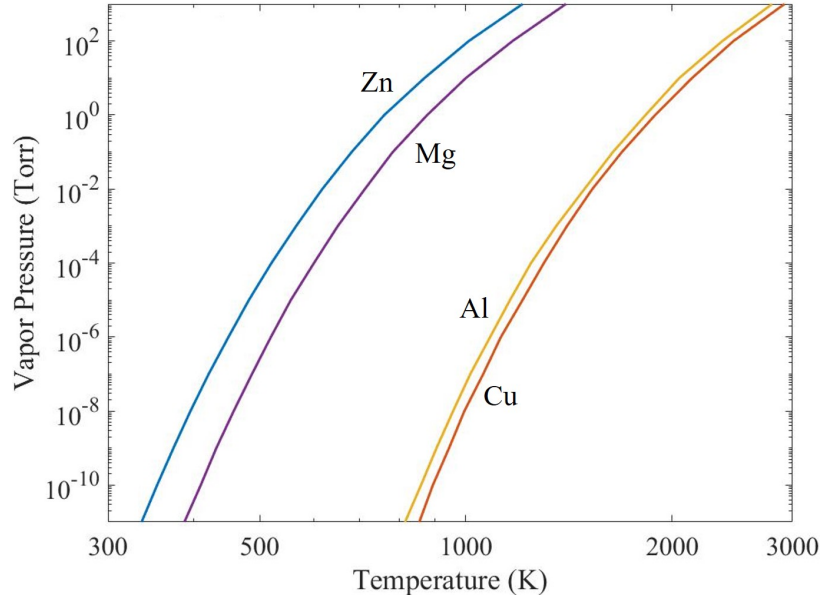


Figure 2.14: Vapor pressure vs. temperature curves for Al and the common 7xxx-series alloying additions. Data replotted from [47].

pressure. As the pressure nears that of a perfect vacuum, λ goes to 1 [49].

EBF³ is thus one of the most susceptible AM processes for elemental vaporization due to the high-vacuum environment of the process chamber, which drives λ close to its maximum value of 1 and increases J_i . With operating pressures as low as 10^{-6} Torr [1], the difference in vapor pressures of Zn and Mg with respect to the chamber pressure is significant, promoting their volatilization from the molten pool. Using Eq. 2.4.1 and the data contained in Fig. 2.14, the vaporization fluxes for Zn and Mg near the melting temperature of Al (640°C) are $0.31 \text{ g/cm}^2\text{s}$ and $0.017 \text{ g/cm}^2\text{s}$, respectively. This is automatically 10x more than if laser welding at atmospheric pressure, where λ is 0.1.

Integrating the vaporization fluxes over time yields the important result that total elemental losses can be accentuated by the time at temperature of a particular area of the bead, as well as the number of beam passes that remelt the same material. Longer time molten allows for additional vaporization of alloying elements, with fluxes given by Eq. 2.4.1. It is expected that weld or deposition schedules which have a slower travel speed and deeper molten pools will exhibit greater elemental losses.

2.4.2 Porosity

Porosity is another common issue in the various welding and AM processes for AAs [50, 32, 36]. Porosity is defined as a discontinuity caused by the entrapment of gas during weld metal solidification [1], and it can originate from the welding atmosphere, oxides or other impurities that are formed on the molten pool surface, dissolved hydrogen in the welding wire, or vaporized alloying constituents. Devletian and Wood [50] discuss the different forms that weld porosity may take - fine, secondary porosity; interdendritic porosity; and large, spherical pores from micropore coalescence in the melt. They note that convection in the weld pool can aid in the nucleation, growth, and escape of porosity in the molten pool, while factors such as rapid solidification rates paired with deep molten pools can entrap porosity in the weld metal.

In AM, porosity can also occur due to lack of fusion defects from improper processing parameters, as well as entrapment of build atmosphere, dissolved gasses in the feedstock, or volatilized alloy constituents.

2.4.3 Solidification Cracking

Solidification cracking, also known as hot tearing or hot shortness in casting [51] and hot cracking in welding [52, 53, 13, 28, 54, 16, 55, 56], is a common problem in certain AAs. While theories differ on the precise mechanisms behind solidification cracking, it is generally accepted that solidification cracking is initiated in the terminal stages of solidification as thermal and solidification strains act upon the solidifying metal [28]. Depending on the grain morphology and the amount, composition, and fluidity of the remaining solute-rich liquid, the remaining liquid may not be able to feed between dendrites and “heal” any voids forming due to excess strain. As a result, micropores can nucleate and form interdendritic cavities, which can then propagate through the molten pool to form extended cracks [57]. As a result, solidification cracking is observed to be interdendritic. Thus, the crack surface should appear dendritic in character, due to crack nucleation occurring during the final stages of solidification where secondary dendrite arms would otherwise be bridging with neighboring grains [13]. Figure 2.15 shows micrographs of a polished sample with interdendritic solidification cracking and a solidification crack surface exhibiting dendritic character [28, 16].

Historically, many researchers have explored solidification cracking susceptibility of various alloys through experimental means, with high-strain tests such as ring-casting [58, 51] and welding-based approaches such as the Varestraint test [59, 53],

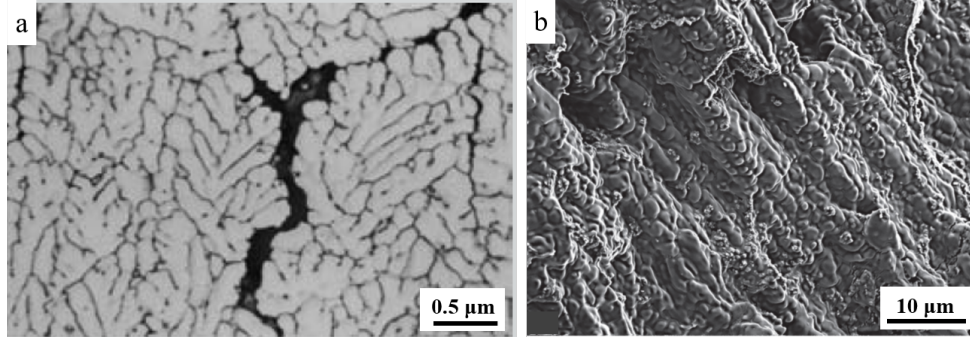


Figure 2.15: (a) Polished cross section through a solidification crack [28], and (b) solidification crack surface from a novel lap welding solidification cracking test [16].

inverted T-joints [55], the Houldcroft test [25], the circular patch test [28], and the Variable Deformation Rate (VDR) test [60]. It is often found that for binary Al alloys, the crack susceptibility curve is Λ -shaped, with susceptibility increasing with alloy content up to a particular composition - often related to the maximum solid solubility of the element in Al - followed by a decrease as more eutectic is formed [58]. It is accepted that at low alloy compositions, there exists little to no eutectic liquid at grain boundaries to cause cracking, while in highly-alloyed materials, there is enough eutectic to “heal” any cracks that may initiate [13].

Researchers have postulated on the physical mechanisms behind solidification cracking, developing theories to explain the dependency of cracking on stresses, strains, and strain rates in solidifying metal [61, 57]. One of the most prominent models is the Rappaz-Drezet-Gremaud (RDG) model, which considers both tensile deformation and solidification shrinkage to compute the pressure drop across the semi-solid mushy zone [61]. When the pressure falls below a certain level, the interdendritic liquid is fractured and a void forms.

A recent advancement in solidification cracking theory came from Kou [62], who devised a criterion for predicting hot cracking susceptibility (HCS) based on the temperature-solid fraction, or T- f_s , diagrams. While some theories cite the overall freezing temperature range as the cause of cracking [51], Kou’s criterion consists of finding the maximum $|dT/d(f_s)^{1/2}|$ in the terminal stages of solidification ($f_s = 0.98$) as a predictor of cracking susceptibility. The greater the $|dT/d(f_s)^{1/2}|$, the more likely that the material encounters difficulty in feeding enough liquid to heal nucleating cracks, as is shown in Fig. 2.16.

By calculating the T- f_s curves for various alloy compositions and then computing the maximum steepness near $f_s = 0.98$, HCS plots can be made as a function of alloy

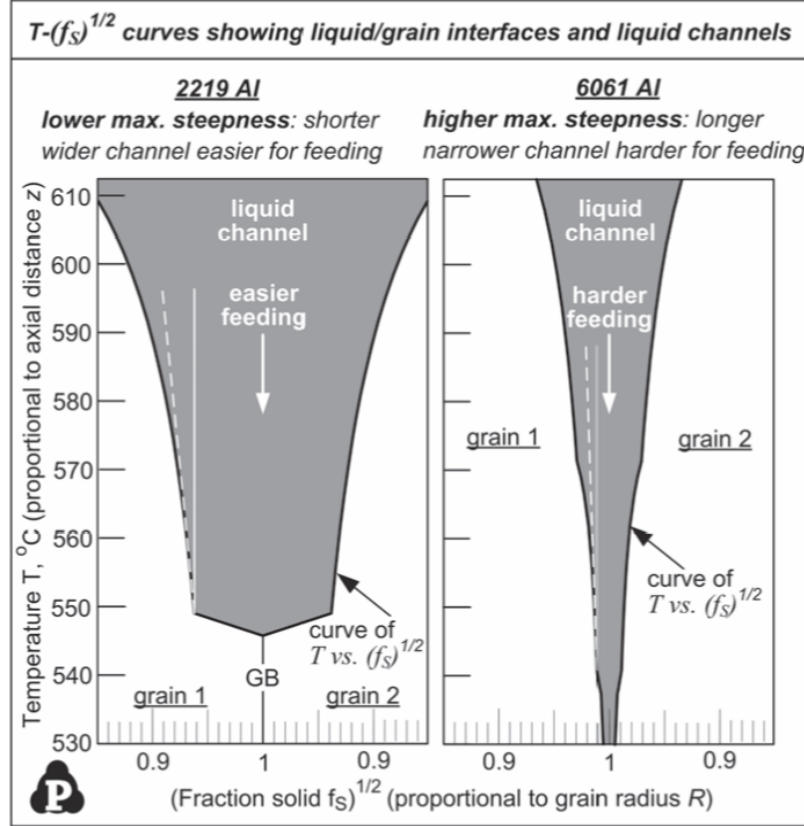


Figure 2.16: Schematic showing the differences in T - f_s curves for alloys with low versus high maximum steepnesses and the ease of liquid feeding to dendrite roots [62].

composition. The curve for binary alloys takes on a Λ shape as is most commonly found in experiments for Al-Cu, Al-Mg, and Al-Si alloys [55, 51, 58]. However, certain welds of Al-Mg do not match the HCS predictions. To explain this, Liu and Kou [63] theorized that back-diffusion, as is common in Al-Mg alloys under certain cooling rates, can alter the crack susceptibility. This means that rejected solute can be reabsorbed into the solidifying matrix, decreasing the overall susceptibility and shifting the peak to a slightly higher alloy composition.

This maximum $|dT/d(f_s)^{1/2}|$ criterion is also extensible to multicomponent alloys provided that the T - f_s diagram may be calculated with realistic solidification models that take into account temperature-dependent segregation ratio, k , and liquidus-line slope, m_L [62]. This criterion can thus generate HCS composition maps for more practical and high-strength alloys [22].

Recommendations for reducing or eliminating solidification cracking include adjusting the weld metal composition, the grain structure, and the welding parameters

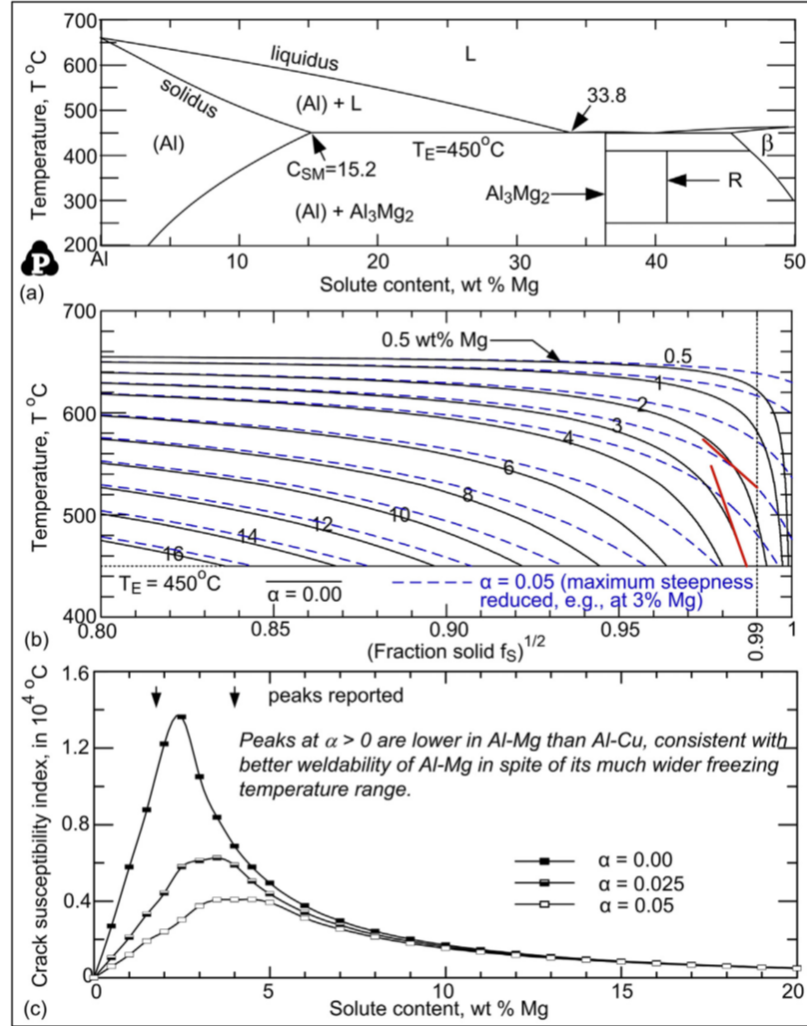


Figure 2.17: Plots showing (a) the Al-Mg phase diagram, (b) the T - f_s plots for various alloy compositions, both with and without a back-diffusion coefficient of $\alpha = 0.5$, and (c) crack susceptibility Λ curves showing the effect of back-diffusion on lessening overall susceptibility and shifting the peak to higher Mg compositions [63].

[28]. If the composition of the base metal or filler wires is particularly susceptible to solidification cracking - as is the case for alloy 6061 - then shifting the composition away from peak susceptibility through dilution with a different filler metal or by changing alloys is recommended [24]. Another successful remedy for eliminating solidification cracking in both welding and additive processes is to refine the grain structure. Small, equiaxed grains are better able to accommodate the strains present in the contracting mushy zone, and they also provide shorter distances from dendrite roots to tips for liquid feeding and healing of cracks [54]. Finally, welding parameters such as arc pulsing or beam rastering can alter the solidification microstructure to

subvert typical solidification crack paths [26, 64].

It is expected that similar solidification cracking issues will be present in EBF³ deposits of 7075, given the alloy's high HCS in welding. This work will investigate whether the same mechanisms as in welding cause cracking in EBF³ deposits, and variations in the manifestation of such cracks.

2.4.4 Liquection Cracking

Liquation cracking is another common problem for AAs during welding [28, 29, 65, 30, 66, 36]. Like solidification cracking, liquation cracking occurs intergranularly. However, while solidification cracks initiate between dendrites in the FZ during solidification, liquation cracking occurs in strained liquated regions in the PMZ [13]. The high temperatures experienced in the PMZ between that of the liquidus (642°C for Al-Cu) and the eutectic temperature (548°C for Al-Cu) cause low-melting point eutectics and certain second phase particles to melt, or liquate [29]. Depending on the time at temperature, some of the PMZ grains themselves may melt on the edges in addition to the liquation-sensitive second phase particles. This liquation may or may not result in cracking, depending on the strains from the nearby FZ. However, the liquated microstructure, shown in Figure 2.18, is nevertheless weakened due to the resulting brittle eutectic particles on grain boundaries and the solute-depleted band adjacent to it [29].

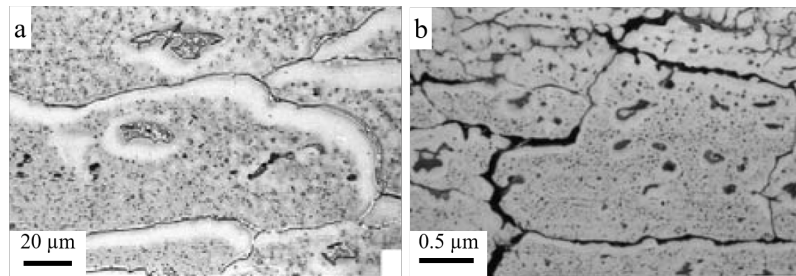


Figure 2.18: (a) Liquated microstructure, consisting of base metal grains decorated with eutectic on the grain boundaries and a solute-depleted α band [29], and (b) liquation cracking occurring intergranularly in the PMZ [28].

Cao and Kou [14] explored the HCS of various AAs to liquation cracking. They found that one condition that frequently produced liquation cracking was when the weld metal f_s is greater than that of the PMZ. The reason for this is straightforward. If the weld metal is more solidified than the PMZ, its contraction will induce significant strains on the PMZ, separating liquated grains if the strain exceeds the capacity of

the thin liquid film. Conversely, if the PMZ solidifies before the weld metal, then the strains of PMZ contraction imposed on the weld metal do not necessarily cause cracking there, since the free surface of the weld bead can accommodate some strain.

To control the f_s balance in the weld metal and PMZ, Kou returns to the T- f_s diagram to design base metal/filler metal combinations that ensure a higher f_s in the PMZ than the FZ. If at any point in the terminal stages of solidification the FZ f_s > PMZ f_s , the material will be susceptible to liquation cracking.

This base and filler metal f_s balance poses a unique problem for AM, since the “base metal” of layer N in an additive deposit is the FZ of layer N-1. Thus, no change in composition is intentionally built into the process to circumvent liquation cracking due to the homogeneity of the deposit.

Some techniques to mitigate liquation cracking in welding are controlling the weld-metal composition, the welding condition, and the base metal [28]. As mentioned previously, selecting a base metal and filler metal combination that results in the PMZ solidifying before the FZ will help ensure that the strains from the FZ will not separate liquated grains. In controlling the welding condition, care may be taken to lower the heat input through high-energy density processes such as EBW, or through multi-pass welding [28]. This will lower the thermal gradients to reduce the extent of the PMZ and its time at temperature. Finally, selecting a fine-grained base metal will prepare the PMZ to better accommodate contraction strains from the FZ. A fine-grained base metal has more granular surface area than a coarser-grained material, spreading out liquation-sensitive particles and lowering the concentration of available low-melting point phases for liquation at grain boundary interfaces [28].

While AM literature does not emphasize liquation cracking for 7xxx-series AM deposits, it is expected that due to the welding heritage of EBF³, liquation cracks should appear in 7075 deposits in this work. This research investigates the mechanisms and appearance of such cracks in EBF³ deposits to understand the relationship of cracking and manufacturing process and explore directions for crack elimination.

Chapter 3

Behavior and Properties of EBF³ Deposited 2219

3.1 Abstract

The popular aerospace alloy 2219 is investigated in this chapter to evaluate its AM compatibility and mechanical properties when deposited with EBF³ as a baseline for the 7075 work. In its wrought form, 2219 has moderate strength, good corrosion resistance, and excellent toughness compared to other AAs, and the alloy is considered readily weldable. It was found in this study that 2219 exhibited excellent compatibility with the EBF³ process, with minimal porosity and no hot cracking or other defects in the deposits. The as-deposited (AD) microstructure varied significantly from that of wrought 2219, resembling a cast microstructure with Al-Cu eutectic particles decorating the grain boundaries. In the T6 heat treated (HT) condition, the microstructure was homogenized, with the majority of the Cu redistributed as fine, strengthening θ' particles. Some globular θ particles remained on grain boundaries after solutionizing due to the 2219 composition exceeding Cu solubility limits. The area-averaged AD and HT grain diameters were on the order of 130 μm , and the HT microstructure was not recrystallized.

The AD and HT microhardness values were 81 and 136 $\text{HV}_{0.3}$, respectively, and compared well with literature values of other 2219 welds and additive deposits. The AD tensile properties were anisotropic, with the LT orientation exhibiting the highest strength and the ST the lowest. The average AD YS, UTS, and %el. values were 18.4 ksi, 38.8 ksi, and 13.7%, and all properties fell between wrought annealed and

T4 values. These values also compared well with those in other 2219 AM studies. The HT properties were isotropic due to the homogenization of the microstructure, with all values falling within 3% of each other. The average HT yield strength (YS), ultimate tensile strength (UTS), and total elongation (% el.) were 43.4 ksi, 63.1 ksi, and 11.2%, respectively, slightly higher than typical T6 wrought values.

The overall lack of defects and good mechanical properties confirmed that EBF³ processing of the alloy is a plausible manufacturing method for use in the aerospace industry. However, despite the alloy's excellent EBF³ compatibility, the 2219 HT YS was limited to 64% that of the 7050-T7 target. This was expected due to the precipitation strengthening limitations of binary Al-Cu alloys. Modifications to the alloy chemistry or thermomechanical processing of the deposits are required to reduce the gap in performance with wrought 7xxx-series properties.

3.2 Background

3.2.1 Wrought 2219

2219 is a member of the 2xxx-series of Al, a family of alloys which have Cu as the primary alloying addition. 2xxx-series alloys are precipitation-strengthened, meaning that their mechanical properties are mainly derived from precipitates evolved during thermal processing rather than from solid solution strengthening or work hardening. The primary strengthening phase in many 2xxx-series alloys, and thus 2219, is Al₂Cu, commonly referred to as the θ phase, which can be found between 53.2 to 53.9 wt.% Cu on the Al-Cu phase diagram in Fig. 3.1 [67].

2219 is commonly used in cryogenic fuel tanks and space structures due to its weldability [68]. A nearly-binary Al-6.3Cu alloy, 2219 is produced in both plate and sheet product forms and is considered readily weldable for most commercial welding methods and tempers, especially in its high strength T6 and T8 tempers [6, 8]. The standard composition limits of the alloy are given in Table 3.1 [69].

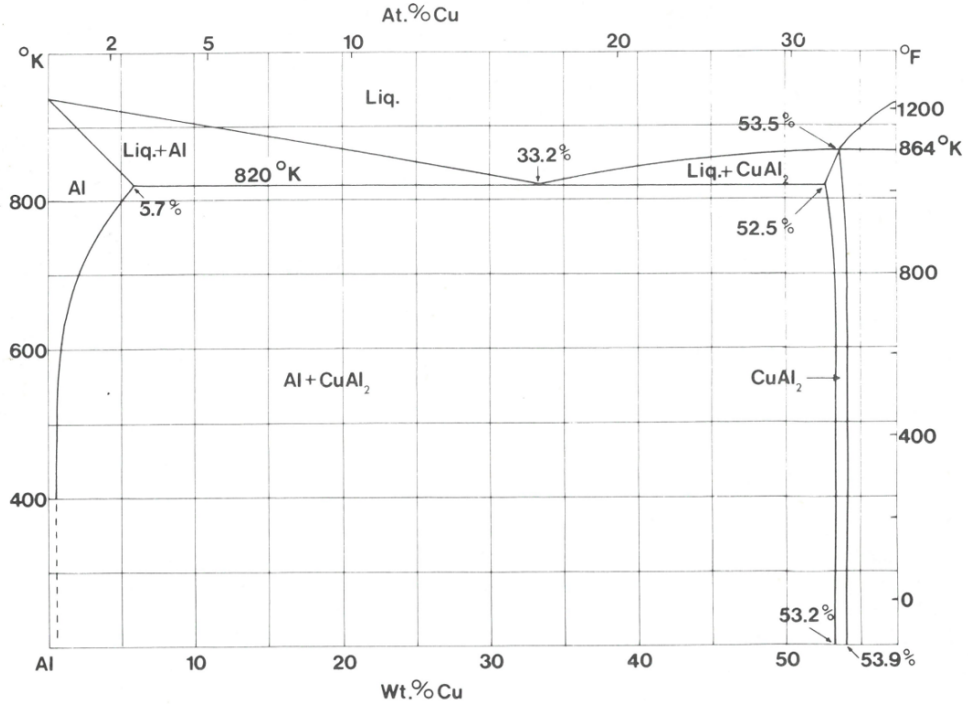


Figure 3.1: Al-Cu partial phase diagram showing the solid solubility limit of Cu in Al at 5.7 wt.%, the Al-Cu eutectic at 33.2 wt.%, and the θ phase, Al_2Cu , at 53.2 to 53.9 wt.% [67].

Table 3.1: ASTM B209-14 chemical composition limits for 2219 [69]^A.

Alloy	Cu	Mn	Fe	Si	Ti	Zn	Mg	Other		Al
								Each	Total	
2219	5.8-6.8	0.20-0.40	0.30	0.20	0.02-0.10	0.10	0.02	0.05 ^B	0.15 ^B	bal.

^A Limits are in weight percent maximum unless shown as a range or stated otherwise

^B V 0.05-0.15, Zr 0.10-0.25

Typically, as-cast 2xxx-series Al exhibits a cored dendritic microstructure of Al α solid solution, with alloying constituents often forming well-connected eutectics in interdendritic spaces and at grain boundaries [70], as shown in Fig. 3.2. The as-cast structure serves as the basis for subsequent hot- and cold-working operations that reduce ingot thicknesses to those of plate and sheet product forms. Once worked to the near-final product, the material is then heat treated and sometimes cold-worked further to obtain desired mechanical properties.

Commercial heat treatments are employed to form a well-distributed population of fine strengthening precipitates from the as-cast structure. The T6 temper involves

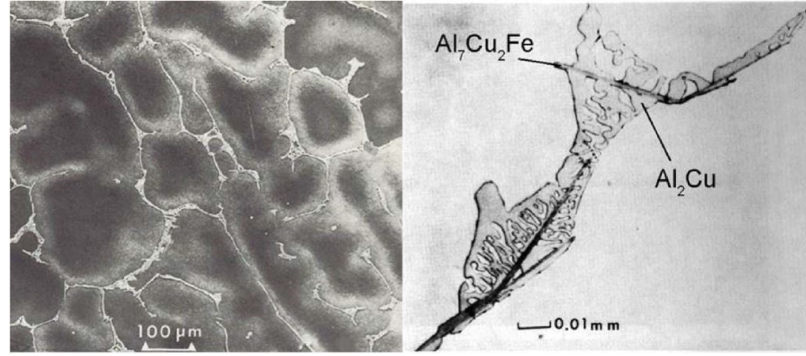


Figure 3.2: As-cast microstructure of 2219 exhibiting (a) cored dendritic structure and (b) Al-Al₂Cu eutectic at grain and interdendritic boundaries, with spindle-like Al₇Cu₂Fe intermetallics [71].

a solutionizing step, where the material is heated just below the eutectic temperature of 547°C to dissolve as much Cu as possible, limited by the maximum solubility of Cu in Al. Since solutionizing is a diffusion-based process, this step occurs on the order of 2 to 4 hours to dissolve most of the Cu before quenching the material in water to lock the Cu in solution. A controlled artificial aging step is then performed for 24 to 48 hours, where the material is introduced to a furnace set near 180°C. To form many θ' precipitates, the aging temperature is designed to first nucleate many fine, coherent Guinier-Preston (GP) zones, which transform into semi-coherent θ'' and θ' intermediate phases [72]. This allows for a well-dispersed population of θ' precipitates, which establishes the high strength of 2219 in the T6 condition. Overaging results in the transformation of θ' to the incoherent θ , which lowers strength.

Other HT procedures such as the T8 temper include controlled cold working of the material between quenching and aging in order to introduce lattice defects such as dislocations and vacancies upon which θ' -type precipitates will preferentially nucleate. This creates an improved distribution of strengthening precipitates and also contributes to some work hardening of the material, which serves to maximize the strength. In contrast, the thermal treatment known as annealing (or the O temper) develops the lowest strength of the material by holding it at a temperature of 400°C for 2 to 3 hours, followed by a slow cool to precipitate coarser θ particles [73].

The typical properties of 2219-O are a YS of 10.2 ksi, an UTS of 24.7 ksi, and a maximum % el. of 18% [74]. Typical tensile properties of 2219-T62 include a YS of 42.1 ksi, an UTS of 60.2 ksi, and a % el. of 10%. The Brinell hardness in the T62 temper is 115.

3.2.2 Welding of 2219

2219 is considered readily weldable for most commercial procedures and alloy tempers [6]. This amenability to welding stems from the alloy's solidification behavior and low susceptibility to hot cracking, a common problem in the welding of other AAs. 2219 arc welds typically employ 2319 as filler wire, and its composition is essentially identical to that of 2219 but with higher levels of Ti to serve as a grain refiner [75].

2219 was selected as the original material for the Space Shuttle External Tank (ET) due to its balance of weldability and strength. With the design of the ET calling for over half a mile of welds, 2219 served as a suitable material for 15 years until missions to construct the International Space Station began. These higher orbital inclination missions required a lighter external tank, issuing in a transition to the lighter Al-Li alloy 2195 and the friction stir welding (FSW) process [68].

Brennecke [76] explored the resulting joint strength, ductility, and microstructure of 2219-T8 EBW joints, with base metal thicknesses ranging from 0.5 in. to 2.375 in. It was found that the high power density of EBW contributed to a 3 to 4x reduction in the EBW FZ and HAZ widths than GTAW joints, as seen in Figure 3.3. As-welded 0.5 in. plates demonstrated a UTS of 47 ksi, with UTS increasing with plate thickness, likely due to greater weld efficiency for heavier gauges. The Tukon hardness of the welds was found to be 75 to 80 in the FZ, 80 to 125 in the HAZ, and 125 to 140 in the base metal.

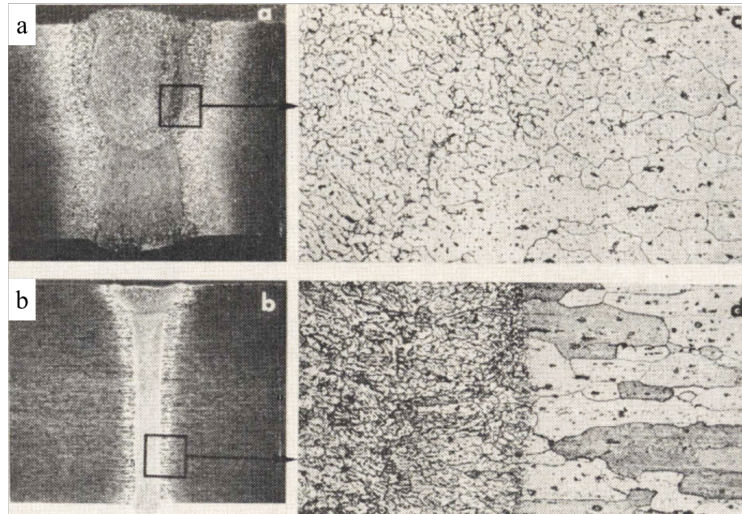


Figure 3.3: 2219 weld microstructures from (a) GTAW and (b) EBW. EBW provides a 3 to 4 times reduction in HAZ and FZ width, as well as increased joint strength [76].

Malarvizhi and Balasubramanian [77] studied the effects of GTAW, EBW, and

FSW on the properties of 2219 joints. It was found that of the two fusion-based processes, EBW produced superior weld joint properties due to a more refined microstructure. However, the solid-state FSW process exhibited higher properties overall since it further refined the microstructure and did not dissolve the strengthening precipitates as did GTAW and EBW.

Malarvizhi et al. found that EBW of naturally aged 2219-T4 caused a 40% decrease in strength from that of the parent metal to 35 ksi due to the dissolution of strengthening Al_2Cu precipitates [78]. However, post-weld artificial aging was found to promote a 10% increase in properties over the as-welded condition due to the precipitation of strengthening phases. The tests showed that the Vickers microhardness measured on the samples was 140 $\text{HV}_{0.05}$ in the unaffected base metal. The as-welded FZ possessed a hardness of 90 $\text{HV}_{0.05}$, while HAZ registered at 110 $\text{HV}_{0.05}$. These hardness values compare well with those found in Brennecke’s work [76], although the UTS value was 10% to 20% lower, possibly due to differing welding parameters and base metal tempers.

3.2.3 Additive Manufacturing of 2219

A number of studies have investigated the compatibility and resulting properties of 2219 with wire-based additive processes that derive their roots from welding [79, 80, 23].

Bai et al. [79] studied the microstructure of 2.75 in. tall walls deposited with a GTA-additive process, the equivalent of TIG or WAAM. They noted differences in microstructures throughout the height of the build, as shown in Fig. 3.4.

It can be seen in Figs. 3.4(a) and (b) that the final layer possesses a dendritic microstructure with a discontinuous $\alpha\text{-Al}_2\text{Cu}$ eutectic. This microstructure is equiaxed and looks like a typical weld FZ microstructure, such as in Fig. 3.3(a). In contrast, the grain structure in lower layers (Figs. 3.4(c)-(f)) has lost its dendritic character and is replaced by grains that are continuously decorated by $\alpha\text{-CuAl}_2$ eutectic on the grain boundaries. The formation of this continuous eutectic is attributed to the partial melting in the HAZ above the eutectic temperature, known as the liquation mechanism in welding. This liquation is most prominent in Figs. 3.4(e) and (f), where the liquid eutectic flowed together and “dripped” into the grain below, a phenomenon which Kou attributes to cellular resolidification of the partially-melted grain [13].

To further this research effort, Bai et al. [80] deposited 2219 with the WAAM process and analyzed tensile properties of thin walls. Their results showed accumula-

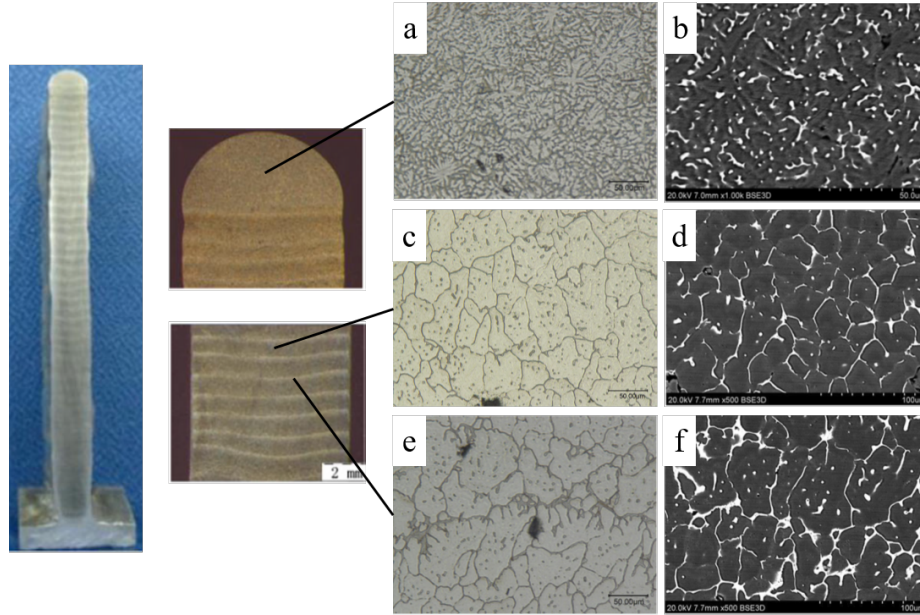


Figure 3.4: Weld microstructures from GTA-additive deposits showing (a) etched dendritic microstructure of the final layer of the deposit, (b) SEM-BSE image of the top layer's dendritic microstructure with discontinuous eutectics, (c) etched microstructure of a lower layer in the build, (d) SEM-BSE image of a layer showing continuous eutectics, (e) etched microstructure of an inter-layer region, and (f) SEM-BSE image of an inter-layer region showing continuous eutectics. Modified from [79].

tion of larger θ phase in the interlayer boundaries rather than the weld centers, which ultimately were traced as the crack initiation sites in tensile tests. These deposits resulted in an average UTS of 34.4 ksi, an average elongation of 10.7%, and an average hardness of 77.5 HV_{0.2} in the as-deposited condition. The hardness was invariant with respect to location across layer centers and interfaces.

Gu et al. [23] explored the deposition and resulting properties of 2219 in the WAAM process using an advanced pulsed cold metal transfer (CMT-PADV) technique. This study essentially eliminated porosity common to welding in the WAAM deposits and created a refined, equiaxed grain structure. This refinement is attributed to the lower heat input from the pulsing process, which allows for AC operation and modifies the thermal profile of the builds. Longitudinal and short transverse tensile specimens were extracted from walls roughly 20 in. long and 8 in. tall, resulting in average YS and UTS values of 16.0 ksi and 37.7 ksi, respectively, and an average elongation of 17% in the as-deposited condition. These properties show a 50% increase in strength over typical 2219-O values, with comparable elongation. The authors suggest that interpass rolling operations could further improve the AD properties.

Prior NASA 2219 EBF³ Work

Initial NASA EBF³ work by Taminger and Hafley [9] explored the processing envelope of 2219, testing seven different combinations of TS, WF, and beam power (AV*BC) to isolate the effects of those three machine parameters. Multiple deposits with linearly varying TS or WF along the length of the build were also produced, resulting in changing height and width of the deposits due to evolving melt pool dimensions. Metallurgical cross sections were prepared to compare the effects of each parameter change. It was found that higher WF rates increased the cooling rate, resulting in a refined microstructure, while increasing TS resulted in shallower molten pools and an increased cooling rate, also contributing to a more homogeneous microstructure with finer equiaxed grains. Duplicate longitudinally-oriented, subsize, flat tensile specimens were prepared from the deposits and tested in the AD and T62 conditions. It was found that within the limited number of samples, 2219 was robust with respect to changing machine parameters, and the tensile properties collapsed into consistent values, particularly for the HT material. Their study achieved a YS and UTS of 17 ksi and 41 ksi in the AD condition and 42 ksi and 61 ksi in the T6 condition, similar to literature values [76, 77]. The AD properties fell between typical 2219-O and -T4 wrought values, while their HT values were slightly higher than T62 typical properties. This work suggests that EBF³ deposition of 2219 is insensitive to changing parameters, despite some parameter sets resulting in more controlled microstructures than others.

Subsequent NASA EBF³ work by Domack and Taminger [11] further developed the body of data surrounding deposition of 2219 with EBF³. Despite parameter changes of power, WF, and TS for the builds, the tensile and elongation values from various deposits differed only by a couple percent within the AD and T62 conditions. Furthermore, the study found that for each parameter set, the tensile and elongation values were isotropic for tensile specimens machined parallel to the longitudinal and vertical directions for both HT conditions. AD properties fell between typical 2219-O and nominal -T4 values, with YS and UTS values of 16 ksi and 39 ksi, while the HT results of 42 ksi and 60 ksi aligned well with typical T62 values. These results compare well with the results from Taminger and Hafley [9]. Microstructural evaluations determined that the AD material exhibited grains with 100 to 200 μm dimensions in the melt pool centers, with grains of 10 to 25 μm at interlayer boundaries. They found an Al-Cu eutectic phase at the grain boundaries and needle-like Fe and Si containing particles. For the T62 material, the microstructure was similar with unrecrystallized grains of both sizes and the Fe and Si precipitates, but with

a mostly dissolved eutectic phase. The fracture surfaces of the tensile specimens in the AD material reflected both shallow grains and lamellar features, correlating to the small equiaxed grains and dendritic structure seen in the micrographs. The T62 condition exhibited fracture morphology with shallow dimples of two sizes, showing transgranular fracture and a transformed microstructure from the AD material.

These studies set the foundation for the present work and are a useful resource in confirming the repeatability and robustness of 2219 deposition with EBF³.

3.3 Experimental Procedures

The 2219 work for this thesis is a subset of a current project studying mechanical properties and corrosion resistance of EBF³-deposited 2219. The project required three walls and a brick-shaped deposit for specimen extraction, with the test matrix including tensile, fracture toughness, stress-corrosion cracking (SCC), and intergranular (IG) corrosion tests. However, only the metallurgical and tensile results will be discussed in this work.

3.3.1 Starting Materials

To deposit wall- and brick-shaped builds of 2219, 2319 wire was selected for its use in other wire-based AM studies [11, 23, 79, 81]. 2319 0.062 in. diameter wire meeting specifications listed in AMS 4191 [75] and AWS A5.10 ER2319 [82] was obtained from Astrolite[®] Alloys, with the measured wire composition given in Table 3.2. In this work, EBF³ deposits made with 2319 wire will be referred to as 2219 to facilitate comparison with 2219 wrought product.

Table 3.2: DCP-AES results from the starting 2319 wire. Results given in wt.%.

Alloy	Cu	Mn	Fe	Si	Ti	Zn	Mg	Al
2319 wire	6.38	0.299	0.136	0.045	0.153	0.016	0.013	bal.

Figure 3.5 shows the 2319 wire microstructure, with the drawing direction indicated with arrows. The precipitates in the wire are evenly dispersed, with both Fe- and Cu-bearing particles present. The Cu-containing particles - likely the θ phase - typically appear in Fig. 3.5(b) as grey, rounded particles with a size of 15 μm or below. The Fe-containing particles appear reddish-brown and are either rounded or elongated in the rolling direction, with a maximum observed dimension of 6 μm .

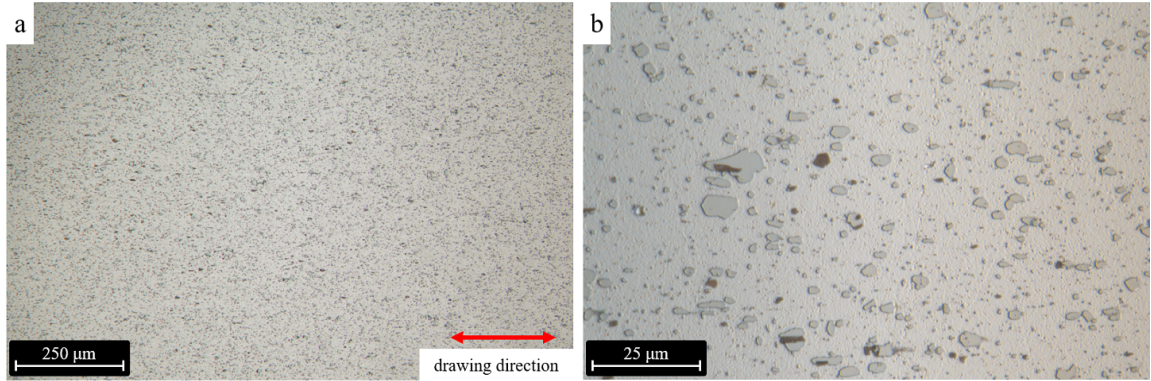


Figure 3.5: Microstructure of the 2319 wire used for constructing the 2219 deposits. (a) 100x view showing the uniform precipitate distribution, and (b) 1000x image of the Cu-bearing (grey) and Fe-bearing (red-brown) phases.

3.3.2 Machine Setup and Deposition Procedures

Figure 3.6 shows the setup and completion of three 2219 wall deposits, with machine and deposit coordinate systems given in Figs. 3.6(a) and (b), respectively. A “window frame” fixture, shown in Fig. 3.6(a), was developed to secure three 0.25 to 1.0 in. baseplates in the EBF³ chamber. Grooves were machined in 0.25 in. 2219 backing plates set beneath the build plates, and thermocouples were set in the grooves so that the thermocouple heads were located below the geometric center of each baseplate.

In Fig. 3.6(b), the deposit-specific coordinate system is composed of the longitudinal (L), long transverse (LT), and short transverse (ST) directions. These follow the longest to shortest dimensions of a build layer, with the L direction corresponding to the travel direction of the EB for the layer, the LT direction corresponding to the layer width, and the ST direction corresponding to the direction normal to the plane of the layer.

Prior NASA work has found that some preheating of the baseplate is necessary in order to promote better adhesion of the deposit to the substrate. Machine code was written to pass a low power, defocused EB across the baseplate surface in a zigzag pattern. This program was repeated until the temperature at the thermocouple below the baseplate reached approximately 120°C. The beam parameters were then changed to those for material deposition and reduced to 40% BC for two beam-only cleaning passes (CP) to burn off oxides in the deposit footprint on the baseplate prior to deposition. Following the CPs, the wire feed was enabled and deposition of 2219 proceeded at full power. The dwell time between layers was determined by monitoring

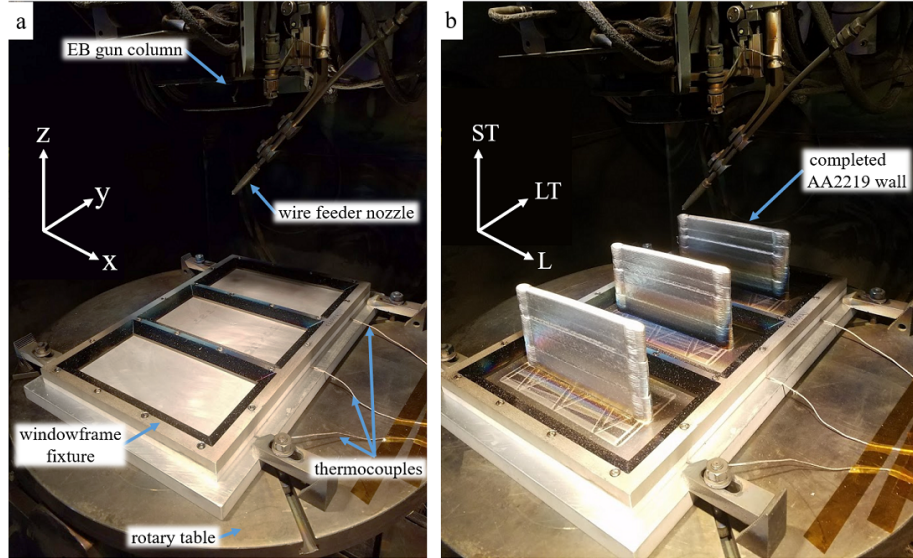


Figure 3.6: (a) Machine setup with windowframe fixture and 0.25 in. baseplates installed, including thermocouples centered beneath each plate. (b) Windowframe fixture securing three co-deposited 2219 walls.

the thermocouples to keep a consistent background temperature averaging 160°C and was typically on the order of a couple minutes every two layers.

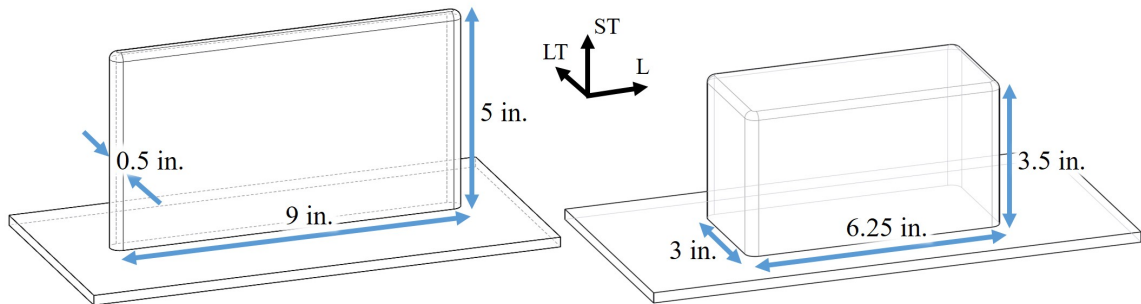


Figure 3.7: Nominal dimensions and coordinate system for wall (left) and brick (right) deposits for specimen extraction.

Figure 3.7 displays the nominal dimensions for the wall and brick deposits. The wall width was specified to be 0.5 in. to fit round, subsize tensile bars oriented longitudinally and vertically, and the brick width was 3 in. to accommodate transverse orientation tensile specimens. Since the width of a deposit depends on the number of adjacent weld beads, the percentage of bead overlap, and the molten pool size, preliminary experiments were run to investigate the efficiency and build quality of generating 0.5 in. wide walls using multiple thin beads versus a single, wide bead. It was found that depositing multiple beads with a small, circular raster pattern side-

by-side to achieve the wall width requirement resulted in a narrowing of the deposit with increasing build height due to surface tension effects, as shown in Fig. 3.8(a). In contrast, a 0.5 in. wide bead was achieved with a single pass by making the raster pattern elliptical, with the long axis of the ellipse parallel to the LT direction and having a 4:1 aspect ratio, the result of which is shown in Fig. 3.8(c). While the dimensional instability of the multibead wall was reduced by gradually increasing bead spacing with build height, as shown in Fig. 3.8(b), the additional beam passes and resulting deposition time rendered the multibead build strategy impractical. Thus, the single bead deposition strategy from the sample in Fig. 3.8(c) was selected for constructing all subsequent wall deposits.

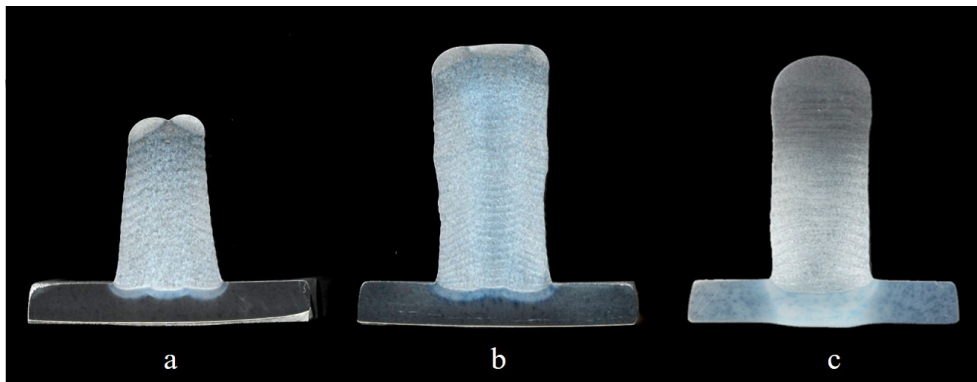


Figure 3.8: Build geometries resulting from varying bead number and spacing. (a) Three beads per layer, no spacing adjustment, (b) three beads per layer with bead spacing adjustment mid-height, and (c) single, wide bead per layer maintaining a consistent width through the build height.

To achieve a 3 in. wide brick-shaped deposit, seven 0.5 in. beads were deposited side-by-side to maintain the same beam parameters as the walls. The brick’s beads were laid down in a “fence and fill” manner to avoid surface tension effects and narrowing of the deposit with increasing height. Figure 3.9 depicts the steps to this deposition procedure and a full-width macro image of a test brick microstructure.

The brick deposition procedure consisted of depositing four 0.5 in. beads with their centerlines spaced by 0.84 in. to create the “fences”, as depicted in Fig. 3.9(a). Once a sufficient lead of five layers was achieved in the fences, the sequence returned to a height of $z = 0$ to deposit a layer of “fill” beads in between the fences, as shown in Fig. 3.9(b). The sequence continued with alternating fence and fill layers, shown in Fig. 3.9(c), maintaining a lead of a few layers in the fences to overcome the width-reducing surface tension effects of the fills. At the conclusion of the brick deposit in Fig. 3.9(d), additional fill layers were added to even out the top surface of the brick.

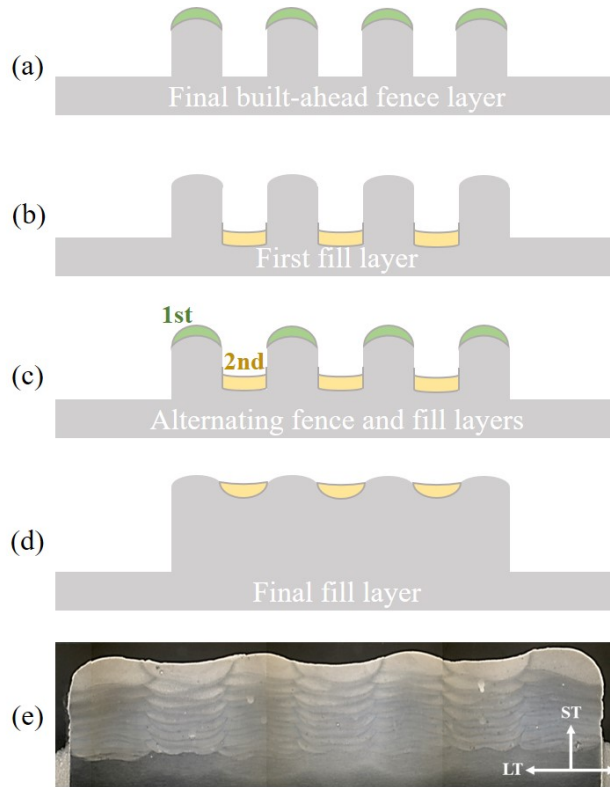


Figure 3.9: Brick deposition sequence of fence (green) and fill (yellow) layers to maintain a consistent, 3 in. width along the build height. (a) Final fence built-ahead layer, (b) first fill layer, (c) subsequent layers alternating with first fences, then fills, followed by (d) the final fill layers to even out the deposit height. This sequence results in (e) an as-built test brick microstructure.

Both fence and fill beads were deposited in an inside-to-outside sequence.

A consistent set of beam parameters was used for the 2219 walls and brick deposits. These parameters, summarized in Table 3.3, were chosen for the excellent surface finish they produced on test deposits, for using mid-range beam energy values, and for producing fully-dense test deposits. These parameters resulted in an energy density of 302 kJ/in^3 , which falls within the range of energy densities of 254 and 532 kJ/in^3 used by Domack and Taminger [11].

In preliminary walls, it was noted that depositing layers in the same direction every time (i.e. with the travel direction identical to the machine's X direction) resulted in material building up at the start of the deposit and trailing off at its end. An interlayer table rotation of 180° was incorporated to balance this disparity in height at build starts and stops. Furthermore, the welding practice of “runbacks” (rb) was implemented to ensure complete geometric stability of the bead. This involved retracing the final 0.5 in. of the bead before turning off the EB to cause the molten

Table 3.3: EBF³ parameters used for the 2219 wall and brick deposits.

Parameter	Value	Units
AV	40	kV
BC	90	mA
BF	323 (near-focused)	A
RF	1	kHz
X/YSF	125/500	%
TS	30	ipm
WF	172	ipm
Δz	0.035	in.

pool to flow back and freeze evenly rather than tailing off at the end of the bead. The combination of runbacks and interlayer rotations corrected all layerwise geometric instabilities for the builds.

While the 2219 walls were deposited on 0.25 in. baseplate, it was found that the multibead build sequence of the brick resulted in significant transverse shrinkage of 0.25 in. baseplate. This shrinkage reduced the deposit width and compromised the stability of the deposit, so the final brick deposit was built on 1 in. baseplate to minimize the shrinkage. Figure 3.10 displays one of the three final walls and the final brick deposit produced with the above parameters and procedures.

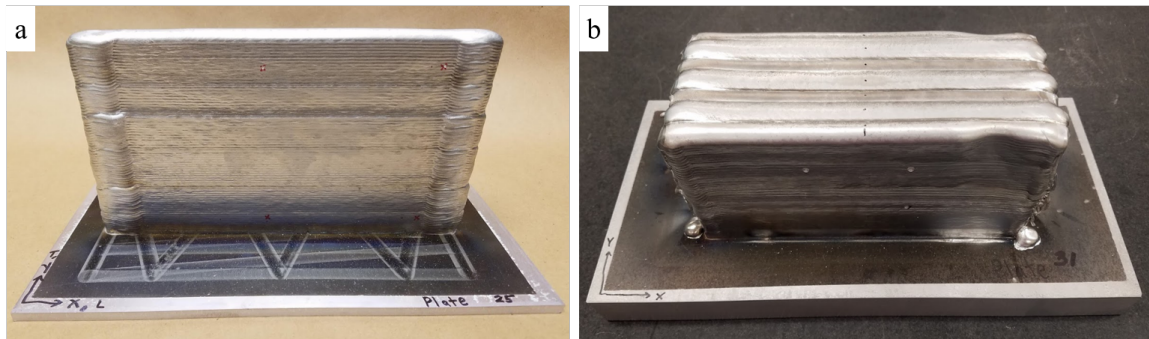


Figure 3.10: Completed (a) wall and (b) brick deposits. Evidence of the zigzag warmup procedure is particularly evident for the wall deposit. For scale, the longest dimension of the baseplate is 12 in.

3.3.3 Deposit Evaluation Procedures and Specimen Preparation

Prior to sectioning the deposits, x-ray computed tomography (XCT) scans were conducted to non-destructively evaluate the builds for flaws. Shallow reference marks were drilled into the side of each deposit so that an origin would appear in the XCT scan. If a significant flaw were found with XCT, its location was measured from the reference mark and specimen extraction from that area was avoided. Depending on availability, either a X-TEK HMXST225 or a Nikon Metrology C2 XCT machine was used with an open chamber tungsten x-ray source to complete the scans. Figure 3.11 depicts the scan setup in the Nikon C2 machine, as well as a XCT data slice in the LT-ST plane. The gradations in grayscale represent changes in x-ray signal, which may indicate density changes or edge effect scattering. When density changes are not attributed to beam scattering, brighter areas represent higher density (less transmission to the detector) and darker areas represent lower density (more transmission). Given the trade-off of scan resolution with scan volume, the entire wall and brick deposits could not be captured in a single scan, so regions of interest were identified in the center of the deposits to capture the majority of the builds. The bead starts and stops and areas very close to the baseplate were excluded from the scans since samples were not extracted from those regions of the deposits. The scan resolution for the wall deposits was 99.8 μm , while the scan resolution for the brick shaped deposit was 66.0 μm . The resulting volumetric scan data was sliced into images in the L, LT, and ST directions using Matlab and observed with ImageJTM to identify deposit flaws.

To adequately sample the microstructure and mechanical properties of EBF³-deposited 2219, tensile and metallurgical specimens shown in the cut plans in Appendix A were used. Tensile specimens of L and ST orientations were extracted from the wall deposits, and tensile specimens with a LT orientation were extracted from the brick deposit. Sections of material in the walls and brick were reserved for metallurgical characterization. The fracture toughness and corrosion samples in the cut plan were prepared for a separate study.

Blanks of all relevant tensile and metallurgical samples were cut from the deposits with a bandsaw and labeled. These were then separated into two groups based upon their intended heat treatment, which can be found in the Appendix A cut plan. Half of the metallurgical and tensile samples were left in the AD condition, meaning that no further thermal processing was performed on them after deposition. The second

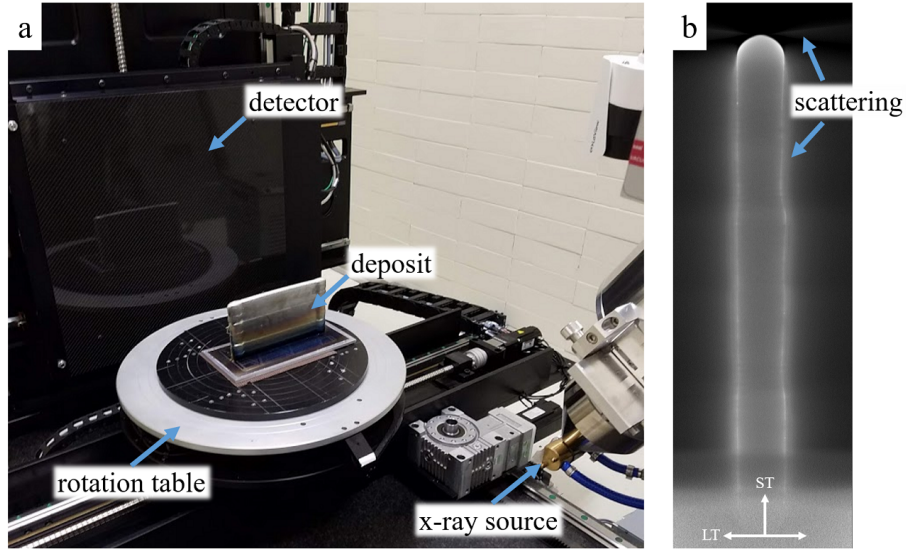


Figure 3.11: (a) Nikon Metrology C2 XCT machine setup for scanning a wall deposit, and (b) sample data from the LT-ST plane showing beam scattering effects.

half of samples were subjected to a standard T62 HT [83], which involves solution heat treating, quenching, and artificial aging of the material to control the location and distribution of precipitates in the Al matrix. The parameters used for this heat treatment are listed in Table 3.4.

Table 3.4: Standard 2219-T6 heat treatment practice used for half of the tensile and metallurgical specimens [83].

Step	Temperature ($^{\circ}\text{C}$)	Time (hr)
Solution HT	535	4
Quench	cold water	-
Age	180	36

After the heat treatment was completed for the specified samples, all specimens were machined to their final geometries. Figure B.1 in Appendix B displays the subsize, round tensile specimen geometry with a 1 in. gauge length used for uniaxial tensile testing. Metallurgical samples were simply squared off with a milling machine so that the faces of the samples were parallel to the L, LT, and ST build directions.

3.3.4 Specimen Characterization and Mechanical Testing Procedures

ASTM E3-11 [84] was followed to prepare the metallurgical specimens. SiC sandpaper was used for grinding the surface roughness down to 1200 grit, and a Buehler MasterPrep 0.05 μm alumina suspension was used for the final polishing step to achieve a mirror finish for both SEM observation and microhardness measurements. The samples were then etched with Kellers reagent for 10 to 15 s for microstructural imaging on an inverted Leica optical light microscope.

Grain size measurements were conducted using electron backscatter diffraction (EBSD) in a Hitachi S-3700N microscope. ASTM E2627 was followed for post-processing the EBSD data [85]. The neighbor confidence interval method was used to clean up the zero-resolution points, and no more than 10% of points were altered during data cleanup. Grain sizes were determined by first assuming that grains must be larger than 100 pixels and must have a misorientation greater than 2° with respect to their neighbors.

X-ray diffraction (XRD) specimens oriented in the LT-ST plane were cut from the AD and HT metallography samples from the wall deposits, originating from halfway through the build height. The XRD samples were roughly 0.5 in. square and 0.125 in. thick. These were polished to 800 grit SiC sandpaper for analysis. A Cu $K\alpha$ x-ray source was used to collect XRD spectra for the samples in a Rigaku Smartlab medium resolution x-ray machine in a Bragg-Brentano configuration. Scans were completed from a 2θ of 10 to 90° , with a step of 0.01° . A voltage and current of 40 kV and 44 mA were used, respectively, as well as a scan speed of $0.05^\circ/\text{s}$ and a $K\beta$ filter.

Vickers microhardness measurements were acquired in the LT-ST plane for the wall deposits utilizing a Struers Duramin 100 universal microhardness machine and following ASTM E384 [86]. A 300 gram-force load with a Vickers pyramidal indenter was used on both the AD and HT samples in a 5 x 10 grid test pattern. The indents were spaced by 0.01 in. in the ST direction to sample across layer boundaries and spaced by 0.071 in. in the LT direction to sample across the deposit width.

Subsize uniaxial tensile specimens with the geometry depicted in Fig. B.1 of Appendix B were tested in accordance with ASTM E8 [87] in both the AD and HT conditions. Specimens were mounted in a MTS 810 universal testing machine with back-to-back extensometers of 1 in. gauge length, with the setup shown in Fig. 3.12. The specimens were loaded with a 0.010 in./min stroke rate until yielding, after which the stroke rate was increased to 0.050 in./min until failure. Extensometer and load

data were recorded at a frequency of 2 Hz. A select number of fracture surfaces were examined in the SEM for analysis of the fracture morphology.

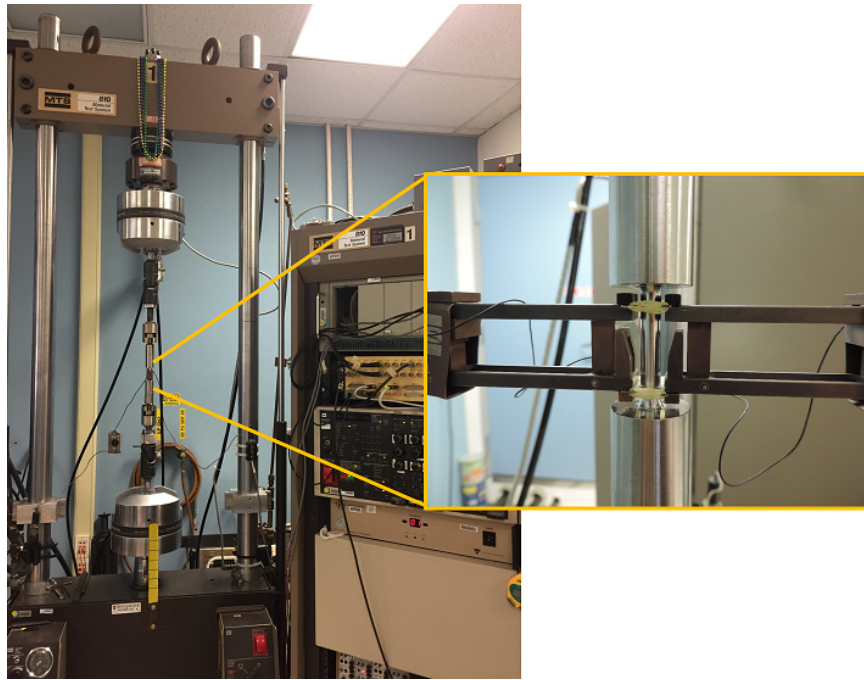


Figure 3.12: Testing configuration for subsize tensile specimens with back-to-back 1 in. gauge length extensometers.

3.4 Results

3.4.1 Non-Destructive Evaluation of Deposits

The XCT results show that the three 2219 wall deposits possessed relatively few indications of density fluctuations. Various small, pore-like indications appeared randomly throughout the height, length, and width of the builds. Figure 3.13 depicts one such indication, measuring 5 pixels (0.499 mm) in diameter. Pores smaller than the scan resolution of 100 μm were not detected by XCT, and only a small number were found during sectioning and polishing of metallurgical samples. Porosity of this size and extent was not deemed detrimental to properties, so the deposits were considered fully dense.

A single, significant defect was detected in Wall 1 and was attributed to a wire jam and beam stoppage event that occurred midway through the build sequence. Figure 3.14 displays successive images through the defect, which consists of a void

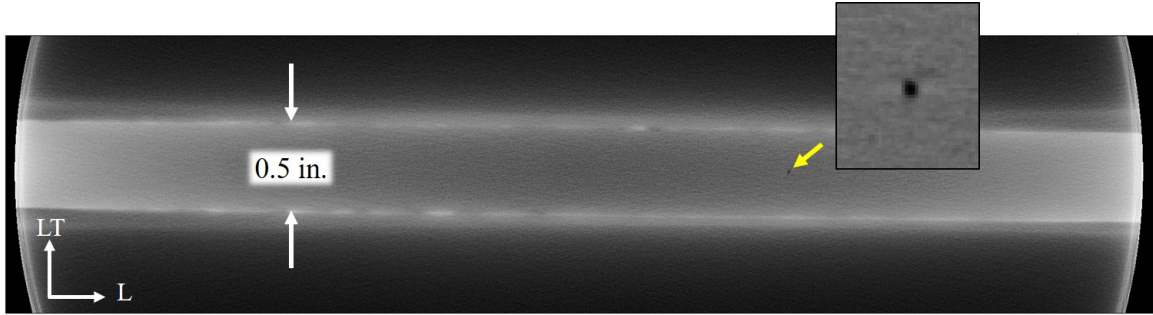


Figure 3.13: Typical XCT scan for a layer within one of the 2219 walls. The black dot denoted by the red arrow is a 0.50 mm indication of a pore, enlarged in the inset.

3.1 mm in height, with cracks emanating down into the build by 1.8 mm. This area was identified before and avoided during specimen extraction.

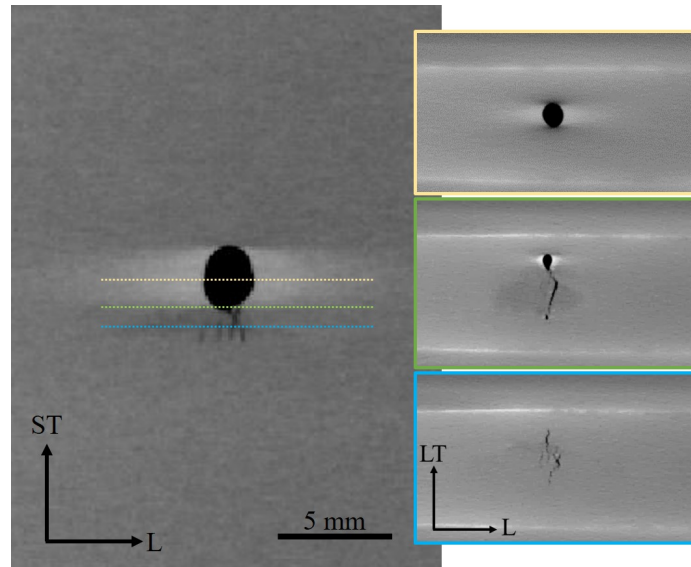


Figure 3.14: Atypical defect attributed to a beam arc-out and subsequent wire stick event. The three successive images represent different slices through the defect at various layer heights.

The XCT data from the brick-shaped deposit showed more indications of density fluctuations than the wall deposits, some occurring in a linear fashion and possibly attributed to the overlaps of the fence and fill beads. Due to the 3 in. thickness of the brick, the x-ray signal was greatly attenuated, leading to poor reconstruction of the scans. Thus, the indications of density change looked larger and more drastic than their actual size and were only used to identify regions of porosity and not for predicting pore sizes.

3.4.2 As-Deposited and Heat Treated Microstructures

The AD and HT microstructures from the 2219 walls and brick differed from those typical of wrought material. The following sections discuss the microstructures observed with optical microscopy and with SEM techniques, including secondary electron (SE) and backscatter electron (BSE) imaging, electron dispersive spectroscopy (EDS), and EBSD.

As-Deposited Wall Microstructure

Figure 3.15 displays an AD microstructure from the LT-ST plane of the Wall 3 MET-1 sample, where the dominant features are solidification structures and a second phase located between dendrites. This resembles what one would observe in welding rather than wrought material, such as the microstructures in Fig. 3.3. These microstructures also resemble those found in other wire additive deposits, such as the WAAM deposits in Fig. 3.4 and the EBF³ deposits by Domack et al. [11].

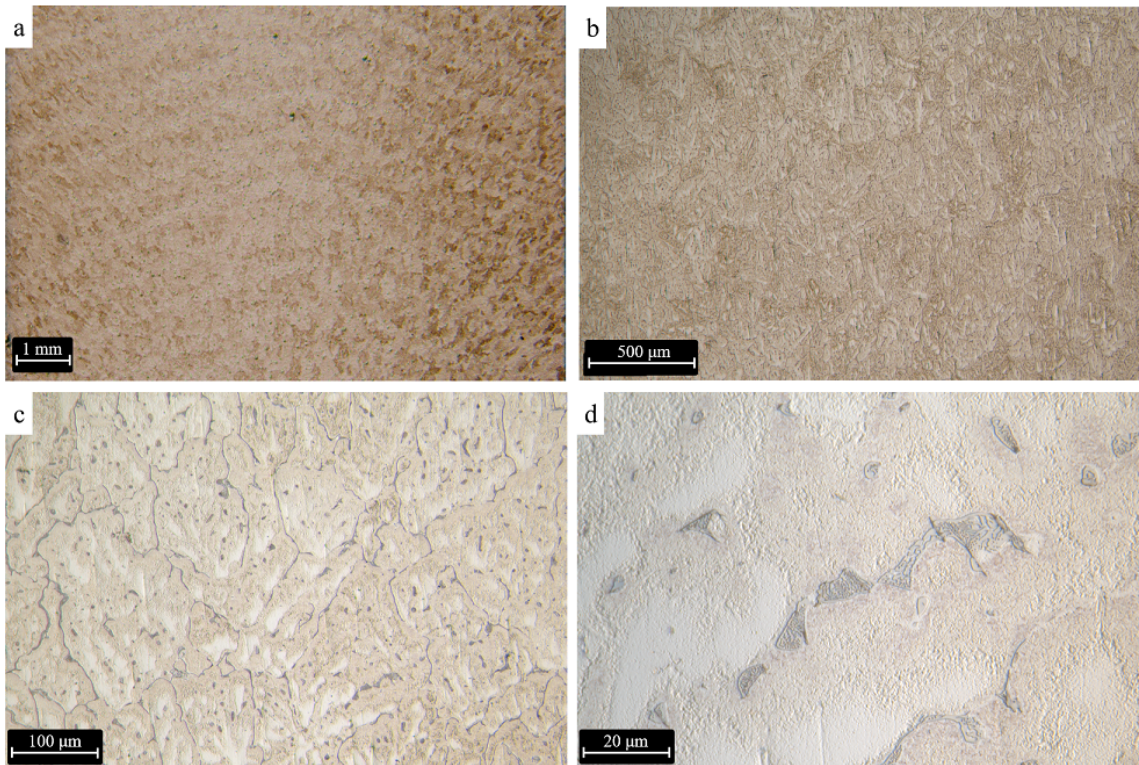


Figure 3.15: Typical LT-ST etched cross section for 2219 AD wall builds. The macroscopic view in (a) shows the layers, while (b) and (c) depict the varying etch response with dendrite coring, and (d) displays the eutectic particles in the microstructure.

It can be seen that grains were slightly elongated in the ST direction, suggestive

of the thermal gradient in a wall deposit. Surprisingly, no significant grain refinement was observed at interlayer boundaries, which was noted in other EBF³ studies [11]. There was also a variation in etch response across the dendritic features, with the dendrite cores appearing brighter and the dendrite edges showing more shading leading up to the interdendritic boundary precipitates. These precipitates appear to occur in two forms - dark, spindle-like needles and lighter, eutectic structures - and were investigated with EDS to determine their relative compositions. Figure 3.16 shows a similar microstructure in the BSE of the SEM, which highlights compositional contrast.

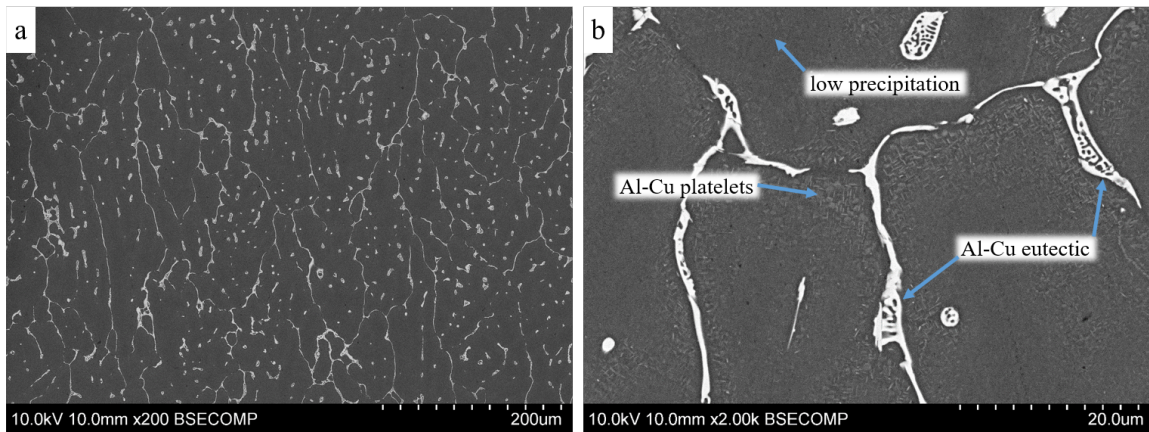


Figure 3.16: (a) Backscatter image of the 2219 AD microstructure, and (b) grain boundaries showing increasing precipitation from core to edges, with Al-Cu eutectic on grain and interdendritic boundaries.

One can note the same eutectic structure at dendritic boundaries, with rounded, fine platelets immediately surrounding them. These correlate closely with the dendritic boundary precipitates and perhaps the regions of darker etching on the dendrite ends in Fig. 3.15. Some of the boundary precipitates in the SEM image appear more spindle-like in nature.

From the linescan in Fig. 3.17, one can see that the eutectic-like precipitate takes on the Al-Cu eutectic composition of approximately 33 wt.% Cu, and a nearby spindle-like precipitate with a composition of Al-22Cu-3Fe. The composition of the darker regions in the dendrite, associated more with dendrite cores, have a net composition around 2 to 3 wt.% Cu. This shows Cu depletion in the cores, while the platelet regions exhibit gradually increasing Cu content leading up to the interdendritic precipitates. These observations are consistent with solidification theory, since solidifying alloys push some solute into the liquid ahead of the solidification front based on the partition ratio, k , until dendrites impinge on each other [88]. In the final stages of

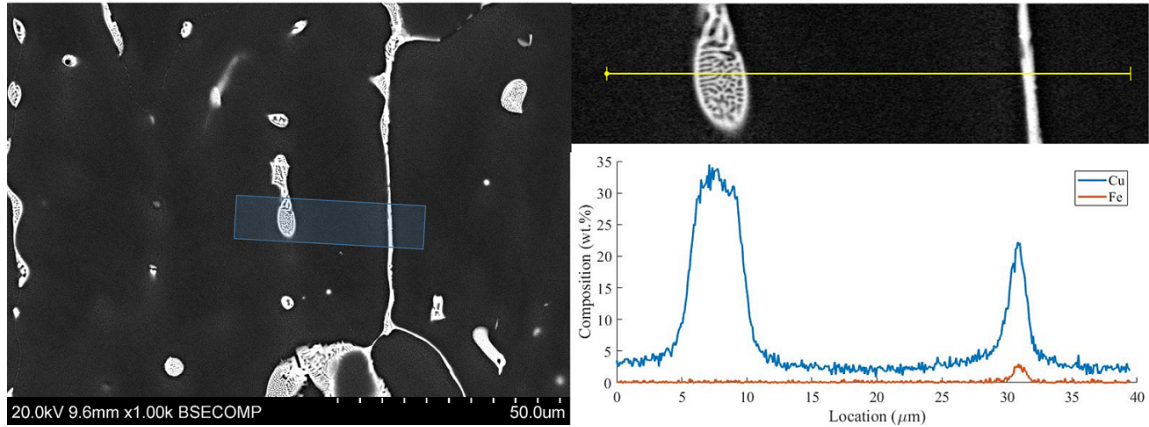


Figure 3.17: Backscatter images and associated linescan sampling regions between interdendritic boundaries showing Cu and Fe concentration in the matrix and the second phase particles. The balance is Al and is not shown for scaling purposes.

solidification, the typical boundary phase composition is the matrix-solute eutectic, which was observed in the AD microstructure.

Heat Treated Wall Microstructure

A microstructure representative of the HT MET 2 sample from Wall 2 is shown in Fig. 3.18. Compared to the AD macrograph in Fig. 3.15(a), the HT macrograph in Fig. 3.18(a) shows no indication of layer boundaries. The microstructure in (b) and (c) reveals grains of similar size to those of the AD material, but with a transformed appearance. In place of the graded etch response across dendritic features in the AD sample, the grains in the HT material show more consistent shading from center to perimeter. There is some linear banding in etch response across entire grains, the cause of which is unclear. At the high magnification in Fig. 3.18(d), it is observed that the grain boundary eutectic particles from the AD sample have been replaced by a smaller quantity of a globular, Cu-containing phase on the grain boundaries. The dark, spindle-like Fe-containing particles also remain in the HT microstructure, as noted by the orange arrows in Fig. 3.18(d).

Figure 3.19 shows an EDS linescan from a HT wall that depicts how the grain centers exhibit the 2219 bulk composition near 6% Cu, and the globular particles show a 50 wt.% Cu content, suggestive of the θ phase. The spindle-like phases are Fe-bearing, with a similar composition as seen in the AD material linescan in Fig. 3.17. Trace Mn content shows up in the spindle-like particle, despite not appearing in the AD scan of a very similar particle. Some large Cu particles were expected

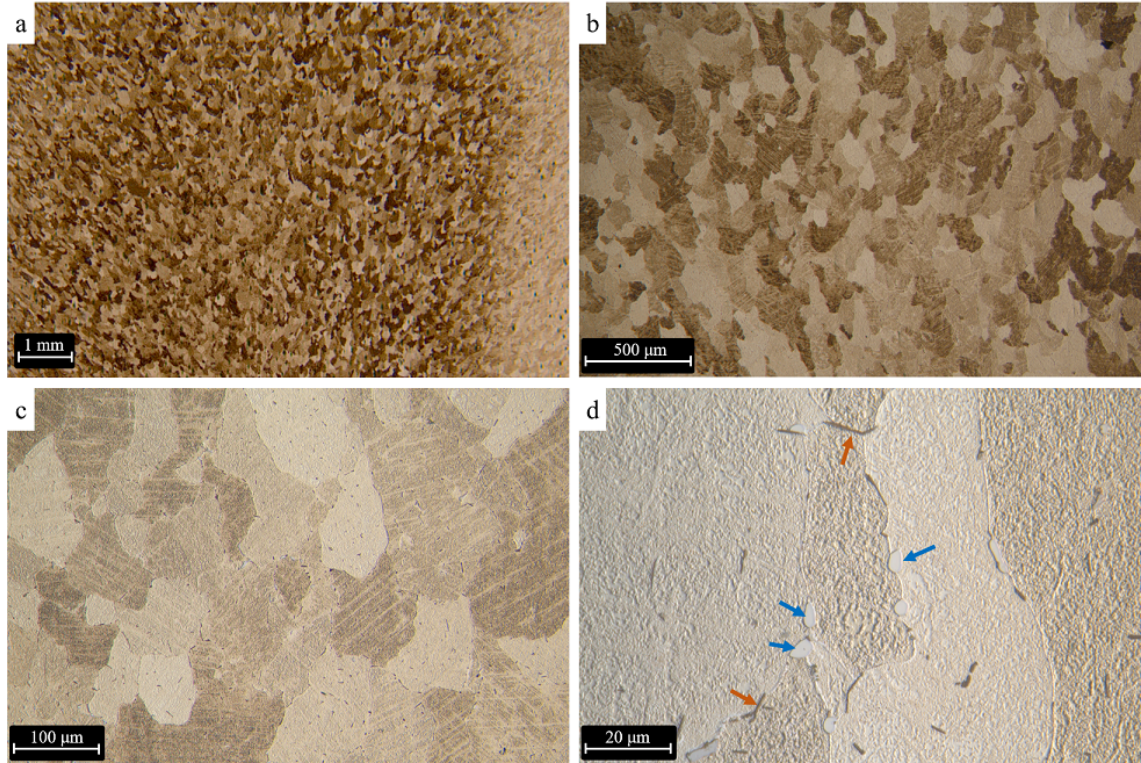


Figure 3.18: (a) Typical etched LT-ST cross section for 2219 HT wall builds with indiscernible layers, and (d) higher resolution image showing orange arrows highlighting Fe-containing phases and blue arrows pointing to the globular Cu-rich phase on grain boundaries.

to remain in the microstructure, since the 6.3 wt.% Cu content of 2219 exceeds the 5.7 wt.% solubility limit shown in the Al-Cu phase diagram (Fig. 3.1), so not all of the Cu may be taken into solution prior to aging. Rather, it appears that some of the Cu remains on the grain boundaries and transforms to the equilibrium θ phase, while the literature suggests that the rest distributes nicely into the bulk of the grains as fine θ' precipitates during aging [67]. Furthermore, the spindle-like Fe intermetallics remain in the same form as in the AD material since they have a high melting point and are stable at the solutionizing temperature for 2219. Thus, the Fe-bearing particles will not be dissolved or spheroidized like the Al-Cu phases.

Brick Microstructure

The HT brick microstructure, shown in Fig. 3.20(a), proved to be more heterogeneous than that of the walls, with the column of melt pools on the left representing a fence and the one to the right representing a fill. It may be noted that fences have melt pools that are concave-down, representing material flow as the melt pool slumps

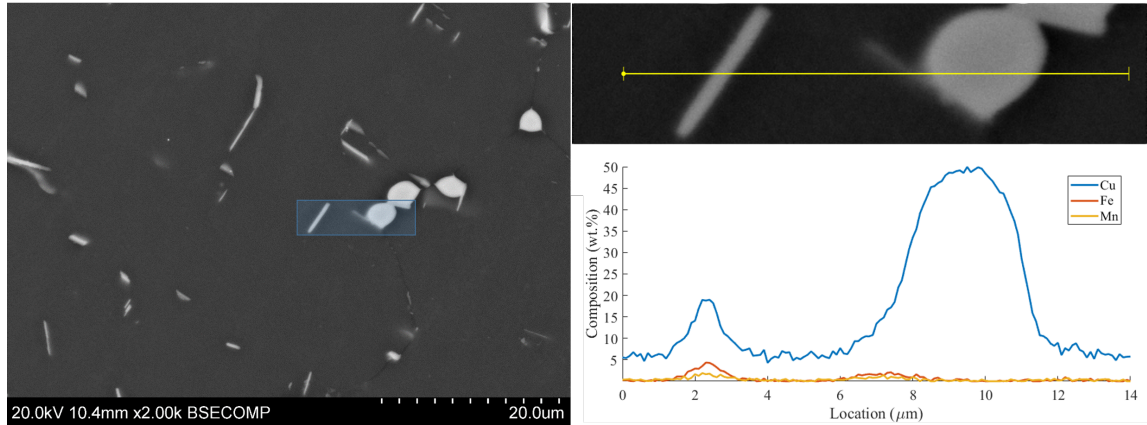


Figure 3.19: Backscatter image of the HT wall microstructure and associated linescan sampling precipitates showing Cu, Fe, and Mn concentrations. The rounded particle has the θ phase composition while the spindle-like particle contains Cu, Fe, and Mn.

over the dome of the previous layer. In contrast, fills have concave-up melt pools due to surface tension effects that cause them to wick onto the surrounding fences.

The fences in Fig. 3.20(b) possess a similar microstructure to the walls, with a consistent grain size throughout the height and little evidence of layer boundaries in the HT condition. The fills in Fig. 3.20(d), however, exhibit finer grains at the interlayer boundaries and coarser grains in the layer centers. This variation in grain size of the fills may be attributed to a faster cooling rate compared to the walls, since each fill is deposited with surrounding fences that are at a lower temperature, allowing more grains to nucleate and thus creating finer grains at interlayer boundaries and the overlaps of the fences and fills. One can note some columnar grain growth in the overlap region of Fig. 3.20(c), since this area was remelted during fill solidification and grains on the boundary grew epitaxially along the thermal gradient towards the fill.

An anomaly was found in some regions of the HT brick microstructure, where large grains grew and overtook certain fill regions during HT. Figure 3.21 displays this phenomenon, located in all of the fills in the MET 2 sample of the brick. Figures 3.21(b) and (c) show two features of note. Region (b) shows a considerable disparity in grain size, with grains smaller than in the typical fill microstructure shown in Fig. 3.20. Other anomalous features included regions of high concentrations of Cu-containing particles, shown in Fig. 3.21(c).

One can also note that the typical brick microstructural behavior resumes in the layers near the top of Fig. 3.21(a), suggesting that some aspect of the AD brick mi-

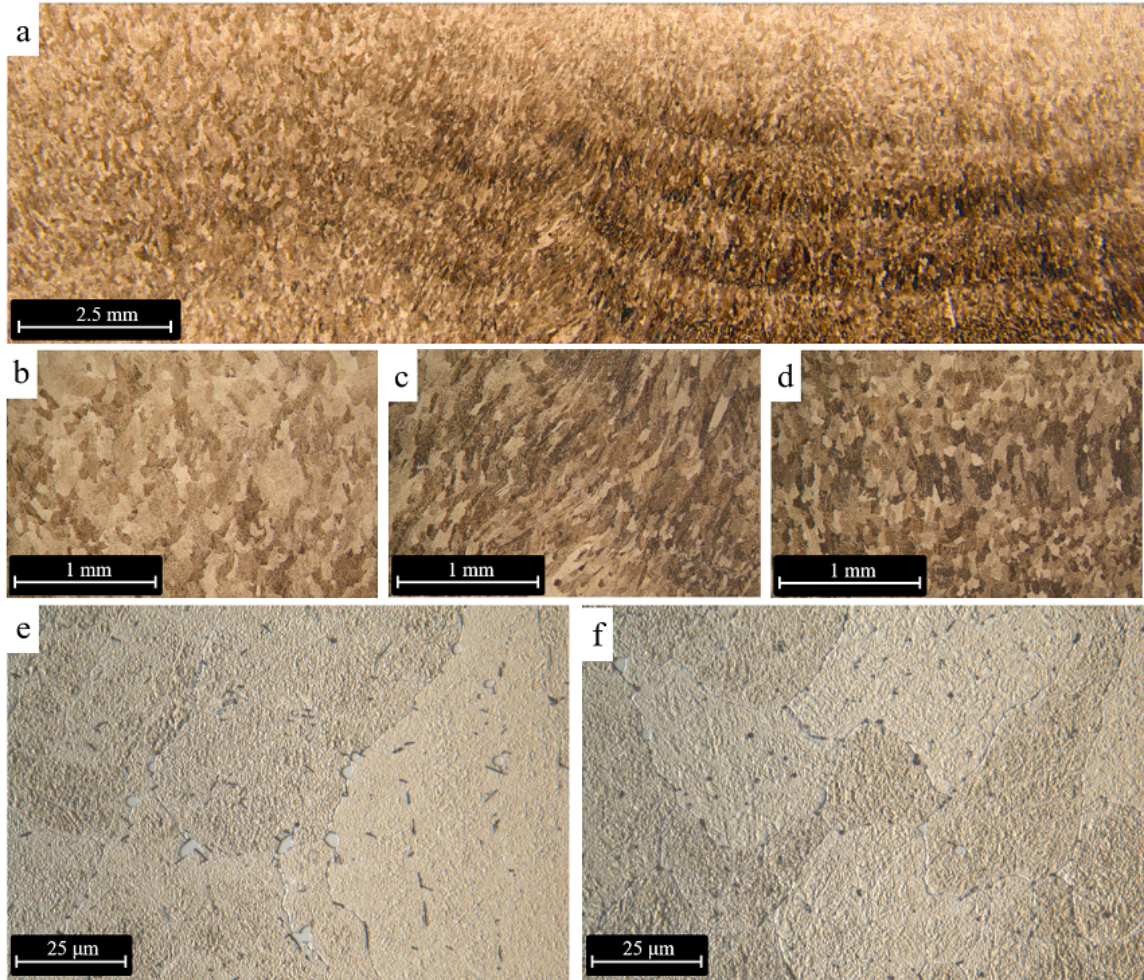


Figure 3.20: HT brick microstructure in the LT-ST plane depicting (a) an overall view of a fence and fill, with subfigures showing 50x images of grain structures for (b) a fence, (c) an overlap, and (d) a fill, and 1000x images showing (e) fence precipitates and (f) fill precipitates.

microstructure predisposed the material to grain growth and second phase precipitation during heat treatment, while some areas higher in the build were not affected. While this phenomenon is not yet fully understood, its effects were realized in two tensile specimens in the mechanical property evaluation in Section 3.4.5.

Grain Size Analysis and EBSD

Grain size measurements - summarized in Table 3.5 - show a similar grain size for the AD and HT walls and the fences in the HT brick. This is likely due to the similar paths for heat flow and thus cooling rates in the two scenarios, since the thermal gradient is vertical. The fills show a reduced grain size, likely due to an increase in

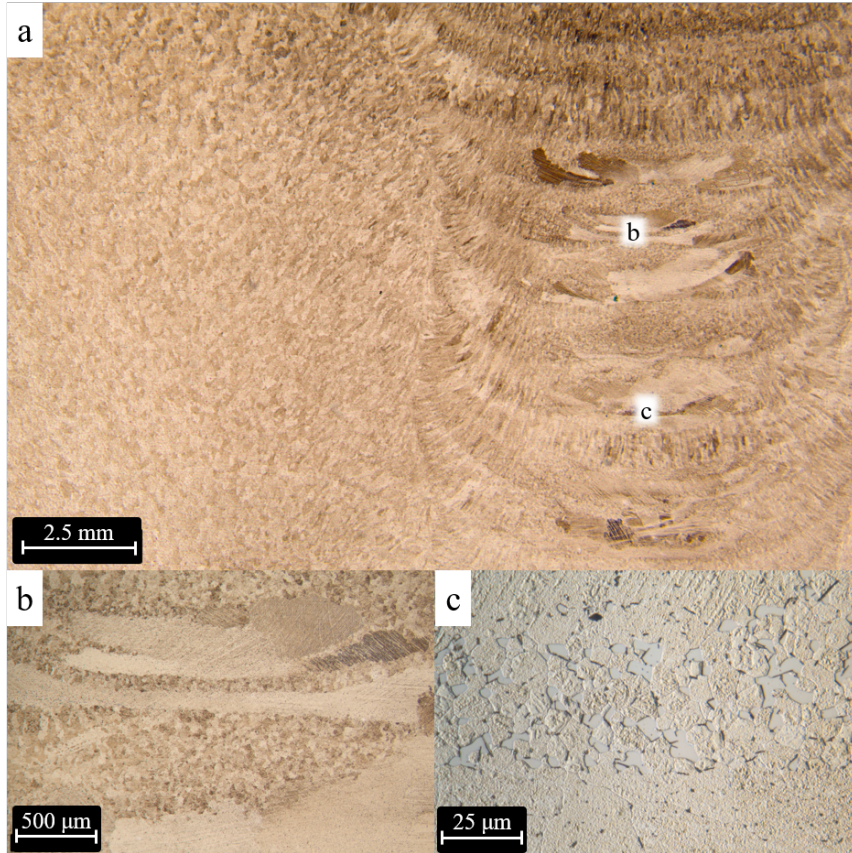


Figure 3.21: Anomalous grain grown occurring in the fills of the HT brick MET-2 sample, with regions highlighting (a) large grain growth and (b) an interconnected, Cu-containing second phase.

the cooling rate for the fills, since heat could also be absorbed by the fences that surround them.

Table 3.5: Average grain size measurements for the 2219 AD and HT walls and the HT brick fences and fills.

Sample	Area-Averaged Grain Diameter (μm)	Vertical Intercept Length (μm)	Horizontal Intercept Length (μm)
AD wall	132.7	63.7	59.4
HT wall	128.2	66.6	53.7
HT brick fence	103.6	50.1	41.8
HT brick fill	69.6	35.0	29.4

Figure 3.22 shows the (a) AD and (b) HT wall microstructures with EBSD. The grain structures look very similar, with grains slightly elongated in the vertical (ST)

direction and a nearly random crystallographic orientation distribution (maximum multiple of uniform density (MUD) values of 1.8 and 1.9, respectively).

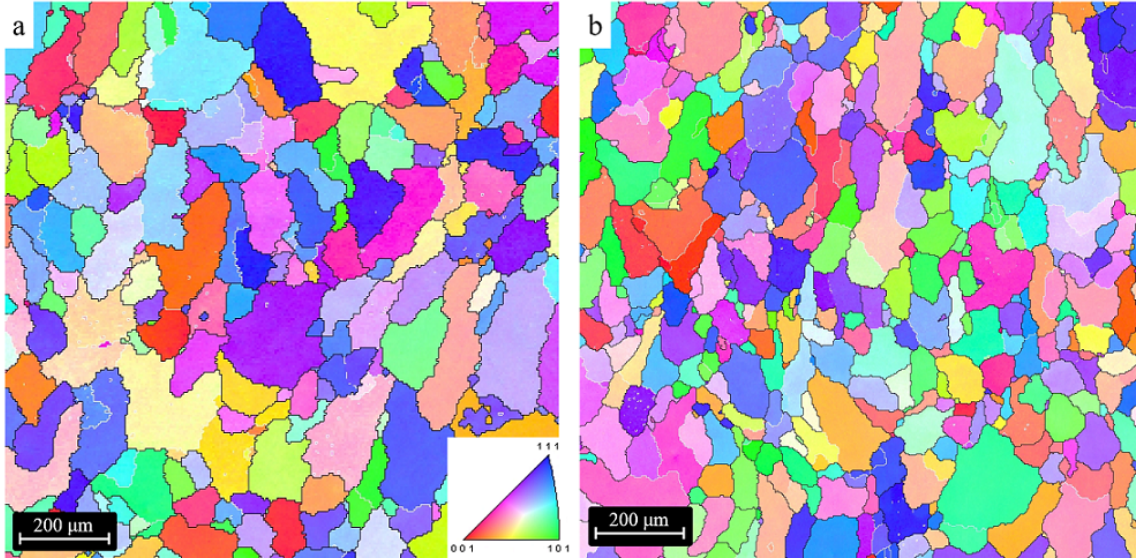


Figure 3.22: EBSD normal direction IPF maps from (a) AD and (b) HT wall LT-ST microstructures.

The near-random texture of the microstructure with EBSD and the nearly identical grain sizes before and after HT confirm that recrystallization during HT did not take place. This makes sense, given that the material underwent no deformation or other processes prior to heat treatment that would warrant recovery and recrystallization to occur.

3.4.3 X-ray Diffraction

The XRD spectra for the AD and HT metallurgical samples are shown in Fig. 3.23. Both samples appear to share similar spectra, with the most prominent peaks corresponding to the Al matrix. Other peaks are associated with the θ phase, which should be present in both samples as it is the equilibrium phase for Cu precipitates in Al alloys. The unmarked peaks are suspected to be associated with the Al-Cu-Fe particles seen in the microstructure, but no significant match for their spectra was found in the available databases. Given the complexity of the EBF³ microstructure and its deviation from an ideal material for XRD analysis (i.e. equiaxed and recrystallized), this is understandable.

The overall intensity of the HT sample's spectra was less than half that of the AD sample, which made some of the minor peaks look less pronounced than in the AD

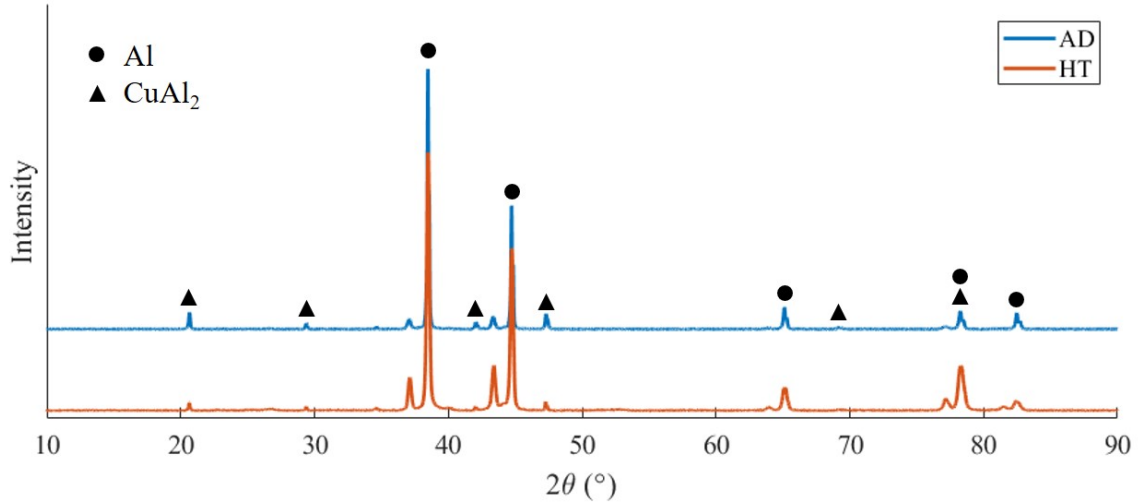


Figure 3.23: XRD results for the as-deposited and heat treated wall metallurgical specimens.

data. To aid in comparison of the presence of smaller peaks, the HT data is scaled in Fig. 3.23 so the 100% peaks are of equal height.

3.4.4 Hardness

The AD 2219 exhibited an average microhardness of 81 ± 2.5 HV_{0.3} from the indents shown in Fig. 3.24. Despite sampling over regions that showed various etch responses corresponding to interlayer boundaries, which were thought to possibly indicate a variation in hardness, no correlation of microhardness with microstructure was found. This invariance may be due to the relatively homogeneous grain size distribution across interlayer boundaries in the walls or the even distribution of precipitates across layers.



Figure 3.24: HV_{0.3} of AD material sampling across deposit layers.

The average microhardness for the HT samples was $136 \pm 1.6 \text{ HV}_{0.3}$, showing even less variation across the sample in Fig. 3.25 than the AD condition. This may be attributed to the more homogeneous microstructure of the HT samples, with Cu mostly dispersed in small θ precipitates rather than in copious eutectics on interdendritic boundaries.

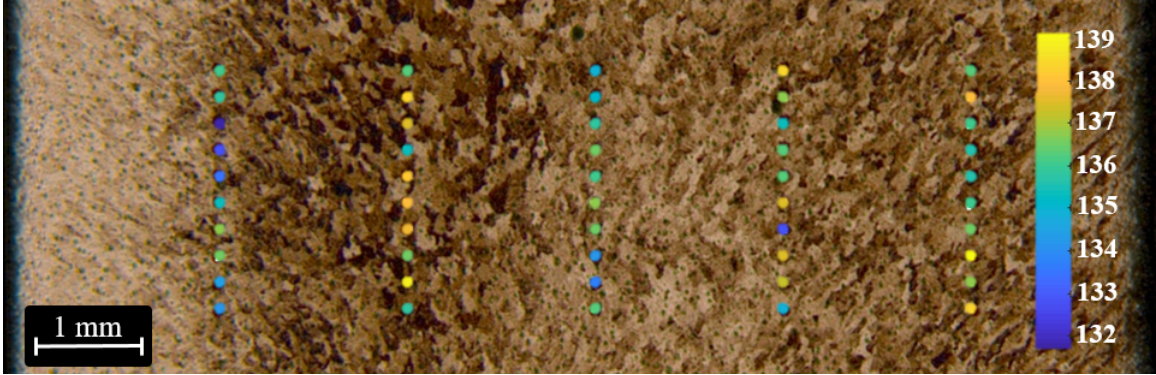


Figure 3.25: $\text{HV}_{0.3}$ of HT material sampling across layers.

The AD hardness values were slightly below those in the literature for single-pass EB welds, measured at 91 HV_5 , and slightly higher than GTA welds with microhardness near 72 HV_5 [89]. The study of WAAM-deposited 2219 reported an AD hardness of $68 \text{ HV}_{0.2}$ [23], or 16% lower than the present EBF³ deposits. The hardness in the present deposits was likely lower than the literature EBW values due to larger grain sizes and the thermal cycling that occurs during EBF³, while greater than that in GTAW and WAAM due to more efficient power usage with an EB source.

The HT material exhibited a hardness that was 13% greater compared to that of wrought 2219-T62 (converted from the Brinell hardness measured with a 500 kg force and a 10 mm ball indenter) [73]. The hardness of 2219-T6 WAAM deposits was reported as $149 \text{ HV}_{0.2}$, which is 10% higher than the present deposits.

Figure 3.26 shows optical views of indents from (a) AD material and (b) HT material. One will notice that the edges of the diamond-shaped indent have some curve to them, especially in the AD sample. It is thought that this variation is due in part to the inhomogeneity of the EBF³ solidification structure.

3.4.5 Tensile Properties and Fracture Surfaces

The results from tensile testing of the AD specimens are reported in Fig. 3.27. The L, LT, and ST results reveal that the material exhibited some anisotropy in strength, with the LT-oriented specimens showing a 25% higher YS and a 10% higher UTS

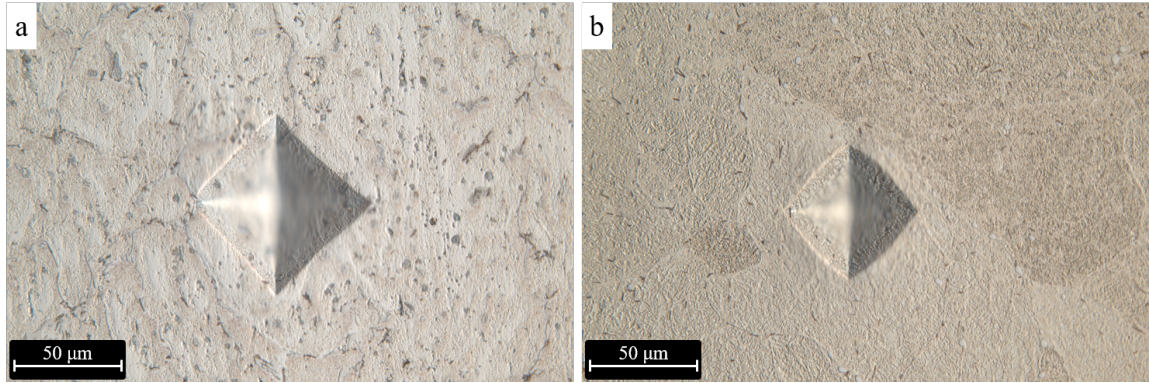


Figure 3.26: HV_{0.3} indents of (a) AD material and (b) HT material. Both indents, particularly for the AD material, exhibit some warping of the indent shape.

than the ST-oriented specimens. The LT specimens were extracted from the brick deposit, so the increase in strength may come from the composite microstructure of fences and fills. The AD strengths for all orientations fell between the typical values for O and T4 tempered material [90]. This makes sense, since the complex thermal history of EBF³ deposits resembles a mix of annealing and natural aging. The typical elongations reported in the Aluminum Standards and Data [90] are for 2 in. gauge lengths, so the obtained elongation values from this study are not directly comparable.

For each specimen orientation, there is little variation in strength, as noted by range bars in Fig. 3.27, except for the YS of the L-oriented specimens. It was found that the samples tested at NASA (L-1 specimens in the Appendix A cut plans) had an average YS of 15.4 ± 0.2 ksi, while the specimens tested offsite (labeled L-2 in Appendix A) possessed an average YS of 18.1 ± 0.5 ksi. This significant difference is likely due to the differing positions of the samples in the deposits, since the NASA samples came from higher in the deposits and thus did not experience the same in-situ aging effects from thermal cycling than did the offsite specimens located 20+ layers lower in the deposits. These differences in YS were reflected inversely in the ductility, where the NASA-tested specimens resulted in an average % el. of $16.4\% \pm 0.3\%$ while the offsite specimens averaged 14% total elongation.

The large error bars for the ST-oriented elongations are attributed to two of the three NASA specimens failing near or outside the knife region of the extensometers.

The fracture surfaces were examined in the SEM, and typical regions for each of the three specimen orientations are shown in Fig. 3.28. All specimens showed mixed features on the fracture surface, with some lamellar-like features of the Al-Cu eutectic composition and dimples containing neatly fractured Al-Cu eutectic particles in their centers. Among the various specimen orientations, the L-oriented specimens appeared

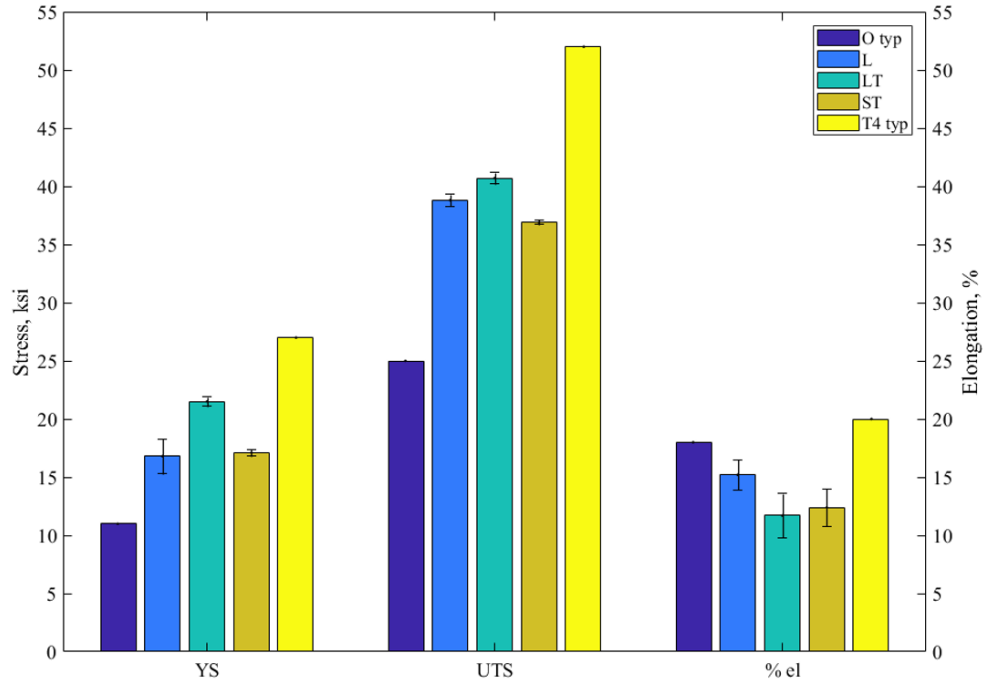


Figure 3.27: AD tensile properties for each sample orientation compared with typical O and T4 temper YS and UTS values and the typical 2 in. gauge length % el. value.

to show the largest conglomerations of ragged lamellar features, while the ST- and LT-oriented specimens showed more dimpled character. The LT specimens appeared to have an overall flatter fracture surface topography, with dimples slightly smaller than the other two orientations. This may be related to the multi-bead construction of the brick, since fracture might preferentially occur on the overlaps of fences and fills; however, further research is needed.

The tensile results for the HT material are shown in Fig. 3.29, along with typical values for wrought 2219-T62 [90]. In contrast to the AD case, where the material performed anisotropically, the average YS and UTS for the various specimen orientations in the HT condition are much tighter in spread. The YS between the three orientations differs by no more than 3%, while the UTS differs by no more than 5% (or by less than 2% if the LT-12 and LT-13 samples from the anomalous microstructural region of the brick are excluded). This near-isotropy in strength is due to the homogenization of the microstructure during HT, since the majority of the Al-Cu eutectic in the AD microstructure was dissolved and redistributed as strengthening precipitates in the matrix. Additionally, no significant discrepancies arose between the NASA and offsite-tested samples, despite their differing heights in the builds, similarly due to the homogenization of the microstructure with HT.

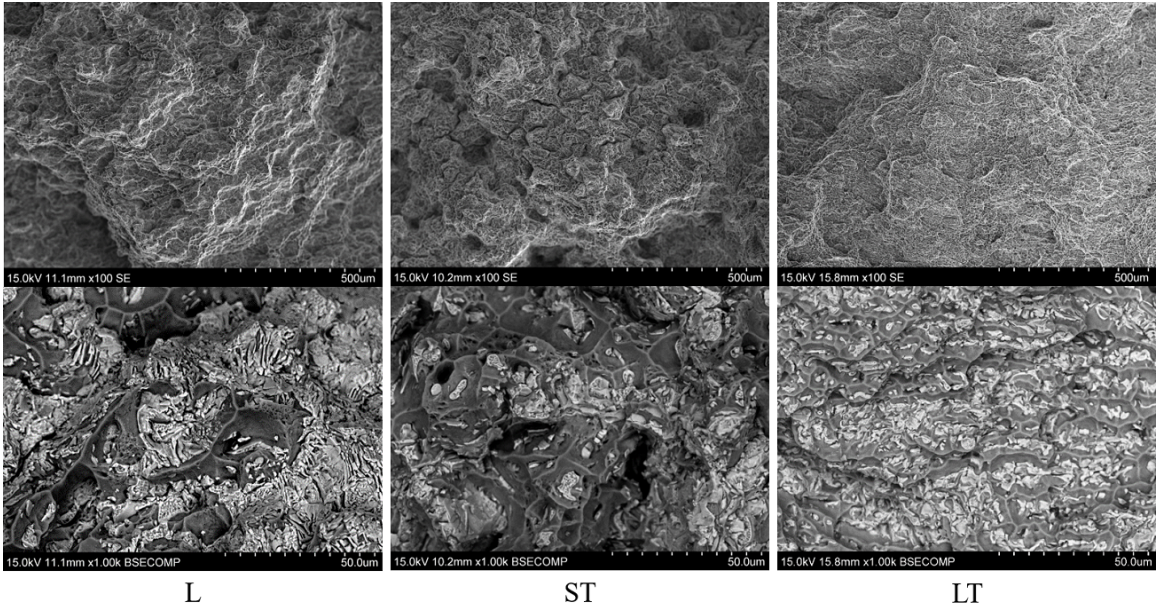


Figure 3.28: Typical AD tensile sample fracture surfaces in the three specimen orientations. 100x topological views are shown in the top row, and 1000x BSE compositional images are shown in the bottom row.

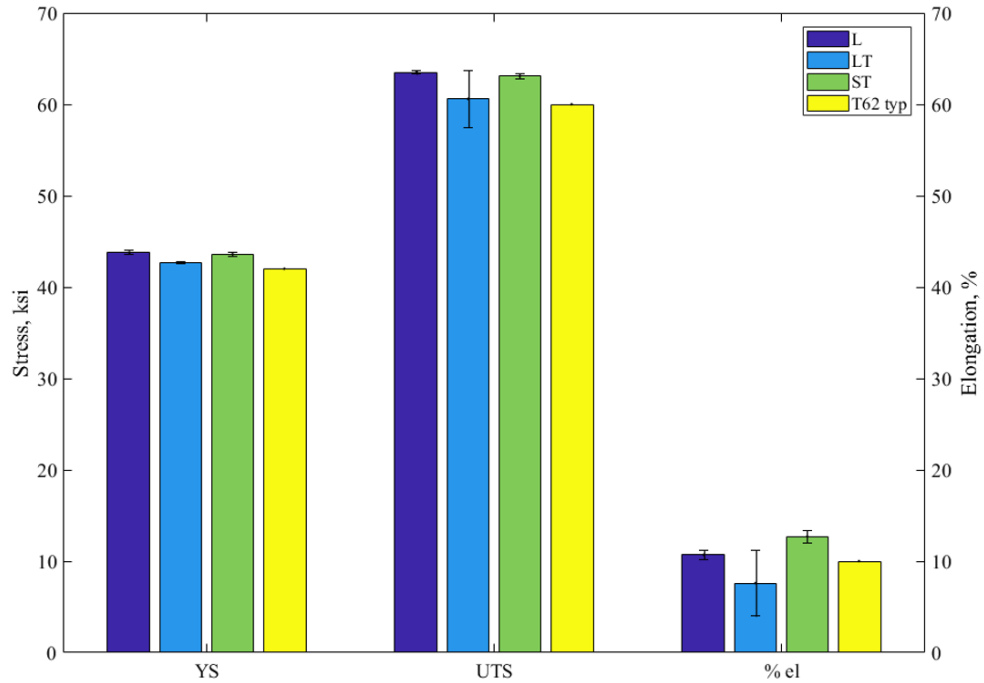


Figure 3.29: HT tensile properties for each deposit direction compared with typical T62 values for a 2 in. gauge length.

Typical fracture surfaces from the HT specimens in the three specimen orientations are shown in Fig. 3.30. These fracture surfaces look more similar between orientations than did those of the AD samples, although the LT-oriented specimens still appear to have the flattest topology. All observed fracture surfaces appear to exhibit two dimple sizes. The larger dimples contain globular Cu-bearing particles and some linearly-shaped constituents, while the smaller dimples contain either fine particles or none at all.

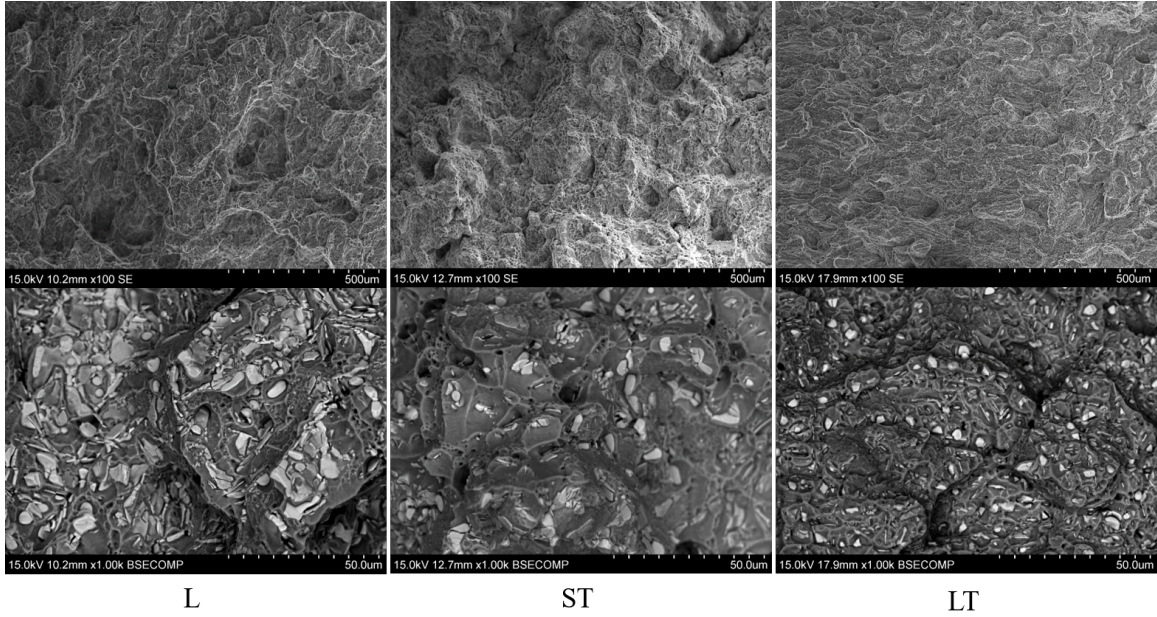


Figure 3.30: Typical HT sample fracture surfaces for the three specimen orientations, with 100x SE images showing fracture surface topology and 1000x BSE images below showcasing precipitate distributions and dimples.

The large error bars for the LT-oriented specimens' UTS and % el. results may be attributed to the outlying specimens LT-12 and LT-13 (see Appendix A cut plan for their locations within the brick). These samples failed prematurely at an UTS of 55.2 ksi and 58.4 ksi, respectively, and at elongations of 2.9% and 4%, respectively. Meanwhile, all other specimens failed between 61.6 to 63.0 ksi and 8 to 12% el. The premature failure of LT-12 and LT-13 coincides with the earlier microstructural finding that showed grain growth and an interconnected second phase in the brick deposit fills (Fig. 3.21).

Figure 3.31(a) shows the macroscopic fracture surface of the LT-13 sample, where a band of anomalous features runs across the diameter. A similar band of features was also seen in the LT-12, although with less definition. The outer surface of the

sample was polished and etched, and it was determined that the “up” direction in the image corresponds to the ST direction of the build.

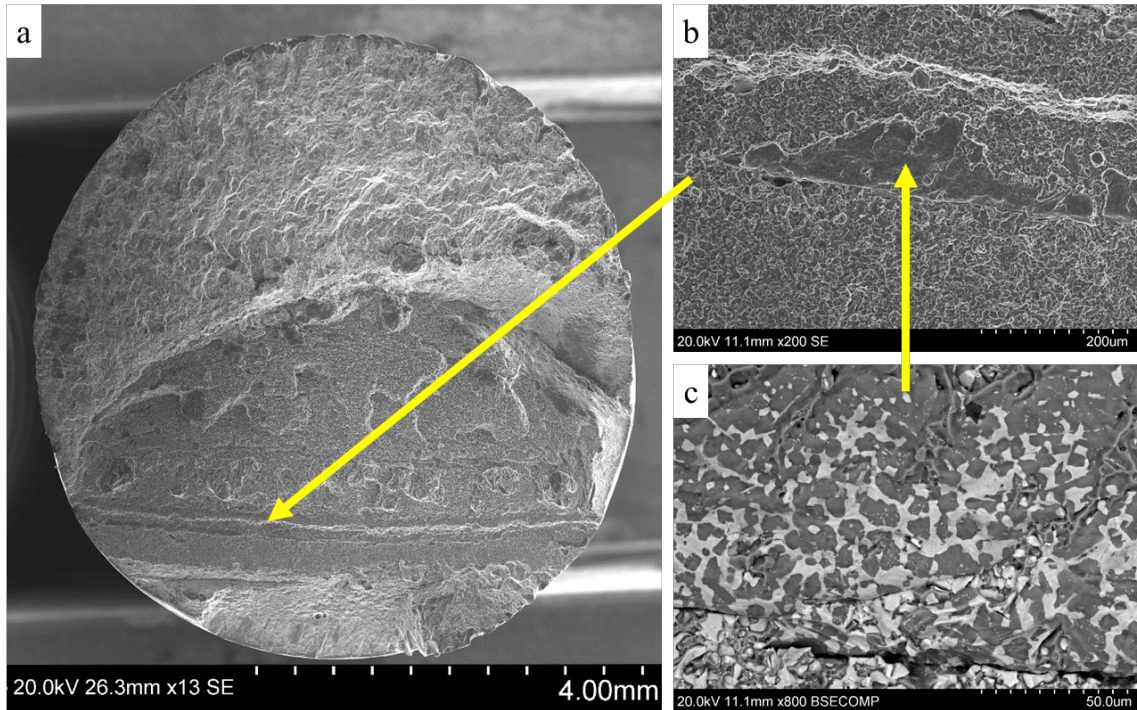


Figure 3.31: Atypical features on the fracture surface of the HT, low-elongation LT-13 specimen, including (a) a macrograph showing banding of atypical features that include: (b) an intercepted large grain and (c) an interconnected θ phase.

Figures 3.31(b) and (c) show higher-magnification images of this anomalous band, where large, smooth regions accompany an interconnected second phase. The large, smooth regions are thought to be associated with the large grains found in the polished microstructure in Fig. 3.21(b), while the interconnected phase exhibited the θ composition and closely mirrors that seen in Fig. 3.21(c).

3.5 Discussion

The following sections discuss the results for the 2219 EBF³ deposits in both the AD and HT conditions. The compatibility of 2219 with EBF³ processing and its potential for meeting the 7050 property targets are also addressed.

3.5.1 As-Deposited Microstructure and Properties

AD Microstructural Discussion

As seen in Section 3.4.2, the 2219 AD microstructure resembles that of a weld or casting due to its compositional coring and eutectic decoration of the grain boundaries. Furthermore, in comparing the AD microstructure to those found in the literature, the EBF³-deposited material resembles a GTA weld (Fig. 3.3(a)) or a WAAM deposit (Fig. 3.4) more than typical EB welds (Fig. 3.3(b)). This is due in part to the higher concentration of Al-Cu eutectic continuously decorating the grain boundaries, as well as to larger, vertically-elongated grains. In contrast, EB keyholed welds (Fig. 3.3(b)) typically are characterized by fine, equiaxed grains and a thin FZ and HAZ. As evidenced by the domed melt pool boundaries in Fig. 3.15(a), the EB did not enter keyholing mode for the 2219 EBF³ deposits. This produced a lower power density that broadened the molten pool and reduced the solidification rate, resulting in deposit microstructures that better resemble those of GTAW welds and additive deposits.

The copious amounts of Al-Cu eutectic on the grain boundaries may be understood from examining the partition coefficient, k [13]. This coefficient determines the degree of segregation of the solidifying metal compared to the liquid composition, and rejects solute (in this case, Cu) ahead of the solid-liquid interface. In the terminal stages of solidification, the final liquid must incorporate the high solute content, resulting in the formation of Al-Cu eutectic at interdendritic spaces and grain boundaries. Thus, the AD structure was expected to possess high amounts of eutectic and a compositional gradient from the grain centers to edges.

In addition to the Al-Cu eutectic, disc-shaped precipitates of approximately 625 nm in diameter were observed in the matrix near grain boundaries in the AD material (Fig. 3.16). While the composition of individual platelets could not be directly measured due to their small size, EDS area scans showed a composition of 4 to 5 wt.% Cu. This suggests that large Al₂Cu particles were precipitated out in areas that would have already contained higher solute than the dendrite cores, which exhibited a composition of 2 wt.% Cu. Fixter et al. found similar plate-like precipitates 740 nm in diameter bordering grain boundaries in 2219 WAAM deposits [91]. The authors labeled the particles as the θ' phase and attributed their appearance to solutionization and precipitation during subsequent layers.

The Fe-bearing particles found throughout the AD microstructure are a consequence of Fe impurities in AAs [67]. The composition measured with EDS was approx-

imately Al-22Cu-3Fe, which does not match the expected composition of Al₇Cu₂Fe [67]. This may be due to sampling volume limits of the EDS/SEM system. Additionally, no Fe-bearing compounds from the available databases appeared to match the unidentified peaks in the XRD data. This may be attributed to the low concentration of Al-Cu-Fe particles in the matrix, making associated peaks part of the noise, or to insufficient references in the available XRD databases. Therefore, the Al-Cu-Fe particles are acknowledged in the microstructure but are not presently identified.

AD Tensile Properties and Discussion

The AD tensile properties (Fig. 3.27) confirmed the results from prior 2219 EBF³ studies, which showed that the AD YS and UTS falls between typical values for O and T4 tempers [11, 9]. While Domack et al. [11] reported less than 2% variations in strength in the L and ST directions, the present work showed variations of 2% and 5% for the YS and UTS, respectively. Low-ductility, lamellar features similar to those seen by Domack et al. [11] appeared on the fracture surfaces of the AD samples (Fig. 3.28). These features are comprised of the Al-Cu eutectic composition and are contained within dimples on the order of the material's grain size.

The results from the L and ST orientations also compare with the WAAM results of Bai et al. [80], which tested specimens in the L and ST orientations from a 100-layer wall deposit. Their average YS and UTS results over both orientations in the AD condition are 15.4 ± 1.8 ksi and 34.1 ± 3.3 ksi, respectively. Averaging the present study's results over the L and ST orientations reveals YS and UTS values of 16.9 ± 1.1 ksi and 37.8 ± 1.1 ksi, respectively. Thus, the present results are quite comparable to those of a similarly-constructed WAAM wall.

This work is the first to document the LT properties of 2219 brick-shaped deposits. The AD YS and UTS in the LT orientation surpassed those of the L specimens by 28% and 5%, respectively. This increase in strength for the LT orientation may be attributed to the composite microstructure of the fences and fills. The grain size results from the HT MET-2 sample and reported in Section 3.4.2 reveal that the grain size in the fills is more refined than that of the fences. This may lead to some grain size strengthening. Furthermore, smaller grains in the fills lead to lower concentrations of Al-Cu eutectic on grain boundaries, reducing the number of potential crack initiation sites in the fills. Interestingly, all AD LT specimens failed at a similar location along the length of the tensile sample. Upon polishing and etching of the outer surface of a tensile bar, it was found that fracture occurred inside a fence.

3.5.2 Heat Treated Microstructure and Properties

HT Microstructural Discussion

The T62 HT material was significantly more homogeneous than the AD material, in both its microstructure and mechanical properties. As seen in Section 3.4.2, the 2219 HT microstructure is comprised of grains with an area-averaged diameter of roughly 130 μm . This microstructure compares better with HT WAAM deposits and T62 wrought material [80] than with as-cast structures and the AD microstructures. This is due to the homogenization of the grain structure with heat treatment and the dissolution and dispersion of Cu from grain boundary eutectics into strengthening precipitates in the matrix.

In place of the grain boundary eutectics observed in the AD material, the HT microstructure exhibits a reduced amount of grain boundary precipitates, taking the form of globular θ particles and spindle-like Al-Cu-Fe particles. It is more difficult to discern grain boundaries in the as-polished condition in the SEM (Fig. 3.19), while in the AD condition the grain boundary eutectics bordered the grains almost continuously. This reduction in grain boundary precipitation is due to the dissolution of the majority of Al-Cu phases during the solutionizing step of HT. The 4 hr solution treatment was sufficiently long and at a high enough temperature to allow interdiffusion and dissolution to occur between the θ particles and the matrix, up to the composition limit of 5.7 wt.% Cu in solution. The extraneous 0.6% Cu and any undissolved θ from the eutectics remained on the interdendritic and grain boundaries and was spheroidized. This spheroidization reduces the surface area of the incoherent θ phase and is beneficial for mechanical properties since high aspect ratio Al-Cu eutectics would be more prone to nucleate cracks during plastic deformation.

The majority of the Al-Cu grain boundary eutectic was redistributed in the Al matrix during solutionizing and precipitated out in fine θ' strengthening precipitates during aging. While this was not directly observed with the available microscopes, the presence of a robust population of strengthening precipitates was evident in the HT tensile results matching typical wrought values. Additionally, the XRD data showed the continued presence of the θ phase despite the reduction in grain boundary θ , pointing towards another source of this signal. Transmission electron microscopy (TEM) would be required to observe these strengthening precipitates, since the literature shows that they are platelets on the order of 10 to 600 nm in diameter [67].

Spindle-like Al-Cu-Fe phases are still observed in the HT microstructure despite the multi-step T62 heat treatment practice. This is because such Fe intermetallics

are typically stable at temperatures well above the Al liquidus. Also incoherent, these particles do not spheroidize like the θ phase because they have lower surface energies for particular crystal planes that encourage needle-like geometries.

Following HT, the grains remain elongated in the ST direction and remain of a similar size and crystallographic texture to those in the AD microstructure. This suggests that recrystallization during HT did not take place. Despite an adequate time at temperature during solutionizing, the lack of recrystallization is understandable since no deformation took place during or following deposition. Thus, there was little need of recovery at high temperatures, which is typically the driving force for recrystallization [92].

The anomalous large grains and interconnected θ phase found in the HT brick fills is still under investigation. It is clear that some predisposition of the AD fill microstructures led to abnormal grain growth during the HT, but the source of this has not yet been observed.

HT Mechanical Properties Discussion

The 40% increase in microhardness in the HT condition may also be attributed to the homogenization of the microstructure and precipitation of strengthening phases during HT. Since no significant variation in hardness with position within the layers was seen with the AD samples, it was expected that the HT material would also exhibit little variation with build microstructure. Over the grid measured for the AD and HT samples, the HT material showed a variation of only 7 HV_{0.3} compared to the variation of 15 HV_{0.3} in the AD condition. This attests further to the increased homogenization of the microstructure with HT.

In contrast to the anisotropy of the AD material, particularly in the LT orientation, the HT material exhibited more isotropic strength values, with less than 2% variation among samples not containing the anomalous brick microstructure. This may be attributed to the microstructural homogenization of the deposits during HT, including in the composite microstructure of fences and fills in the brick. The tensile properties compare well with typical wrought T62 values, with the YS and UTS values for the HT material averaging 43.5 ± 0.5 ksi and 63.1 ± 0.6 ksi, respectively. These correspond to 3% and 5% increases over the typical T62 wrought values.

Despite the isotropy of strength in the HT material, the ductility of the deposits was not isotropic. The ST orientation exhibited the highest elongation of $12.7\% \pm 0.7\%$ for a 1 in. gauge length, while the L and LT orientations followed with

average elongations of $10.7\% \pm 0.5\%$ and $9.7\% \pm 2.0\%$. This anisotropy in elongation may be due to the varying presentation of grain boundaries in the microstructure. The ST direction is aligned with the slightly elongated axis of grains, while the L and LT directions are transverse to the smaller dimensions of grains. The fracture morphology appears ductile, with well-developed dimples on all samples except for those containing the interconnected second phase.

The L and ST values from this study fall within 5% of those obtained by Domack et al. in the HT condition [11]. The machine parameters from this study fell within the range of their three parameter sets in terms of energy per unit volume deposited, while the unit volume deposition rate for this study exceeded theirs by more than 300%. Thus, the variation in mechanical testing results may be considered consistent in light of the relatively few number of samples tested for both studies, in addition to the significant changes in deposition rate and other machine and environmental parameters.

In comparing the L and ST properties with T62 results from WAAM-deposited material of Bai et al., it is found that the present HT material exceeded the YS and UTS values of $38.4 \text{ ksi} \pm 3.3 \text{ ksi}$ and $56.6 \text{ ksi} \pm 4.0 \text{ ksi}$ by over 10% [80]. The WAAM deposits apparently exhibited more prevalent porosity on the fracture surfaces, which was attributed to a reduction of area that increased effective stress to reduce strength.

3.5.3 EBF³ Compatibility and Meeting the 7050 Property Target

2219 demonstrated excellent compatibility with the EBF³ process, particularly for linear geometries such as the wall deposits. The porosity levels were very low, with fewer than 30 detectable indications of pores at the 100 μm scan resolution in the available scan area. These and some smaller pores were also distributed throughout the microstructure irrespective of layer boundaries. This contrasts the results of WAAM deposits from Bai et al. [80], which exhibited high populations of 50 μm pores on interlayer boundaries. The porosity in the present 2219 deposits is attributed to residual hydrocarbons or dissolved hydrogen in the wire, since the vacuum environment of EBF³ precludes atmospheric contamination of the molten pool compared to ambient processes like WAAM.

The microstructures and resulting tensile properties also attest to the compatibility of 2219 with EBF³, with limited anisotropy of the columnar grains and dissolvable eutectic on the grain boundaries. Furthermore, the random crystallographic texture

developed by EBF³ deposition is encouraging from a properties standpoint since it reduces the anisotropy in strength and elongation. However, the profuse amount of Al-Cu eutectic completely bordering the grain boundaries warrants homogenization during heat treatment for improvement of strength and isotropy, since the Cu is mostly tied up in brittle grain boundary particles rather than matrix strengthening precipitates. Future investigations could examine beam parameters and background temperatures that reduce heat input to the deposit while still maintaining a fully dense deposit. This would reduce distances over which segregation will occur, as well as the size of the HAZ to improve AD properties. However, for a maximum response in strength, HT is still recommended.

One unresolved aspect of EBF³ compatibility is the large grain growth and interconnected θ phase that was observed in the brick deposit. Since this presents a more complex geometry utilizing adjacent beads, the thermal history of the deposit is also much more difficult to predict and control with the current fence and fill build sequence. It is expected that certain conditions within the brick's build sequence formed a microstructure that was predisposed to issues in HT. Unfortunately, no AD material from the brick was reserved for microstructural analysis, so repeated builds would be required to probe this issue further. However, this phenomenon occurred in another AA brick, so it is evident that the issue is not of compatibility of 2219 with EBF³ but rather with build-specific parameters and sequences that warrant further investigation.

Regarding the 7050-T7 property targets set forth in Section 1.2, EBF³-deposited 2219-T62 achieved 64% and 83% of the typical 7050-T7 YS and UTS values, respectively. It was not expected that 2219 would reach the 7050-T7 property target due to the strengthening limitations of the θ phase. To reduce the gap in properties between the two materials, other methods of strengthening would be necessary.

Equation 3.5.1 relates the different sources of strength for polycrystalline engineering materials:

$$\sigma_y = \sigma_m + \sigma_{gb} + \sigma_{wh} + \sigma_{ss} + \sigma_p, \quad (3.5.1)$$

where σ_m is the intrinsic strength of the Al matrix; σ_{gb} is grain boundary strengthening; σ_{wh} is strengthening from work hardening; σ_{ss} is solid solution strengthening; and σ_p is precipitation strengthening [93].

The Hall-Petch equation for grain boundary strengthening (σ_{gbs}) is given in Eq. 3.5.2:

$$\sigma_{gb} = ad^{-1/2}, \quad (3.5.2)$$

where a is a constant and d is the grain diameter [93]. This shows an inverse-squared relationship of grain diameter with strength, suggesting that a 50% reduction in grain diameter will result in 4x the strengthening contribution from grain boundaries. Since grain boundary strengthening is only one component of strengthening in precipitation-hardened alloys, this will unfortunately not have a significant enough effect on the mechanical properties to meet the 7075-T7 targets.

Tempers such as the T8 include an additional stretching step, which increases the dislocation density in the material between solutionizing and aging, creating additional heterogeneous nucleation sites for a better dispersed precipitate population. However, the complex geometry of anticipated additive parts would preclude the possibility of a post-deposition stretch, requiring some other method for inducing dislocations for strengthening. This could be achieved by means of inter-pass rolling during deposition and subsequent HT [23], or through post-build deformation techniques such as shot peening or Arconic's AmpliforgeTM process.

While these methods would certainly increase the strength of EBF³-deposited 2219 due to grain boundary and dislocation strengthening, it is unlikely that the resulting properties would reach the 7050-T7 property target. However, these routes would modestly increase the properties while also retaining the beneficial EBF³ compatibility.

3.6 Summary

The effects of EBF³ processing on the mechanical properties and microstructure of 2219 have been studied and compared with those of wrought alloys 2219-O, -T4, and -T62. From these deposition trials and analyses, the following observations are made:

1. The present study confirms prior NASA work demonstrating the EBF³ compatibility of 2219 over a wide range of build parameters. No cracks or vaporization losses affected the deposits.
2. Compared to WAAM deposits from the literature, the porosity and defect levels of the EBF³-deposited 2219 were equivalent or lower. Additionally, the resulting AD and HT strengths were equivalent or higher.

3. The microstructure of the EBF³-deposited material deviates from that of conventional wrought product. The AD condition exhibited more of a GTAW or cast microstructure, with copious Al-Cu eutectics decorating grain boundaries and significant compositional coring within grains. The HT microstructure appeared more similar to wrought 2219-T62, with θ' precipitates in the matrix and low grain boundary precipitation. The HT microstructure was unrecrystallized and retained the slightly-elongated grains from the AD microstructure.
4. Average YS in the AD material varied from 16.8 ksi in the L orientation to 21.5 ksi in the LT orientation. Likewise, UTS varied from 38.8 ksi to 40.7 ksi in the L to LT orientations, respectively. All AD strength values fell between typical values for O and T4 wrought product.
5. The HT material responded more isotropically, with less than 3% variation in YS and UTS based on orientation. The HT YS and UTS of 43.4 ksi and 63.1 ksi, respectively, were consistent with typical wrought 2219-T62 values.
6. As expected from the limitations of 2xxx-series alloys, the 2219 strength levels fell short of the 7050-T7 property target set forth in Section 1.2, suggesting that additional deformation processes would be necessary to reduce the gap in properties. However, the material served as a weldable baseline of comparison for 7xxx-series alloys, which were found to suffer from severe hot cracking and other defects with EBF³ deposition.

Chapter 4

Behavior and Properties of 7075

4.1 Abstract

Aluminum alloy 7075 was investigated to study how an alloy with high cracking susceptibility in welding would perform with EBF³ processing, contrasting the ease of deposition and excellent performance of alloy 2219. In their wrought form, 7xxx-series alloys possess the highest strength achievable with aluminum, with good toughness and corrosion resistance. The high alloy contents of Zn and Mg, and frequent addition of Cu in certain alloys, contribute to the formation of high volume fractions of strengthening precipitates. While the alloy composition improves the mechanical properties, it also increases the hot cracking susceptibility during welding. This susceptibility generally renders the alloys 'unweldable', except for careful welding with 4xxx- or 5xxx-series filler metal or occasionally with high-energy density processes such as EBW. Due to the welding basis of EBF³, it was expected that 7075 would exhibit hot cracking and other defects seen in the welding literature. This study investigated the deposition of 7075 with EBF³ to determine whether high-strength, crack-free deposits could be fabricated.

A series of 7075 deposits were fabricated to study the resulting chemistry, defects, and microstructure from different machine parameters and baseplate conditions. Varying degrees of solidification and liquation cracking were discovered across all 7075 deposits, with solidification cracking intensified by increasing baseplate thickness and liquation cracking increased with deposit temperature. Solidification cracks in wall deposits were typically manifested as 'macrocracks' beginning at the baseplate intersection and progressing through the build height. These cracks were readily observed

with low-resolution XCT scans. In contrast, liquation 'microcracks' occurred within the deposits on a much finer scale and were only observable in polished cross sections or high-resolution XCT scans.

Due to the extensive cracking in the deposits, no mechanical specimens were able to be extracted from the 7075 walls. Instead, examinations of the microstructure, crack morphology, porosity, and microhardness were pursued in this research, with the microhardness allowing assessment of the potential for 7075 AM material to meet the 7050-T7 property targets if the cracks were eliminated.

Fractography from opening deposit macrocracks revealed crack surfaces covered in dendritic features, confirming the solidification origin of the cracks. Small regions of the crack surfaces near crack tips showed smooth, grain-like features, which suggested a liquated boundary between a solidification crack and uncracked material. Various particles were observed on the crack surfaces, often high in Zn, Mg, and Cu content.

Typical wall deposit microstructures exhibited area-averaged grain sizes of 92 to 140 μm . The primary exception to this was the Plate 60-C8 deposit microstructure, which was comprised of two vertical bands of equiaxed, 38 μm grains alternating with 152 μm grain regions due to keyholing of the rastered electron beam. While solidification cracks were common in all other deposits, the grain size mismatch in the 60-C8 microstructure disrupted solidification crack nucleation and propagation in the deposit. The degree of liquation cracking in this deposit compared to other deposits was reduced by a factor of 4.

These results demonstrate the beneficial effect of grain refinement on reducing both solidification and liquation cracking - a common solution in both welding and AM literature. Analysis was also completed to explore the less common alloy design route for avoiding cracking, where increasing Cu content in 7xxx-series alloys was found to decrease hot cracking susceptibility. Future work combining alloy design with grain refinement was proposed for successful deposition 7xxx-series alloys with EBF³.

4.2 Background

4.2.1 Wrought 7075

As one of the highest strength AAs, 7075 is used primarily in fuselage stringers and frames, upper wing stringers, and floor beams in aircraft [5]. 7075 is a precipitation-strengthened alloy, with major alloying additions of Zn, Mg, and Cu. High Zn:Mg

ratios produce the best strength and response to heat treatment due to the formation of the $MgZn_2$ phase. Cu additions are known to slightly reduce stress corrosion susceptibility, increase the percent elongation, and also result in better fatigue resistance [70]. The composition limits of 7075 are given in Table 4.1.

Table 4.1: ASTM B209-14 chemical composition limits for 7075 [69].

Alloy	Zn	Mg	Cu	Cr	Fe	Si	Mn	Ti	Other		Al
									Each	Total	
7075	5.1-6.1	2.1-2.9	1.2-2.0	0.18-0.28	0.50	0.40	0.30	0.20	0.05	0.15	bal.

The cast ingot microstructure and corresponding wrought plate microstructure of 7075 are shown in Fig. 4.1 [74]. The as-cast structure shows multiple phases consisting of insoluble Fe- and Si-containing phases, as well as a pseudobinary eutectic of aluminum and $MgZn_2$. This eutectic may have Al or Cu as substitutes for Zn. The wrought structure is characterized by long, pancake shaped grains from the working processes, some of which may remain unrecrystallized due to $ZrAl_3$ dispersoid banding [74].

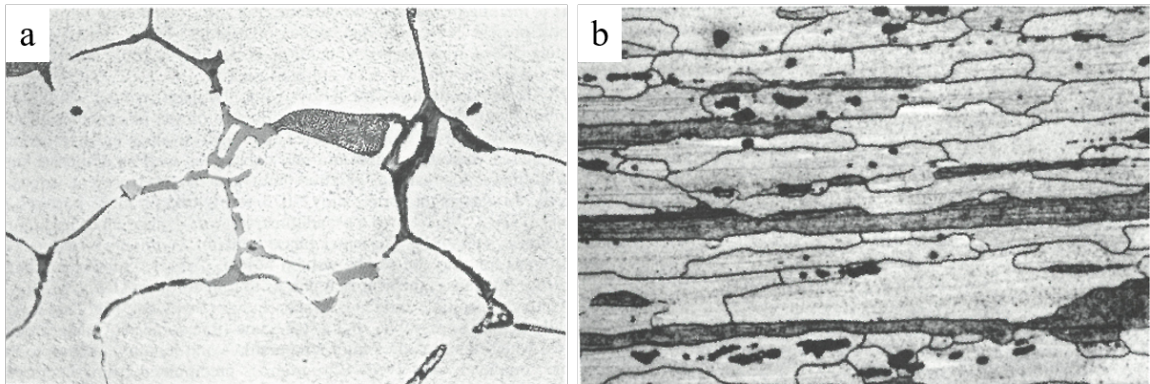


Figure 4.1: (a) 445x as-cast microstructure of ingot 7075, with coarse eutectic and second phase particles on the grain boundaries and fine precipitates from ingot cooling in grain interiors. (b) 445x wrought plate microstructure showing recrystallized (light) and unrecrystallized (dark) grains. [74].

7075 exhibits excellent mechanical properties due to the formation of the η' phase, $MgZn_2$, and also derives strength from Mg and Zn remaining in solution [70]. Table 4.2 compares properties for 7075 under various heat treatments, with T6 being the highest strength temper for the alloy but also the most susceptible to corrosion. It is known that overaging 7075 - and most 7xxx-series Al alloys - to a T7 temper results in a mild reduction in strength but much improved corrosion resistance.

Table 4.2: Typical tensile properties for 7075 plate under various heat treatments, with percent elongation reported for 2 in. gauge length [74].

Condition	YS (ksi)	UTS (ksi)	% el. (%)
T651	73.3	82.7	9
T735X	63.1	73.3	7

Studies have found that other thermal treatments such as the Retrogression and Re-Aging (RRA) treatment can improve corrosion resistance while retaining more strength than the T7 temper [94]. However, these treatments do not improve weldability of 7xxx alloys.

4.2.2 Welding of 7xxx-Series Aluminum

Fusion welding of 7xxx-series Al is limited by the pervasive issues of solidification and liquation cracking, described in Sections 2.4.3 and 2.4.4. 7075 is particularly susceptible to these issues due to its solidification mechanics, whereby the growth rate of dendrites in the primary direction outmatches the growth rate of these dendrites thickening and coalescing [62]. This results in the formation of long channels from the dendrite tips to roots, a condition that can lead to cracking when transverse strains on the dendrites outmatch the backflow of liquid into the created voids [62, 54].

Figure 4.2 shows the setup and typical results of circular patch testing in welding, a common method for assessing an alloy’s solidification and liquation crack susceptibility [28]. The high clamping constraint of the base metal and the circular weld track geometry cause high transverse stresses on the weld that result in weld hot cracking.

As seen in Fig. 4.2(b), solidification cracks nucleate near the edge of the FZ and turn towards the weld centerline, running perpendicular to melt pool tracks (yellow dotted arcs). The centerline of the weld represents the region of highest strain during thermal contraction and solidification of the molten metal, so cracking typically occurs on that centerline. In contrast, liquation cracking in such welds occurs parallel to the welding direction and runs along the FZ-base metal border in the PMZ. As seen in Figs. 4.2(b) and (c), solidification and liquation cracks rarely coexist in the same region, since the formation of one provides stress relief to the formation of the other.

The welding community has explored the two major avenues for reducing solidification cracking susceptibility of 7xxx-series Al welds, as described in Section 2.4.3. With regards to the grain refinement route, Kou used oscillating arcs in GMAW to agitate the melt pool, breaking off dendrite tips to serve as heterogeneous nucleation

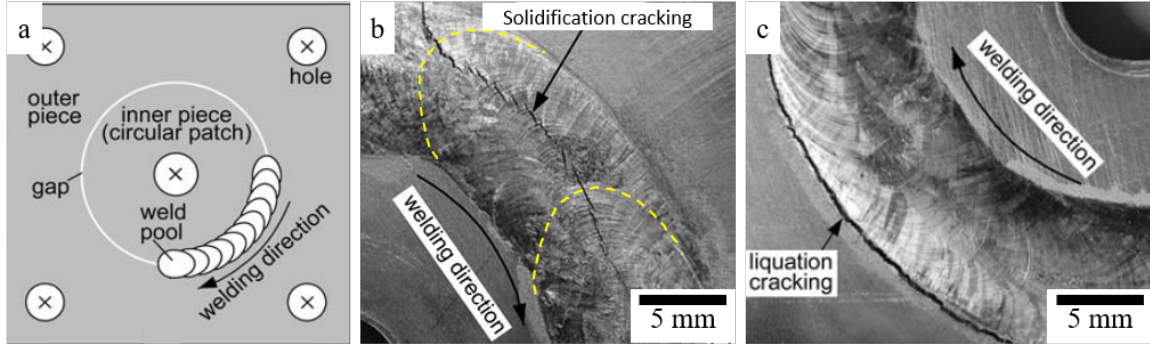


Figure 4.2: (a) Setup of the circular patch test for welding, with (b) solidification cracks nucleating at the FZ edge and growing along the weld centerline perpendicular to melt pool tracks (yellow dotted lines), and (c) liquation cracks running parallel to the weld line outside the FZ. Modified from [28].

sites and affecting the solidification path [64]. Matsuda et al. introduced inoculants such as Zr in combination with pulsed energy sources to produce an equiaxed grain structure in the fusion zone for exponential decreases in solidification cracking [25]. Dudas and Collins also used grain refinement via Zr additions to the filler metal to eliminate solidification cracking in an Al-Zn-Mg alloy [95].

The more common avenue for avoiding cracking in fusion welding of 7xxx-series alloys is to alter the weld metal composition through the use of a filler metal. It is known that 4xxx- and 5xxx-series alloys can significantly reduce the susceptibility to solidification cracking [13]. Kou explains this through the $|dT/df_s^{1/2}|$ criterion, since the additional Si in 4xxx-series alloys increases the amount of eutectic liquid available to backflow between columnar dendrites to heal solidification cracks [62]. In 5xxx-series Al, the additional Mg serves to increase the dihedral angle of the liquid interdendritic film, also reducing the solidification cracking susceptibility [62].

The main drawback to welding with 4xxx or 5xxx filler metals is the reduction of strength in the weld joint, since these alloy families are non-heat treatable [62]. As a result, solid-state welding processes such as FSW are the preferred method for welding of 7xxx-series materials.

4.2.3 Additive Manufacturing of 7xxx-Series Aluminum

Due to the well-known challenges of welding 7xxx-series Al, the number of research programs studying AM of this family of materials has lagged well behind those for other alloy families, such as the 2xxx series. The sections below describe the present state of AM research for both powder and wire feedstock of 7xxx Al.

Powder-Based AM

Most 7xxx-series Al powder-based AM research has encountered severe cracking problems in additive parts [17, 19]. The high power density and solidification rates of SLM processes can result in high strain rates in the molten pool, exacerbating the liquid feeding problem in the final stages of solidification [17]. Furthermore, the alloying element losses in both atmospheric and vacuum environment may drive the composition of the melt pool to a more crack-susceptible chemistry. These problems are inherent to 7xxx alloys due to the volatility of Zn and Mg from the molten pool and necessitate some modification to the AM process or feedstock to circumvent the cracking susceptibility.

A landmark study published in 2017 by Martin et al. [17] demonstrated the successful AM of 7075 with the SLM process. Their initial attempts in printing the material showed extensive cracking in printed parts due to hot cracking. Their initial microstructure - shown in Fig. 4.3 - demonstrated large columnar grains separated by large cracks. The resulting mechanical properties from such samples were very low, only exhibiting an UTS of 4 ksi and a 0.4 % el. before failure.

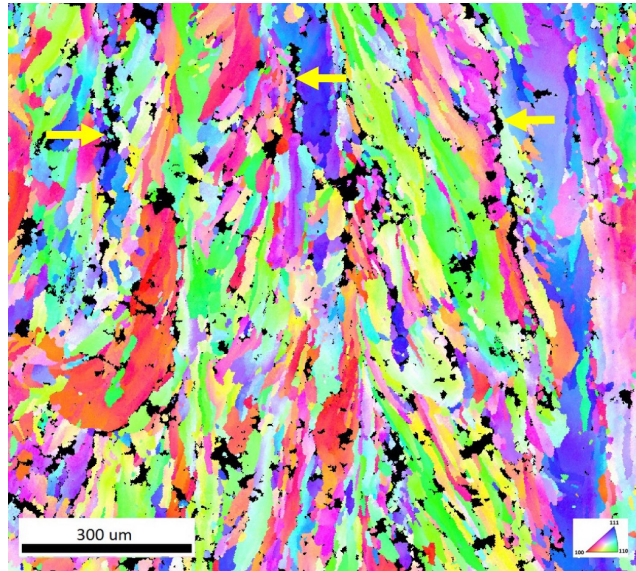


Figure 4.3: Cracking between columnar grains in SLM-printed 7075, with arrows added for clarity [17]. The build direction is vertical in this image.

However, when Zr nanoparticles are added to the 7075 powder feedstock, crack-free deposition of 7xxx Al was achieved due to a refined grain structure. This grain refinement can be attributed to the Zr additions, which dissolved to form Al_3Zr crystals in the melt and serve as heterogeneous nucleation sites given the matching

lattices of the crystals with the Al matrix. This new and abundant distribution of heterogeneous nucleation sites allowed for grain nucleation ahead of the solidification boundary, promoting the fine, equiaxed microstructure shown in Fig. 4.4(b) rather than the columnar structure obtained previously. The authors note that no difference existed in the Scheil T - f_s solidification curve, shown in Fig. 4.4(a), but rather the fine equiaxed structure was better equipped to deform to accommodate the strains associated with solidification and avoid cracking. The 7075 + Zr material was relatively pore-free and completely crack-free, resulting in an UTS between 55.5 to 60.5 ksi and elongations of 3.8% to 5%. These values fall short of the properties for wrought 7075 - likely due to the reported alloying constituent losses of 25% Zn and 32% Mg. However, this successful deposition of a 7xxx-series alloy is promising for other AM of traditionally unweldable wrought alloys and provides insight into methods for avoiding solidification cracking in the microstructure. While the paper did not mention any contributions of liquation or liquation cracking to the incompatibility of the material, it is very possible that these factors also played a role. As discussed in Section 2.4.4, grain refinement is one of the methods of reducing liquation sensitivity since it increases the grain boundary surface area, thereby reducing the density of liquation-sensitive second phases on grain boundaries [28].

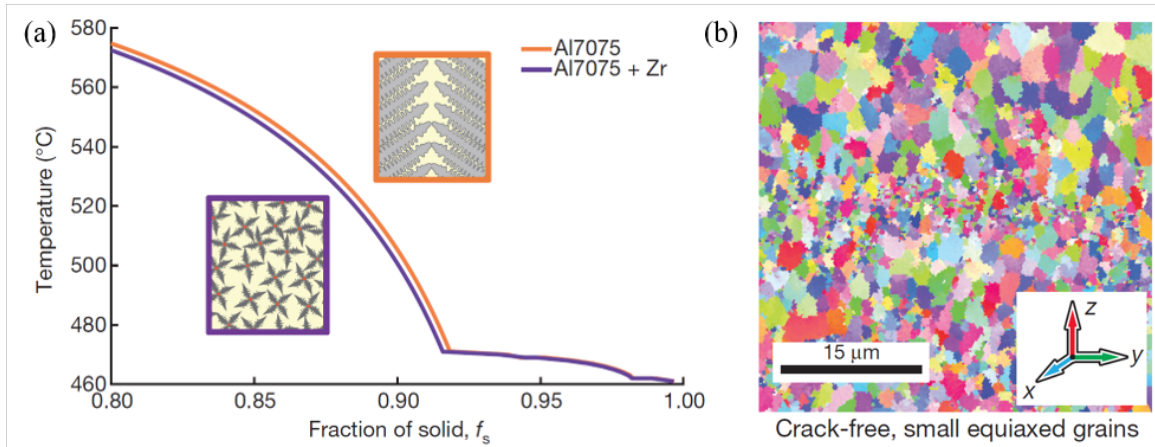


Figure 4.4: (a) Scheil solidification curves for the unmodified 7075 powder and the 7075 + Zr nanoparticle-dusted powder. (b) Microstructure transformed to fine, equiaxed grains that can accommodate strains during solidification to produce crack-free 7075 SLM deposits [17].

Recently, other research groups have approached the problem of 7xxx-series Al cracking in LPBF AM through similar grain refining techniques. Zhou et al. [21] pre-alloyed Al-6Zn-2Mg powder feedstock with 1 wt.% Sc + Zr additions to form $\text{Al}_3(\text{Sc}, \text{Zr})$ precipitates that acted as grain refiners. These particles served as het-

erogeneous nucleation sites during solidification, promoting a similar fine, equiaxed microstructure. They achieved AD properties of 56.0 ksi UTS and 18.4% elongation and T6 HT properties of 63.2 ksi and 11.1% elongation. The properties achieved by Zhou et al. slightly exceed those of Martin et al., likely due to differing starting alloy compositions and vaporization losses during processing.

Wire-based AM

No published work was found for the deposition of 7xxx-series Al using high deposition rate AM processes such as EBF³ or WAAM. However, recent research from Gu et al. [96] on WAAM of Al-Cu-Mg alloys showed the presence of solidification cracks within 9 in. long, 30-layer deposits. The researchers used dual-wire deposition of Al-Cu and Al-Mg wires to alter the chemistry of deposits to assess susceptible crack compositions. The authors noted the presence of solidification “macro cracks” running through the height of the deposit for more susceptible compositions, as well as “micro cracks,” which they attributed both to the solidification and liquation cracking mechanisms. Figure 4.5 shows the WAAM deposit and associated microstructures.

While not a 7xxx-series alloy, this paper is valuable for showing the presence of solidification and liquation cracks in large-scale deposits built with a high deposition rate additive process. Such features are anticipated to appear in the similarly-susceptible 7xxx-series deposits in this study.

4.3 Experimental Procedures

EBF³-deposited 7075 contained significant defects, including solidification and liquation cracks, alloying element losses, and porosity. Rather than using one parameter set to deposit material for mechanical testing specimens as for 2219 - which would produce useless samples due to the poor compatibility of 7075 with EBF³ - the 7075 work aimed at understanding the origin and character of the cracking. Linear walls of varying parameters were built to investigate whether the solidification phenomena could be controlled with machine parameters or environmental factors to decrease or eliminate some of the defects.

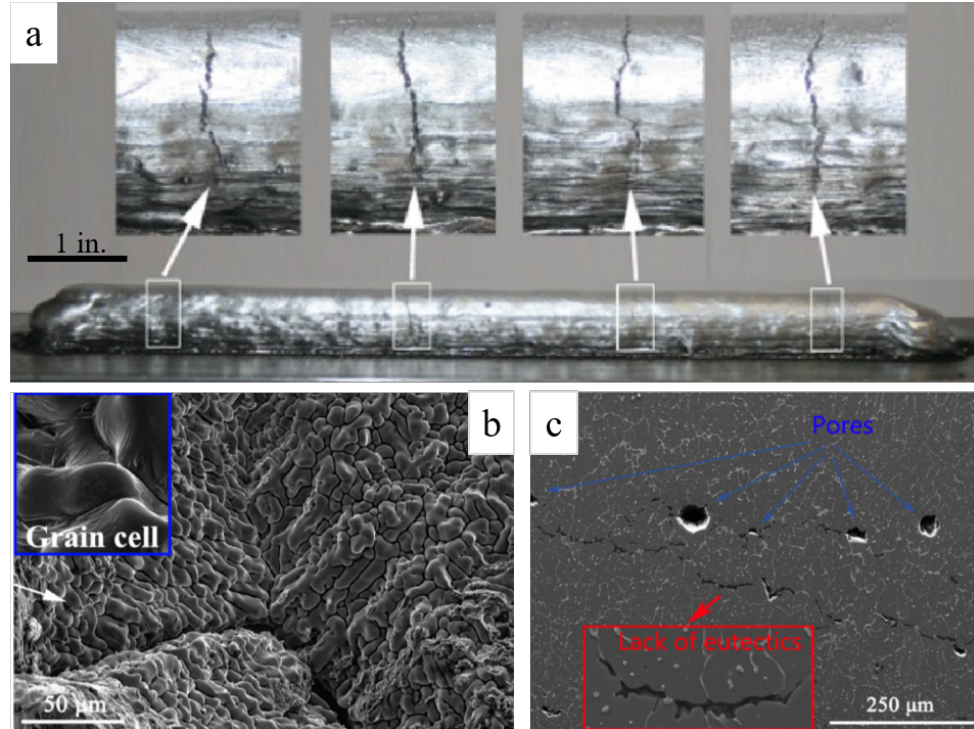


Figure 4.5: (a) WAAM deposit made from co-depositing Al-Cu and Al-Mg feedstock to tailor chemistry and assess HCS. Solidification “macro cracks” run through the height of the deposit for certain susceptible compositions. (b) Fracture surface of a macro crack, and (c) polished cross section revealing liquation cracking in a deposit without macro cracks. [96].

4.3.1 Starting Materials

The deposits were fabricated using 0.062 in. diameter wire obtained from All Metals, Inc. The composition of the 7075-T6062 wire measured via DCP-AES and complying with ASTM E1097-12 is shown in Table 4.3. 7075-T7351 0.25 in. and 1 in. baseplate was cleaned and installed in the machine, and the same warm-up and cleaning pass procedure was performed as in Section 3.3.2.

Table 4.3: Compositions of the starting 7075-T6 wire and 0.25 in. 7475-T7351 baseplate measured with DCP-AES by Luvak Laboratories, Inc. Results given in wt.%.

Alloy	Zn	Mg	Cu	Cr	Fe	Si	Mn	Ti	Al
7075 wire	5.70	2.42	1.52	0.22	0.14	0.093	0.016	0.025	bal.
7475 plate	5.65	2.27	1.50	0.218	0.074	0.043	0.0089	0.014	bal.

The etched wire microstructure is shown in Fig. 4.6, where (a) shows the overall distribution of particles in the wire and (b) shows individual particles and faint grain

boundaries.

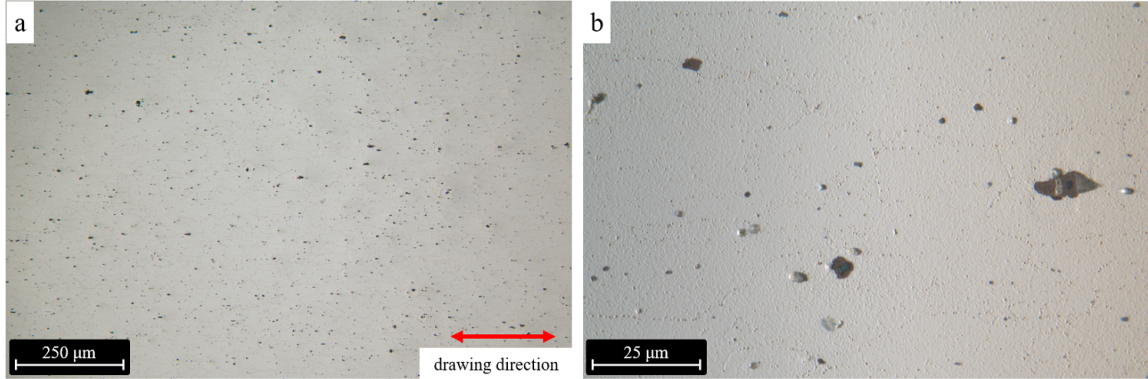


Figure 4.6: Etched microstructure of the 7075 wire used for constructing the deposits. (a) 100x view showing the particle distribution in the wire, and (b) 1000x image of the bulky, Al-Fe-Cu particles and other smaller particles containing Zn or Cu.

EDS results showed that most large particles in the Fig. 4.6(b) microstructure were constituents containing Al, Fe, and Cu. These particles were generally oblong, with a maximum dimension between 4 to 8 μm , and had an average composition of either Al-22.1 Fe-6.6 Cu-3.3-Zn-1.1 Mg or of Al-25.6Cu-11.0Fe-2.0Zn-0.8Mg. Such constituents are typically insoluble at the melting temperature of Al [70].

A small number of round particles with a diameter of 1.3 μm were observed, with a composition around Al-5.7Zn-3.6Fe-2.4Cu-2.4Mg. These correspond to the smaller, round particles in Fig. 4.6(b). Other fine particles were noted at grain boundaries in the material but were too small for composition to be measured with EDS.

4.3.2 Deposition Setup

Nearly all deposits utilized the window-frame fixture developed for the 2219 deposits and described in Section 3.3.2. Deposits for this study still incorporated the nominal 0.5 in. wide wall deposit geometry, shown in Fig. 4.7, since its linearity is most comparable to weld geometries. However, no deposits were built to the 5 in. height target, since geometric instabilities or cracks necessitated premature termination of the build.

Various procedures for turning off the EB at the end of a layer were tested to determine which maintained the geometric stability of the build to avoid drips and wire jams. The molten 7075 was discovered to be more viscous than molten 2219, so the runback procedure used for 2219 builds in Section 3.3.2 caused craters at the ends of the 7075 builds. A second procedure, termed “DOW” in the EBF³ G-code,

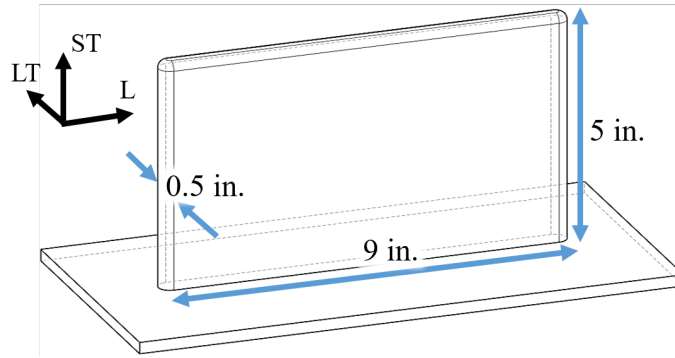


Figure 4.7: Target wall deposit geometry for the 7075 builds.

involved ramping down the beam current over the final 0.050 in. of the deposit. This eliminated cratering and improved the stability of the deposit ends. In certain short builds, the beam was simply shut off at the end of the layer.

Deposits were built on either 0.25 in. or 1 in. baseplate, the latter of which was selected to evaluate the effect of stress state on cracking. The average build temperature was monitored by the thermocouple under the baseplate and was kept relatively constant by varying the pause time between layers. Machine parameters were varied to affect the deposit composition and thus the susceptibility to cracking.

4.3.3 Specimen Analysis Procedures

Full-height specimens for metallurgical characterization were cut from the deposits with a bandsaw within a couple days of deposition in order to screen the deposits for cracks, porosity, and chemistry changes as a function of varying parameters. These specimens were sectioned prior to XCT scanning, which resulted in only partial deposits remaining for XCT scans. Further metallurgical specimens were cut from the remainder of the deposits as necessary after XCT. All metallurgical samples were polished with the same procedures used in Section 3.3.4 for optical microscopy, SEM, and EBSD.

Samples for microhardness were likewise prepared with the same procedure as for 2219 in Section 3.3.4, with the microhardness tests performed following EBSD on the same samples.

Specimens for compositional analysis were sent to Luvak Laboratories, Inc. for DCP-AES analysis. The 5 to 10 g samples were extracted to exclude the top layer and the bottom few layers in order to avoid areas with compositions that might differ from the bulk due to lack of remelting or mixing from the baseplate. While some

samples were analyzed for their full chemistry, others were only screened for their Zn and Mg content, since those were the primary volatile elements for EBF³ of 7075.

4.3.4 Nondestructive Testing

Nondestructive XCT scans were performed on the largest sections of specific deposits to document density-based defects such as cracks and large pores. The resolution of these scans was limited on average to 70 μm due to the size of the partial deposits being scanned. This resolution was useful in identifying regions of the deposits that would merit further examination with high-resolution XCT and metallurgical characterization, or for sectioning around a crack to open it and evaluate the cracking mechanism.

For higher-resolution scans of specific areas in deposits, full-height 0.4 to 0.5 in. diameter cylinders were cut from the deposits using wire-electrical discharge machining (wire-EDM). Since the cylinders had an effective radius of 0.2 to 0.25 in. compared to the 3 to 4 in. effective radius of partial linear deposits, the x-ray source could be brought much closer to the sample to increase the geometric magnification during sample rotation for XCT scanning. This resulted in an increase in the resolution to the order of 7 μm . This high resolution limited the size of the scan area, requiring multiple scans along the cylinder height to cover regions from the baseplate intersection to the top of the deposit. The cylindrical geometry was chosen so that the sample thickness was invariant with rotation during XCT scanning, resulting in less beam scattering and clearer images.

4.3.5 Cracking Analysis Methods

A significant portion of the cracking analysis involved carefully opening deposit “macrocracks” to observe the crack surface morphology. These macrocracks were found to typically initiate near the baseplate and extend upwards through the deposits, usually at an angle of around 70° to the horizontal. Cracks were angled oppositely on the two sides of the wall, and some would grow to reach the full width of the deposit while others would only break the surface on one side.

Cracks of interest were identified from low-resolution XCT scans of the deposits, and sections of material surrounding the cracks were excised with either a bandsaw or a wire EDM. Typically, these cracks were ones that appeared to extend through the entire width of the wall without many branches that would make it difficult to

open the crack. If a crack did not immediately fall open once cut from the deposit, then the sample was mounted in a diamond slow-speed saw and carefully sectioned until the crack could be opened. For some specimens, careful gripping and manually loading in tension was used to open the crack. Initial investigations demonstrated that cutting fluids would leave residue on the crack surface, obscuring observation of the crack morphology beneath. Thus, all subsequent cutting operations involved rinsing specimens with water and methanol and thoroughly drying out cracks to prevent as much contamination or corrosion of the crack surfaces as possible.

Once split open, the two crack halves were cleaned in an ultrasonically-pulsed bath of methanol and loaded into a SEM for observation of the crack surface. Macroscopic and microscopic images of the fracture surfaces were taken to capture the general crack surface morphology and dendrite-scale features. EDS was used to obtain a general sense of the composition of secondary phases and precipitates exposed on the crack surfaces. Figure 4.8 shows the steps of extracting and opening sections of a macrocrack from a deposit.

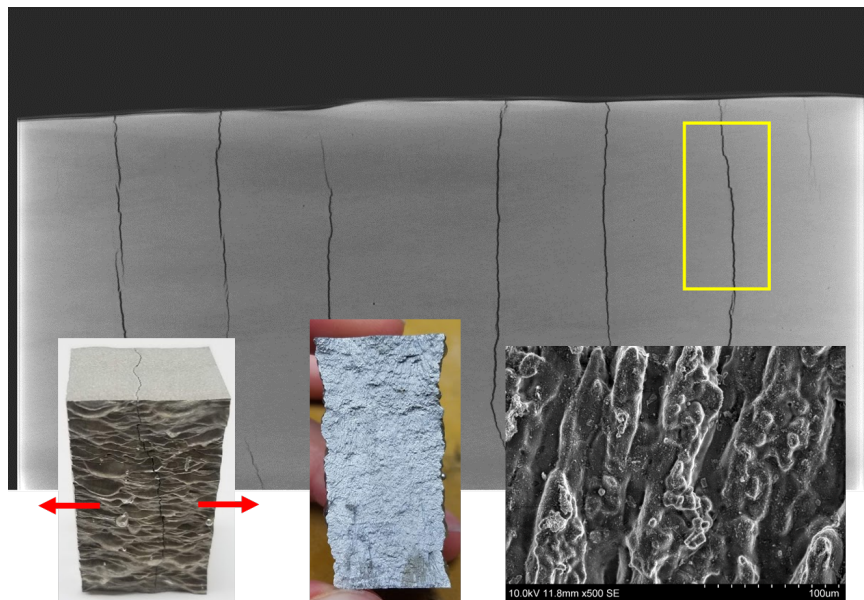


Figure 4.8: Procedure for identifying and opening macrocracks for observation of the crack surface morphology in the SEM.

Some deposits also contained regions of “microcracks”, which were barely or not discernible with the $70\ \mu\text{m}$ XCT scans. Figure 4.9 shows a micrograph comparing the full-deposit and cylindrical specimen voxel sizes with a typical microcrack in a deposit. While some $70\ \mu\text{m}$ scans showed shadowy regions of microcracking, crisp images of the microcracks were only made possible by the $7\ \mu\text{m}$ scans and metallurgical cross

sections.

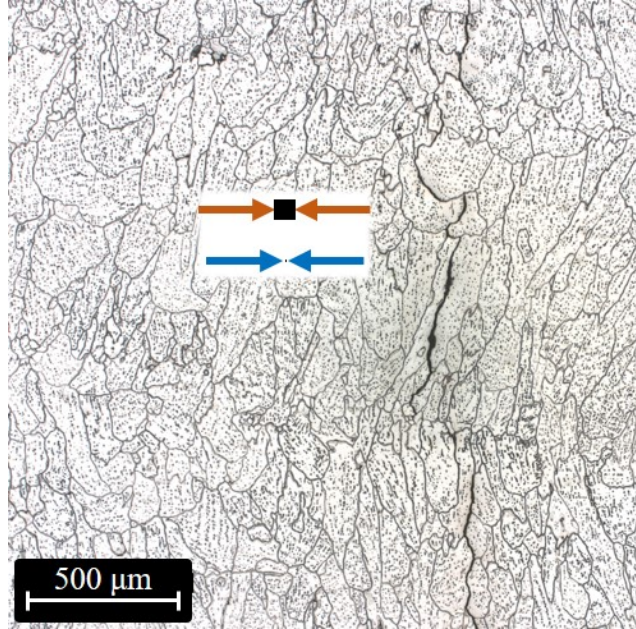


Figure 4.9: Comparison of a typical intergranular microcrack with a 70 μm voxel of a full-deposit XCT scan (orange arrows) and the 7 μm voxel size of a 0.4 in. diameter cylindrical specimen (blue arrows).

ImageJTM was employed to highlight cracks in various data sets, including XCT low- and high-resolution scans and in optical images of few-layer deposits which could not be scanned with XCT. The program allowed tracing of the cracks to tabulate crack lengths, spacings, and densities from image analysis.

4.4 Results

4.4.1 7075 Deposition Series Overview

Three rounds of 7075 deposition trials were conducted with EBF³. Series 1 (Plates 19-20 and 45-53) implemented lessons learned from prior depositions to observe if alloying element losses and cracking could be reduced or controlled. Series 2 (Plate 60) was implemented after a process optimization study to reduce porosity in a proprietary aluminum alloy. Eight 4 in. long, 1 in. tall walls were printed on Plate 60, where macrocracking was eventually eliminated. Finally, Series 3 (Plates 68-73) returned to the beam parameters and starting baseplate temperature from Plates 46 and 50 to study how macrocracks initiated in the first few layers of 9 in. long deposits

on both 0.25 in. and 1 in. baseplates.

Tables 4.4 and 4.5 summarize the deposits in these series and their associated machine parameters and environmental conditions to illustrate the parameter space studied in this research. The following sections describe the motives behind these choices.

Series 1a - Varying Beam Focus and Travel Speed

Series 1a includes Plates 19-20 and 45-47 and represents the first 7075 deposits of the work. The beam focus and travel speed were adjusted to reduce alloying element losses, and both macrocracks and microcracks were discovered in the Series 1a deposits.

Plate 19 replicated the machine parameters of the 2219 walls, which included a beam focus (BF) condition of $BF = 323$, or 18 points under-focused. The deposit was built with the same deposition procedure as the 2219 walls (including runbacks) but was limited to 28 layers to study the material behavior before attempting a full 5 in. tall wall. Furthermore, it was expected that alloying element losses would occur due to the volatility of Zn and Mg under vacuum while at the melting temperature of Al (see Fig. 2.14), so this deposit was limited in height to check the composition before proceeding to taller builds. Due to viscosity differences between 2219 and 7075, the runbacks at the deposit ends resulted in a crater and large slump that led to dripping and discontinuity of the build layer with increasing height. Figure 4.10 shows the Plate 19 deposit, with the inset highlighting a macrocrack (yellow arrow) and the crater formed during the runbacks (blue arrow).



Figure 4.10: Image of the completed Plate 19 deposit. The inset shows an end of the deposit with slumping and cratering from the runbacks, as well as a macrocrack.

The deposition procedure for Plate 20 eliminated runbacks to reduce this geometric instability at the deposit ends while maintaining the same beam parameters, clamping scenario, and a similar average background temperature as Plate 19. It was

Table 4.4: EBF³ parameters used for the 7075 Series 1 and 2 deposits. For all deposits, $AV = 40$ kV and $WF = 172$ ipm. Note - these will be updated to normalize parameters when the thesis is submitted.

Plate	BC (mA)	BF (mA)	TS (ipm)	RF (kHz)	X/Y/SF	Δz (in.)	Layers	BP (in.)	T (°C)	Ends
Plate 19	90	323	30	1	125/500	0.035	28	0.25	195	rb
Plate 20	90	323	30	1	125/500	0.035	28	0.25	170	none
Plate 45	90	305	24	1	109/550	0.037	82	0.25	150	rb
Plate 46	90	305	40	1	109/550	0.025	90	0.25	170	rb/DOW
Plate 47	90	305	40	1	109/550	0.025	30	0.25	155	DOW
Plate 48	90	305	40	1	109/550	0.025	62	1.0	225	DOW
Plate 49	90	305	40	1	109/550	0.025-	172	1.0	300	DOW
Plate 50	90	305	40	1	109/550	0.018	86	1.0	170	DOW
Plate 51-1	90	305	100	1	245/245	N/A	1	1.0	155	N/A
Plate 51-2	80	305	100	1	245/245	N/A	1	1.0	150	N/A
Plate 51-3	70	305	100	1	245/245	N/A	1	1.0	150	N/A
Plate 51-4	60	305	100	1	245/245	N/A	1	1.0	145	N/A
Plate 51-5	50	305	100	1	245/245	N/A	1	1.0	140	N/A
Plate 51-6	40	305	100	1	245/245	N/A	1	1.0	140	N/A
Plate 51-7	35	305	100	1	245/245	N/A	1	1.0	135	N/A
Plate 51-8	30	305	100	1	245/245	N/A	1	1.0	135	N/A
Plate 51-9	25	305	100	1	245/245	N/A	1	1.0	135	N/A
Plate 52	95	305	60	1	109/550	0.025	64	1.0-O	185	DOW
Plate 53	90	305	40	1	109/550	0.018	52	1.0-O	260	DOW
Plate 60-C1	90	305	40	10	109/550	0.025	40	0.25	85	none
Plate 60-C2	90	305	40	10	245/245	0.025	40	0.25	135	none
Plate 60-C3	90	350	40	10	245/245	0.025	40	0.25	110	none
Plate 60-C4	90	350	40	1	245/245	0.025	40	0.25	120	none
Plate 60-C5	90	350	24	1	109/550	0.025	40	0.25	120	none
Plate 60-C6	90	350	24	1	109/550	0.03	34	0.25	158	none
Plate 60-C7	90	350	24	1	109/550	0.037	28	0.25	95	none
Plate 60-C8	90	341	24	1	109/550	0.037	28	0.25	160	none

Table 4.5: EBF³ parameters used for the 7075 Series 3 deposits. For all deposits, AV = 40 kV and WF = 172 ipm.

Plate	BC (mA)	BF (mA)	TS (ipm)	RF (kHz)	X/YSF (in.)	Δz (in.)	Layers	BP (in.)	T (°C)	Ends
Plate 68-0L	90	305	40	1	109/550	N/A	0	1.0	159	DOW
Plate 68-1L	90	305	40	1	109/550	N/A	1	1.0	155	DOW
Plate 68-2L	90	305	40	1	109/550	0.018	2	1.0	130	DOW
Plate 69-6L	90	305	40	1	109/550	0.018	6	1.0	165	DOW
Plate 69-20L	90	305	40	1	109/550	0.018	20	1.0	167	DOW
Plate 69-40L	90	305	40	1	109/550	0.018	40	1.0	170	DOW
Plate 70-0L	90	305	40	1	109/550	N/A	0	0.25	155	DOW
Plate 70-1L	90	305	40	1	109/550	N/A	1	0.25	147	DOW
Plate 70-2L	90	305	40	1	109/550	0.018	2	0.25	140	DOW
Plate 71-6L	90	305	40	1	109/550	0.018	6	0.25	155	DOW
Plate 71-20L	90	305	40	1	109/550	0.018	20	0.25	160	DOW
Plate 71-40L	90	305	40	1	109/550	0.018	40	0.25	175	DOW
Plate 72-3L	90	305	40	1	109/550	0.018	3	1.0	160	DOW
Plate 72-4L	90	305	40	1	109/550	0.018	4	1.0	153	DOW
Plate 72-5L	90	305	40	1	109/550	0.018	5	1.0	157	DOW
Plate 73-8L	90	305	40	1	109/550	0.018	8	1.0	155	DOW
Plate 73-10L	90	305	40	1	109/550	0.018	10	1.0	170	DOW
Plate 73-12L	90	305	40	1	109/550	0.018	12	1.0	165	DOW

discovered that the Plate 19 and 20 parameters resulted in 45% Zn and 29% Mg losses during deposition.

The parameters for the next deposit, Plate 45, further defocused the electron beam to 36 points under focus, adjusted the raster size from a 0.25 to a 0.2 aspect ratio to increase deposit width, and reduced the travel speed by 20%. Similar under-focusing of the beam was found to reduce elemental losses in the proprietary alloy deposits, while reducing the travel speed increased solidification time and reduced solidification strain rates that might affect cracking. Despite geometric instabilities at the deposit ends and a wire stick event that occurred in the center of the deposit, the deposit was stable enough to achieve 4x the number of layers as Plate 19. This set of conditions allowed for observation of the cracking behavior and deposit chemistry with greater build height. Tall, angled “macrocracks” were observed on the deposit surfaces, despite lower alloy losses of 33% Zn and 19% Mg.

In an effort to further reduce alloy losses and cracking, as well as to achieve more stable deposit ends, Plate 46 was deposited with a 67% higher travel speed and a 0.012 in. smaller Δz than for Plate 45 in order to increase the solidification rate and permit less time for alloying constituents to escape from the molten pool. The composition of the deposit reflected this change, as only 25% Zn and 11% Mg losses occurred. Plate 46 also exhibited less macrocracking than Plate 45, with fewer cracks on the deposit surfaces and a significant reduction in the number of cracks observed near the baseplate. Halfway through Plate 46, a new bead-stopping sequence (termed DOW) was implemented to ramp down the beam power over the last 0.050 in. of the deposit to stabilize the deposit ends.

Plate 47 was intended to repeat the Plate 46 parameters and implement the DOW command for bead stops for the full deposit height. However, a suspected issue with the baseplate clamping and the heat flux of the warmup passes caused significant warping of the baseplate, resulting in one of the long edges of the baseplate escaping the fixture and warping upward. Thus, the deposit footprint was biased towards the opposite edge of the plate and was terminated after 30 layers due to suspected loss of contact between the thermocouple and the baseplate.

From the Series 1a deposition trials, it was found that defocusing the beam to 36 points under focus, increasing the travel speed to 40 ipm, and utilizing the DOW beam-stopping procedure reduced elemental losses and improved the geometrical stability of deposits. Macrocracks were observed on the deposit surfaces optically and with XCT. Additional metallography and high-resolution XCT analysis showed that the material between macrocracks also suffered from thin microstructural cracks, or

“microcracks.”

Series 1b - Varying Baseplate Thickness and Background Deposition Temperature

Due to concerns over the reliability of thin baseplate after observing the significant warpage in Plate 47, 1 in. thick 7075-T7351 baseplate was used for the deposits in Series 1b (Plates 48-53). In addition, the baseplate temperature was adjusted through ceramic standoffs and pauses to study the effects of temperature on cracking.

For Plate 48, the same parameter set from Plates 46 and 47 was replicated, but executed with an average background temperature 70°C higher. More prominent cracks were noted on the outside surfaces of the deposit, raising questions as to whether the higher temperature or the thicker baseplate was the cause of cracking.

To study the effects of a high preheating and deposition temperature on cracking, the preheat temperature for Plate 49 was increased to 300°C while retaining the Plate 46 machine parameters. This was accomplished by decreasing Δz by 0.007 in. to account for thinner layers spreading from the higher temperature. Plate 49 was built the tallest, with an input of 172 layers since the deposit geometry appeared very stable during deposition. However, upon removal from the build chamber, it was discovered that the deposit contained wide macrocracks that were angled approximately 65° near the baseplate and turned vertically after the first 0.6 in. of the deposit height. These cracks appeared in a near-periodic fashion along the length of the deposit, suggesting high stresses in operation, with an average spacing of 0.70 in. Furthermore, the elevated temperature of deposition resulted in significant alloy losses, with 36% Zn and 19% Mg lost from the deposit. Figure 4.11 shows a side view of the Plate 49 deposit, with visible macrocracks highlighted in yellow.

The same parameter set from Plates 46 and 49 was repeated for the next deposit, Plate 50, but with a baseplate temperature comparable to that of Plate 46 to evaluate the effect of baseplate thickness on deposit macrocracking. Prominent cracks angled around 65° were also observed in this build, but remaining angled throughout the entire build height rather than turning vertically, as observed in Plate 49. The composition of Plate 50 was very similar to that of Plate 46 since these builds were deposited with the same machine parameters and baseplate temperature.

A different approach was used for Plate 51 to study whether bead size affected cracking. Nine 9 in. long, single-layer deposits were printed on Plate 51 with a small, circular raster pattern and decreasing beam current value for each deposit. If cracking



Figure 4.11: Image of the completed Plate 49 deposit, with macrocracks highlighted in yellow and widened for visibility.

could be eliminated with smaller beads, a multi-bead approach could be used to build the specified wall geometry defect-free. However, fine cracks were observed on the top surface of all single-layer deposits of Plate 51, indicating solidification cracking, so the approach was abandoned in favor of larger beads for reduced deposition time.

In an effort to reduce the constraint of the 1 in. T7351 baseplate, 1 in. thick baseplates were annealed (7075-O) to see if a reduction in baseplate strength would minimize the cracking in the deposits while still preventing baseplate warpage during deposition. Plates 52 and 53 were deposited on the 7075-O baseplate, with Plate 52 having a 50% higher travel speed than the parameter set for Plates 46-50. The processing changes resulted in balling of deposit layers and poor cohesion. Plate 53 was then printed with the Plate 46-50 parameters on 7075-O plate, but significant macrocracking was still observed.

These Series 1b deposits demonstrated that baseplate thickness influences the length and height of deposit macrocracks, as does the background printing temperature. The single-layer, small bead deposits showed that cracking occurred in the first layer and that changing beam current was not sufficient to eliminate cracks in single-layer deposits.

Series 1 Deposition Summary

From this array of tests, the analysis of the 7075 Series 1 focused on three main deposits: Plates 46, 49, and 50. Based on the selected machine parameters and bead start/stop sequence, these deposits were the most stable of Series 1 and were built tallest. These plates exhibited two different average deposition temperatures and baseplate thicknesses, such that comparing two plates would result in isolating a

single differing parameter. Table 4.6 lists these comparisons.

Table 4.6: Isolated variable changes between 7075 Series 1 deposits.

Plates	Comparison
46 & 50	4x baseplate increase
50 & 49	2x average background temperature increase

In-depth characterization of Plates 46, 49, and 50 for composition, defects, microstructure, and hardness will shed light on the effects of varying thermal and baseplate parameters on 7075 deposits. These results are given in Sections 4.4.2-4.4.6.

Series 2 - Further Variation of Beam Focus and Travel Speed

The purpose of the Series 2 deposits on Plate 60 was to evaluate parameter sets which resulted in reduced porosity and deposit roughness for 4 in. long builds of a proprietary alloy. These parameter changes included circularizing the raster pattern and increasing the raster frequency, which did not reduce cracking, while reducing the travel speed and over- or sharp-focusing the beam eliminated steady-state macrocracking and reduced internal microcracking.

X-ray radiographs of these builds on Plate 60 (labeled C1-C8) are shown in Fig. 4.12, with visible cracks highlighted in yellow and parameter changes noted in white text below each deposit.

Previous studies with the proprietary alloy showed that beam focus and melt pool shape play a significant role in the degree of vaporization of alloying elements. C1 repeated the parameters from Plate 46, save the fact that the raster frequency was inadvertently programmed to be 10 kHz rather than 1 kHz and the average background temperature was half that of Plate 46. C2 was given a circular raster pattern with the same area as the elliptical one for C1, a technique which reduced porosity in the proprietary alloy builds.

To study the effects of over-focusing the beam, the BF was changed to 9 points over focus for build C3. After this build, it was discovered that there was a registration error between a layer and its 180° subsequent layer counterpart, so calibrations took place to correct this. The C3 parameters were repeated for C4 but with a 1 kHz raster frequency, used for all subsequent deposits. Wire shoot-outs and other associated instabilities occurred for the C4 deposit, so the circularized raster pattern for low-frequency builds was abandoned.

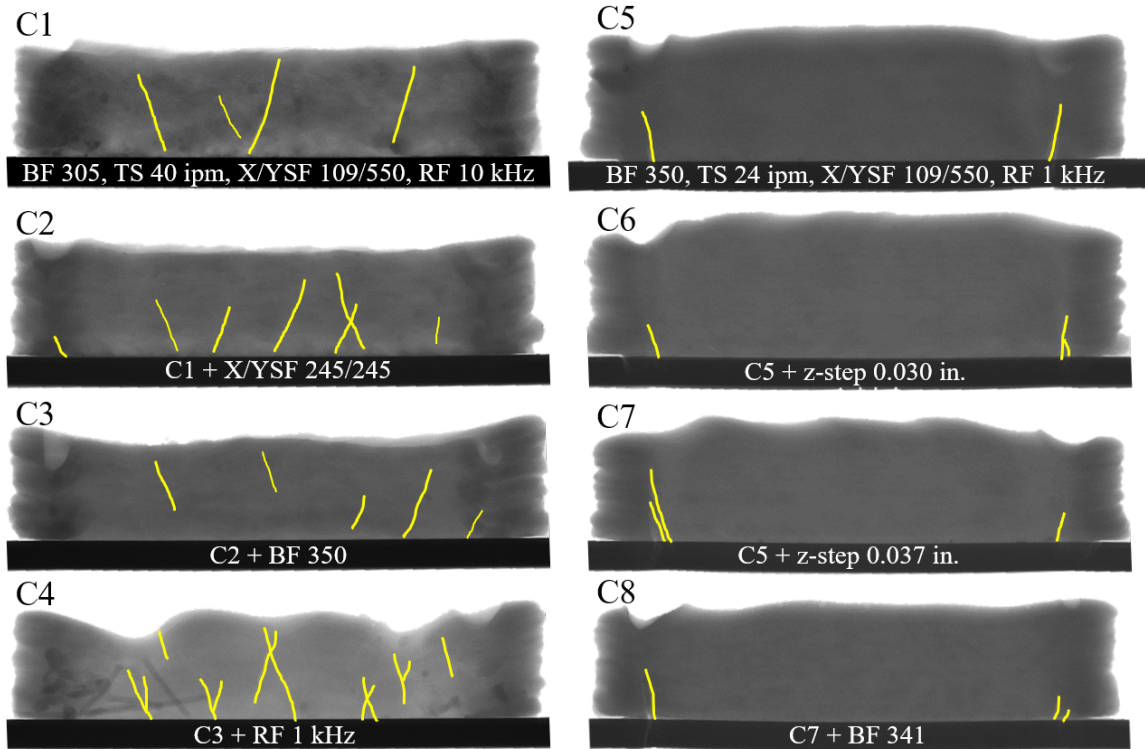


Figure 4.12: Radiographs of the 4 in. 7075 deposits built on Plate 60.

The BF = 350 over-focused condition was continued for C5, but the travel speed was reduced by 40% to 24 ipm to minimize wire shoot-outs. This produced the most geometrically stable and smooth deposit of C1-C5, so the subsequent C6 and C7 builds kept the same machine parameters and varied Δz from 0.025 in. to 0.030 and 0.037 in. to study whether a smaller remelt depth might have an effect on defects.

The final deposit on Plate 60, C8, had a focused (keyhole) beam condition (BF = 341) to investigate the effect of focus on internal defects and composition. Microstructural analysis for builds C7 and C8, discussed in detail in Section 4.4.3, revealed significant grain refinement below the keyhole of the raster profile, correlating with the elimination of macrocracking in addition to the 40% slower travel speed. However, builds C7 and C8 demonstrated the greatest alloy losses of all deposits, with C8 exhibiting a 53% loss in Zn and a 19% loss in Mg.

Series 2 Deposition Summary

While no full-deposit XCT scans were captured for these builds due to time constraints, radiographs were taken to document the deposit profiles and large macro-

racks. Figure 4.12 compares the radiographs of builds C1-C8 on Plate 60, which show angled macrocracks for C1-C4 and the elimination of macrocracks in the steady-state region for C5-C8. This elimination of macrocracks prompted high-resolution XCT scans of C8, shown in Section 4.4.4, as well as metallurgical cross sections and EBSD analysis.

Series 3 - Studying Macrocrack Initiation and Propagation

The Series 3 deposits on Plates 68-73 were designed to elucidate macrocrack initiation and propagation in the early layers of wall deposits on both 0.25 in. and 1 in. thick baseplates. These included a cleaning pass and single- and multi-layer builds to evaluate crack evolution with increasing layers. All deposits in Series 3 used the under-focused, elliptically-rastered parameters from Plates 46-50, with an intended baseplate temperature around 170°C. The parameters, number of layers, and temperature for each deposit in Series 3 are documented in Table 4.5. It was expected that cracking in the early layers should resemble cracking seen in the welding literature, since the constraints on the weld pool would be similar for layers close to the baseplate.

Plates 68-69 and 70-71 share the same build plan, shown in Fig. 4.13, except on 1 in. and 0.25 in. baseplates, respectively. The Plate 68-69 deposits on 1 in. baseplate were intended to reflect how high baseplate constraint would accentuate cracking, as seen in Plate 50, whereas the Plate 70-71 deposits on 0.25 in. baseplate were designed to examine how a 4x reduction in baseplate thickness would affect cracking, as in Plate 46.

The build plan included three 9 in. deposits per plate. Plates were clamped in the window frame fixture with 50 in-lbs torque on all bolts to ensure consistent constraint. To reduce differences in constraint with respect to the starting point for the edge deposits, the plate was rotated for the third deposit so that each deposit began at the starred ends shown in Fig. 4.13.

A significant change in cracking behavior was observed between builds of 2 and 6 layers, as seen in the optical macrographs in Fig. 4.14. In the 1- and 2-layer deposits, cracks are angled perpendicular to the melt pool lines and turn nearly parallel to the weld direction near the centerline of the deposit. In the 1-layer deposit, these cracks are spaced on average by 0.26 ± 0.09 in., while cracks in the 2-layer deposit have an increased average spacing of 0.42 ± 0.18 in. The crack turning is related to transverse tensile stress from the baseplate during solidification, and similar cracks parallel to

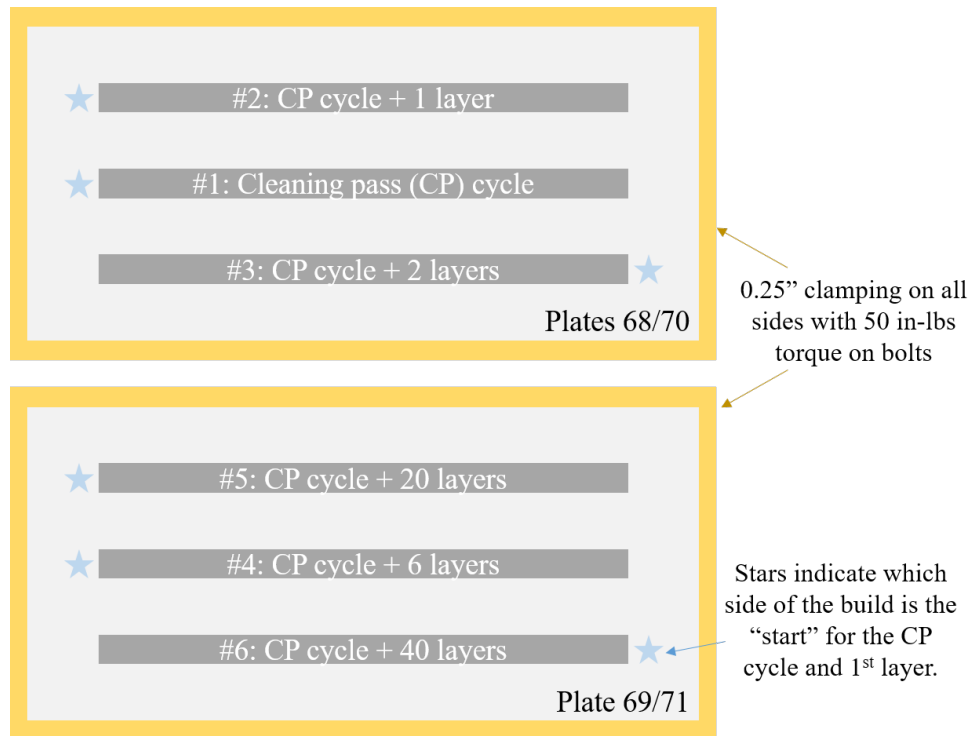


Figure 4.13: Build plans for Plates 68-71, where 68-69 were built on 1 in. plate and 70-71 were built on 0.25 in. plate to compare the effects of constraint on developing cracks in few-layer builds in 7075.

the weld line are seen in the welding literature.

In contrast, cracks breaking the surface of deposits of 6 or more layers were characterized by short, angled cracks that began near the deposit edge and terminated without reaching the deposit centerline. At a height of 6 layers and above, there is no longer transverse stress from the baseplate to cause cracks parallel to the weld direction. This abrupt change in cracking behavior led to the deposition of Plate 72 on 1 in. thick baseplate, which included builds of 3, 4, and 5 layers in the #1, #2, and #3 slots in Fig. 4.13 to elucidate macrocrack evolution. Comparing the cracks in deposits on Plates 68 and 72 demonstrates that the increase in crack spacing and decrease in length occurred between 2 and 3 layers in build height.

Plate 73 was then deposited on 1 in. baseplate to bridge the gap in build height between 6 and 20 layers in Plate 69, where a transition from sporadic to aligned, more evenly-spaced cracks was seen. Builds of 8, 10, and 12 layers filled the #4, #5, and #6 slots shown in Fig. 4.13. The 8-layer build showed somewhat sporadic cracking like the 6-layer build, but beginning with 12 layers the builds took on a more even character, leading up to the 20- and 40-layer builds from Plate 69.

Figure 4.14 shows a summary of Series 3 surface-breaking cracks on 1 in. baseplates. These images were taken with a stereo microscope and stitched to form a composite image for each deposit. The deposit cracks were traced in yellow and widened with ImageJ to highlight their locations in the builds and to compute average crack length and spacing.

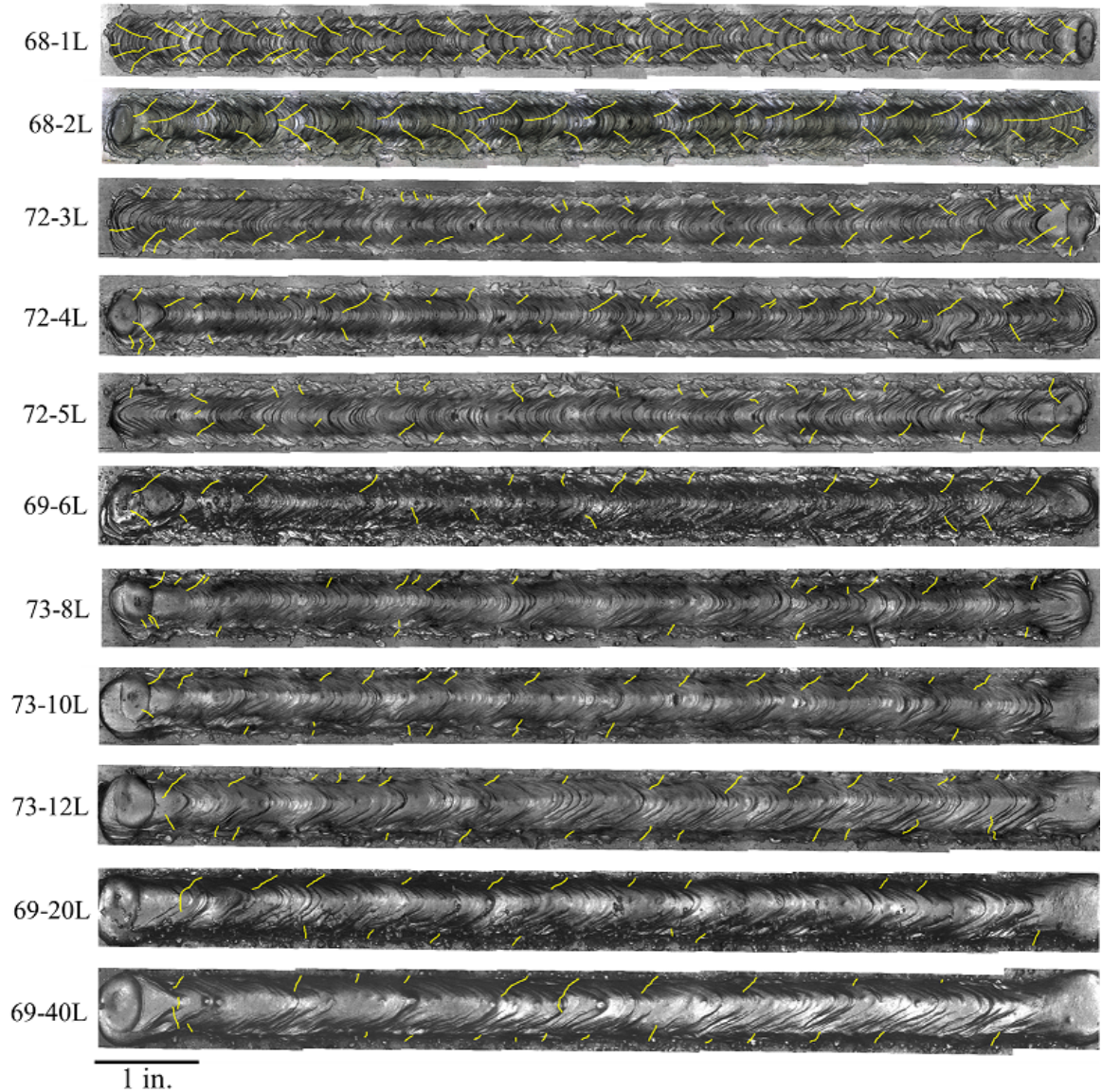


Figure 4.14: Series 3 deposits on 1 in. baseplate highlighting the macrocrack initiation and progression with increasing number of layers. Only cracks that broke the top surface and were visible with the stereo microscope were highlighted.

Figure 4.15 compares the surface-breaking solidification cracks for single-layer deposits made on 1 in. baseplate (Plate 68-1L) and 0.25 in. baseplate (Plate 70-1L).

It is observed that the cracks on the 1 in. baseplate deposit are more regular and also turn to follow the weld line, whereas cracks in the 0.25 in. baseplate deposit are irregular and shorter due to less constraint from the baseplate. There is an asymmetry in degree of cracking for each side of the deposit on thinner plate, likely due to uneven constraint between the adjacent build on the same plate (below) and the clamping fixture (above). The reduced crack length in the 0.25 in. deposit thus agrees with the reduced macrocracking seen in the full deposit made on 0.25 in. baseplate (Plate 46) compared to the 1 in. plate (Plate 50).

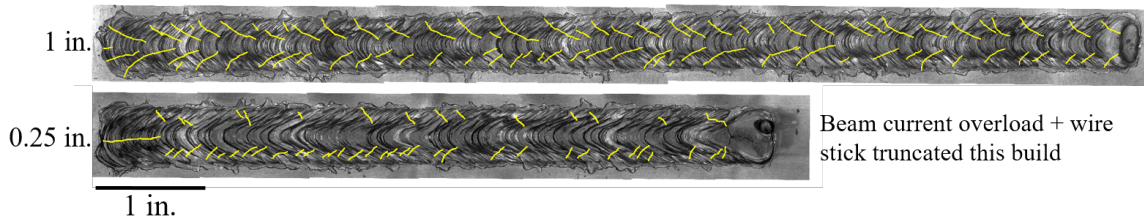


Figure 4.15: 1-layer deposits on 1 in. (Plate 68-1L) and 0.25 in. (Plate 70-1L) baseplate. Cracks in 68-1L turn to follow the weld line, while cracks in 70-1L are shorter due to less constraint from the baseplate.

4.4.2 Deposit Composition

The composition of the deposits varied from the starting wire chemistry due to the vaporization of some Zn and Mg content in the vacuum environment of EBF³. The amount of elemental losses depends on a number of parameters, including beam power, which increases the degree of superheat above the melting point of Al in the molten pool which promotes higher vapor pressures of Zn and Mg; beam focus, which affects local superheating, with more focused conditions accentuating losses; and travel speed, which affects the time spent molten of a particular volume element. All of these factors together also affect the volume that is remelted and available to lose volatile alloying constituents. Other factors such as raster frequency and raster shape were explored in separate trials with the proprietary alloy and seem to suggest a relation to vaporization losses as well.

Table 4.7 shows the results from DCP-AES analysis of the wire and deposits. The compositions of the Plate 46 and 50 deposits were within 3% of each other. This minimal variation makes sense, since these builds were deposited with the same machine parameters and average background temperature but on baseplates of differing thickness.

Table 4.7: Wire and deposit chemistries as measured via DCP-AES analysis by Luvak Laboratories Inc.

Material	Zn (wt.%)	Mg (wt.%)
7075 wire	5.70	2.42
Plate 19	3.16	1.73
Plate 45	3.81	1.97
Plate 46	4.26	2.15
Plate 49	3.67	1.97
Plate 50	4.15	2.11
Plate 60-C7	2.06	1.47
Plate 60-C8	2.66	1.97

A significant difference in composition may be noted between Plates 49 and 50, with Plate 49 exhibiting an 8% higher Zn loss and a 6% higher Mg loss than Plate 50. These deposits shared the same beam parameters, but the background printing temperature for Plate 50 was reduced to slightly more than half that of Plate 49. The higher solute losses in the Plate 49 deposit may be attributed to a smaller thermal gradient between the melt pool and the bulk temperature of the deposit, which would permit each layer to remain molten for longer to allow for more vaporization losses. As seen in the vapor pressure vs. temperature curve in Fig. 2.14, the vapor pressures of Zn at 170°C and 300°C are separated by three orders of magnitude, resulting in a much greater driving force for Zn (and likewise, Mg) evaporation at higher background temperatures.

Comparison of the results from Plates 45 and 46 revealed the effect of a 67% increase of travel speed on composition, where the Plate 46 deposit retained 8% more Zn and 7% more Mg than Plate 45. This is expected, since faster travel speeds reduce the time for elemental losses to occur.

With a focused beam and a travel speed of 24 ipm, the Plate 60-C8 deposit exhibited the second most alloying element losses, with a 64% Zn loss and a 39% Mg loss from the starting wire composition. Comparing the composition of Plate 45 with Plate 60-C8 reveals that increasing the beam focus from BF = 305 to BF = 341 resulted in an additional 30% loss in Zn and no measurable loss in Mg for the same travel speed.

The deposit that lost the most Zn and Mg was C7, despite C8 exhibiting a keyhole condition involving the most superheating. This is likely due to C7 having a higher surface area to volume ratio from its shallower melt pools, allowing more solute to escape during solidification than rapidly-freezing keyholed melt pools in C8. Compared

to Plate 45, which shared the same travel speed, C7 lost 46% more Zn and 25% more Mg due to overfocusing the beam.

The results show that there were significant alloying element losses that drove the deposit compositions away from that of 7075 wrought product. The elemental losses are expected to exhibit a measurable reduction in hardness and strength due to lower solute available to form strengthening precipitates compared to the original wrought material.

4.4.3 As-Deposited Microstructures

Polished cross sections were observed in the SEM to study the precipitates and cracking in the deposits of interest, as well as for EBSD grain size analysis. Samples were then etched and observed with optical microscopy to study the overall microstructure and cracking of the deposits.

All deposits showed evidence of liquation and liquation cracking at the deposit-baseplate intersection. Figure 4.16 depicts the typical liquated microstructure at the baseplate intersection, with significant precipitation of second phases on grain boundaries. From the linescan in Fig. 4.16(d), it is found that some of the liquated phases are an Al-28Zn-14Cu-13Mg eutectic. Some voids at the grain boundaries are visible in Figs. 4.16(b) and (c), which correlate with the low-density regions seen in high-resolution XCT scan data, shown in Section 4.4.4. There are also heavy amounts of precipitation within the grains, as observed in Fig. 4.16(c), suggestive of the material sitting at elevated temperatures for long amounts of time - a condition also conducive to liquation.

The thickness of the liquated region below the deposit in the baseplate exhibited some variation depending on parameters and temperature of the baseplate during deposition. In addition, the thickness changed depending on the measurement location, as liquated regions between the bounds of the raster pattern directly below the deposit were thicker than regions on the outer edge of the FZ. In Plate 49, the thickness of the liquated region below the deposit was on the order of 0.8 mm, while near the outer edge it measured only 0.3 mm. In contrast, the liquated region for Plate 46 (170°C lower baseplate temperature) was on the order of 0.7 mm below the deposit and 0.2 mm on the outer edge.

In addition to the liquation cracks found at the deposit-baseplate intersection, other fine-scale microcracks were observed throughout the deposit microstructures. Figure 4.17 shows a typical region of microcracks from the Plate 49 deposit. These

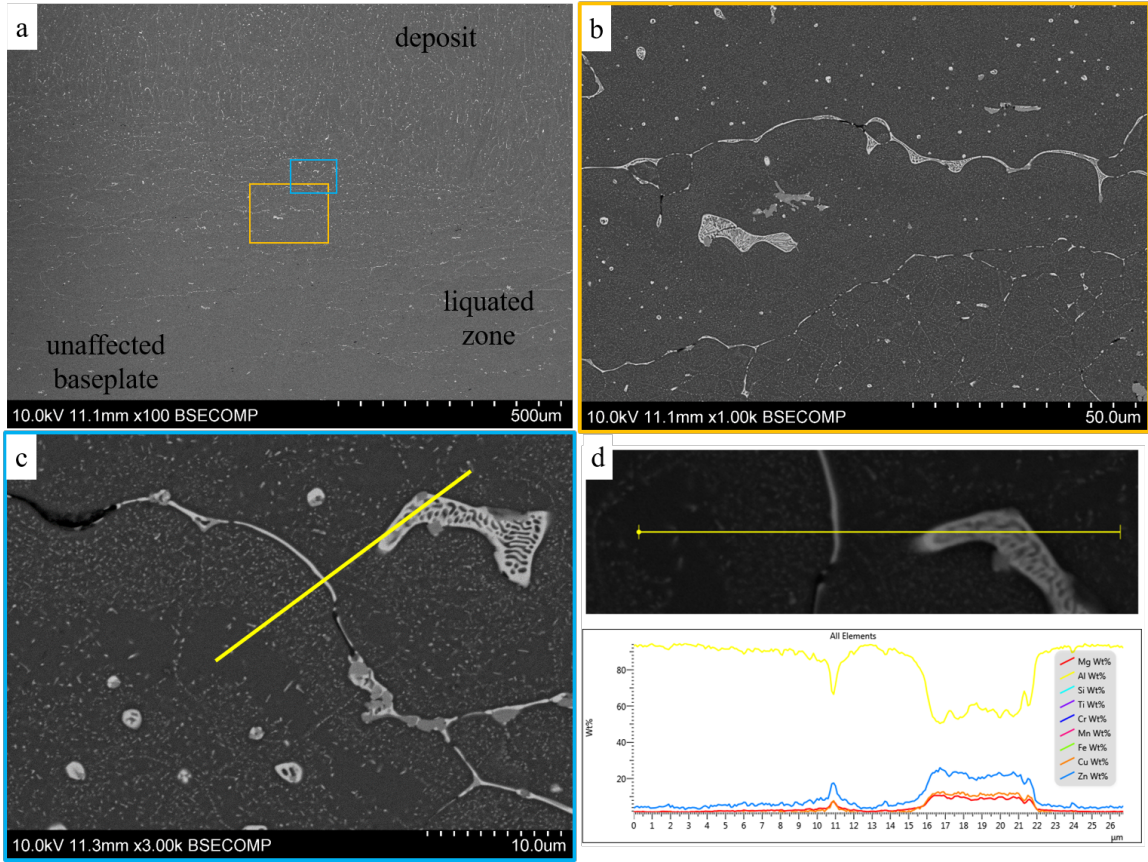


Figure 4.16: (a) Polished microstructure showing the intersection of the Plate 49 deposit with the baseplate, (b) copious grain boundary liquation, (c) region outlined in blue for linescan, (d) linescan showing Al-28Zn-14Cu-13Mg eutectic draping the grain boundaries.

were found in XCT scans (Section 4.4.4) to always occur below the topmost layer of wall deposits. Given the microstructural scale of these cracks, polished cross sections were the optimum method for studying their behavior in the deposits.

Such regions of microcracks typically appeared remote from the deposit macrocracks. The L-ST plane was found to be the best direction to observe these cracks, since they typically formed perpendicular to the weld line for the deposits. Furthermore, microcracks were only observed between large or elongated grains in the microstructure.

In high-resolution XCT scans of Plates 46, 49, and 50 in Section 4.4.4, lower-density regions were found separating the topmost layer's FZ and the deposit below. Polished cross sections, such as in Fig. 4.18, show that those low-density regions may form from shrinkage between dendrites at that interface, coupled with Mg-rich precipitates. Both shrinkage voids and Mg-rich particles would appear with a lower

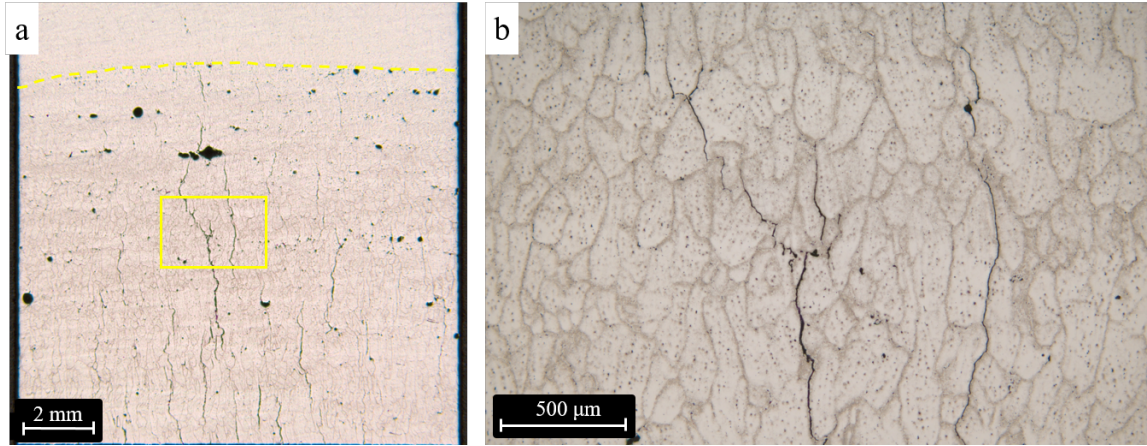


Figure 4.17: (a) L-ST etched cross section showing a field of microcracks below the FZ boundary (dotted yellow line) in Plate 49, and (b) 50x micrograph showing two of these interdendritic microcracks running between elongated grains in the microstructure.

density than the Al matrix in XCT and backscatter mode (BSE) of the SEM. This low-density band in Fig. 4.18(a) is approximately 220 μm thick.

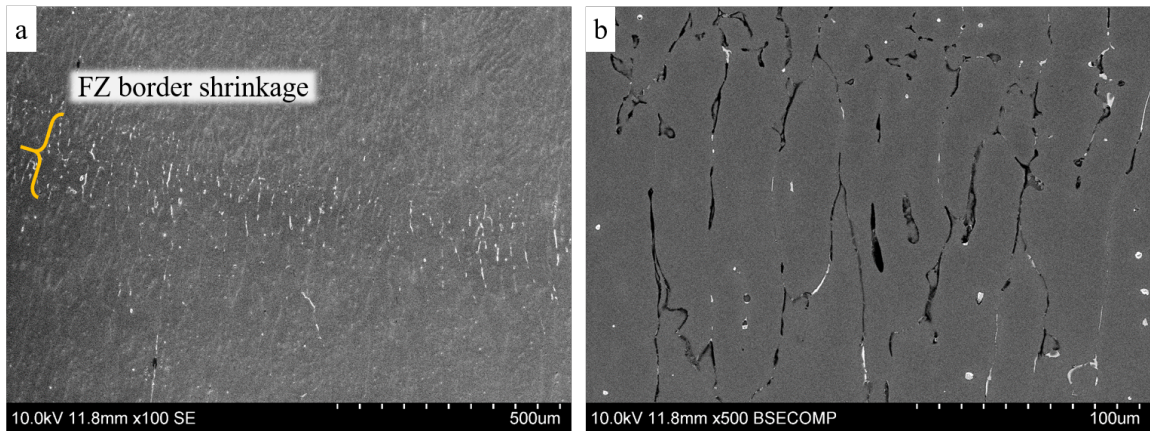


Figure 4.18: (a) Shrinkage at the border of the topmost layer's FZ with the layers below, (b) 500x image of the low-density region, with Mg-rich particles and voids inhabiting the interdendritic spaces.

The metallurgical sample for Plate 49 happened to intersect one of the large macrocracks, so the intercepted crack surface was imaged as a preview of its surface morphology. Figure 4.19 depicts a topological image of the crack intersecting the polished cross section, and a higher magnification image showing the dendritic character of the macrocrack surface. The dendrites show that the crack formed while metal was still solidifying, a feature typical of solidification cracks.

Plate 49 also exhibited regions of grain boundary segregation, or liquation. These

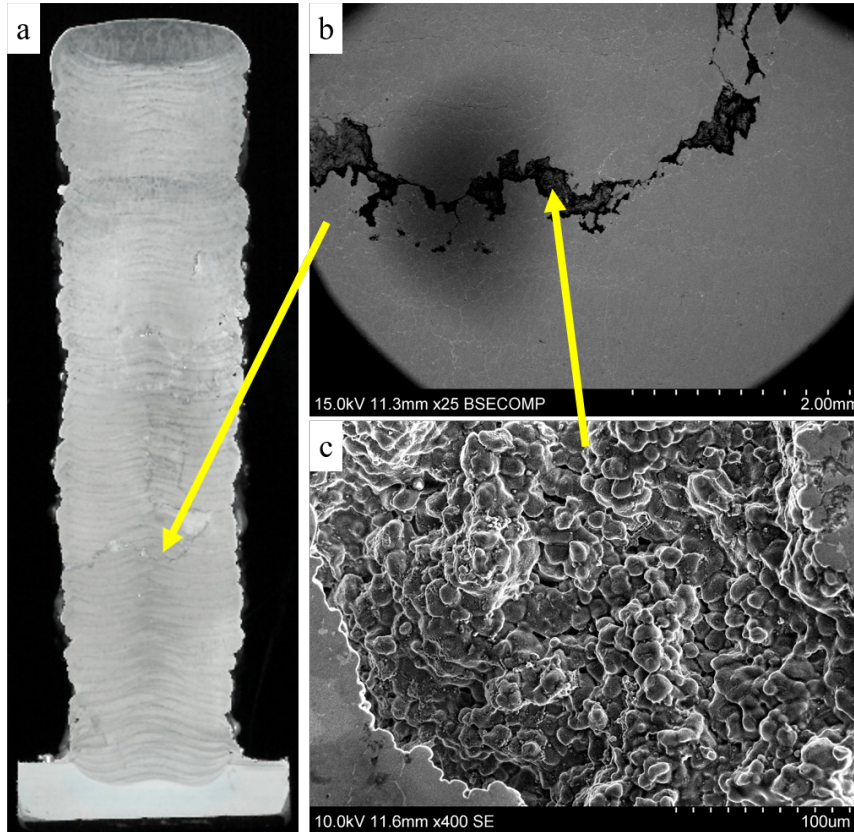


Figure 4.19: (a) The initial Plate 49 metallurgical sample intercepted a macrocrack running through the deposit. (b) BSE image highlighting the intercepted macrocrack. (c) The exposed crack surface appears to have a dendritic character.

were sometimes accompanied by long microcracks on the grain boundaries, likely from insufficient solute available to heal the cracks formed by strains on the liquated grains. Figure 4.20

In contrast to the macrocrack and microcracks in the Plate 49 metallurgical sample, the Plate 46 sample only demonstrated microcracks. These microstructural-level cracks were found with high-resolution XCT and confirmed in polished cross sections to run intergranularly in both the vertical and horizontal directions. Figure 4.21 depicts such cracks, with Fig. 4.21(a) showing the location of a small microcrack between elongated grains, and (b) showing a 1000x view of the microcrack and Al-28Cu-10Mg-4Zn particles unable to fill it.

Figure 4.22 depicts the deposit macrostructure and microstructure of Plate 60-C8, which vastly differs from what was seen in Plates 46 and 49. Of all the 7075 deposits, C8 possesses the sharpest and deepest melt pools, which is understandable given it is the only parameter set with a focused beam. This deep melt pool shape looks similar

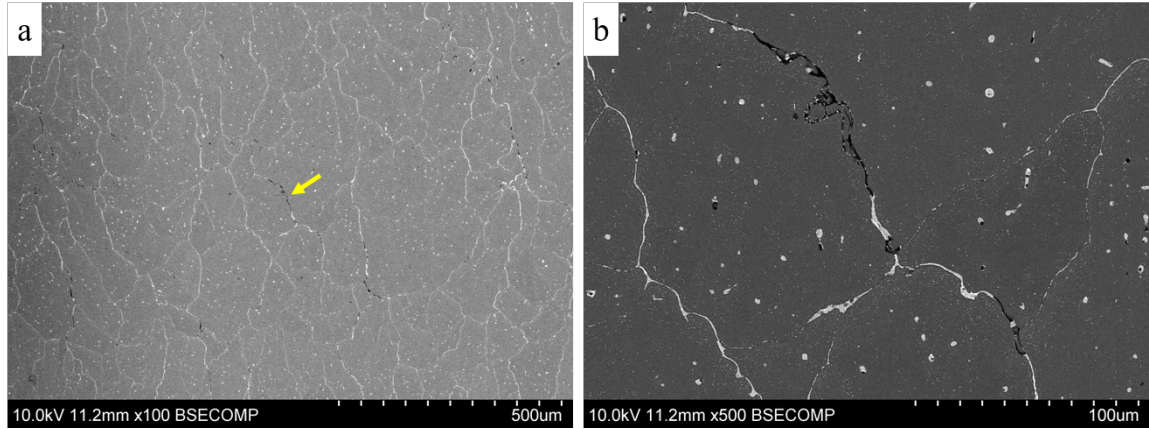


Figure 4.20: (a) 100x BSE image from the Plate 49 deposit showing liquated grains with low-density regions corresponding to microcracks, (b) 500x BSE image showing a microcrack and liquated grain boundaries.

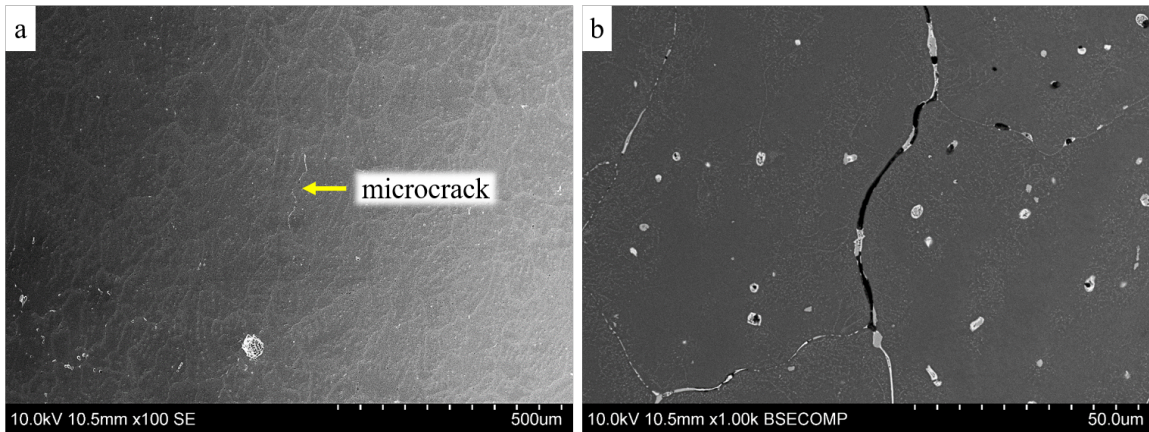


Figure 4.21: (a) 100x SE image showing elongated grains in the Plate 46 microstructure, with a microcrack denoted by the yellow arrow. (b) 1000x BSE image of the microcrack, as well as nearby eutectic and Al-28Cu-10Mg-4Zn precipitates decorating other grain boundaries.

to the keyhole melt pools in welding, where a high depth-to-width ratio promotes thin HAZs and finer grain structures, shown in Fig. 3.3(b).

As seen in Fig. 4.22(b), the regions of deep molten pools are characterized by fine, equiaxed grains, while the regions outside of the focused melt pools possess large grains elongated in the direction of the melt pools. This contrast in grain size and shape was also not observed in other EBF³ deposits and is attributed to the special case of a focused, rastered beam. As will be seen in Section 4.4.4, this contrast in grain size disrupted the typical macrocrack formation of other deposits and greatly reduced the microcrack density as well, in spite of alloy losses of 64% Zn and 39%

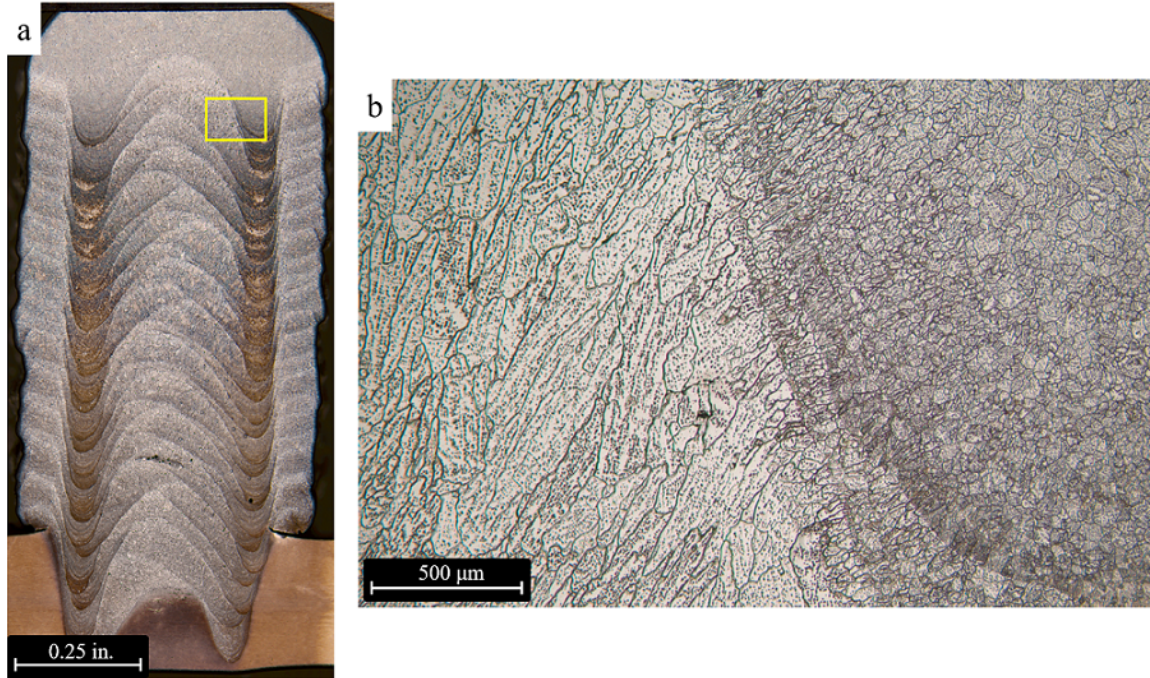


Figure 4.22: (a) Polished and etched LT-ST cross section of the Plate 60-C8 deposit. The pointed, heavily-etched regions of the deposit are where the sharply-focused and rastered beam struck the sample. (b) Higher magnification image showing the border between the deep melt pool with fine, equiaxed grains and the region outside containing large, elongated grains angled towards the keyholed region.

Mg.

Grain Sizes and EBSD

Samples from Plates 49, 50, and 60-C8 were prepared in the LT-ST plane for EBSD to study the grain sizes and orientations in the microstructures. Table 4.8 lists the grain size measurements obtained from the EBSD scans, which are discussed subsequently. The measures of grain size are area-averaged grain size, which assumes a circular grain shape and the average is weighted by area rather than by total number of grains, as well as vertical and horizontal intercept lengths as a measure of grain anisotropy.

Figure 4.23 shows the (a) image quality (IQ) map and (b) associated EBSD IFP normal direction map for the Plate 49 sample. The IQ map shows microcracks running between certain grains in the microstructure. The EBSD IFP map shows the distribution of grain sizes and orientations for the sample, which is characterized by a number of large grains elongated in the ST direction, as well as some smaller grains

Table 4.8: 7075 deposit grain sizes as measured by EBSD. Three measures of grain size are given - area-averaged grain diameter, vertical intercept length, and horizontal intercept length - for comparison to other samples, as well as to quantify the degree of anisotropy in grains.

Sample	Area-Averaged Grain Diameter (μm)	Vertical Intercept Length (μm)	Horizontal Intercept Length (μm)
49	217.0	117.0	65.3
50 below crack	91.8	51.6	36.1
50 above crack	138.6	72.4	46.0
60-C8 large	151.8	71.2	54.6
60-C8 fine	38.4	19.8	19.3

likely denoting a layer boundary. The area-averaged grain size is 217 μm , greater than any other sample observed in this study. The average grain aspect ratio given by the vertical and horizontal intercept lengths is around 1.8, although some of the longest grains in Fig. 4.23(b) have an aspect ratio over 6.3.

This elongated microstructure and large grains are likely correlated to the high background temperature of the deposit, since slower cooling rates would allow larger grains to form and grow epitaxially. Despite these grain size statistics, the microstructure still possessed a fairly random texture, with a maximum multiple of uniform density (MUD) value of 2.4.

The typical Plate 50 microstructure, given in Fig. 4.24(a), was less anisotropic than that of Plate 49. The averaged aspect ratio was on the order of 1.4, with an area-averaged grain diameter of 91.8 μm .

A second EBSD scan, shown in Fig. 4.24(b) was taken for Plate 50 in a region above a macrocrack running through the sample. In contrast to the relatively small grains in the typical Plate 50 microstructure, the area-averaged grain diameter was 50% greater, with an average grain aspect ratio of 1.6. This increase in grain size and aspect ratio is due to the region of the macrocrack being thermally cut off from the material directly below it. Thus, heat was not able to dissipate effectively, resulting in a higher local temperature and allowing grain growth to occur.

Two regions in the Plate 60-C8 microstructure were observed with EBSD and are shown in Fig. 4.25. The first was the large-grained region between the bands of fine, equiaxed grains, shown on the left in Fig. 4.22(b). This region consisted of grains with an area-averaged grain diameter of 151.8 μm , which is larger than those observed in the typical Plate 50 sample. The average aspect ratio of grains in this region was

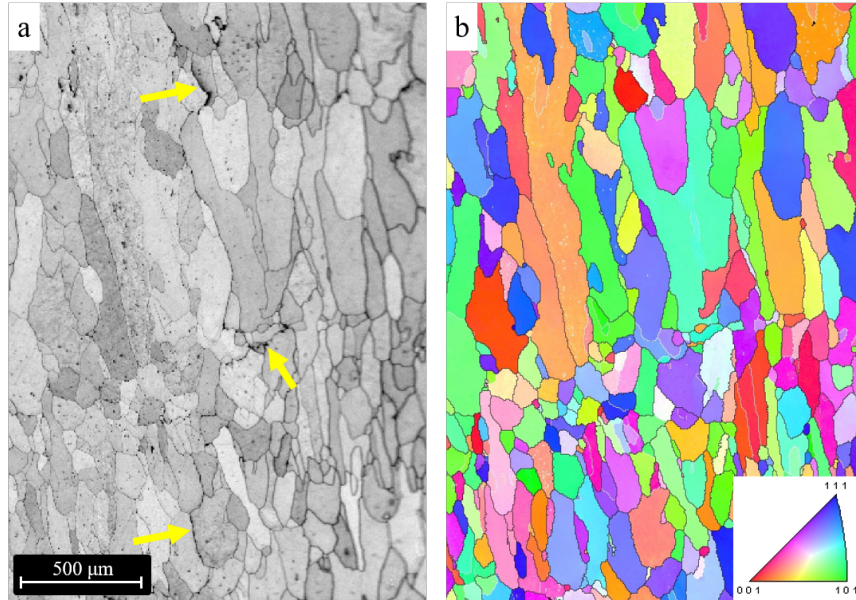


Figure 4.23: (a) Image quality map showing microcracks running between elongated grains in the Plate 49 microstructure, (b) EBSD IFP normal direction map showing grain orientations and sizes.

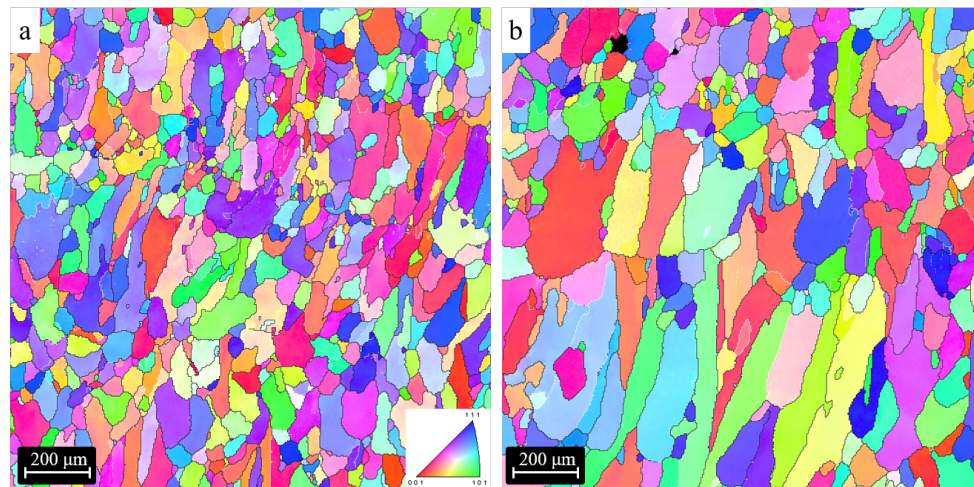


Figure 4.24: (a) EBSD IFP normal direction map showing grain orientations and sizes in a typical region in the Plate 50 microstructure, (b) EBSD map showing larger grains in a region directly above a macrocrack which lost thermal conductivity with the deposit below.

measured to be 1.3, although the vertical and horizontal intercept measurements do not account for the tilt in the microstructure due to thermal gradients from the sharply-focused regions. The aspect ratio is thus expected to be greater than the number computed from Table 4.8. Fig. 4.25(a) shows microcracks running between the elongated grains in the microstructure.

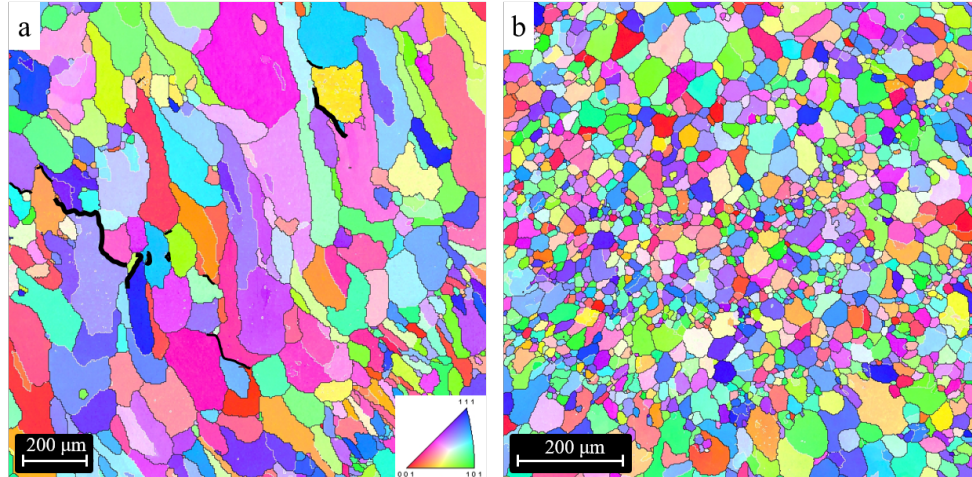


Figure 4.25: (a) EBSD IFP normal direction map showing elongated grains in the large-grained region of the Plate 60-C8 microstructure. Microcracks between large grains are outlined and bolded in black for emphasis. (b) EBSD map showing refined, equiaxed grains in the sharp-focused region of 60-C8 sample.

In contrast to the large grained regions of the Plate 60-C8 sample, the two bands of fine grains (Fig. 4.25(b)) show a 4x reduction in grain size. Furthermore, the grains in these regions are equiaxed, owing to faster cooling rates from the quenching effect of the keyholed beam. This region is also characterized by a low MUD value of 1.4, which makes sense since regions under the keyholed beam freeze rapidly and would not have time to grow epitaxially.

As will be seen in Section 4.4.5, this microstructural banding and mismatch in grain size disrupts the typical macrocrack formation and reduces the density of microcracks as well.

4.4.4 Non-Destructive Evaluation

Unlike the 2219 deposits, which were scanned immediately following deposition, the 7075 deposits were not sent for XCT analysis immediately. Rather, the deposits were sectioned for metallurgical samples once removed from the EBF³ chamber to quickly check the deposit chemistry with EDS before proceeding to subsequent builds. As a result, no full-deposit XCT scans exist for the 7075 Series 1 and 2 trials. However, full scans were captured for the 40-layer deposits from Plates 69 and 71.

Later, high-resolution scans were desired to examine regions of microcracking that were barely visible in the low-resolution, partial-deposit XCT scans. Cylindrical specimens were extracted from regions of interest within certain deposits to gain

three-dimensional information on fine-scale cracking and porosity distributions.

Low-Resolution XCT Scans

XCT scans were completed on the largest remaining section of each of the Series 1 plates. The resolution for these scans varied from 50 to 75 μm depending on the size of the remaining portion of the deposit. These 70 μm scans displayed larger pores and macrocracks that resulted from various parameter sets.

Figure 4.26 shows the XCT data for select Series 1 deposits, with parameter sets denoted in Table 4.3. The most apt comparisons in cracking state may be made between Plates 46 and 50, and Plates 49 and 50, the former of which shows the effect of quadrupling baseplate thickness on the stress state and the latter of which shows the effect of halving the background printing temperature.

From Fig. 4.26, it is observed that most macrocracks for Plates 49 and 50 initiate at the baseplate intersection and propagate through the deposits' height at an angle of approximately 65° degrees. Table 4.9 lists results for the average crack angle, width, and spacing for each deposit. While cracks remain angled where they appear in Plates 46 and 50, the cracks turn vertically at a height of 0.6 in. from the baseplate in the Plate 49 deposit.

Table 4.9: Summary of macrocrack properties in notable Series 1 deposits.

Plate	Avg. Spacing (in.)	Crack Width (in.)	Angle w BP
46	0.78	0.007	$75.7^\circ \pm 3.0^\circ$
49	0.70	0.011	$63.5^\circ \pm 4.8^\circ$
50	0.47	0.009	$67.6^\circ \pm 3.1^\circ$

The Plate 49 deposit demonstrated a higher average crack spacing and wider cracks than Plate 50. The Plate 46 deposit did not exhibit measurable cracks near the baseplate intersection, but the two cracks near the top of the deposit were measured to occur at an angle of 75.7° to the baseplate and were spaced by 0.78 in.

Figure 4.27 shows slices from XCT scans for the two 40-layer deposits in the Series 3 study, with Plate 69 deposited on 1 in. baseplate and Plate 71 on 0.25 in. baseplate. Both images show cracks initiating near the baseplate and traveling through the deposit height at an angle of 70° with respect to the horizontal. The images in Fig. 4.27 are composite images with scan slices from each face of the deposit overlaid to show how the crack presentation changes within the deposit. Cracks that are angled

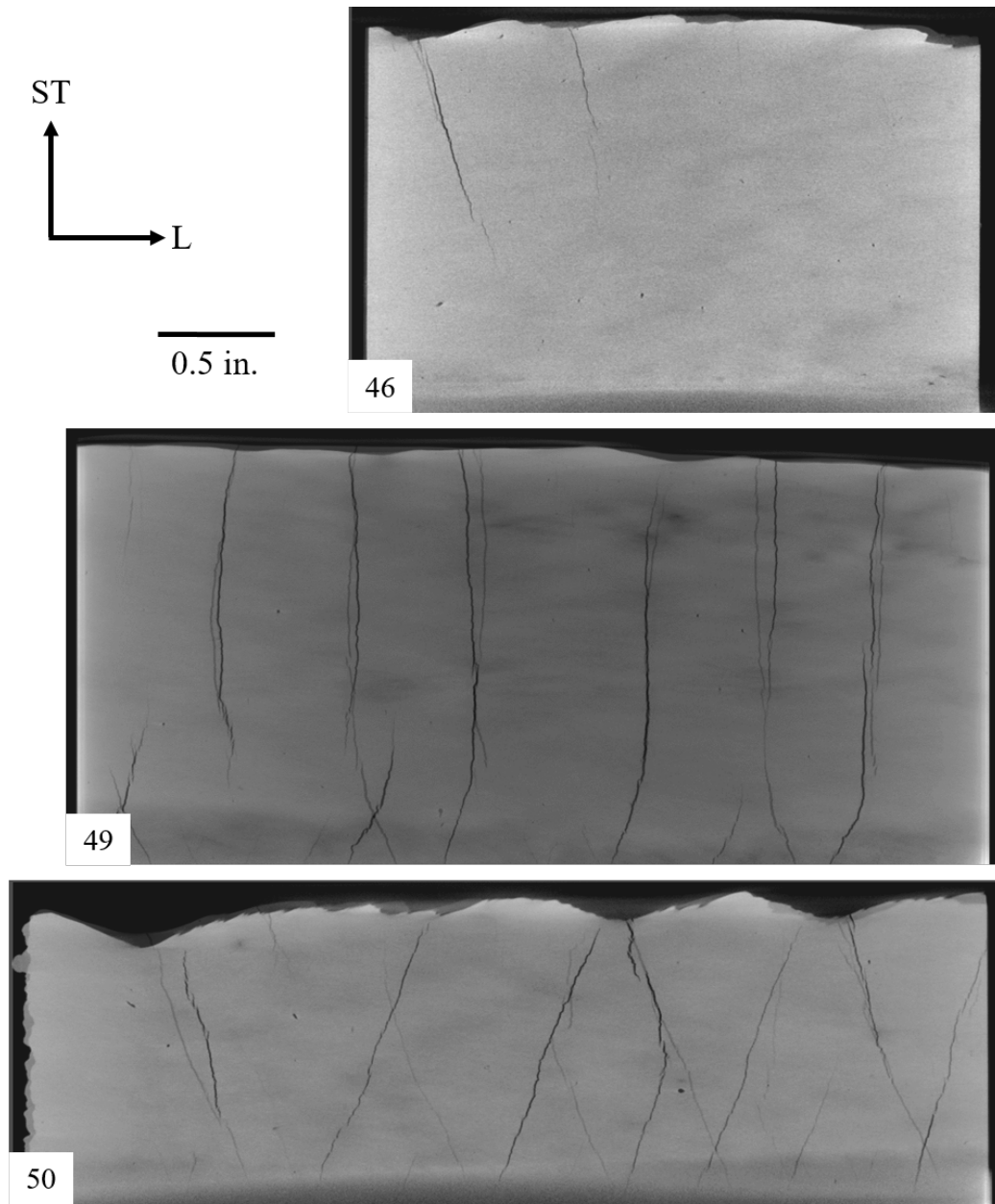


Figure 4.26: Low-resolution XCT composite images of the Plate 46, 49, and 50 deposits highlighting macrocracks on the front (darker) and back (lighter) faces of each deposit.

at a positive 70° are on the “front” face of the deposit, while those angled oppositely appear on the back face of the deposit.

The 1 in. baseplate scan for Plate 69 shows cracks with average spacing of 0.55 in. These cracks extend through nearly the full height of the deposit, although all but one terminate shy of the top of the deposit. The cracks in the Plate 69 deposit penetrate

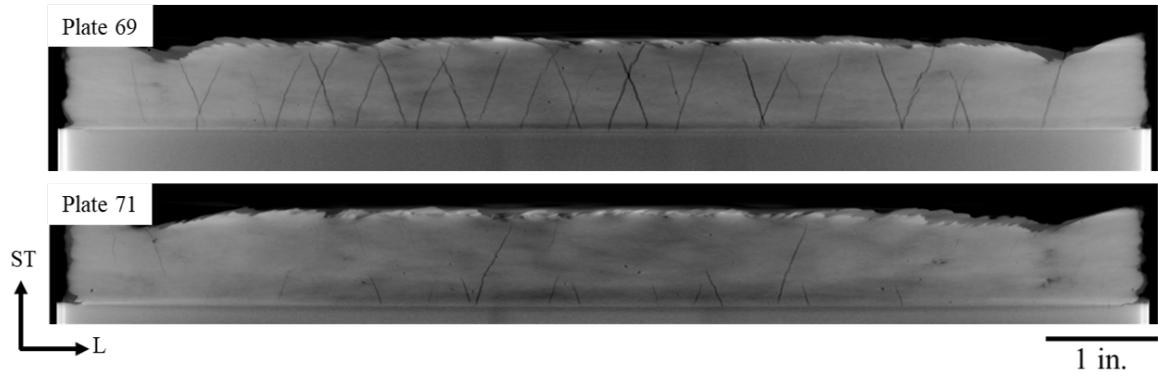


Figure 4.27: XCT composite images of the Plate 69 and 71 40-layer deposits showing macrocracks on the front and back faces of each deposit.

nearly half the deposit width, averaging 0.21 in. in length. The Plate 71 scan shows an average crack spacing of 0.8 in., and their penetration into the deposit width is reduced to 0.16 in. at most. Furthermore, the Plate 71 cracks have a shorter extent through the deposit height than those in Plate 69 due to reduced baseplate constraint. These scans show that thinner baseplates result in fewer and shorter macrocracks.

The low-resolution XCT scans sometimes depicted blurry regions of what were suspected to be microcracks, shown in Figs. 4.28(a) and (b). These regions typically appeared between macrocracks. As expected, the faint, vertical indications of cracks in Fig. 4.28(b) were confirmed through polished cross sections to be microcracks between elongated grains in the microstructure, shown in Fig. 4.28(c).

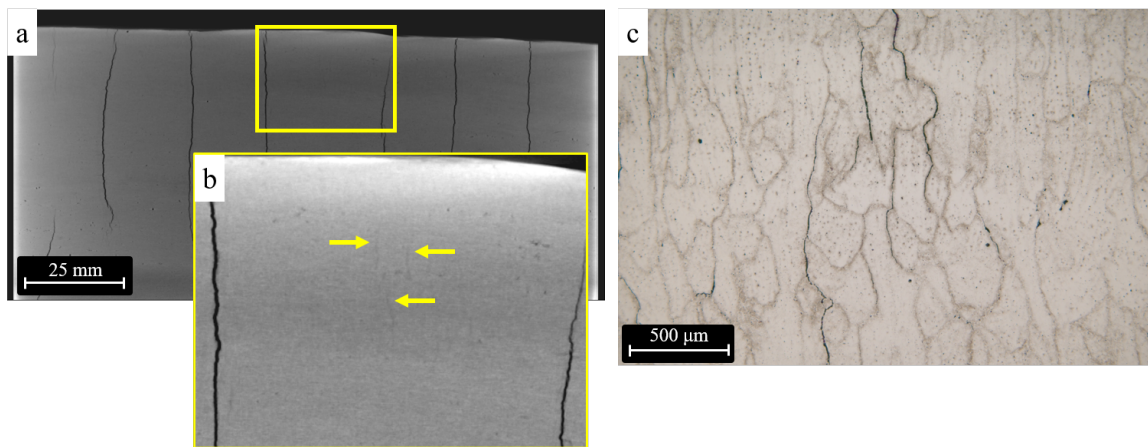


Figure 4.28: (a) 70 μm XCT scan showing (b) blurry regions of microcracks. (c) A polished cross section of this region better captures the microstructural level cracking between columnar grains.

It is important to note that cracks with widths near or below the resolution of

the XCT scans, such as in Figs. 4.9 or 4.28(c), may not appear in coarse XCT scans. Thus, the non-destructive evaluation should serve as a guide for identifying regions of cracking larger than the scan resolution but not judge a deposit “defect free” without metallurgical analysis proving so.

High-Resolution XCT Scans

To sample a smaller region of a deposit for a higher resolution XCT scan, 0.4 to 0.5 in. diameter cylinders were extracted from various deposits with a wire-EDM. These cylinders sampled smaller regions containing the topmost layer and microcracks for Plates 46, 49, 50, and 60-C8, as well as a macrocrack for Plate 50.

The 7 μm scans were analyzed with ImageJ to highlight the microcracks and generate results for comparing the degree of microcracking between deposits. Four evenly-spaced slices were isolated from each XCT scan as a pseudo-random sampling of the microstructure. Figure 4.29 displays a representative slice from each deposit, with microcracks highlighted in yellow and widened for ease of viewing.

The plane of the slices was chosen for each deposit as the direction (L or LT) normal to the majority of the cracks in that region. This resulted in the selection of a LT-normal plane for Plates 46, 49, and 50 and a L-normal plane for Plate 60-C8. These slices were used for calculating average crack length, longest crack, and crack density for each deposit. The crack measurement results are given in Table 4.10.

Table 4.10: Comparison of microcracking between Plates 46, 49, 50, and 60-C8. Refer to Fig. 4.29 for a representative XCT slice from which this data was generated.

Plate	Average Crack Length (μm)	Longest Crack (μm)	Crack Density ($\mu\text{m}/\mu\text{m}^2$)
46	384	1948	0.00027
49	649	4723	0.00050
50	533	3111	0.00021
60-C8	200	610	0.000092

As Table 4.10 displays, the microcrack density is closest between Plates 46 and 50, both of which share the same background printing temperature and parameter set but differ by their baseplate thickness. Plate 50 exhibits a 40% increase in the average crack length over Plate 46, and its longest observed crack is 60% greater than that of Plate 46. These differences may be related to the greater baseplate thickness of Plate 50, although a greater statistical basis would be required. Plate 49 exhibited the greatest cracking metrics of the observed deposits, with essentially double the

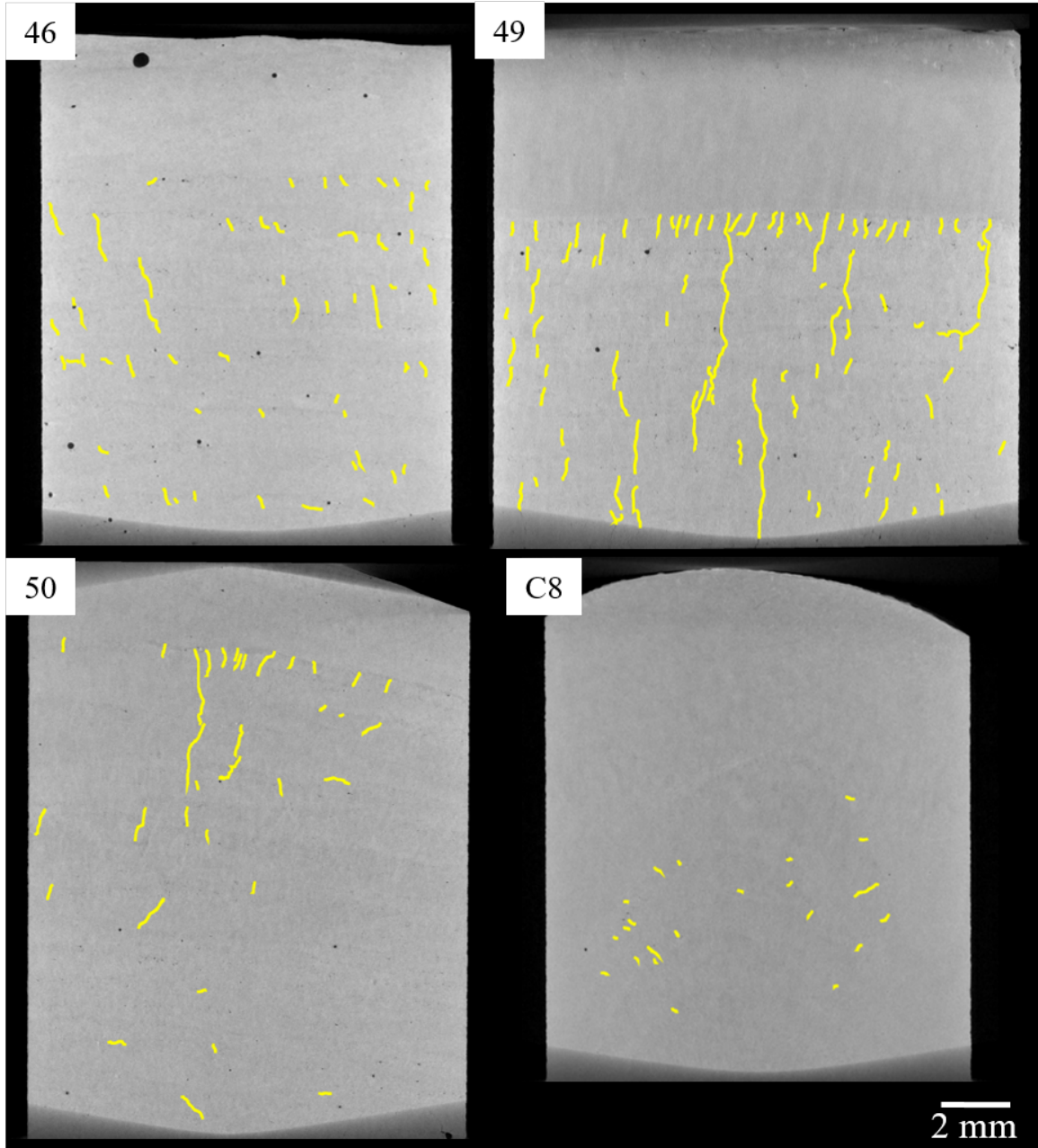


Figure 4.29: Comparison of microcracking between Plates 46, 49, 50, and 60-C8. Note that the planes selected for cracking image analysis depending on the major direction of the cracks so that the slices would be selected normal to the cracks.

crack density of Plates 46 and 50. Plate 49 also demonstrated the highest average crack length and the longest crack of all the observed deposits.

In stark contrast to the other samples, Plate 60-C8 demonstrated the lowest levels of microcracking across the board. With the primary crack direction aligned with the L direction rather than the LT, and with cracks angled perpendicular to the melt pool,

C8 exhibited a 2.9x and 5.4x lower crack density than Plates 46 and 49, respectively. Furthermore, its average crack length and longest crack were much lower than those of Plate 46, which exhibited the next lowest cracking. Thus, C8 represents a significant improvement in microcracking over other deposits. These results, coupled with the lack of macrocracking in the steady-state region of C8, demonstrate that this build has a significant reduction in cracking compared to the other deposits.

In addition to the microcracking seen near the top layer of the deposit, segregation and thin cracks were also detected at the baseplate intersection for scans taken with the cylinders from Plate 46 and 50. Figure 4.30 shows an XCT scan of the intersection of the Plate 46 deposit with the baseplate. The brighter strips occurring right at the interface are traces of grain boundary liquation. In contrast, the dark streaks at the interface are evidence of liquation cracks, which form from molten pool contraction straining liquated baseplate grains and overcoming the strength of the liquated material.

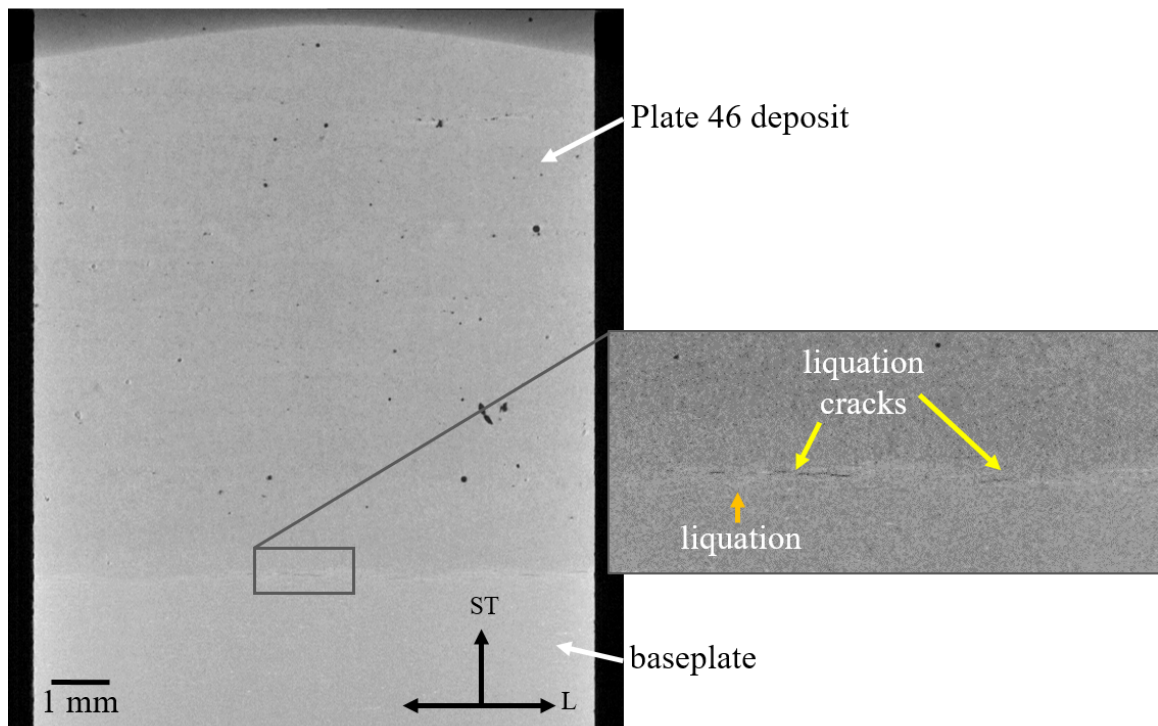


Figure 4.30: 8 μm XCT scan of the Plate 46 deposit highlighting the intersection of the deposit with the baseplate. The inset shows an enlarged region where both liquation and liquation cracking occur at the interface. The change in contrast between the deposit and baseplate is due to the vaporization of alloying constituents in the deposit, making it less dense.

The above findings were confirmed and clarified through metallurgical cross sec-

tions, which were shown in Section 4.4.3. These help overcome the limitations of XCT scan resolution.

4.4.5 Fractography

The sections below contain the SEM micrographs taken of crack surfaces after splitting open various macrocracks in Plates 46, 49, and 50. These depict general fracture morphology, with dendritic structures suggesting solidification cracking.

Solidification Cracking Features

As defined by Kou [28], solidification cracking occurs in the FZ of weld metal. Such cracking proceeds interdendritically, leaving gaps between neighboring dendrites. As a result, dendritic features are expected on solidification crack surfaces. There may be interdendritic second phases on the crack surface from the remaining liquid film that could not heal the cracks.

Macrocracks were identified and opened from Plates 46, 49, and 50. The cut plans for these walls are documented in Appendix C, which shows the locations of macrocrack samples, metallurgical samples, and high-resolution XCT cylinders superimposed on the partial-deposit XCT scan.

Plate 46 crack surfaces were of interest since this plate had the fewest macroscopic cracks of Plates 46, 49, and 50. Two samples intersecting macrocracks high in the build were extracted via EDM to capture the entire deposit width, as shown in Fig. C.1. Figure 4.31 displays the macroscopic crack surface for Plate 46's "Crack 1", as well as micrographs of particular crack surface features.

The majority of the crack surface for this sample was dendritic in character, with various presentations of dendrite fingers versus trunks. Figures 4.31(a) and (b) show a typical dendritic region with a secondary crack branching perpendicularly from the macrocrack surface. Figures 4.31(c) and (d) show a different region, where the typical, knobby dendrites are replaced with horizontally-banded dendritic features. These dendrites seem to be coated in a thin, denser Al-10Zn-5Mg phase, suggestive of the final liquid in solidification. This sample will be discussed further with regards to liquation cracking.

Two crack surfaces in Plate 49 were examined, as is shown in the cut plan in Fig. C.2 in Appendix C. Both exhibited similar features, so fractographs from Crack 2 are shown. Crack 1 was extracted with a bandsaw, while Crack 2 was extracted at

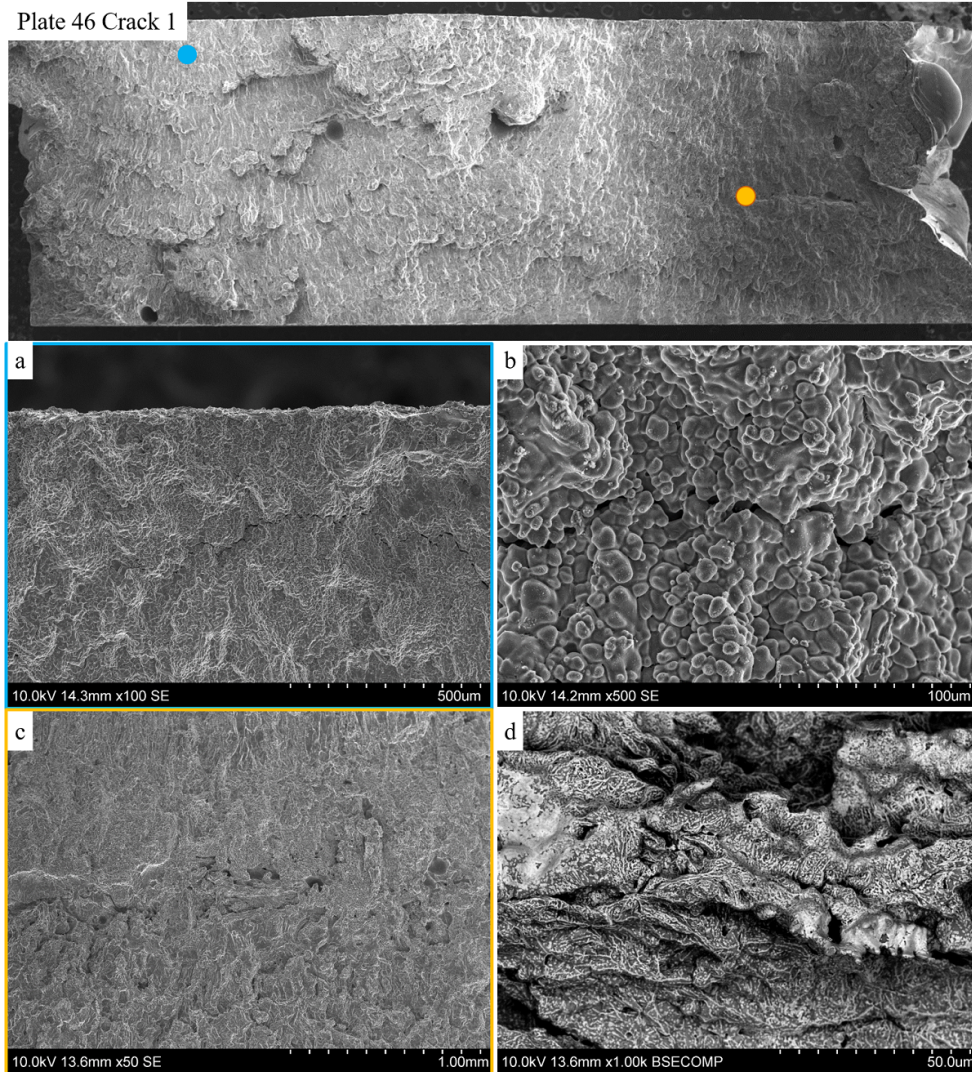


Figure 4.31: (a) Typical dendritic region of the crack surface, (b) 500x image of the dendrites and a secondary crack, (c) Another dendritic region, with horizontal features, (d) 1000x BSE image showing a thin, Al-10Zn-5Mg film coating dendritic features

the same time as the cylinder by EDM. Fig. 4.32 displays the Crack 2 surface and its resident dendritic features.

The dendrites shown in Fig. 4.32(a) show preference of the vertical direction for growth, suggestive of the columnar grains seen in the microstructure. Higher magnification SE and BSE images in Fig. 4.32(b) and (c), respectively, show the fine-scale dendrites, Fe-containing spindle-like particles, and feathery precipitates decorating the interdendritic spaces.

A macrocrack from Plate 50 was also intercepted and examined in the SEM to observe the character of its fracture surface, with the cut plan given in Fig. C.3.

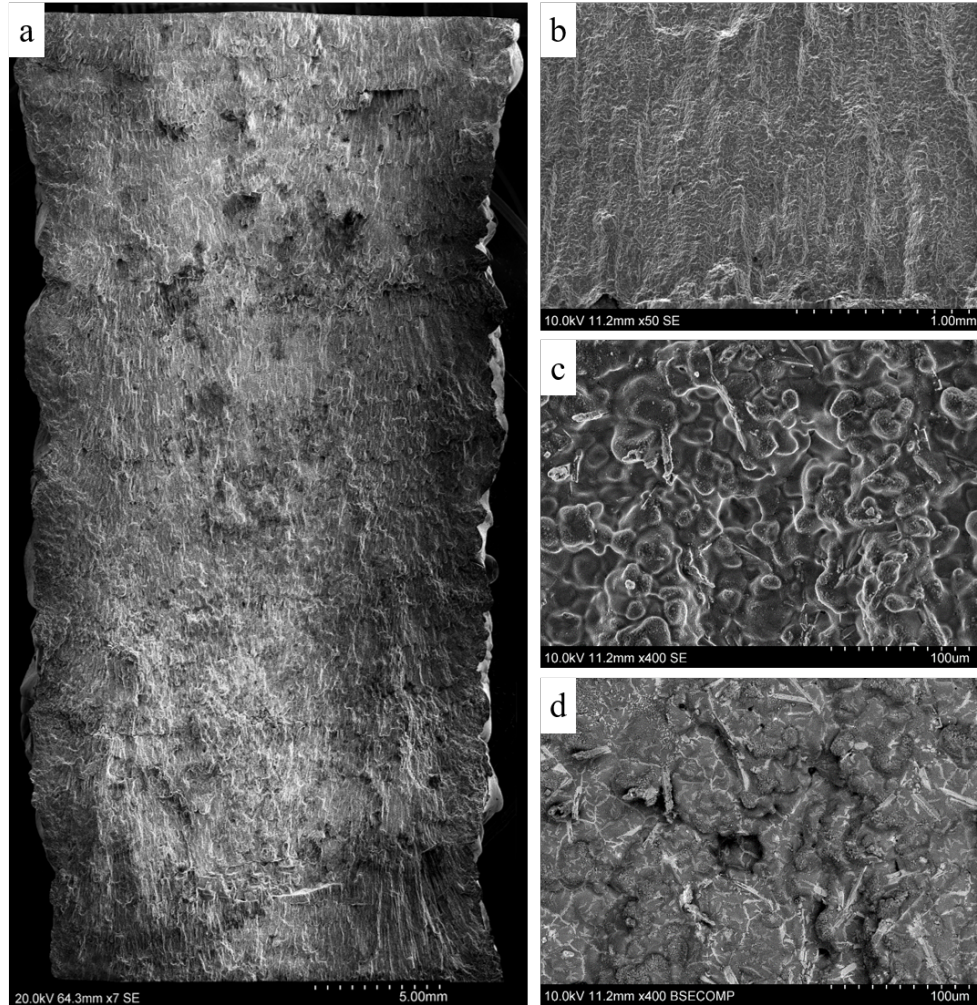


Figure 4.32: (a) Plate 49 overall Crack 2 surface, with (b) typical dendritic region of the crack surface, (c) and (d) are SE and BSE images, respectively, of the dendrite tips and feathery precipitates decorating them.

Much like the Plate 46 and 49 macrocrack surface, the Plate 50 surface was covered primarily in dendrites. Figure 4.33 depicts the macroscopic crack surface and three dendritic regions.

Figures 4.33(b) and (c) show typical dendritic regions as seen previously, while Fig. 4.33(d) highlights an area that has neighboring patches of dendritic and smooth regions. Of Plates 46, 49, and 50, the Plate 50 crack surface showed the most mixing of such smooth regions, with the majority of the crack surface still dominated by dendritic features.

Such regions on the crack surfaces exhibit too low a surface roughness to be formed by dendrites, so another mechanism is necessary for their formation. It is believed that such surfaces were formed by the liquation mechanism, which is discussed next.

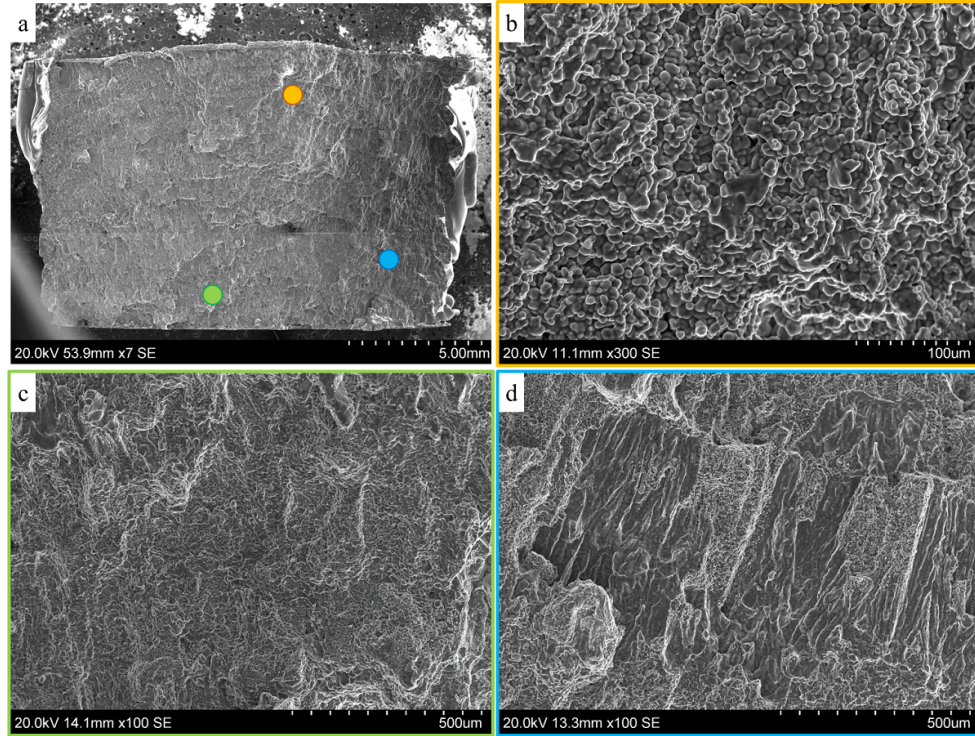


Figure 4.33: (a) Plate 50 crack surface macrograph, (b) and (c) are typical dendritic regions on the surface, and (d) patchy dendritic and smooth regions.

Liquation Features

Kou defines liquation cracking as cracking that occurs in the HAZ of a weld, where the temperature sits between the eutectic temperature and the melting temperature. This causes low-melting point eutectics at grain boundaries to melt, or liquate. Strains induced by the solidification and contraction of a nearby molten pool may overcome the strength of the liquated films, causing grains to separate. Thus, evidence of liquation cracking on crack surfaces should appear smooth - as if fully-formed grains were pulled apart. Solidified remnants of a very thin liquid film might be present on the surface, although they may not be observable with SEM due to resolution limits.

While the majority of the Plate 46 Crack 1 surface was covered in dendritic features, one region near an edge displayed different behavior. Figure 4.34 highlights these regions of interest. At the corner of the sample - which had not cracked before the sample was pulled apart - fractured eutectic is visible on nearly all surfaces, as shown in Figs. 4.34(c) and (d). Between that fractured region and the bulk of the sample surface containing dendritic features lies a region of smooth, almost-equiaxed granular features. This region is shown in Figs. 4.34(a) and (b). A mechanism different from typical fracture or solidification cracking is needed to explain such smooth

features on a crack surface. These features would thus corroborate the theory of liquation cracking, since previously-formed grains are melted at their borders and separated with nearby solidification strains.

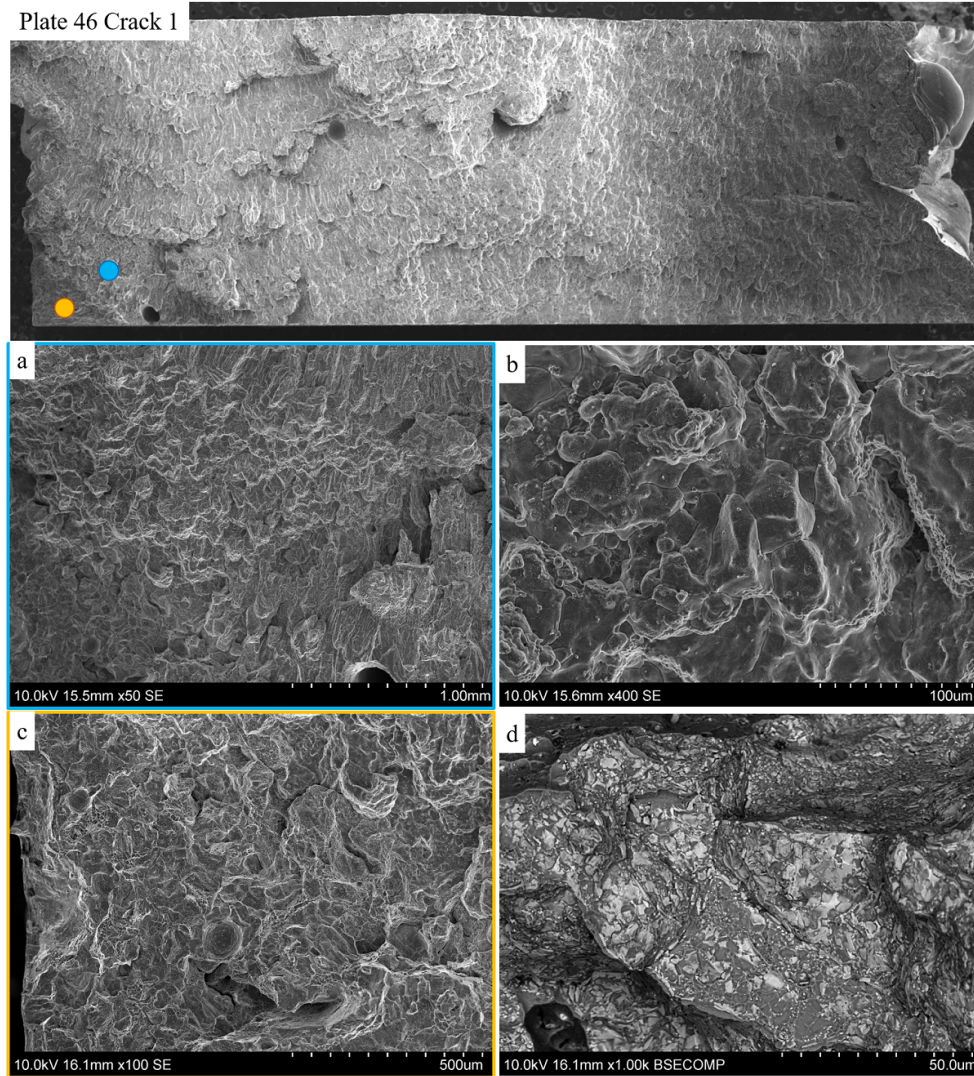


Figure 4.34: (a) Region composed completely of smooth, almost-equiaxed grain-like features, (b) 400x image showing such grains, (c) region neighboring the smooth-grained region where fracture has occurred (from crack separation) preferentially along grain boundary eutectics, and (d) 1000x BSE image showing those eutectics.

Another example of this liquative bordering occurred in a sample extracted from near the baseplate intersection of Plate 49, with its location shown in the cut plan in Fig. C.2. This sample was extracted to see the behavior of the crack surface near the baseplate intersection, where the macrocracks originate. Since the macrocracks only extend through part of the width so close to the baseplate, it was thought that such

a sample might elucidate the crack formation and character nearer the baseplate. To avoid cutting near the crack tip, the sample was separated in the tensile machine to complete fracture while preserving the character of the crack tip.

Figure 4.35 shows the crack surface from this near-baseplate sample. Examination of the crack surface with the BSE mode of the SEM showed the line dividing the original crack from the newly-fractured surface, since the latter had a very similar appearance to the fracture surface in Fig. 4.34(d).

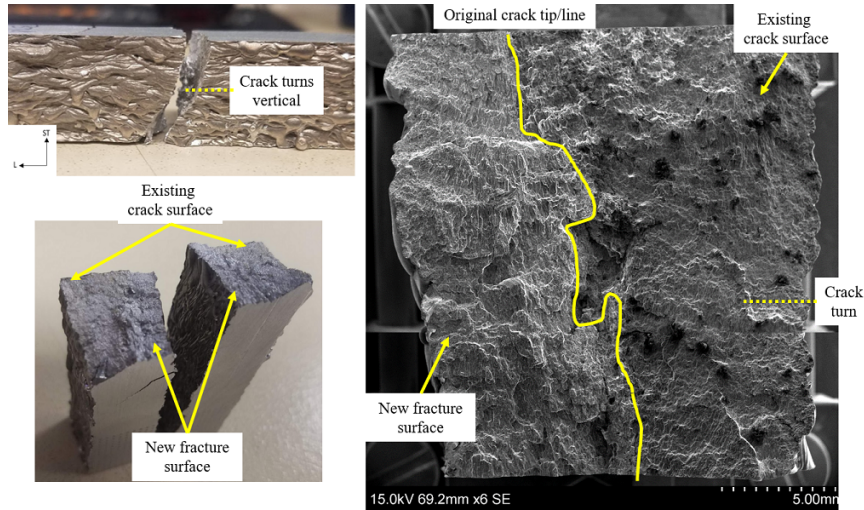


Figure 4.35: Near-baseplate fractured sample to open the partial-width macrocrack. The image on the right shows the crack surface containing the existing and newly-fractured crack surfaces. The yellow line divides the new fracture from the old and shows an increase in the macrocrack width with increasing height in the deposit.

Figure 4.36 displays various features of the partial-width macrocrack fracture surface. Much like the small region at the bottom left of the Plate 46 macrocrack, it was found that the entire border of the newly-fractured surface was covered in similarly smooth, grain-like features, as shown in Figs. 4.36(b) and (c). Outside of this border, the majority of the crack surface was again dendritic in character, like Fig. 4.36(a).

A new feature appears on the crack surface in a couple places and is demonstrated in Fig. 4.36(d). This feature is located right outside the originally cracked area near the baseplate and combines the low surface roughness of liquated grains with the fractured eutectic particles of the new crack surface. It is postulated that this is an example of partial grain bridging, where at high solid fractions the grain had mostly coalesced with a neighboring grain, but not enough eutectic liquid overcame contraction strains to fully join the two grains. A few other regions of similar character are interspersed in the newly-fractured region.

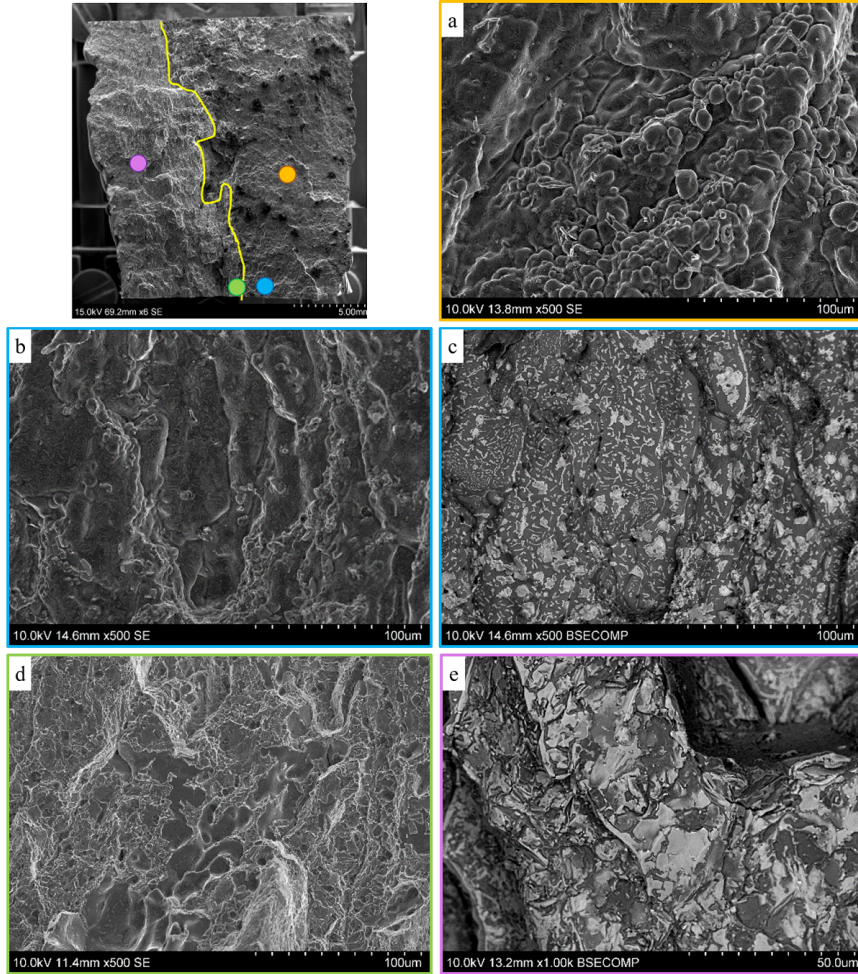


Figure 4.36: Near-baseplate macrocrack map, with subfigures showing (a) typical dendritic character of the majority of the existing crack surface, (b) and (c) SE and BSE images of smooth, liquated features at the crack tip, (d) partial grain bridging near the crack tip, and (e) BSE image of the newly-fractured surface, with fracture through Al-31Cu-10Mg-4Zn eutectics.

4.4.6 Hardness

Vickers microhardness measurements were taken for Plates 49, 50, and 60-C8, since these were deposits of interest that exhibited the most unique compositions. Both the large- and fine-grained regions of Plate 60-C8 were measured to capture differences in hardness with grain morphology. Table 4.11 summarizes the results.

It is observed that the microhardness values for Plates 49 and 50 are very close, despite Plate 49 losing 13% more Zn and 7% more Mg than Plate 50, as shown in Table 4.7. These measurements are also within range bars of the Plate 60-C8 deposit's fine-grained region, which likely has a higher hardness due to increased grain boundary

Table 4.11: Results from Vickers microhardness grids taken from the center of deposits on Plates 49, 50, and 60-C8. The Zn and Mg contents of the deposits are included for comparison of hardness with composition.

Plate	Microhardness (HV _{0.3})	Zn (wt.%)	Mg (wt.%)
49	116.5 ± 5.3	3.67	1.97
50	116.3 ± 6.1	4.15	2.11
60-C8 (large grains)	103.0 ± 5.6	2.66	1.97
60-C8 (fine grains)	111.4 ± 3.3	2.66	1.97

area. The Plate 49 and 50 hardness measurements do not overlap with the Plate 60-C8 large-grained region, which exhibited the lowest measured hardness of 103.0 ± 5.6 HV_{0.3}. Given that the Plate 60-C8 deposit has 40% lower Zn content than Plate 49, this drop in hardness for regions of similar grain size is understandable.

Most hardness indents were not perfectly square, with curved edges from the AD material state. This effect was noted previously in the 2219 deposits in Section 3.4.4.

Since no 7075 material was heat treated due to the pervasive hot cracking, hardness measurements were not completed for material in the HT state to directly compare with wrought 7xxx-series values. Handbook values [74] indicate that the Brinell hardness 7075-O hardness is 60 HBN (converts below 80 HV₁), while 7075-T6 hardness is 150 HBN (converts to 149 HV₁). No hardness values were found for comparison with the T4 state, since naturally-aged 7075 plate is not a common 7xxx-series product form.

4.5 Discussion

The following sections discuss the characterization and analysis results of the 7075 EBF³ deposits. Special attention is paid to trends in the cracking mode and subsequent approaches to reduce cracking.

4.5.1 Variations in Microstructure and Composition with Processing Parameters

The typical 7075 microstructure exhibited grains on the order of 150 μm in diameter, with a columnar aspect ratio (calculated from the average vertical and horizontal intercept lengths reported in Table 4.8) between 1.3 and 1.8, with some grains in the

microstructure exhibiting aspect ratios as high as 7. As seen in Fig. 4.20(a), most grains were continuously bordered by second phase particles.

EDS of second phase particles with a homogenous appearance showed compositions on the order of Al-25Cu-10Mg-3Zn, while those with a eutectic appearance showed compositions averaging Al-24Zn-12Cu-9Mg. Results from the topmost layer of a deposit showed the interdendritic eutectic phases averaging Al-11Zn-7Cu-6Mg. In both cases, there is high Zn, Mg, and Cu segregation at the grain boundaries, which equates to low melting point phases that can be liquated at temperatures below the melting point of the matrix during deposition of subsequent layers. The difference in phase composition from those in the middle of the deposit to the final layer may be attributed to the single heat cycle experienced by the top layer during its original solidification. With additional thermal cycles from subsequent layers, grain boundary segregation increases by the liquation mechanism, consistent with the higher solute content of the Al-24Zn-12Cu-9Mg eutectics observed in the bulk of the deposit.

The majority of the grain size results in Section 4.4.3 are consistent with the 132.7 μm area-averaged AD grain size observed in the 2219 builds in Section 3.4.2. However, the 2219 deposits had an average grain aspect ratio of 1.1, compared to ratios ranging from 1.3 to 1.8 observed in the 7075 deposits. The microstructure in the 2219 deposits was also more homogeneous, potentially due to the established build sequence and lack of defects such as cracks and vaporization losses, which both impact the thermal history of the build.

The increase in grain size with temperature - seen in both the Plate 49 sample and in the Plate 50 region above the macrocrack - is consistent with nucleation and growth theory, since smaller undercooling results in lower nucleation rates of the solid phase and higher grain growth rates [88]. Likewise, the rapid cooling rate within keyhole regions of Plate 60-C8 resulted in fine, equiaxed grains due to increased undercooling.

The variations in build composition correlate with changes in the machine and environmental parameters. It was observed that focusing the EB resulted in higher vaporization losses, particularly of Zn, due to increased superheat causing a higher vaporization flux. In contrast, increasing travel speed led to a reduction in solute loss due to an increased solidification rate.

In addition, differences in the build composition due to background printing temperature also are present. In the case of the Plate 49 deposit, a higher deposit temperature corresponded to a decrease in the solidification rate due to a lower thermal gradient between the molten layer and the deposit below. This results in a longer lifetime of the molten pool, which causes greater losses due to the high vapor pressure

of the solute.

Section 4.5.4 will later discuss how the composition of the deposits due to such vaporization losses contributes to increased solidification cracking susceptibility.

4.5.2 Solidification Cracking

Combining the results from Series 1 and Series 3, it may be concluded that the macrocracks dispersed throughout a majority of the 7075 deposits are driven by solidification cracking, as described in Section 2.4.3. Two compelling pieces of evidence bolster this claim.

The foremost evidence for solidification cracking as the mechanism for macrocrack formation is the high solidification crack density in the Series 3 few-layer deposits. The top surface of the single-layer bead, shown in Fig. 4.37, displays cracks breaking the surface in a periodic fashion. These cracks begin at the edge of the weld bead and are oriented perpendicularly to the melt pool solidification tracks, turning parallel to the weld line near the center of the bead.

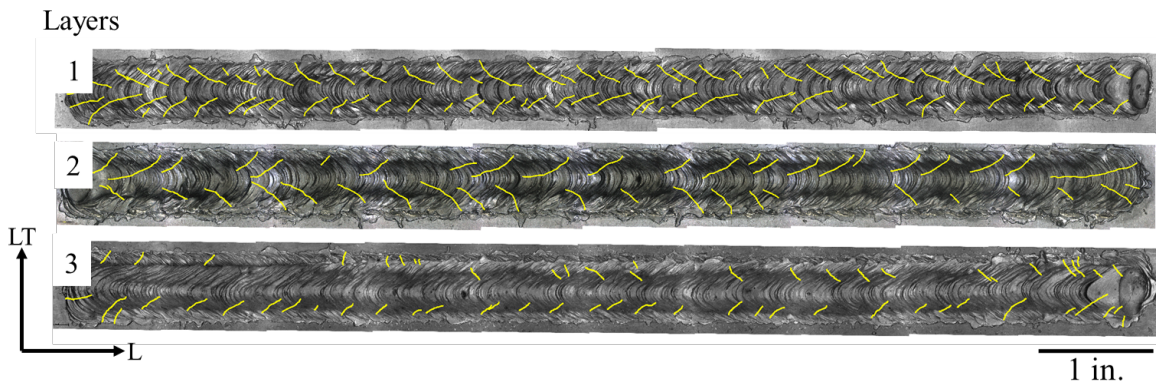


Figure 4.37: Comparison of the Plate 68-1L, 68-2L, and 69-3L builds. Note the changing crack shape and orientation with increasing number of layers, particularly between 2 and 3 layers.

Kou defines solidification cracking as cracking that occurs during weld solidification [13], and so these cracks in the first layer may decisively be labeled as solidification cracks since they are located within the weld bead. To label macrocracks as solidification cracks, the results must show that the cracks observed in the single-layer deposit propagate through additional layers, or that separate solidification cracks were nucleated and formed the macrocracks.

As Fig. 4.37 shows, the addition of a second layer appears to mask evidence of the first layer's cracks, since all surface-breaking cracks in the second layer remain

oriented perpendicular to melt pool tracks going the opposite direction. The fact that the cracks in the 2-layer deposit break the surface suggests that solidification cracking is still the dominant cracking mechanism. In addition, it was observed that the crack spacing was greater in the 2-layer deposit compared to that of the 1-layer deposit. This suggests that the cracks from the first layer may have lowered the stress on the second layer, since fewer cracks are needed to accommodate the stress for the same length of the deposit. Table 4.12 compares the crack statistics for the 1-, 2-, and 3-layer builds in Fig. 4.37.

Table 4.12: Average crack spacing, length, and density for solidification cracks in the Plate 68-1L, 68-2L, and 69-3L builds shown in Fig. 4.37.

Layers	Average Spacing (in.)	Average Length (in.)	Crack Density (in. ⁻¹)
1	0.26 ± 0.09	0.23 ± 0.10	4.9
2	0.42 ± 0.18	0.28 ± 0.10	2.8
3	0.33 ± 0.18	0.14 ± 0.06	1.7

Table 4.12 shows that the single-layer deposit has the lowest average crack spacing of 0.26 in., coupled with the highest crack density of 4.9 in⁻¹. This result is in agreement with observations, given that the first layer is closest to the baseplate and experiences the highest constraint during solidification. The 2-layer deposit has a 1.6x greater crack spacing and a 1.8x lower crack density, which may suggest that cracks from the first layer are not fully “healed” and provide a level of stress relief for the second layer. The average crack length is slightly higher for 2 layers than 1, but the curved shape is maintained for both deposits.

Figure 4.38 demonstrates this concept of incomplete solidification crack healing with subsequent layers, as a solidification crack from the first layer is not filled in by the second layer. This provides some stress relief to the second layer, substantiating the decreased crack density seen for the 2-layer deposit in Table 4.12. In both layers, the solidification cracks are constrained to the layer in which they were nucleated and do not join together or extend into the baseplate.

In contrast to the solidification cracks present on the surfaces of the 1- and 2-layer deposits, the cracks on the 3-layer deposit in Fig. 4.37 have roughly half the length and crack density of the 2-layer deposit. This trend continues for deposits greater than three layers, as the crack presentation on the top surface of the deposit shifts to shorter cracks that only capture the angled behavior near the deposit edge, but do not propagate to the centerline of the deposit. This transition could signal a shift from

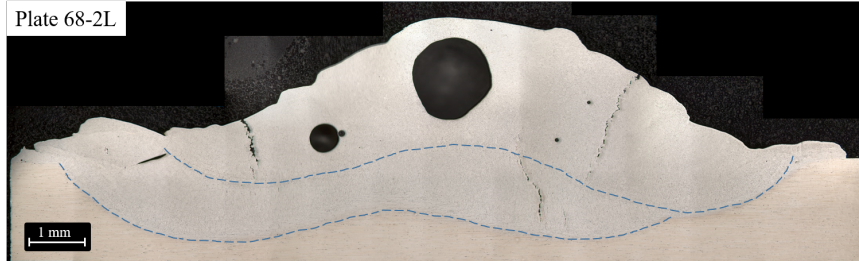


Figure 4.38: Composite image of the two-layer deposit from Plate 68, with the FZ boundary of each layer outlined with a dashed line.

a welding-type constraint in few-layer deposits to a more additive-type constraint with additional build height. In other words, the stresses driving crack appearance and propagation for more than two layers is characterized by the geometry of the additive deposit rather than the constraint of the baseplate. Thus, it is expected that with increasing layers, the cracks in additive deposits will change in appearance from cracks in the welding literature that are parallel to the weld direction and centered mid-width in the FZ, as shown in Fig. 4.2 [28].

Figure 4.39 depicts the proposed solidification cracking sequence, whereby curved cracks with both perpendicular and parallel components appear in the first and second layers due to stresses from the baseplate in both the longitudinal and transverse directions (indicated by red arrows). In contrast, adding the third layer results in short short cracks with only perpendicular components to the travel direction, suggesting a shift in constraint type to that of a linear additive deposit. This figure also demonstrates the strain relief that the cracking in the first layer provides to the second, since increased crack spacing was observed for layers 2 and 3.

The tallest deposit of Series 3 consists of 40 layers - slightly less than half the height of the 86-layer Plate 50 deposit - and exhibits similar crack angles and crack spacings to those of Plate 50. This confirms that the macrocracking behavior of the 40-layer deposit is headed towards the total behavior of Plate 50, and so macrocracks observed in the Series 3 deposits are well-suited for explaining the early stages of cracking for taller builds.

Figure 4.40 includes XCT images from the Plate 50 cylinder near the deposit-baseplate intersection. In the L-LT cross section in Fig. 4.40(a), three thin solidification cracks (yellow arrows) are angled in the same orientation as the surface-breaking cracks from build 68-1L. They are spaced on average by 0.20 in., consistent with the average spacing of 0.26 in. for the 68-1L cracks. Another solidification crack (blue) appears on the opposite side of the deposit centerline but with the same orientation

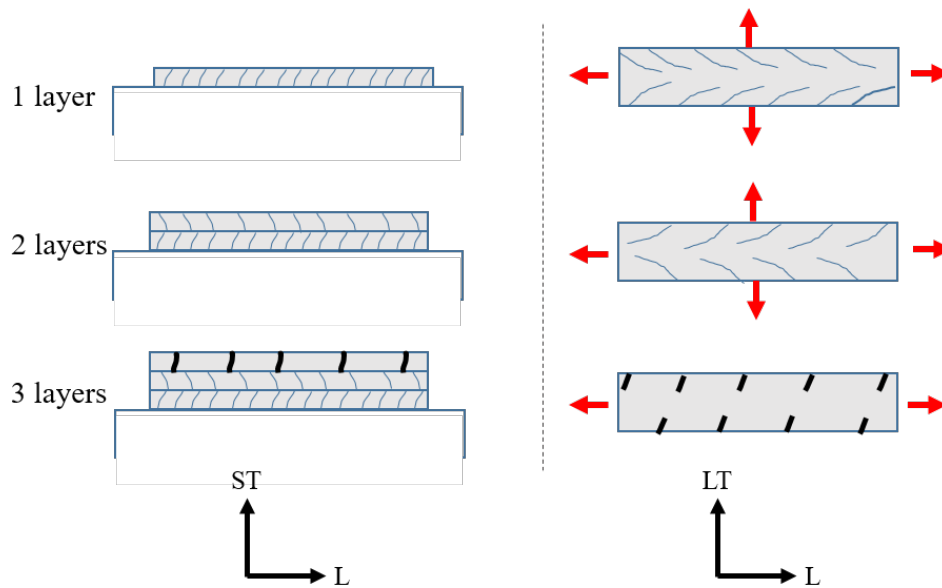


Figure 4.39: Sketches showing curved solidification cracks indicating welding-type constraint in layers 1 and 2, and short, thick macrocracks forming perpendicular to the deposition direction in layer 3, indicating additive-type constraint.

as the three cracks marked by yellow arrows, suggesting that it was formed in a subsequent layer. This crack spans the first and second layers and is attributed to the more widely-spaced, surface-breaking cracks seen on build 68-2L. All four of these cracks terminate at or before the FZ-baseplate boundary, indicative of solidification cracks.

The LT-ST cross section in Fig. 4.40(b) captures two of these near-baseplate solidification cracks from the first couple layers of the build, corresponding to the cross section in the L-LT view denoted by the white dotted line. The LT-ST view also captures the tip of a wide Plate 50 macrocrack that appears to extend within a couple layers of the deposit-baseplate intersection. This initiation of a macrocrack unrelated to the first- and second-layer cracks is consistent with the observation of a change in cracking behavior for deposits with more than 2 layers, as shown in Fig. 4.14.

A secondary, important piece of evidence for linking solidification cracking with the macrocracking seen in the deposits is the predominantly dendritic nature of the macrocrack surfaces. As described in Section 4.4.5, all cracks that were opened and observed with the SEM showed dendritic areas, such as those shown in Figs. 4.31 and 4.32. These included a partial-width crack near the baseplate intersection from Plate 49 and full-width cracks from Plates 46, 49, and 50. In all of these deposits,

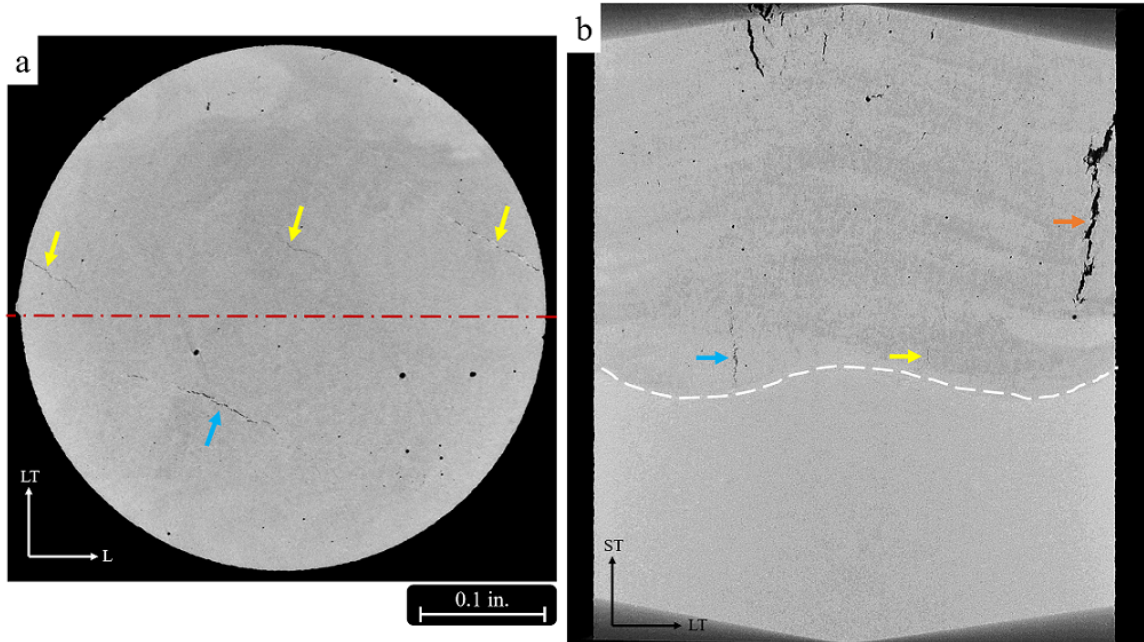


Figure 4.40: High-resolution XCT data from the Plate 50 intersection with the baseplate. (a) The L-LT view shows fine solidification cracks from the first layer (yellow) and a larger solidification crack (blue) spanning the first and second layers. The centerline of the deposit is noted by the red dashed line. (b) The LT-ST view intercepts two of the first and second-layer cracks from the L-LT view, with a macrocrack (orange) formed at a height around that of the third layer. The FZ boundary is noted by a dashed white line.

the majority of the crack surfaces are covered by dendrites.

The presence of dendritic features in the open cracks strongly suggests that cracking occurred during the solidification process. Such dendritic features can develop only when the material is still molten and the dendrites are growing into a region where they cannot encounter other material against which to coalesce and form a grain boundary. Such cracks must then form in regions that either (1) lack enough liquid to fill between dendrites to close the crack, or (2) are separated enough such that the dendrites solidify into free space.

To confirm that the macrocracks are driven by the solidification cracking mechanism, other modes of cracking seen in welding and AM must be ruled out. These include liquation hot cracks, which would exhibit smooth, granular features on the crack surface [13]. Such features were typically not observed on the macrocrack surfaces, though some regions near crack tips showed liquated features. A final mode of cracking that occurs in welds and additive deposits is residual stress cracking, or “cold” cracking. This occurs when thermal residual stresses overcome the tensile

strength of the material after cooling, and crack surfaces exhibit features of overload rupture. These include dimples or other tearing features, which were unanimously not observed on crack faces. Thus, the macrocracks must have nucleated and occurred primarily by the solidification cracking mechanism.

Effects of Constraint on Solidification Cracking Extent

Two pairs of deposits elucidate the effects of constraint on the extent of solidification cracking. The first pair are the deposits made on Plates 46 and 50, which were built to similar heights of 90 and 86 layers on 0.25 in. and 1 in. baseplate, respectively. Figure 4.41 compares macrocracks from these two deposits, with the L-ST views showing overlaid scan data from the front and back faces of the deposit and the L-LT view showing macrocrack extent near the baseplate intersection for both deposits.

These images show that angled macrocracks exist for both deposits near the baseplate, with the cracks in Plate 50 continuing through the height, while cracks in Plate 46 terminate after a few tenths of an inch. These cracks also propagate into less of the deposit width, with Plate 46 cracks only extending 0.08 in. into the deposit width compared to Plate 50 cracks extending 0.17 in. on each side.

The number of full-width cracks are also reduced for Plate 46, with only two major cracks observed with 70 μm XCT scans in the top half of the deposit. These cracks did not nucleate near the baseplate unlike most macrocracks, so it is expected that geometrical variances necessitated macrocrack formation higher in the deposit. In comparison, the Plate 50 cracks never terminated, propagating through the deposit height from initiation sites near the baseplate. While this comparison is not ideal since the deposits were not from the same controlled experiment, it does provide insight into the impact of baseplate thickness.

The second pair of deposits are from the two 40-layer, Series 3 deposits 69-40L and 71-40L. L-LT XCT scans taken from near the baseplate and 3/4 the height of the deposit are shown in Fig. 4.42. Table 4.13 lists the associated crack spacings, lengths, and densities for the deposits at the two measured heights.

As seen from the comparison of the XCT scans in Fig. 4.42 and the data in Table 4.13, a similar average crack length near the baseplate occurs for both the Plate 69-40L deposit (on 1 in. baseplate) and the 71-40L deposit (on 0.25 in. baseplate). The crack density of the latter, however, is almost half that of the deposit on thick baseplate. Furthermore, the deposit on thicker baseplate has cracks that propagate through the

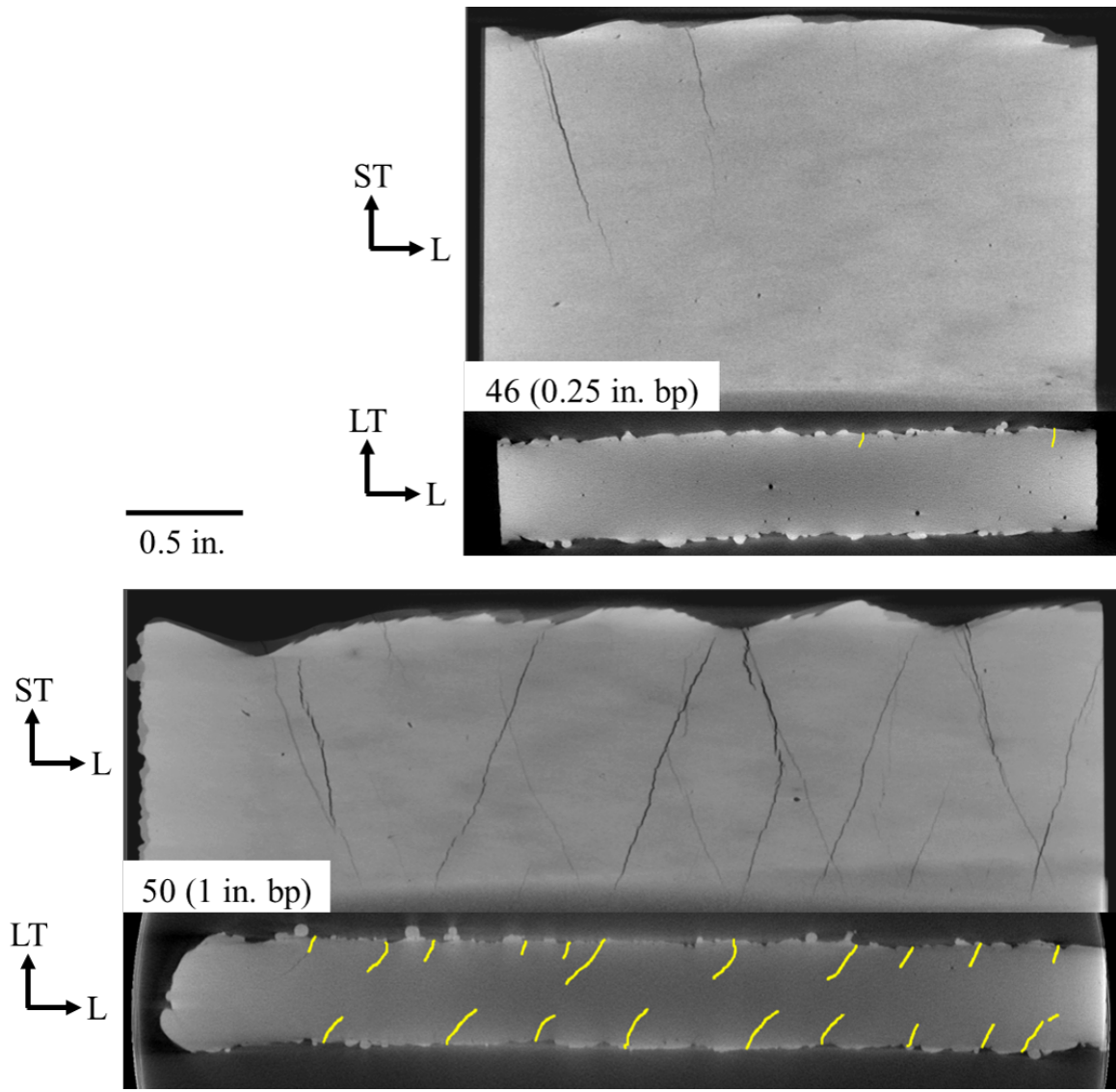


Figure 4.41: L-ST and L-LT low-resolution XCT scans of the Plate 46 and 50 deposits on 0.25 in. and 1 in. baseplate, respectively, showing the effects of a 4x baseplate increase on deposit macrocracking. Macrocracks are highlighted in yellow and widened for clarity in the L-LT views.

height of the build, while most cracks in 71-40L terminate halfway through the build height. Overall, the crack density of 71-40L is roughly half that of 69-40L, regardless of height. This is consistent with the observations in the Plate 46 and 50 comparison noted earlier, where the deposit on thinner baseplate showed less macrocracking. The higher level of macrocracking in 71-40L compared to the Plate 46 deposit is likely due to higher constraint from neighboring builds on Plate 71 and controlled clamping forces in the fixture, while the deposit on Plate 46 was isolated on its baseplate and

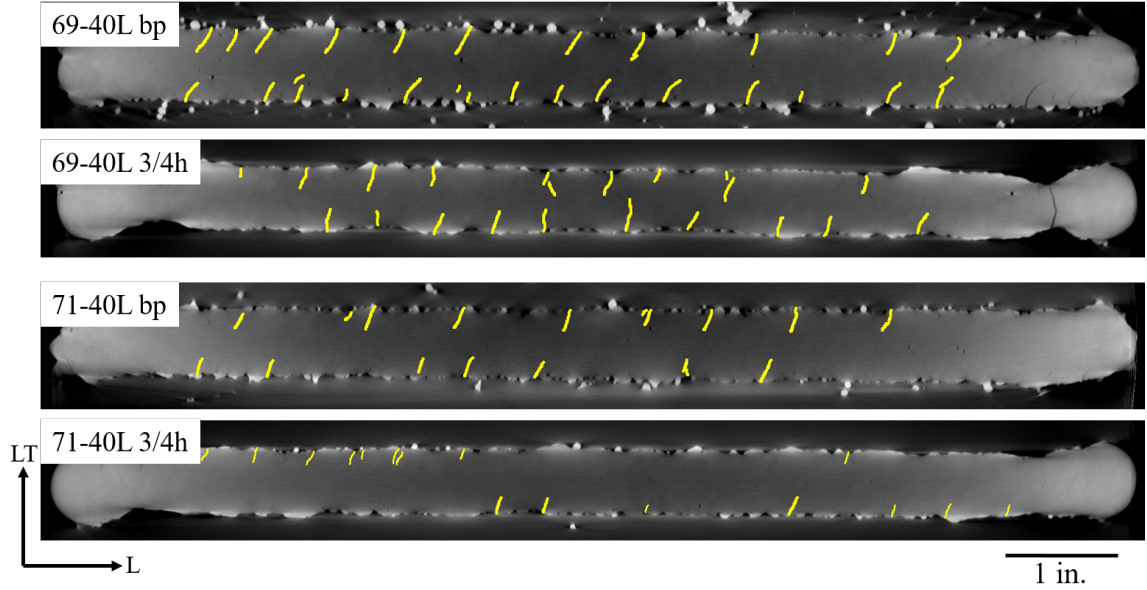


Figure 4.42: L-LT low-resolution XCT scans near the deposit intersection and at 3/4 the height of the Plate 69-40L (1 in. bp) and 71-40L (0.25 in. bp) deposits. Macrocracks are highlighted in yellow and widened for clarity.

Table 4.13: Average crack spacing, length, and density for macrocracks in the 40-layer builds on Plates 69 and 71 and shown in Fig. 4.42.

Layers	Average Spacing (in.)	Average Length (in.)	Crack Density (in. ⁻¹)
69-40L bp	0.58 ± 0.25	0.18 ± 0.07	1.2
69-40L 3/4h	0.63 ± 0.21	0.17 ± 0.06	0.92
71-40L bp	0.77 ± 0.30	0.15 ± 0.06	0.68
71-40L 3/4h	0.79 ± 0.85	0.12 ± 0.03	0.49

fixture clamping was not controlled.

Thus, the effect of 4x the baseplate thickness for deposits of similar height and background temperature results in a higher density of wider cracks that propagate through a greater height of the deposit. This increase in constraint is demonstrated by greater stiffness of 1 in. thick plate than 0.25 in. plate when calculating normal stresses in bending.

Effects of Grain Refinement on Solidification Cracking

One of the most interesting solidification cracking observations from this work occurred in the Plate 60-C8 deposit, where the use of a focused EB and slow travel

speed resulted in significant grain refinement, eliminating solidification cracking in the steady state region of the build. This grain refinement occurred in two bands on the LT-ST cross section, corresponding to the regions below the vertices of the elliptical raster pattern. Here, the EB penetrated deeper with a higher aspect ratio, known as keyholing. The formation of melt pools deeper into the sample resulted in an increase in the local solidification rate due to the temperature distribution of the surrounding bulk material. The rapid solidification within these regions resulted in a greater undercooling, resulting in the formation of fine, equiaxed grains rather than more columnar, epitaxially-grown grains observed outside of these boundaries.

The bands of grain refinement thus appear to disrupt the solidification cracking mechanism in a build which theory suggests should have the most susceptible composition of all 7075 deposits. The disruption of solidification cracking by grain refinement is well-documented in welding and additive literature [25, 26, 17, 21]. The Plate 60-C8 deposit suggests that even partial grain refinement through the formation of a banded microstructure is sufficient to prevent the initiation and propagation of solidification cracks on 0.25 in. plate for a 4 in. long deposit. Further deposits are needed to explore whether the additional constraint of a full 9 in. long deposit or depositing on 1 in. baseplate will outweigh the beneficial effects of grain refinement on suppressing solidification cracking.

4.5.3 Liquation and Liquation Cracking

A Liquated Microstructure

Figure 4.43 compares BSE micrographs from the Plate 46 (a) deposit-baseplate intersection and (b) a typical region in the deposit microstructure. It is observed that similar features are present despite the images coming from vastly different microstructural regions. These features include heavy, nearly continuous precipitation on grain boundaries - characteristic of grain boundary melting, or liquation - and round particles in grain interiors. The microstructure in Fig. 4.43(a) shows more eutectic particles than (b), likely due to the higher solute content in the baseplate. Nevertheless, some eutectic particles were observed on grain boundaries in the deposit microstructure.

This comparison in Fig. 4.43 highlights the important point that the same mechanism of liquation below the FZ is operating, whether in the baseplate during welding or in the deposit below subsequent additive layers. This is critical to understanding the microstructure of these EBF³ deposits, since near-total grain boundary liquation

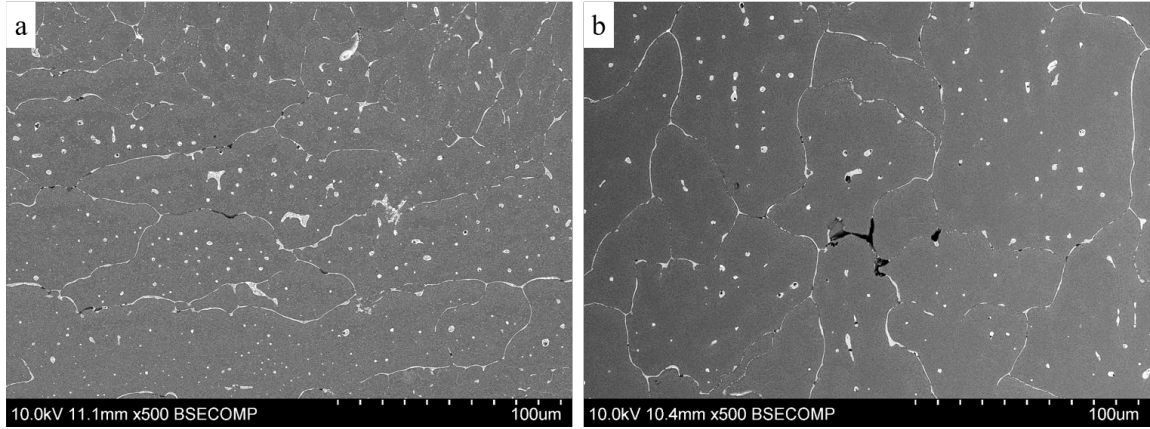


Figure 4.43: BSE images from the Plate 46 microstructure comparing liquation at (a) the deposit-baseplate intersection with (b) a typical region in the deposit.

(as evidenced by the complete bordering of the grains by second phase particles) is a sign of high heat input from the build process and the tendency for additional segregation to occur during subsequent layers. The large grains have a higher concentration of liquation-sensitive particles on grain boundaries compared to a fine-grained material with more granular surface area, so large-grained microstructures are more susceptible to liquation and cracking.

A liquated microstructure implies that the AD properties of this material will be poor compared to those of wrought material, since long secondary phase particles on grain boundaries will typically act as crack nucleation sites during plastic deformation and the solute bound in those phases is not contributing towards strengthening precipitates. Furthermore, Huang and Kou note precipitate-free α bands bordering liquated grain boundaries in weld PMZs, which would further contribute to poor properties due to slip localization [65]. Provided that liquation cracking does not occur in the liquated microstructure, this segregated microstructure can be transformed with subsequent heat treatment, as was noted in the 2219 microstructures (Section 3.4.2).

Liquation Cracking in EBF³ Deposits

Solidification cracking is almost exclusively reported in the literature as the mechanism driving cracks in additive deposits, with the remainder generally classified as “hot cracks.” The difference in operational mechanism between solidification and liquation cracking is important to acknowledge, since the approach to reduce or eliminate solidification cracking may not fully address liquation cracking, and vice versa.

This is most evident in the Plate 60-C8 deposit, where the bands of refined grains disrupted the solidification cracking mechanism from forming macrocracks. Liquefaction cracking, while still present, exhibited a reduced crack density compared to other deposits from Series 1.

As described in Section 2.4.4, liquefaction occurs in the PMZ of a weld, where eutectics or other second phase particles with low-melting points liquate at temperatures below the matrix material liquidus. Cracking in these liquated regions proceeds when the strain field from the nearby contracting weld pool exceeds the strength of the molten grain boundary films. This liquefaction cracking was observed in the 7075 Series 1 and 2 deposits, where the 7 μm XCT scans in Fig. 4.29 show the drastic delimitation of microcracks stemming down from the root of the final layer of the deposit. By definition, liquefaction cracks cannot occur in a weld FZ (and thus the final layer of an additive deposit), so this behavior conclusively labels such microcracks occurring internal to the deposit and stemming from below the topmost layer as liquefaction cracks.

Due to their microstructural-level scale, liquefaction cracks are much more difficult to identify non-destructively in large additive deposits compared to surface-breaking solidification cracks or macrocracks. Fig. 4.44 shows low- and high-resolution XCT scans of a region of liquefaction cracking, as well as the associated polished cross section.

Due to the crack thickness, the low-resolution XCT is at the edge of the detection limit for liquefaction cracking in the examined samples. In comparison, high-resolution XCT scans and polished cross sections show the extent of liquefaction cracking, particularly for fine cracks, although they require destructive evaluation.

From these and other XCT scans and micrographs in Sections 4.4.3 and 4.4.4, it is observed that most liquefaction cracks in the deposits are oriented predominantly vertically, with the crack plane normal parallel to the L direction, or the solidification direction of the molten pool. This makes sense, since the microstructure is elongated in the ST direction, so strains from a weld pool passing in the L direction would separate liquated grains in that direction.

In the Plate 60-C8 sample, liquefaction cracks were observed between elongated grains in the large-grained bands of the microstructure. In contrast to all other liquefaction cracks observed in Series 1 deposits, the liquefaction cracks in Plate 60-C8 were angled with the large grains toward the fusion zone boundary of keyholed melt pools, with most crack planes parallel to the welding direction. This is likely due to the strain field of solidifying keyholed melt pools, which would dominate in the direction marked with arrows in Fig. 4.45 to cause cracks of this orientation.

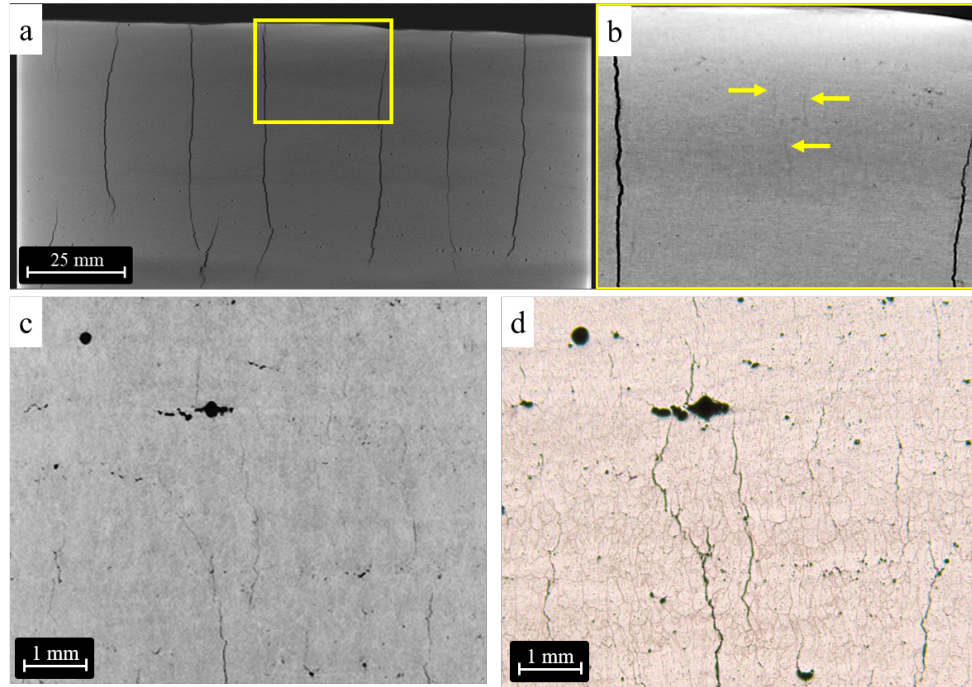


Figure 4.44: Images from the Plate 49 deposit showing (a) 70 μm XCT scan with (b) faint indications of microcracks marked with arrows. (c) 7 μm XCT scan of the cylindrical sample clearly showing liquation cracks, and (d) polished and etched cross section of the cylindrical sample showing the same.

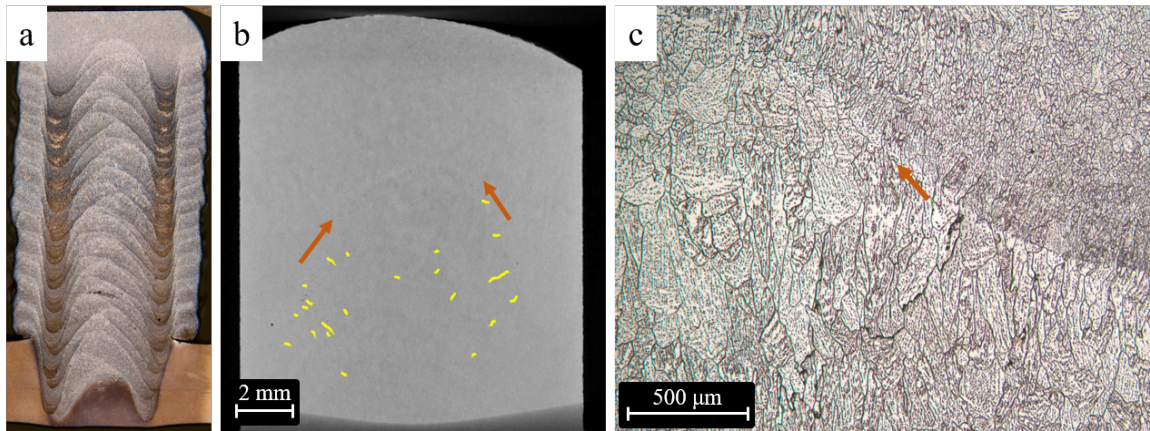


Figure 4.45: Images from the Plate 60-C8 deposit showing the (a) LT-ST polished and etched C8 macrostructure, (b) 7 μm XCT scan of the top deposit layers showing liquation cracks, and (c) 200x image showing a liquation crack stemming from below the root of the FZ in a coarse-grained region of the microstructure. Orange arrows denote the direction of keyholed melt pool solidification and associated strains.

In contrast to the large-grained regions of the Plate 60-C8 microstructure, liquation cracks were not observed in the fine-grained regions. This can be explained by

the increased grain boundary surface area in the refined microstructure compared to a coarse-grained microstructure, the latter of which disperses low-melting point phases over a larger area. Since these liquation-sensitive phases are not concentrated on a few grain boundaries for a fine grained material, they are less likely to liquate and produce cracks.

Effects of Temperature on Liquation Cracking Extent

As shown by the data in Table 4.10, the 130°C increase in baseplate temperature for Plate 49 compared to Plate 50 played a role in the extent of liquation cracking below the topmost layer of the two deposits. Figure 4.46 compares typical 7 μm XCT scans of regions of liquation cracking in Plates 49 and 50.

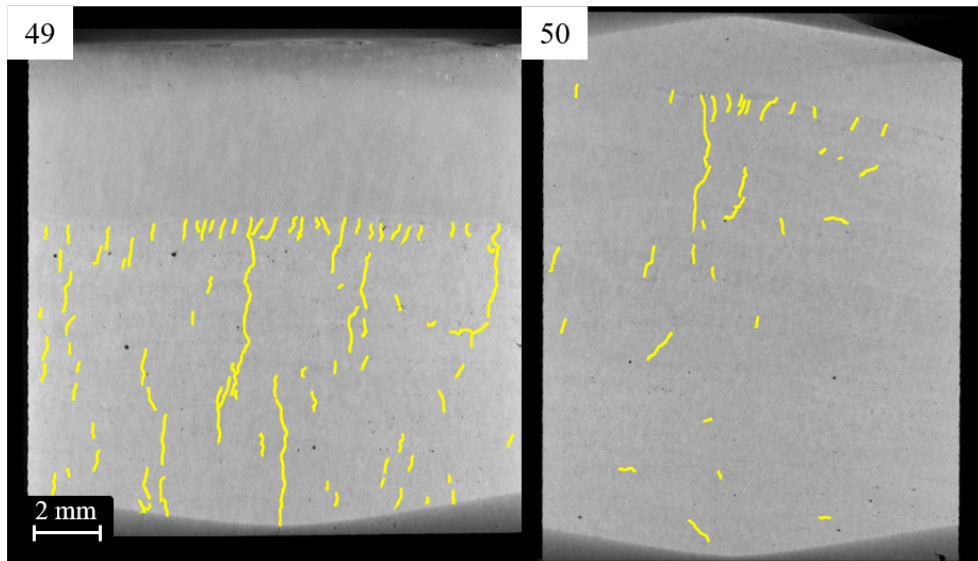


Figure 4.46: 7 μm XCT scans showing liquation cracks emanating from the root of the final layer in both the Plate 49 and Plate 50 microstructures. Due to the higher deposit temperature and larger grain size of Plate 49, cracks are 22% longer than those of Plate 50.

These images show a 22% increase in average crack length for the 300°C Plate 49 deposit compared to the 170°C Plate 50 deposit. This increase in crack length should be related to the depth of material below the topmost layer experiencing temperatures between the liquidus (640°C) and eutectic temperature (462°C), i.e. the PMZ. Given the larger thermal gradient between the temperatures of the molten pool and baseplate in the Plate 50 deposit, the size of the PMZ should be smaller than that of Plate 49. As a result, a greater depth of the Plate 49 deposit is liquated with

each layer deposited, resulting in liquation cracks joining and propagating through additional layers.

The Plate 49 microstructure also exhibited large columnar grains that are 1.5x to 2.x larger than grains in the Plate 50 microstructure (see Table 4.8). Since the Plate 49 microstructure not only exhibited larger grains but also grains with higher aspect ratios, it was more susceptible to longer liquation cracks. This is because large-grained microstructures have less grain boundary surface areas than microstructures with smaller grains, resulting in a higher concentration of liquation-sensitive phases. The smaller grain boundary surface area of the Plate 49 microstructure likely resulted in increased concentration of liquation-sensitive particles on the grain boundaries, further predisposing them to liquation and cracking.

Liquated Features on Crack Surfaces

A small percentage of the opened crack surfaces exhibited smooth features that could not be explained by the solidification cracking mechanism. In most cases, these regions occurred at macrocrack tips as the boundary between the uncracked material and the solidification crack. The best example of this phenomenon is the partial-width crack sample from near the base-plate intersection of Plate 49 (shown in the cut plan in Fig. C.2). As shown in Fig. 4.47, smooth grains were observed at the boundary of the cracked and uncracked regions of the deposit.

This area of the original crack tip contrasts the brittle fracture along secondary phases in the uncracked region and the dendritic features of the rest of the solidification macrocrack. Smooth grains are present, with some eutectic and high-solute particles appearing on their surfaces. These grains on the border of the cracked and uncracked region would have had the opportunity to coalesce with neighboring grains to form smooth surfaces, but would have experienced sufficiently high temperatures from the neighboring material to liquate and separate at the crack tip.

A second case of liquated regions occurred at the corner of the Plate 46 Crack 1 sample. In this case, the bottom corner of the sample intersected a small, uncracked region. This small ligament was fractured during the procedure to open the crack manually, causing a small, ductile fracture region in the corner. Smooth grains were observed bordering this uncracked area as well. This sample and the partial-width crack from Plate 49 provide evidence that liquated grains often characterize the crack tips of solidification macrocracks in the 7075 deposits.

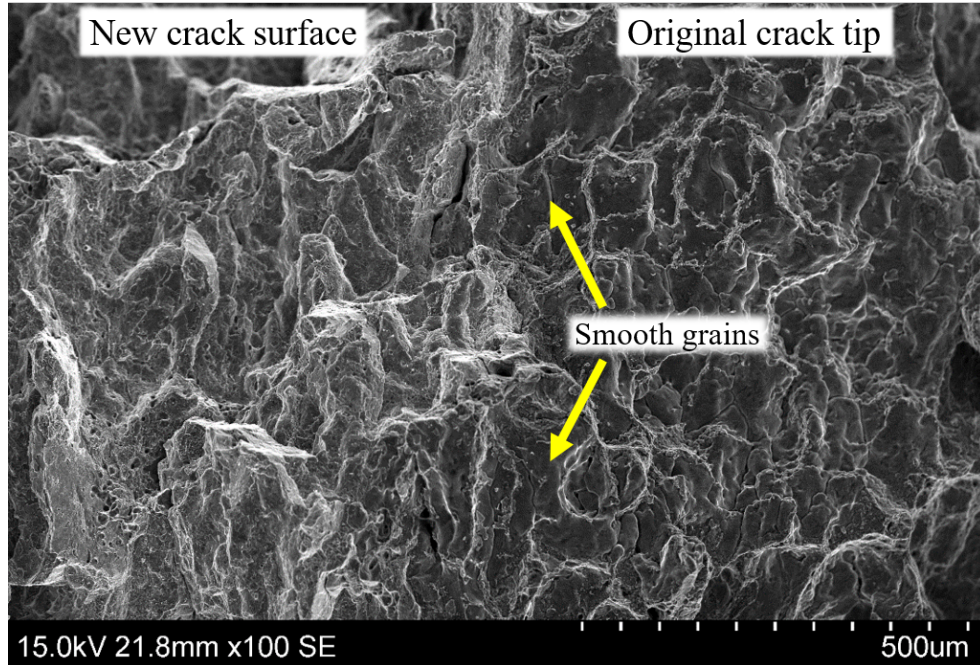


Figure 4.47: Micrograph showing a region of the original crack tip of a partial-width macrocrack from near the baseplate intersection of Plate 49. The crack tip is characterized by smooth-grained features (examples denoted with arrows), while the new crack surface created by breaking open the sample is characterized by fracture at grain boundary eutectic particles.

Liquation and Cracking at the Deposit-Baseplate Intersection

It is also important to acknowledge that liquation cracking was observed at the deposit-baseplate intersection for all polished 7075 cross sections, including Plate 60-C8. While this may not initially seem important, especially if the additive deposit is to be cut off and used separately from its substrate, it is a critical problem for components such as integrally stiffened panels, since such cracking could cause delamination of the stiffener from its substrate at low stresses.

The liquation cracking appearing at the deposit-baseplate intersection looks much more similar to that seen in the welding literature, since it occurs in the traditional microstructure of the base metal HAZ rather than within the complex, layered microstructure of the deposit's HAZ. Figure 4.48 compares a typical 7075 liquated weld PMZ from the literature [65] with the liquated and cracked microstructure of the Plate 49 deposit intersection.

Both microstructures show heavy segregation at grain boundaries and interiors, with eutectic particles high in Zn, Mg, and Cu decorating the microstructure. The grains in both samples are elongated horizontally due to the rolling direction of the

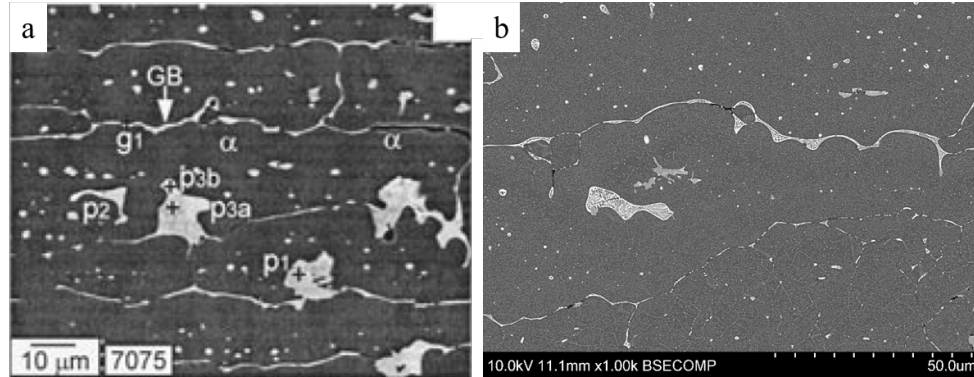


Figure 4.48: Comparison of (a) liquation and liquation cracking occurring below an 7075 weld in the PMZ and (b) liquation and small cracks in the PMZ below the first deposit layer in Plate 49.

plates. As a result, liquation cracks appearing in welds and below the deposit are typically oriented horizontally and parallel to the welding direction.

In the case of the Plate 60-C8 deposit, a significant amount of liquation cracking was observed at the deposit-baseplate intersection. This may be due to both the lack of solidification cracking in the deposit and the high energy density of the focused EB. Typically, liquation and solidification cracking do not occur in high densities near each other, since each type of cracking provides strain relief to the other. In the case of the Plate 60-C8 sample, the lack of solidification cracking due to the bands of refined grains resulted in increased strain at the deposit-baseplate intersection and promoted liquation cracking. In addition, the deep, keyhole melt pools from the C8 deposit provided concentrated regions of high heat, which increased the depth of the PMZ below the deposit footprint and resulted in significant liquation cracking, as shown in Fig. 4.50.

Figure ?? shows a sketch of the proposed liquation cracking sequence, whereby liquation cracks form below the fusion zone of the first layer of the additive deposit. These cracks form between the elongated grains in the rolled plate microstructure, resulting in a horizontal orientation in the baseplate.

With increasing number of layers, liquation microcracks begin forming higher in the deposit in regions between the macrocracks. These microcracks are oriented vertically due to the elongated grains in the ST direction, with crack planes perpendicular to the travel direction due to the high volumetric shrinkage and thermal strains from solidification in that direction. The liquation depth, Γ , is measured as the region within the PMZ that has sufficient time to liquate and form cracks. This liquation depth is discussed in greater detail in Appendix D.

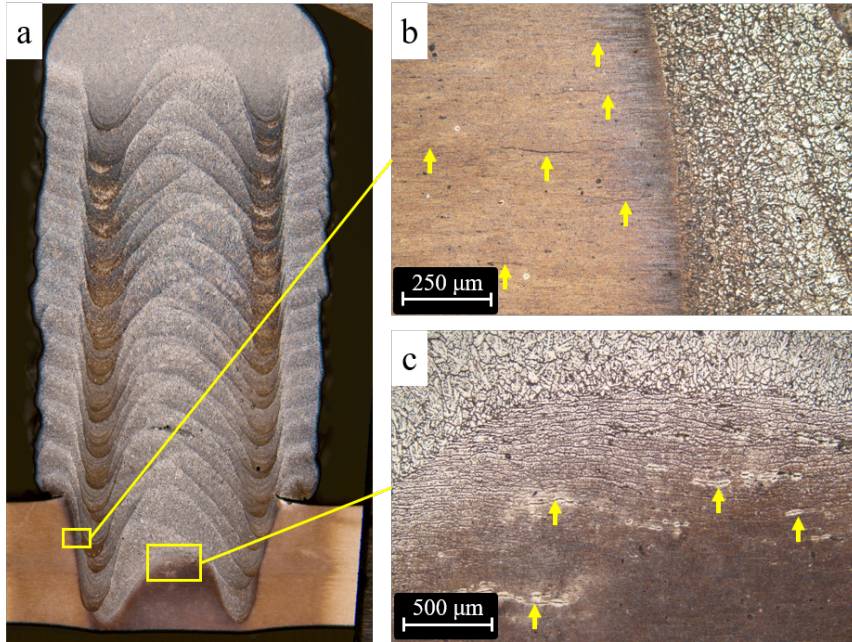


Figure 4.49: (a) Plate 60-C8 deposit, with regions of liquation cracking marked. (b) Region outside the deposit footprint with horizontal liquation cracks in the baseplate, and (c) region of extensive liquation and liquation cracking below the deposit footprint.

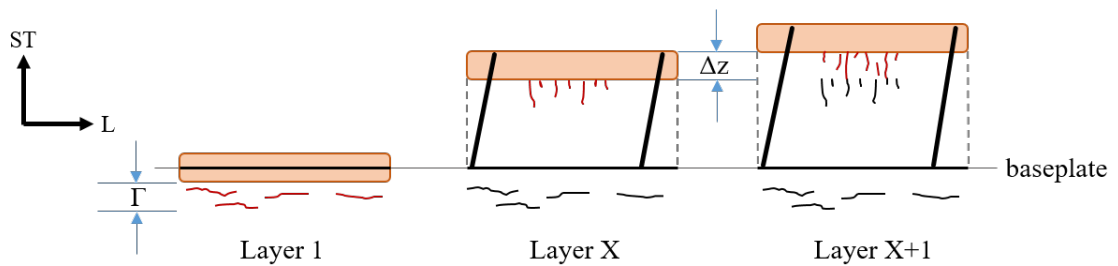


Figure 4.50: Proposed sequence of liquation crack formation, where cracks shown in red formed during the deposition of that layer and black cracks were formed previously.

4.5.4 Effect of Composition on Cracking and Hardness

The vaporization losses of Zn and Mg from the 7075 molten pool play a crucial role in determining the solidification cracking susceptibility and affect the maximum achievable strength of the resulting deposits. The following sections discuss calculations to determine the susceptibility of particular deposit chemistries to solidification cracking, as well as the effect of vaporization losses on the hardness of the AD material.

Solidification Cracking Susceptibility Predictions

Based on the model proposed by Kou [62], the $T-f_s^{1/2}$ diagrams for the deposit compositions in Table 4.7 were computed using the Thermo-Calc 2013 software and the TCAL2 database. The $T-f_s^{1/2}$ diagrams were calculated using the Scheil solidification model, which assumes (1) complete diffusion in the liquid, (2) no diffusion in the solid, (3) equilibrium at the solid-liquid interface, and (4) a constant partition ratio, k [13]. While the EBF³ process does not meet all of these criteria due to higher solidification rates than in torch welding, the analysis still provides insight into compositional trends that may affect cracking in EBF³ deposits.

The maximum steepness in the terminal stage of solidification - a measure of solidification cracking susceptibility proposed by Kou [62] - was calculated by plotting the quaternary Al-Zn-Mg-Cu Scheil $T-f_s^{1/2}$ curves for each wire and deposit composition. Vaporization losses account for the changes in chemistry and thus the $T-f_s^{1/2}$ behavior, leading to different predictions of the solidification cracking susceptibility via the criterion set forth by Kou [62]. Figure 4.51 shows these solidification curves, and Table 4.14 reports the maximum slope for each.

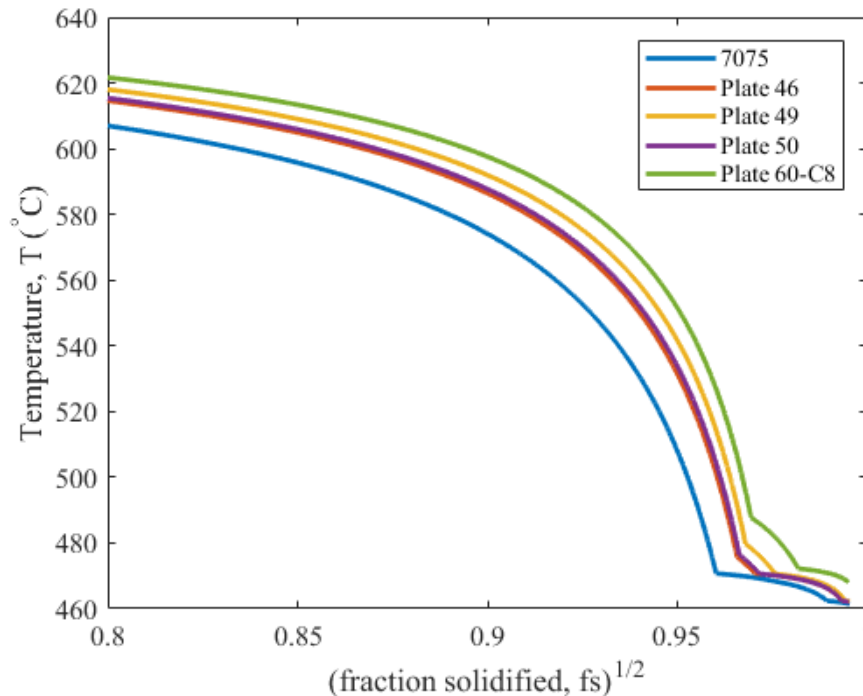


Figure 4.51: Scheil solidification $T-f_s^{1/2}$ diagrams for the 7075 wire composition and various deposit compositions.

It is observed that the greatest differences in slope and shape of the $T-f_s^{1/2}$ curves

Table 4.14: Maximum steepness $|dT/d(f_s)^{1/2}|$ criterion for solidification cracking as set forth by Kou [62]. The criterion is applied to T- $f_s^{1/2}$ curves for the 2219 and 7075 wire compositions, as well as for the 7075 deposits of interest.

Material	Maximum steepness $ dT/d(f_s)^{1/2} $ ($^{\circ}\text{C}$)
7075 wire	4778
Plate 46	5505
Plate 49	5792
Plate 50	5581
Plate 60-C8	5807

are between the 7075 wire composition and the Plate 60-C8 curve. This makes sense, since these materials represent the compositional bounds of the present 7075 study.

The 7075 wire has the earliest knee in the curve, occurring at $f_s^{1/2} = 0.96$, or $f_s = 0.92$. This means it contains the greatest amount of solute of all the 7075 materials tested, since the knee in the curve corresponds to the formation of the eutectic liquid or other second phases in the terminal stages of solidification. The order of kneeing thus follows with increasing vaporization losses, so Plate 46 has the next highest solute content and knees at a lower $f_s^{1/2}$ value than Plates 49 and 60-C8. Plates 46 and 50 have nearly identical curves and maximum slopes due to their very similar compositions.

By Kou's criteria, curves with increasing $|dT/d(f_s)^{1/2}|$ at the kneeing point or $f_s^{1/2} = 0.99$ - whichever comes first - are more susceptible to solidification cracking. One will note that the maximum steepness for Plates 49 and 60-C8 are similar, around 5800°C , despite an additional 1 wt.% loss of Zn for Plate 60-C8. Based on knowledge of the Λ curves in welding literature, it is likely that a peak susceptibility occurs between the two compositions, and so further alloy losses beyond those of 60-C8 would lead to reduced susceptibility.

These predictions of susceptibility will not necessarily be reflected in the total solidification crack area across the deposits due to the complicating factors of varying baseplate thickness, background printing temperature, and grain refinement. The optimum experiment for comparing susceptibilities would include comparing the total length of surface-breaking cracks for single-layer deposits of different parameter sets (and likely compositions). While this study did not include such deposits for the 0.5 in. wide beads, a comparison between the XCT data from near the baseplate intersections of Plates 49 and 50 may be made, since these deposits differed just by

their average background temperature and resulting composition. Figure 4.52 compares the XCT data from 1.2 mm above the baseplate intersection, with macrocracks highlighted in yellow for clarity.

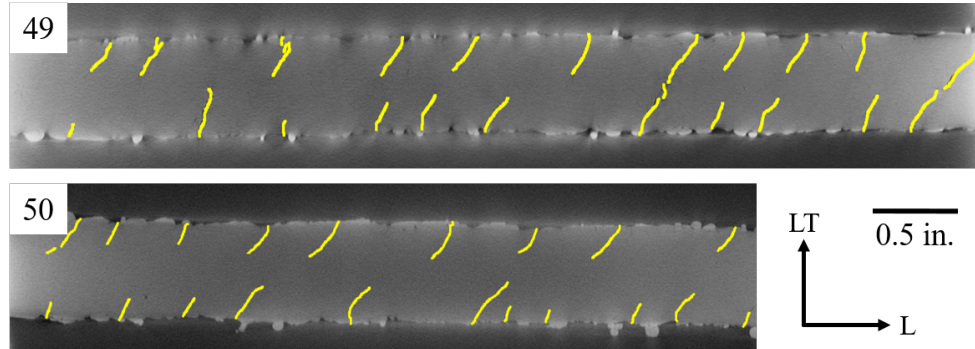


Figure 4.52: Comparison of macrocrack densities for Plates 49 and 50 at a height of 1.2 mm above the baseplate intersection.

Table 4.15 summarizes the results from this comparison. Plate 49 exhibited an average crack length that was about 0.9 mm longer than in Plate 50, as well as a slight increase in the crack density, which was measured as total crack length divided by the analyzed area of the deposit. These higher cracking statistics for Plate 49 correlate with its 200°C higher slope predicted by the $T-f_s^{1/2}$ calculations.

Table 4.15: Comparison of the macrocrack densities measured with low-resolution XCT scans at a height of 1.2 mm above the baseplate intersections for Plates 49 and 50.

Statistic	Plate 49	Plate 50
Average crack length (mm)	5.24	4.28
Crack density (mm^{-1})	0.0681	0.0621

Further work is needed to validate crack susceptibility predictions with crack densities from single-layer deposits of varying parameter sets. While these predictions have limited applicability to the current deposits, they will prove useful when discussing future directions for alloy development to compose alloys will less susceptible compositions.

Liquation Cracking Susceptibility Predictions

A second way that Kou utilizes the $T-f_s^{1/2}$ diagrams is to explain the susceptibility of certain baseplate-welding wire combinations to liquation cracking in welding

[28, 14]. Kou notes that a necessary but not sufficient condition for liquation cracking is that the weld metal f_s is greater than the PMZ (base metal) f_s for the same temperature. In other words, the weld and base metal combination is susceptible to liquation cracking if the weld metal $T-f_s^{1/2}$ curve is further to the right than that of the base metal at some point in the terminal stages of solidification. Kou cites four conditions that prompt such susceptibility to result in cracking: (1) sufficient contraction during solidification, (2) significant restraint to limit contraction, (3) significant liquation due to high solute content or high heat inputs, and (4) little nearby solidification cracking to relax strains in the PMZ [14].

This condition explains why many of the 7075 deposits experienced liquation cracking near the deposit-baseplate intersection, since all deposits have $T-f_s^{1/2}$ diagrams to the right of the 7075 diagram, shown in Figure 4.51. Thus, deposits made on 7075 baseplate solidified before the liquated baseplate, imposing additional strains from their solidification on the PMZ and causing cracking around the deposit footprint. The significant liquation cracking seen beneath the deposit footprint of Plate 60-C8 may be explained by the concentrated heat input from the focused beam, in addition to the lack of nearby solidification cracking to relieve strains in the PMZ. In contrast, Plate 49 also experienced liquation cracking near the baseplate, but these cracks are attributed to higher constraint from the 1 in. baseplate and a large PMZ from the high baseplate temperature.

To avoid liquation cracking at the deposit-baseplate interface, a baseplate composition that freezes before that of the deposits should be selected. This deposit-baseplate combination should be designed accounting for vaporization losses in the deposit. Alternatively, 7075 baseplate could be used if the deposit composition were enhanced with additional Zn and Mg to offset vaporization losses (and assuming that solidification cracking is avoided).

It is more difficult to utilize this condition to explain the liquation cracking seen within the additive builds. This is because the “base metal” of an additive layer is the previous additive layer. By the time of its solidification, layer N has lost roughly the same amount of solute as layer N-1, so the two $T-f_s^{1/2}$ diagrams are essentially overlaid. This overlay will not yield additional useful insight into prediction of liquation cracking for the deposits, save that the PMZ and the weld metal are resolidifying at nearly the same rate. Local fluctuations in composition and grain size might dictate the solidification rates and allow liquation cracking to occur. Thus, in areas with little to no solidification cracking, such as in areas between the large macrocracks, liquation cracking was observed.

Effect of Composition on Hardness

As seen in Section 4.4.6, little change in microhardness was measured between Plates 49 and 50, despite 13% and 7% differences in Zn and Mg content. This may be due to the fact that the material tested is in the AD state, so a significant amount of solute is residing on grain boundaries rather than contributing to precipitation strengthening that would be reflected in the hardness. It is expected that with heat treatment of the two samples, Plate 50 would exhibit a higher hardness due to a greater amount of retained solute.

The coarse-grained region in the Plate 60-C8 deposit was 13 HV_{0.3} lower than the Plate 49 and 50 deposits, suggesting that the additional 1 wt.% Zn lost in C8 compared to 49 had a noticeable impact on the hardness. Contrasting the coarse-grained region of C8, the fine-grained region exhibited a hardness almost equivalent to those of Plates 49 and 50, likely due to the impact of grain boundary strengthening in this region.

Comparison of the 7075 AD hardness values with typical Brinell hardness values from the literature [74] revealed that the deposits' hardness are above that of annealed material but roughly 40 HV₁ below that of peak-strength material. Comparing all of these values to the 7050-T7451 Brinell hardness of 138 BHN (converts to 141 HV₁) [7], one will note that they fall short of the properties target. This makes sense, since the comparison is made between AD material and artificially-aged, wrought material. For more apt comparisons to determine if the 7050-T7 properties target may be met, the 7075 deposits would have to be artificially aged for the effect of the alloying element losses on properties to be fully realized. It is expected that heat treating the material will reduce but not close the gap in hardness due to the significant vaporization losses of the deposits.

4.5.5 Directions for Crack Mitigation and Elimination

The following sections outline the two major avenues for addressing both solidification and liquation cracking in traditionally unweldable AA such as 7075.

Grain Refinement

Currently, grain refinement is the primary approach discussed in the literature for avoiding cracking [17, 21]. In SLM, this is accomplished by functionalizing the powder feedstock with lattice-matching nanoparticles [17] or through prealloying the feedstock

with inoculants such as Zr or Sc [21]. However, this presents some difficulty for EBF³ since traditional wire feedstock would have to be pre-alloyed in a custom melt, or the 7075 wire could be co-deposited with a master alloy containing inoculants. Another possible approach could utilize the particle-dusting techniques from Martin et al. for the powder in powder-cored tubular wire, a new feedstock form in development for EBF³ and other welding and additive processes [46].

In addition to heterogenous nucleation through inoculation as a means of grain refinement, other methods such as beam pulsing in combination with introducing inoculants in the FZ have been demonstrated in welding [25, 26]. These may be applicable with EBF³ since the machine has the capability to pulse the wire and the beam, as well as alter the raster frequency of the beam. A level of success has already been seen with beam parameters causing grain refinement, such as the 38 μm bands of grains in the Plate 60-C8 sample.

The literature cites various reasons why grain refinement may reduce or completely eliminate cracking. Firstly, grain refinement typically transforms grains from columnar to equiaxed in shape [27, 17] and usually substantially reduces their diameter. A fine, equiaxed microstructure is more robust with respect to solidification cracking since shorter distances from dendrite tips to roots allow for easier feeding of the final solute-rich liquid [54]. Furthermore, smaller grains accommodate strains better and experience a lower strain rate at the grain boundary [57]. This decreases the solidification cracking susceptibility and may serve to heal any interdendritic pre-cracks forming.

In addition, a refined grain structure increases the granular surface area, thus diluting the low-melting point secondary phases and eutectic present on the grain boundaries [28]. This dilution would reduce the susceptibility to liquation cracking, since the low-melting point phases are more dispersed. Such dispersed phases may not completely liquate a grain boundary to allow contraction strains from a nearby FZ to cause cracking.

Since grain refinement reduces a material's susceptibility to both solidification and liquation cracking, this is a promising direction for future developmental work with EBF³ of 7xxx alloys and other cracking-sensitive materials. Certain limitations may exist, including the effectiveness of grain refinement for complex geometries such as overlaps in scan tracks or its robustness in anomalous beam conditions and resulting microstructures.

Alloy Design

The second and currently less common avenue for avoiding cracking in additive builds is that of alloy design. This is likely due to the increased cost of designing custom melts from which to atomize powder or draw wire, particularly for laboratories that desire high-purity feedstock. For the EBF³ process at LaRC, the most accessible means of altering the wire chemistry is through the co-deposition of two weld wires at different speeds to obtain the desired chemistry. It is presently assumed that the beam raster would sufficiently incorporate the two wires for an even distribution of their respective chemistries to create a new alloy composition.

To circumvent solidification cracking in welding, Kou proposes finding a filler wire that dilutes the crack-susceptible base metal and achieves a less susceptible composition based on the $|dT/d(f_s)^{1/2}|$ index [62]. Since the present work involves additive manufacturing, where the base metal for layer N is the FZ of layer N-1, the designed composition will need to be for the deposit feedstock. This designed alloy should also take into account alloying element vaporization, particularly if the AM process takes place in a vacuum environment as for EBF³.

A recent patent by Borchers et al. [4] proposes a 7xxx-series alloy with a composition of 5.5% to 6.0% Cu, 2.9% to 3.4% Zn, and 1.4% to 1.9% Mg. A compromise of the 2219 and 7075 compositions, this alloy was presumably designed to reduce solidification cracking susceptibility of 7xxx alloys while increasing the strength from that of 2xxx alloys. Figure 4.53 compares the Scheil solidification diagrams for the 2219 and 7075 wire compositions, in addition to this newly-patented alloy (here termed Alloy X).

An immediately obvious feature from the Scheil plots in Fig. 4.53 is that the freezing range of 2219 is roughly 80°C narrower than those of 7075 and Alloy X. This is often attributed to reduced susceptibility to solidification cracking in welding literature, since the T- f_s curve needs to accommodate a smaller drop in temperature during solidification, which likely reduces the maximum slope. The knee in the 2219 T- $f_s^{1/2}$ curve occurs at $f_s^{1/2} = 0.93$, after which the Al-Cu eutectic forms at a temperature of 544°C.

In contrast, the knee in the 7075 curve occurs at a temperature 73°C lower than that of 2219 and at a $f_s^{1/2} = 0.96$. This contributes to a significantly higher steepness, and thus solidification cracking susceptibility, shown in Table 4.16.

As observed in its T- $f_s^{1/2}$ diagram in Fig. 4.53 and its maximum steepness in Table 4.16, Alloy X is predicted to have a significantly reduced susceptibility to solidification cracking compared to 7075. This may be attributed to the additional 4% to 4.5% Cu,

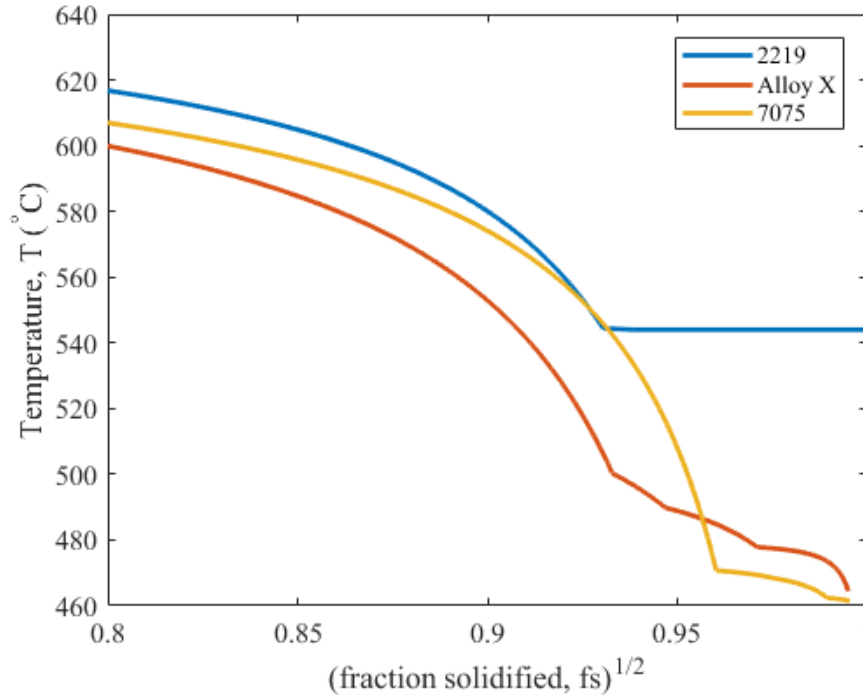


Figure 4.53: Scheil solidification $T-f_s^{1/2}$ plots for the 2219 and 7075 wire compositions, as well as for Alloy X, a recently-patented Al-Cu-Zn-Mg alloy.

Table 4.16: Comparison of the solidification cracking susceptibility as measured by the $|dT/df_s^{1/2}|$ criterion set forth by Kou [62], where increasing slope corresponds to increased crack susceptibility.

Alloy	Knee $f_s^{1/2}$	Knee T (°C)	$ dT/d(f_s)^{1/2} $ (°C)
2219	0.93	544	1736
Alloy X	0.93	500	2581
7075	0.96	471	4778

which moves the knee of the $T-f_s^{1/2}$ curve to $f_s^{1/2} = 0.93$ and a temperature of 500°C . This is in spite of 2.9% to 3.4% Zn and 1.4% to 1.9% Mg additions, which are on the order of the remaining Zn and Mg in the 7075 deposits after losses.

Thus, the further addition of Cu to the 7075 composition after alloying losses thus reduces the predicted susceptibility to solidification cracking by almost double. This prediction is of significant interest to alloy design, since the remaining Zn and Mg in Alloy X composition is expected to result in a higher strength alloy compared to 2219 while reducing susceptibility to solidification cracking compared to conventional 7075.

Furthermore, coupling a modified composition with grain refining additions such as Zr or Sc will further reduce susceptibility to cracking, leading to additive deposits that come closer to meeting the 7050-T7 property targets. Further work and deposition of such an alloy chemistry is needed to validate the EBF³ compatibility of such deposits and their resulting strength.

4.6 Summary

The resulting microstructure, defects, and properties of 7075 under EBF³ processing were examined through three deposition series. From the results and discussion of this effort, the following observations are put forth:

1. Solidification cracking was observed in the steady state region of most 7075 deposits, although the periodicity, width, and location of each deposit's cracks varied with deposit constraint and cooling rate. Solidification cracks were manifested as half- or full-deposit width 'macrocracks' running up the sides of tall deposits, or breaking the top surface of few-layer deposits.
2. Baseplate thickness influenced the solidification cracking extent and frequency along the deposit length, with deposits on 1 in. baseplate (Plates 49 and 50) exhibiting full-height cracks spaced on the order of 0.5 to 0.75 in. Deposits on 0.25 in. baseplate (Plate 46, 71-40L) exhibited truncated cracks that began at the baseplate or higher in the build but were not continuous over the deposit height.
3. Liquation cracking was observed in all deposits from polished cross sections and high-resolution XCT scans. These 'microcracks' were on the microstructural scale and occurred between elongated grains below the final layer of deposits. Longer liquation cracks correlated with higher deposit temperature during processing.
4. Liquation and liquation cracking was observed at the intersection of the 7075 deposits with the baseplate, as predicted by the Scheil $T-f_s^{1/2}$ curves and brought about by high welding temperatures and/or high constraint from thick baseplate.
5. Grain refinement in the Plate 60-C8 sample disrupted the onset of solidification cracking in the deposit, resulting in a crack-free steady-state region of the

deposit. Liquation cracking was also substantially reduced in the large-grained regions of the microstructure and eliminated in the fine-grained regions.

6. The alloy losses of Zn and Mg resulted in an average AD hardness of 116 HV_{0.3} for a range of deposit compositions from 3.7% to 4.2% Zn and 2.0% to 2.1% Mg (Plates 49 to 50). Large-grained regions of a deposit with greater alloy losses of 2.7% Zn and 2.0% Mg (Plate 60-C8) resulted in an average HV_{0.3} of 103, while fine-grained regions in the same deposit were on par with those of deposits with smaller losses.
7. The hardness values of the 7075 alloy in the AD condition were well below those of conventional 7050-T6. It is expected that with heat treatment, the deposits' hardness will approach that of the conventional alloy, with some variation given the alloy losses.
8. While the 7050-T7 property target may be achieved via subsequent heat treatment of the 7075 deposits, the EBF³ compatibility of the material remains to be established. Future research is needed in areas of grain refinement and alloy design techniques to circumvent or substantially reduce susceptibility to cracking.

Chapter 5

Conclusions and Future Work

5.1 Conclusions

This thesis investigated the AM compatibility and resulting properties of two AAs (2219 and 7075) deposited with the EBF³ process. Due to the integrity of 2219 deposits, mechanical testing specimens were fabricated and demonstrated tensile properties comparable to those of wrought material. The 7075 deposits suffered from vaporization losses of Zn and Mg that resulted in extensive hot cracking in the deposits, preventing the extraction of mechanical test specimens. The following conclusions maybe drawn from this work:

1. The excellent AM compatibility of 2219 with the EBF³ process compared to 7075 resulted from 2219 having a smaller solidification temperature range and abundant Al-Cu eutectic, which prevented the initiation of solidification cracks. While liquation was noted in the 2219 AD microstructure and at the deposit-baseplate intersection as heavy decoration of eutectic on grain boundaries, liquation cracking was not observed.
2. Tensile properties of 2219 AD material were anisotropic, but all values were between those for annealed and T4 wrought products, consistent with prior EBF³ work [9, 11]. The HT material exhibited isotropic tensile properties comparable to those of typical T62 wrought values due to the homogenization of the liquated microstructure in HT.
3. Significant losses of Zn and Mg were observed in the deposits due to their high vapor pressures at the melting temperature of Al. Slow travel speeds led to an

increase in losses due to increased molten residence time, while near-focused and focused beam parameters led to the greatest losses due to superheating of the molten pool. Due to these Zn and Mg losses, it is unlikely that 7075 deposits would achieve 7075-T7 wrought properties since there is less solute available for the formation of a critical volume fraction of strengthening precipitates.

4. Deposition of the 7075 material resulted in extensive hot cracking, with wide solidification “macrocracks” running through the height of the deposit and liquation “microcracks” appearing below the final layer of the deposit. Solidification cracking was intensified by increasing baseplate thickness and alloying element losses, while liquation cracking increased with deposit temperature and elongated grain morphologies.
5. Metallurgical and fractographic analyses confirmed that these cracks developed by the same hot cracking mechanisms documented in literature for welding, but with differing presentations in the additive deposits. In the first two layers, solidification cracks nucleated at the edge of the bead perpendicular to melt pool tracks and turned parallel to the deposition direction near the build centerline. Solidification cracks in higher layers shifted from parallel to the deposition direction to transverse due to the absence of baseplate constraint.
6. Liquation cracks also developed by the same mechanism as documented in welding literature. These cracks were observed at the baseplate intersection, where cracks nucleated at the fusion zone boundary and extended through the partially melted zone between base metal grains. The formation of liquation cracks at the deposit-baseplate intersection occurred due to the fusion zone solid fraction exceeding that of the partially melted zone, based on their respective compositions. Liquation cracks were also observed directly below the topmost layer of all deposits and between elongated grains in the microstructure, with higher deposit temperature increasing the average length and number of cracks.
7. Bands of refined grains induced by the high energy density of a focused EB resulted in the elimination of solidification cracking in the steady-state region of a deposit (7075 Plate 60-C8) and a 4x reduction in the liquation crack density below the deposit’s final layer. This corroborates trends seen in welding [13] and AM [17] literature that indicate grain refinement as a primary means of eliminating both types of cracking, since a refined microstructure accommodates solidification strains better and disperses liquation-sensitive particles over

a larger granular surface area than a columnar microstructure.

8. Alloy design is also crucial to the reduction of solidification and liquation cracking. Results from calculations of the Scheil $T-f_s^{1/2}$ diagrams showed that Zn and Mg losses increased the hot cracking susceptibility index of 7075 deposits up to 20% with increasing slope in the terminal stages of solidification. Exploration of new 7xxx-series alloy compositions with high Cu [4] resulted in a 1.9x lower HCS index than for 7075 but a 1.2x higher index than for 2219. This decrease in the predicted susceptibility is expected to result in a significant reduction, and possibly elimination, of solidification cracks in deposits of the new alloy.

5.2 Future Work

The successful deposition of the 2219 material and its tensile properties warrant further investigation of the material response with EBF³ deposition. Work to study secondary properties (fracture toughness and corrosion) is underway, while investigation of other properties like fatigue and compression testing are still remaining. Additionally, deposition and testing of more complex structures such as a curvilinear-stiffened panel [97] would be critical to demonstrating the viability of production of AM integrally-stiffened structures with EBF³.

In contrast to the straightforward deposition of 2219, a significant amount of work remains for successful EBF³ deposition of 7075 and 7xxx-series alloys in general. The first step is to implement the focused beam parameters on a full-scale deposit, both on 0.25 in. and 1 in. baseplate, to investigate whether banding of beam-induced grain refinement is enough to disrupt all solidification cracking in long and tall deposits. Other grain-refining techniques to investigate are concurrent beam and wire pulsing [13], in addition to inoculation with Zr or Sc alloy additions [17, 21].

A second avenue of research should involve the co-deposition of 7xxx- and 2xxx-series alloys, or the use of a custom-melt alloy, to study the effects of alloy modifications on solidification cracking extent. Co-deposition with a master alloy could also compensate for the elemental losses of Zn and Mg from the molten pool to achieve a higher volume fraction of strengthening precipitates from more retained solute, as well as reducing the HCS by increasing the amount of eutectic in the final stages of solidification. It is expected that similar success of alloy design for lowering the HCS index will be seen as in welding, where altering the chemistry of the deposit changes the solidification pathway and can lead to a reduction in cracking. Investigation of

the Scheil model and higher-fidelity models for predicting the $T-f_s^{1/2}$ diagrams from which to calculate the HCS index is also warranted, given the limitations of the Scheil model.

Ultimately, a combination of alloy design and grain refinement will be necessary to solve both the solidification and liquation cracking issues in the deposition of 7xxx material. This has broad impacts, since deposition of 7xxx-series alloys with EBF³ (or other additive processes) would enable the manufacture of high-strength, integrally-stiffened aircraft components and meet the research goal of developing an AM-compatible, drop-in replacement for 7050-T7.

Appendix A

AA2219 Deposit Cut Plans

This appendix provides the cut plans for the AA2219 wall and brick deposits. Samples that are labeled are those tested and analyzed in this work. Samples with black labels were tested or analyzed at LaRC, while specimens with white lettering were tested offsite. Unlabeled samples relate to other studies and are not discussed here.

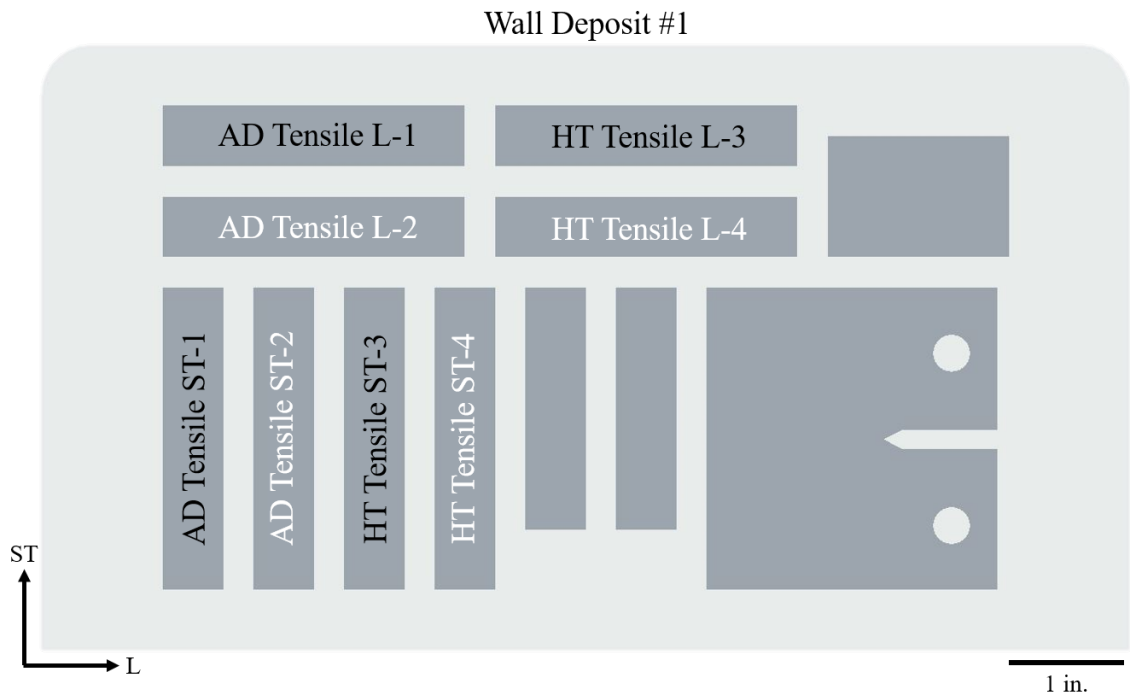


Figure A.1: Cut plan for the first of three co-deposited AA2219 walls.

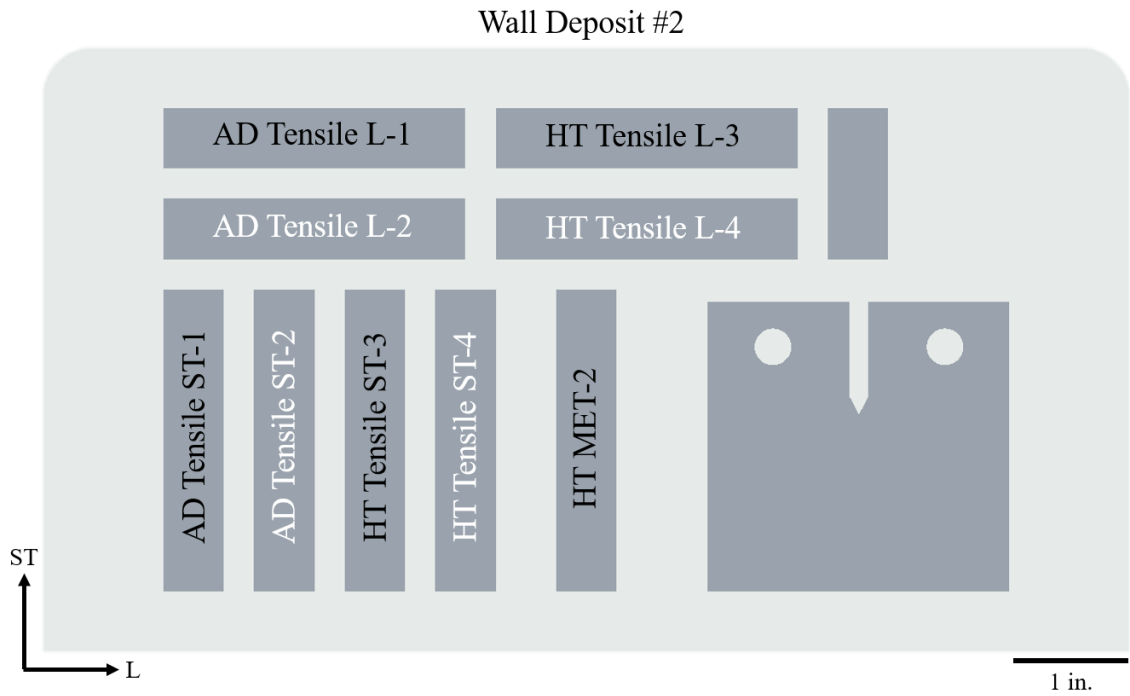


Figure A.2: Cut plan for the second of three co-deposited AA2219 walls.

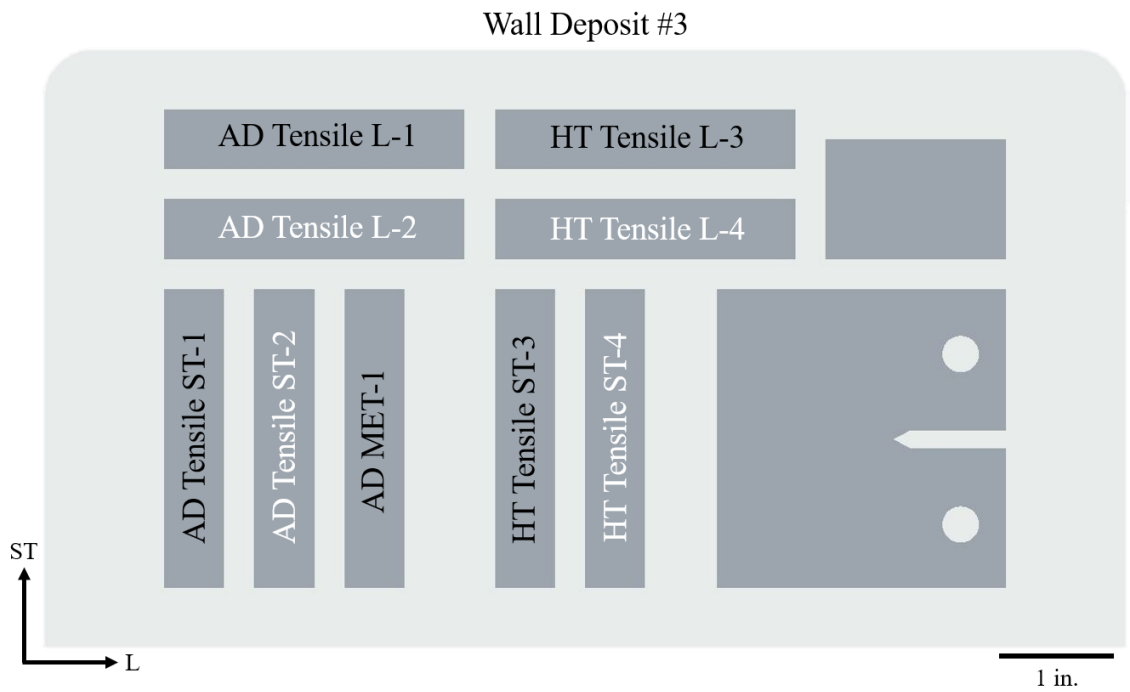


Figure A.3: Cut plan for the third of three co-deposited AA2219 walls.

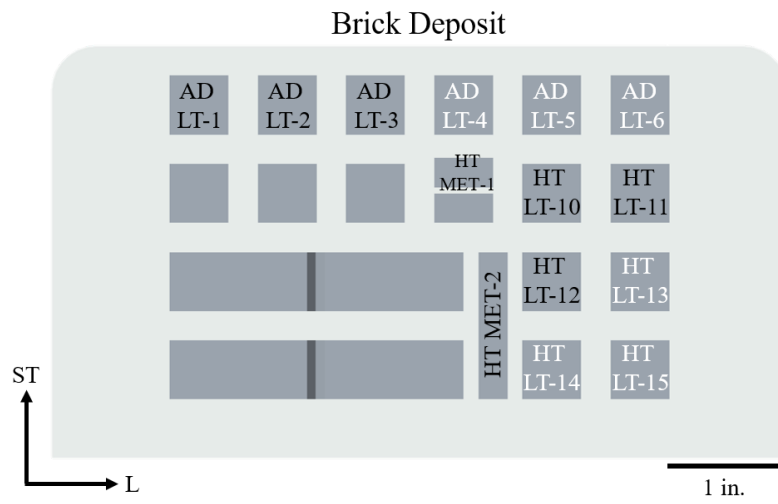


Figure A.4: Cut plan for the AA2219 brick deposit.

Appendix B

Sub-size Tensile Specimen Drawing

This appendix provides the engineering drawing for the subsize tensile specimen used for testing the mechanical properties of the AA2219 wall and brick shaped deposits.

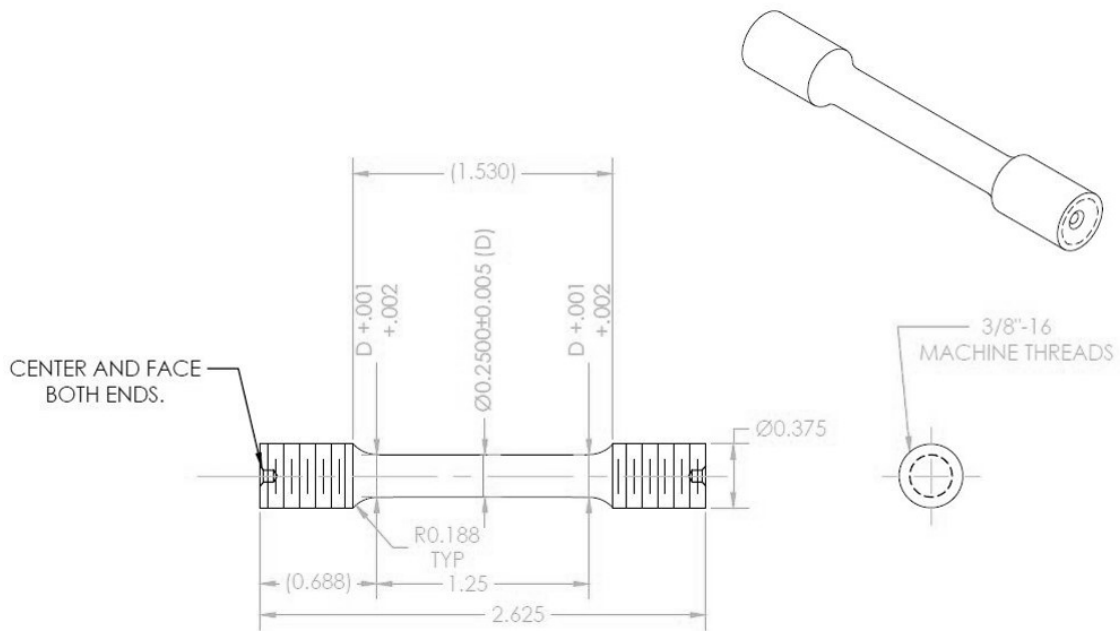


Figure B.1: Subsize tensile specimen drawing in compliance with ASTM E8 [87].

Appendix C

7075 Deposit Cut Plans

This appendix provides a guide to the locations of cuts for crack examination and extraction of cylindrical XCT scans in the 7075 deposits. Crack surfaces are labeled and referenced in the text.

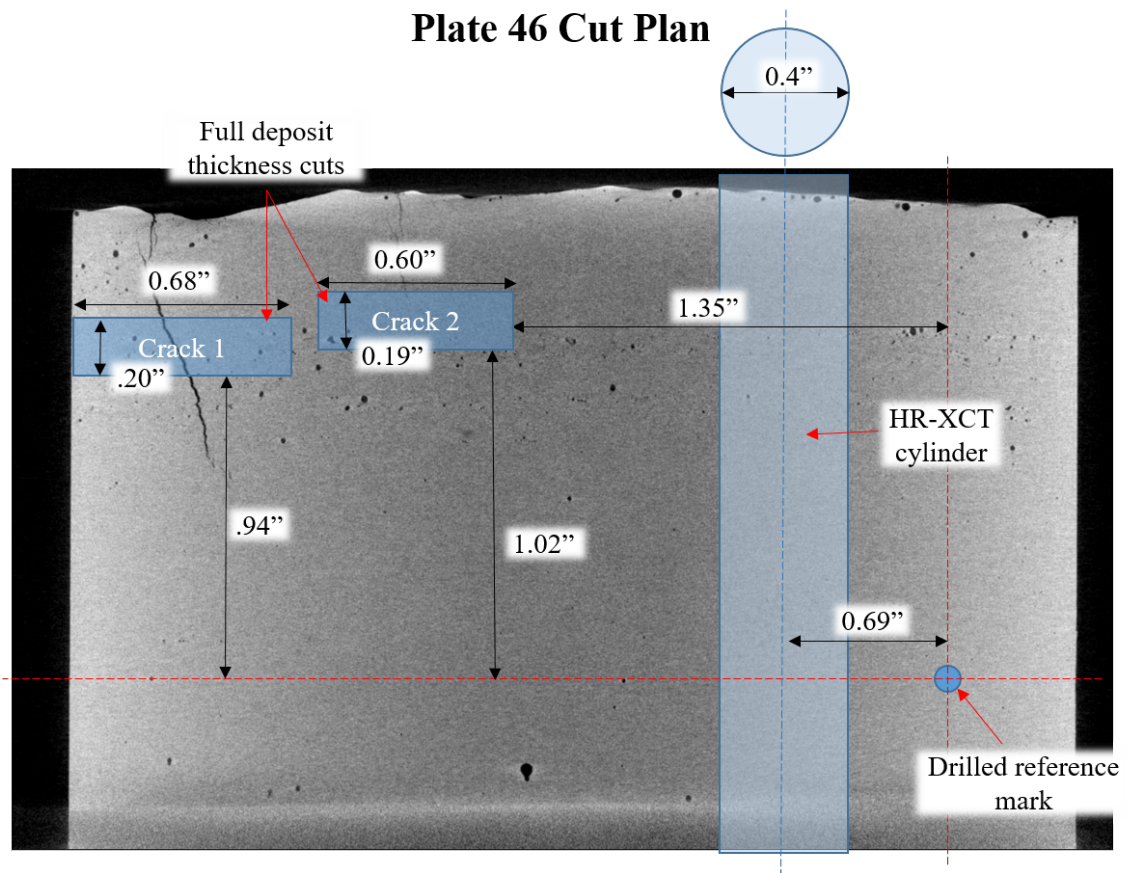


Figure C.1: Cut plan for Plate 46, which includes specimens containing two full-width cracks and a 0.4 in. cylindrical specimen for high resolution XCT scans.

Plate 49 Cut Plan

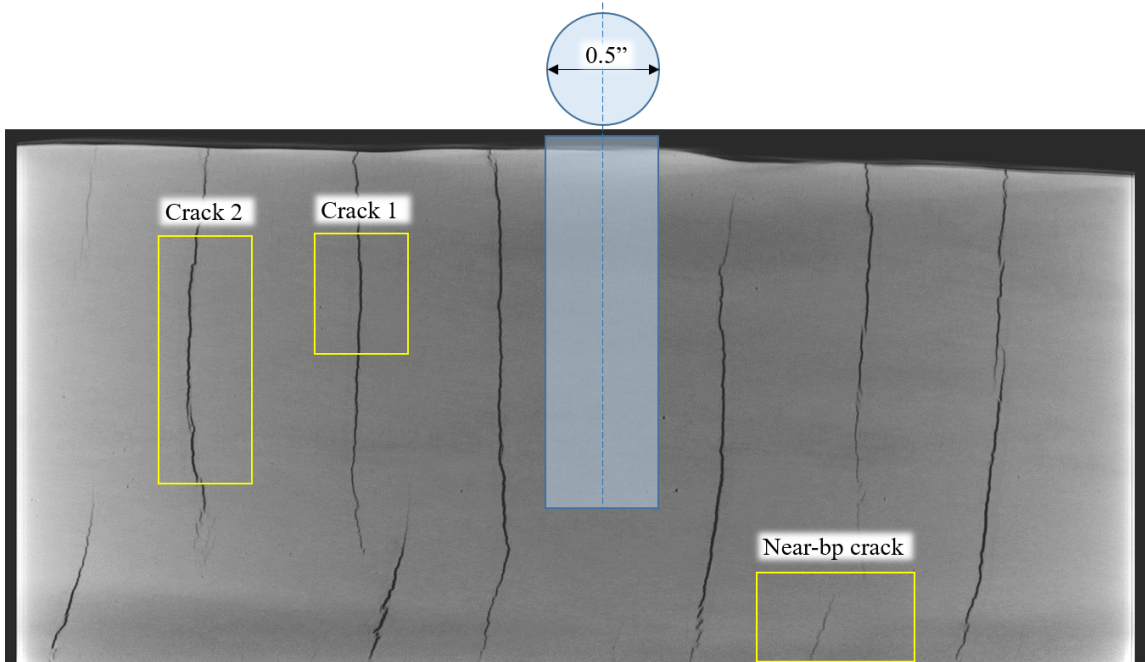


Figure C.2: Cut plan for Plate 49, which includes specimens surround two full-width macrocracks in addition to a near-baseplate, partial-width crack. A 0.5 in. cylinder was extracted from the region high in microcracking for high-resolution XCT.

Plate 50 Cut Plan

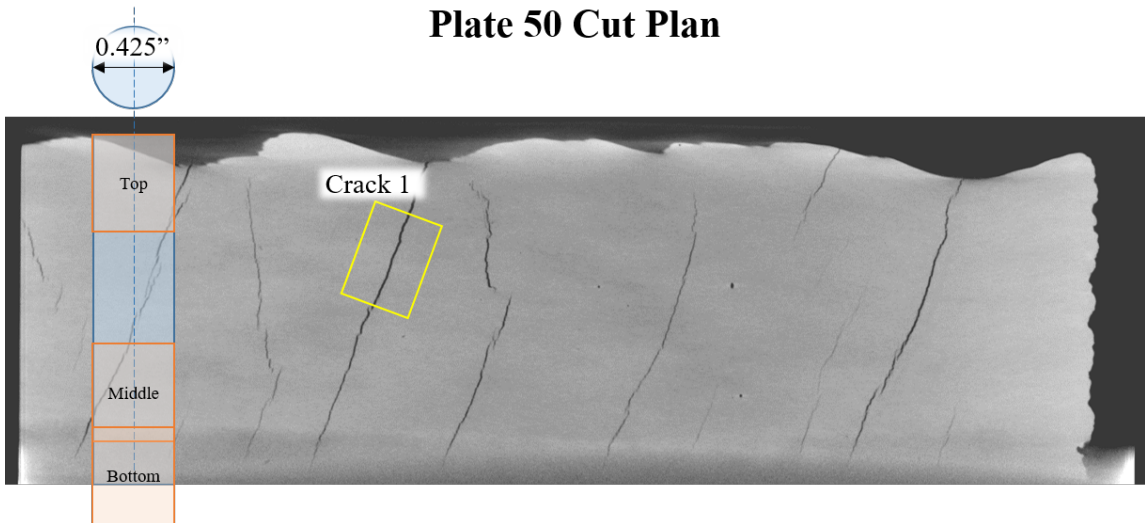


Figure C.3: Cut plan for Plate 50, which includes a specimen surrounding a full-width macrocrack, as well as a 0.425 in. cylinder. Three regions were examined with high-resolution XCT scans: the interaction of two macrocracks in the middle of the deposit, as well as solidification cracks at the deposit-baseplate intersection and liquation cracks near the top of the deposit.

Plate 60-C8 Cut Plan

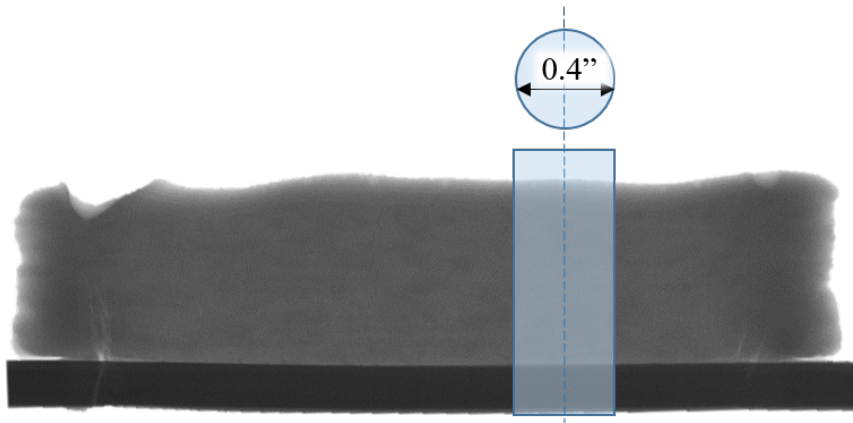


Figure C.4: Cut plan for Plate 60-C8, which includes a 0.4 in. cylinder for high-resolution XCT scans below the top layer of the deposit. Metallurgical cross section sample not shown.

Appendix D

Solidification Rate and Liquation Depth Analysis

This appendix provides a summary of thermal analysis completed by Christopher Lang at NASA Langley as part of a larger effort of thermal modeling for additive manufacturing [98].

D.1 Thermal Model Setup

Thermal analysis of 9 in. long, single-bead EBF³ deposits was completed to (1) estimate the solidification rate of the deposits and (2) provide estimates of the liquation depth below each layer's fusion zone.

The analysis was run using the Sierra Mechanics multi-physics finite element code [99] as a 3D symmetric transient diffusion problem governed by the heat diffusion equation for $T(\mathbf{x},t)$:

$$\rho c_p \frac{\delta T}{\delta t} - \nabla \cdot (k \nabla T) = S + Q \quad (\text{D.1.1})$$

where ρ is the material density, c_p is the heat capacity, $\delta T/\delta t$ is the transient temperature change, and k is the thermal conductivity. S is the phase change source term for solidification given by:

$$S = -\rho L_f \frac{\delta f_L}{\delta t}, \quad (\text{D.1.2})$$

where L_f is the latent heat of fusion and the derivative is the change in the fraction

liquid, f_L , with time.

The boundary conditions for the simulations were:

1. $(k\nabla T) \cdot \mathbf{n} = q_s$ - Top surface
2. $T = T_B$ - Bottom surface
3. $(k\nabla T) \cdot \mathbf{n} = 0$ - All other surfaces
4. $T(\mathbf{x}, 0) = T_i$ - Initial temperature

where q_s defines the heat flux due to radiation.

The EBF³ electron beam power source was modeled with overlapping conical volumetric heat sources [100], shown in Fig. D.1(a). This approximated the W-shaped melt pools from the elliptical raster pattern, a symmetric half of which is shown in Fig. D.1(b).

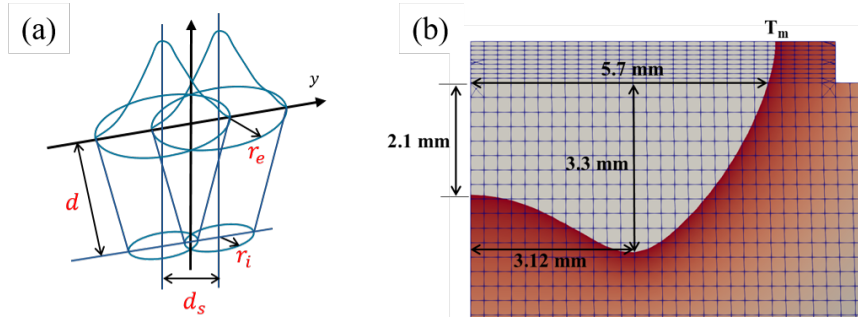


Figure D.1: Double conical volumetric heat source used for thermal modeling.

To calibrate the volumetric heat distribution within the double conical source, the parameters labeled in red in Fig. D.1(a) were related to melt pool geometries and measured from a sample deposit. The parameters and melt pool shape from Plate 19 were used for the analysis. Fig. D.1(b) shows the calibrated melt pool parameters. Table D.1 lists the EBF³ machine parameters and Al thermal properties used in the analysis.

The 9 in. x 0.5 in. x 0.031 in. deposit layer was added to the model instantaneously, and the heat source was then translated over the material with the same parameters as in the EBF³ build trials. The cooling rate was measured at two points - Point A on the top of a deposit layer, and Point B below that layer. Figure D.2 shows a schematic of the model setup demonstrating (a) the symmetric, single scan track design and (b) the reference points A and B.

Table D.1: EBF³ machine parameters and Al properties used in the thermal model.

Parameter	Value
Travel speed	[24, 30, 40] ipm
Layer thickness	0.031 in.
Base temperature	195°C
Power	3600 W
Absorptivity/emissivity	0.9/0.1
$T_{solidus}$	462°C
T_{melt}	556°C
$T_{liquidus}$	640°C
Latent heat L_f	358 J/g
Mesh size	0.011 in.

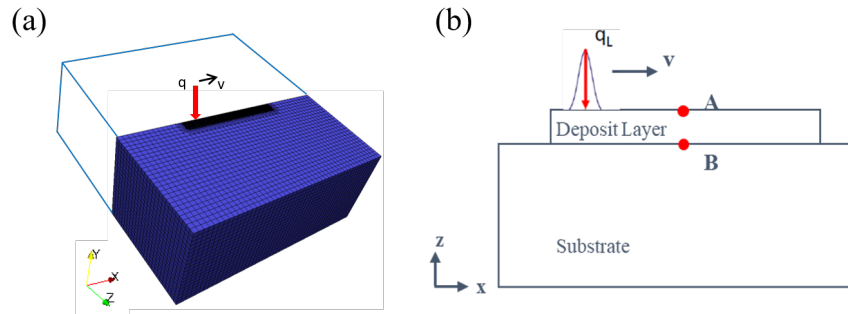


Figure D.2: (a) Single scan track symmetric model, (b) Model setup, with reference points A and B marked.

The heat source calibrated for the Plate 19 deposit (30 ipm travel speed) was also used for the 24 ipm (Plate 45) and 40 ipm (Plates 46-50) conditions to gain insight into the dependence of solidification rate on travel speed. This assumption could introduce error for the 24 and 40 ipm cases, since the beam focus differed for the various plates and affects the dimensions of the double conical heat source. However, the simulations were run as a first-order estimation of cooling rate, acknowledging that values may have slight changes with an optimized power source.

D.2 Results

D.2.1 Solidification Rate Predictions

The solidification rates at reference points A and B in Fig. D.2(b) are reported in Table D.2 for the three travel speed conditions.

Table D.2: Results from the thermal analysis showing the predicted solidification rates as a function of travel speed. Note that the volumetric heat source was not optimized for the 24 and 40 ipm cases.

Travel speed (ipm)	Cooling rate A (°C/s)	Cooling rate B (°C/s)
24	454.4	445.6
30	530.8	517.4
40	644.5	622.0

As expected, the solidification rate increased with increasing travel speed, ranging from 450°C/s for the slowest case to nearly 650°C/s for the fastest travel speed. The average dendritic arm spacing of dendrites in the top layer of the Plate 68-3L deposit was found to be 5.43 μm . This dendritic arm spacing corresponds to a solidification rate near 550°C/s, which is within the range found with the thermal analysis.

The general trend in melt pool shape with increasing travel speed included shallower melt pools, corresponding to less remelt of previous layers, as well as a decreased width.

D.2.2 Liquation Depth Analysis

The resulting temperature field solutions from the model were also used to study the depth of material below the molten pool track of Plate 19 where temperatures rose above the eutectic temperature, T_E , of 462°C. The thickness of this region, L , was measured to be 1.3 mm, as shown in Fig. D.3(a). However, optical micrographs of the Plate 19 sample revealed that evidence of liquation and liquation cracking was limited within 0.56 mm. of the melt pool boundary, as shown in Fig. D.3(b).

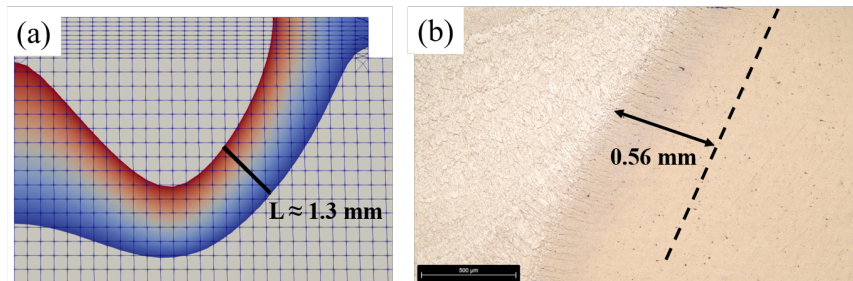


Figure D.3: (a) Simulated melt pool, with liquated region of $L = 1.3$ mm and temperatures 660-462°C colored. (b) Deposit-baseplate intersection micrograph showing evidence of liquation and liquation cracking with a maximum thickness of 0.56 mm.

This discrepancy in liquated depth predictions and physical evidence may be understood by the time at temperature of this critical thickness of 0.56 mm, hereafter referred to as Γ . Figure D.4 shows three images from the simulation representing the lower, maximum, and upper time limits bounding the partial melting of Γ .

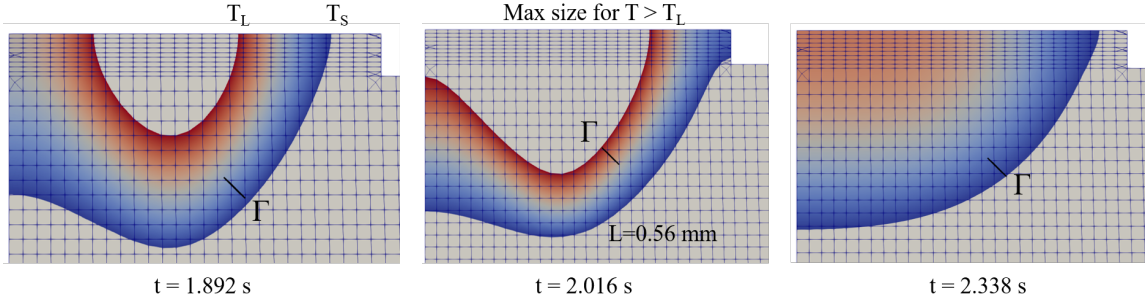


Figure D.4: Three snapshots in time showing the (a) lower and (c) upper limits when Γ is partially melted, and (b) the maximum size of the partially melted zone.

The time spent molten for Γ was found to be 0.45 s. Since evidence of liquation and liquation cracks were only observed within this thickness below the molten pool, it is believed the molten time of Γ represents the critical cracking time for the relatively homogeneous base metal microstructure.

It is expected that increasingly heterogeneous microstructures, such as those within the additive deposits, will have more rapid liquation kinetics due to higher density of low-melting point phases on grain boundaries. Furthermore, with increasing build height, the deposit will retain more heat during deposition, resulting in a lower thermal gradient between the molten pool and bulk temperature of the deposit and increasing the liquation depth. While analysis was not completed for multi-layer deposits, it is expected that the liquation depth is greater than 0.56 mm, and thus greater than the typical Δz step height.

Bibliography

- [1] ASM Handbook Vol. 6A. *Welding Fundamentals and Processes*. ASM International, 2011.
- [2] P. Joshi, S. Mulani, W. Slemph, and R. Kapania. Vibro-acoustic optimization of turbulent boundary layer excited panel with curvilinear stiffeners. *Journal of Aircraft*, 49(1):52–65, 2012.
- [3] P. Dunning, B. Standford, H. Kim, and C. Jutte. Aeroelastic tailoring of a plate wing with functionally graded materials. *Journal of Fluids and Structures*, 51:292–312, 2014.
- [4] T. Borchers, Y. Gu, J. Lin, K. Williams, J. Williams, and J. McMichael. Aluminum alloy compositions, products and methods of making the same. *WO Patent 2018-157159 A1*, pages 210–220, 2018.
- [5] *Aerospace Materials and Material Technologies*, chapter Aluminum Alloys for Aerospace Applications. Springer, 2017.
- [6] MMPDS-12. *Metallic Materials Properties Development and Standardization (MMPDS)*. Battelle Memorial Institute, 2017.
- [7] ASM Handbook Vol. 2B. *Properties and Selection of Aluminum Alloys*. ASM International, 2019.
- [8] AMS 4599. *Aluminum Alloy Sheet and Plate, Solution and Precipitation Heat Treated (2219-T81/-T851), Rev. A*. SAE International, Danvers, MA, 2017.
- [9] K. Taminger and R. Hafley. Characterization of 2219 aluminum produced by electron beam freeform fabrication. *In proceedings of the 13th Annual Solid Freeform Fabrication Symposium*, 2002.

- [10] K. Taminger, R. Hafley, and M. Domack. Evolution and control of 2219 aluminium microstructural features through electron beam freeform fabrication. In *Aluminium Alloys 2006 - ICAA10*, volume 519 of *Materials Science Forum*, pages 1297–1302. Trans Tech Publications, 7 2006.
- [11] M. Domack and K. Taminger. Metallurgical mechanisms controlling mechanical properties of aluminum alloy 2219 produced by electron freeform fabrication. *NASA TM-2006-214316*, 2006.
- [12] AMS 4078. *Aluminum Alloy Sheet and Plate, 7075 (-T73 Sheet, -T7351 Plate)*, Rev. K. SAE International, Danvers, MA, 2018.
- [13] S. Kou. *Welding Metallurgy, 2nd ed.* John Wiley and Sons, Inc. Hoboken, NJ, 2003.
- [14] G. Cao and S. Kou. Predicting and reducing liquation-cracking susceptibility based on temperature vs. fraction solid. *Welding Journal*, 85:9s–18s, 2006.
- [15] M. Holzer, K. Hofmann, V. Mann, F. Hugger, S. Roth, and M. Schmidt. Change of hot cracking susceptibility in welding of high strength aluminum alloy aa 7075. *Physics Procedia*, 83:463–471, 2016.
- [16] T. Soysal and S. Kou. A simple test for assessing solidification cracking susceptibility and checking validity of susceptibility prediction. *Acta Materialia*, 143:181–197, 2018.
- [17] J. Martin, B. Yahata, J. Hundley, J. Mayer, T. Schaedler, and T. Pollock. Factors affecting porosity in aluminum welds - a review. *Nature*, 549, 2017.
- [18] W. Reschetnik, J.-P. Bruggemann, M.E. Aydinov, O. Grydin, K.-P. Hoyer, G. Kullmer, and H.A. Richard. Fatigue crack growth behavior and mechanical properties of additively processed en aw-7075 aluminum alloy. *Procedia Structural Integrity*, 2:3040–3048, 2016.
- [19] N. Kaufmann, M. Imran, T. M. Wischeropp, C. Emmelmann, S. Siddique, and F. Walther. Influence of process parameters on the quality of aluminum alloy en aw 7075 using selective laser melting (slm). *Physics Procedia*, 83:918–926, 2016.
- [20] C. Galy, E. Guen, E. Lacoste, and C. Arvieu. Main defects observed in aluminum alloy parts produced by slm: From causes to consequences. *Additive Manufacturing*, 22:165–175, 2018.

- [21] L. Zhou, H. Pan, H. Hyer, S. Park, Y. Bai, B. McWilliams, K. Cho, and Y. Sohn. Microstructure and tensile property of a novel alznmgsczr alloy additively manufactured by gas atomization and laser powder bed fusion. *Scripta Materialia*, 158:24 – 28, 2019.
- [22] J. Liu and S. Kou. Susceptibility of ternary aluminum alloys to cracking during solidification. *Acta Materialia*, 125:513–523, 2016.
- [23] J. Gu, B. Cong, J. Ding, S. Williams, and Y. Zhai. Wire + arc additive manufacturing of aluminium. *In proceedings of the 25th Annual Solid Freeform Fabrication Symposium*, 2014.
- [24] N. Coniglio, C.E. Cross, T. Michael, and M. Lammers. Defining a critical weld dilution to avoid solidification cracking in aluminum. *Welding Journal*, 87(9):237s–247s, 2008.
- [25] F. Matsuda, K. Nakata, K. Tsukamoto, and S. Johgan. The vdr cracking test for solidification crack susceptibility on weld metals and its application to aluminum alloys. *Transactions of JWRI*, 14(2):99–104, 1985.
- [26] E.J. Michaud, H.W. Kerr, and D.C. Weckman. Temporal pulse shaping and solidification cracking in laser welded al-cu alloys. *Proceedings of the 4th International Conference of Trends in Welding Research*, pages 153–158, 1995.
- [27] Y. Le and S. Kou. Welding parameters and the grain structure of weld metal - a thermodynamic consideration. *Metallurgical Transactions A*, 19(4):1075–1082, 1988.
- [28] S. Kou. Solidification and liquation cracking issues in welding. *JOM*, 55(6):37–42, 2003.
- [29] C. Huang and S. Kou. Partially melted zone in aluminum welds - liquation mechanism and directional solidification. *Welding Journal*, 79:113s–120s, 2000.
- [30] C. Huang and S. Kou. Liquation cracking in full-penetration al-cu welds. *Welding Journal*, 83:50s–58s, 2004.
- [31] G. Chen, B. Wang, S. Mao, P. Zhong, and J. He. Research on the “∞”-shaped laser scanning welding process for aluminum alloy. *Optics and Laser Technology*, 115:32–41, 2019.

- [32] A. Mertens, J. Delahaye, and J Lecomte-Beckers. Fusion-based additive manufacturing for processing aluminum alloys: State-of-the-art and challenges. *Advanced Engineering Materials*, 19(8), 2017.
- [33] E. Burke. Qualification & certification of additively manufactured parts for nasa applications. NASA Safety Center, Webinar.
- [34] D. Ding, Z. Pan, D. Cuiuri, and H. Li. Wire-feed additive manufacturing of metal components: Technologies, developments, and future interests. *International Journal of Advanced Manufacturing Technology*, 81:465–481, 2015.
- [35] S.W. Williams, F. Martina, A.C. Addison, J. Ding, G. Pardal, and P. Colegrove. Wire+arc additive manufacturing. *Materials Science and Technology*, 32(7):641–647, 2016.
- [36] T. DebRoy, H.L. Wei, J.S. Zuback, T. Mukherjee, J.W. Elmer, J.O. Milewski, A.M. Beese, A. Wilson-Heid, A. De, and W. Zhang. Additive manufacturing of metallic components - process, structure and properties. *Progress in Materials Science*, 92:112–224, 2018.
- [37] D. Herzog, V. Seyda, E. Wycisk, and C. Emmelmann. Additive manufacturing of metals. *Acta Materialia*, 117:371–392, 2016.
- [38] Sciaky Inc. Advantages of wire vs. powder am.
- [39] B. Koscielny. *The Effect of the Inter-Layer Time Interval on Selective Laser Melted Inconel 718*. Thesis, University of Virginia, 2019.
- [40] L. Kren. Arconic goes all-in on am. 2018.
- [41] A. Nyirady. Sciaky’s ebam process achieves qualification through lockheed martin testing. 2018.
- [42] P. Gradl, S. Greene, C. Protz, B. Bullard, J. Buzzell, C. Garcia, J. Wood, and K. Cooper. Additive manufacturing of liquid rocket engine combustion devices: A summary of process developments and hot-fire testing results. *54th AIAA/SAE/ASEE Joint Propulsion Conference*, 2018.
- [43] K. Taminger and R. Hafley. Electron beam freeform fabrication for cost effective near-net shape manufacturing. *In proceedings of the NATO/RTO AVT-139 Specialists’ Meeting on Cost Effective Manufacture via Net Shape Processing*, 2006.

- [44] K. Taminger, R. Hafley, and D. Dicus. Solid freeform fabrication: An enabling technology for future space missions. *In proceedings of the International Conference on Metal Powder Deposition for Rapid Manufacturing*, 2002.
- [45] Programming manual: Electron beam weld system. *Sciaky Inc.*, 2002.
- [46] D. Gonzales, S. Liu, M. Domack, and R. Hafley. Using powder cored tubular wire technology to enhance electron beam freeform fabricated structures. In *TMS 2016 145th Annual Meeting & Exhibition*, pages 183–189, Cham, 2016. Springer International Publishing.
- [47] R. Honig. Vapor pressure data for the solid and liquid elements. *RCA Laboratories Review*, 23(4):567–586, 1962.
- [48] *Thermo-Calc Software TCAL2 Al Alloys database*. 2014.
- [49] X. He, T. DebRoy, and P.W. Fuerschbach. Alloying element vaporization during laser spot welding of stainless steel. *Journal of Physics D: Applied Physics*, 36:3079–3088, 2003.
- [50] J. Devletian and W. Wood. Factors affecting porosity in aluminum welds - a review. *Welding Research Bulletin*, 290, 1983.
- [51] P. Jennings, A. Singer, and W. Pumphrey. Hot-shortness of some high-purity alloys in the systems aluminum-copper-silicon and aluminum-magnesium-silicon. *Welding Journal Research Supplement*, 74:227–248, 1948.
- [52] J.C. Borland and J.H. Rogerson. Examination of the patch test for assessing hot cracking tendencies of weld metal. *British Welding Journal*, 8:494–499, 1963.
- [53] C. Chang. Hot-shortness of some high-purity alloys in the systems aluminum-copper-silicon and aluminum-magnesium-silicon. *Materials Science and Technology*, 29(4):504–510, 2013.
- [54] N. Coniglio and C. E. Cross. Initiation and growth mechanisms for weld solidification cracking. *International Materials Reviews*, 58(7):375–397, 2013.
- [55] J. D. Dowd. Weld cracking of aluminum alloys. *Welding Journal*, 31:448s–456s, 1952.

- [56] L. Katgerman and D.G. Eskin. *Hot Cracking Phenomena in Welds II*, chapter In Search of the Prediction of Hot Cracking in Aluminum. Springer, Berlin, Heidelberg, 2008.
- [57] N. Coniglio and C. E. Cross. Mechanisms for solidification crack initiation and growth in aluminum welding. *Metallurgical and Materials Transactions A*, 40A:2718–2728, 2009.
- [58] W. Pumphrey and J. Lyons. Cracking during the casting and welding of the more common binary aluminum alloys. *Journal of the Institute of Metals*, 74:439–455, 1948.
- [59] S. H. Hwang H. T. Kim, S. W. Nam. Study on the solidification cracking behaviour of high strength aluminum alloy welds: Effects of alloying elements and solidification behaviours. *Journal of Materials Science*, 31:2859–2864, 1996.
- [60] F. Matsuda, H. Nakagawa, K. Nakata, and H. Okada. The vdr cracking test for solidification crack susceptibility on weld metals and its application to aluminum alloys. *Transactions of JWRI*, 8(1):85–95, 1979.
- [61] M. Rappaz, J.-M Drezet, and M. Gremaud. A new hot-tearing criterion. *Metallurgical and Materials Transactions A*, 30A:449–455, 1999.
- [62] S. Kou. A simple index for predicting the susceptibility to solidification cracking. *Welding Journal*, 94:374s–388s, 2015.
- [63] J. Liu and S. Kou. Crack susceptibility of binary aluminum alloys during solidification. *Acta Materialia*, 110:84–94, 2016.
- [64] S. Kou and Y. Le. Altering grain orientation and weld solidification cracking. *Metallurgical Transactions A*, 16(10):1887–1896, 1985.
- [65] C. Huang and S. Kou. Liquefaction mechanisms in multicomponent aluminum alloys during welding. *Welding Journal*, 81:211s–222s, 2002.
- [66] N.F. Gittos and M.H. Scott. Heat-affected zone cracking of al-mg-si alloys. *Welding Journal*, 60(6):95s–103s, 1981.
- [67] L.F. Mondolfo. Part 2 - binary alloys. In *Aluminum Alloys*, pages 211–416. Butterworth-Heinemann, 1976.

- [68] J. Pilet, M. Worden, M. Guillot, D. Diecidue-Conners, and K. Welzyn. AIAA technical paper - external tank program - legacy of success. *AIAA SPACE 2011 Conference and Exposition. Long Beach, California.*, 2011.
- [69] ASTM B209-14. *Standard Specification for Aluminum and Aluminum-Alloy Sheet and Plate*. ASTM International, West Conshohocken, PA, 2014.
- [70] L.F. Mondolfo. Part 4 - commercial alloys. In *Aluminum Alloys*, pages 691–883. Butterworth-Heinemann, 1976.
- [71] W. Boettinger. The solidification of multicomponent alloys. *Journal of Phase Equilibria and Diffusion*, 37(1):4–18, 2016.
- [72] I. J. Polmear. *Light Alloys: Metallurgy of the Light Metals*. Edward Arnold Publishers, 1981.
- [73] V. Weiss and J.G. eds. Sessler. Aerospace structural metals handbook. volume ii. non-ferrous alloys. 1963.
- [74] J. E. Hatch. *Aluminum: Properties and Physical Metallurgy*. Metals Park, Ohio: American Society for Metals, 1984.
- [75] AMS 4191. *Aluminum Alloy, Welding Wire 6.3Cu - 0.30Mn - 0.15Ti - .10V (2319), Rev. J*. SAE International, Danvers, MA, 2015.
- [76] M. N. Brennecke. Electron beam welded heavy-gage aluminum alloy 2219. *Welding Journal*, 44(1):27s–39s, 1965.
- [77] S. Malarvizhi and V. Balasubramanian. Effect of welding processes on aa2219 aluminum alloy joint properties. *Transactions of Nonferrous Metals Society of China*, 21:962–973, 2010.
- [78] S. Malarvizhi, K. Raghukandan, and N. Viswanathan. Effect of post weld aging treatment on tensile properties of electron beam welded aa2219 aluminum alloy. *International Journal for Advanced Manufacturing Technologies*, 37:294–301, 2008.
- [79] J.Y. Bai, C.L. Fan, S. B. Lin, C.L. Yang, and B.L. Dong. Effects of thermal cycles on microstructure evolution during gta-additive manufacturing. *International Journal of Advanced Manufacturing Technology*, 87:2615–2623, 2016.

- [80] J. Bai, C. Yang, S. Lin, B. Dong, and C. Fan. Mechanical properties of 2219-al components produced by additive manufacturing with tig. *International Journal of Manufacturing Technologies*, 86:479–485, 2015.
- [81] R. Sun, L. Li, Y. Zhu, W. Guo, P. Peng, B. Cong, J. Sun, Z. Che, C. Guo, and L. Liu. Microstructure, residual stress and tensile properties control of wire-arc additive manufactured 2319 aluminum alloy with laser shock peening. *Journal of Alloys and Compounds*, 747:255–265, 2018.
- [82] AWS A5.10. *Welding Consumables - Wire Electrodes, Wires and Rods for Welding of Aluminum and Aluminum alloys - Classification, 11th ed.* American Welding Society, Danvers, MA, 2017.
- [83] AMS2770P. *Heat Treatment of Wrought Aluminum Alloy.* SAE International, 2019.
- [84] ASTM E3-11. *Standard Guide for Preparation of Metallographic Specimens.* ASTM International, West Conshohocken, PA, 2011.
- [85] ASTM E2627-13. *Standard Practice for Determining Average Grain Size Using Electron Backscatter Diffraction (EBSD) in Fully Recrystallized Polycrystalline Materials.* ASTM International, West Conshohocken, PA, 2013.
- [86] ASTM E384-16. *Standard Test Method for Microindentation Hardness of Materials.* ASTM International, West Conshohocken, PA, 2016.
- [87] ASTM E8. *Standard Test Methods for Tension Testing of Metallic Materials.* ASTM International, West Conshohocken, PA, 2016.
- [88] R. O’Hayre. *Materials Kinetics Fundamentals.* John Wiley & Sons, 2015.
- [89] S. Rao, G. Reddy, K. S. Rao, M. Kamaraj, and K. P. Rao. Reasons for superior mechanical and corrosion properties of 2219 aluminum alloy electron beam welds. *Materials Characterization*, 55:345–354, 0 2005.
- [90] *Aluminum Standards and Data 2017.* Aluminum Association, Arlington, VA, 2017.
- [91] J. Fixter, E. Eimer, Z. Pinter, B. Chehab, and P. Prangnell. Potential for in-situ solutionisation of wire and arc additive manufactured (waam) 2xxx aluminum alloys. *Proceedings of the 16th International Aluminum Alloys Conference*, 2018.

- [92] L.F. Mondolfo. Part 1 - pure and commercial aluminum. In *Aluminum Alloys*, pages 1–210. Butterworth-Heinemann, 1976.
- [93] R. Hertzberg, R. Vinci, and J. Hertzberg. *Deformation and Fracture Mechanics of Engineering Materials*. John Wiley & Sons, 2013.
- [94] J. M. Papazian. Differential scanning calorimetry evaluation of retrogressed and re-aged microstructures in aluminum alloy 7075. *Materials Science and Engineering*, 79:97–104, 1986.
- [95] J. H. Dudas and F. R. Collins. Preventing weld cracks in high-strength aluminum. *Welding Journal*, 45(6):241s–249s, 1966.
- [96] J. Gu, J. Bai, J. Ding, S. Williams, L. Wang, and K. Liu. Design and cracking susceptibility of additively manufactured al-cu-mg alloys with tandem wires and pulsed arc. *Journal of Materials Processing Technology*, 262:210–220, 2018.
- [97] D. Havens, S. Shiyekar, A. Norris, R.K. Bird, R. Kapania, and R. Olliffe. Design, optimization, and evaluation of integrally-stiffened al-2139 panel with curved stiffeners. *NASA/TM-2011-217308*, 2011.
- [98] C. Lang. Unpublished work. *NASA*, 2019.
- [99] Sandia National Laboratory. *Sierra Mechanics Finite Element Software*, 2019.
- [100] C. Wu, H. Wang, and Y. Zhang. A new heat source model for keyhole plasma arc welding in fem analysis of the temperature profile. *Welding Journal*, 85(12):284s–291s, 2006.
- [101] ASM Handbook Vol. 3. *Alloy Phase Diagrams*. ASM International, 2007.
- [102] AMS 4050. *Aluminum Alloy Plate, Solution Heat Treated, Stress Relieved, and Overaged (7050-T7451), Rev. J*. SAE International, Danvers, MA, 2014.
- [103] W. Frazier. Metal additive manufacturing: A review. *Journal of Materials Engineering and Performance*, 23(6):1917–1928, 2014.
- [104] J.Y. Bai, C.L. Fan, S. B. Lin, C.L. Yang, and B.L. Dong. Mechanical properties and fracture behaviors of gta-additive manufactured 2219-al after an especial heat treatment. *Journal of Materials Engineering and Performance*, 26(4):1808–1816, 2017.